DEPARTMENT OF APPLIED MATHEMATICS AND THEORETICAL PHYSICS
CENTRE FOR MATHEMATICAL SCIENCES

UNIVERSITY OF CAMBRIDGE

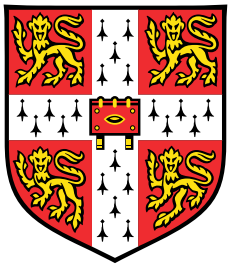

Magnetic Fields and Stellar Oscillations

by

Shyeh Tjing Loi

CORPUS CHRISTI COLLEGE

This dissertation is submitted for the degree of Doctor of Philosophy

Submitted: December 2018

Declaration

This dissertation is the result of my own work and includes nothing which is the outcome of work done in collaboration except as declared in the Preface and specified in the text.

It is not substantially the same as any that I have submitted, or, is being concurrently submitted for a degree or diploma or other qualification at the University of Cambridge or any other University or similar institution except as declared in the Preface and specified in the text. I further state that no substantial part of my dissertation has already been submitted, or, is being concurrently submitted for any such degree, diploma or other qualification at the University of Cambridge or any other University or similar institution except as declared in the Preface and specified in the text.

Abstract

Author: *Shyeh Tjing Loi*

Title: *Magnetic fields and stellar oscillations*

Stars are fluid bodies in which pressure, buoyancy, rotation and magnetism provide the restoring forces for wave propagation. Constructive interference of these waves generates global modes of oscillation. With sufficiently precise photometry, stellar oscillations can be detected through the periodic variations they induce in a star's brightness. Understanding the connection between the internal structure of a star and the properties of its normal modes is the focus of stellar oscillation theory, which generally regards rotation and magnetism to be weak perturbations compared to pressure and buoyancy. The discovery several years ago that a sizable fraction of red giant stars exhibit abnormally low dipole mode amplitudes relative to the rest of the population (the "dipole dichotomy" problem), suggesting the existence of a damping process localised to the deep interior, has presented a puzzle for theoreticians as it is not predicted in the standard framework. The restriction of this phenomenon to those stars with masses high enough to previously have hosted core dynamos points to the possible role of a hidden, relic magnetic field. It is the goal of the work presented herein to explore the nature of the interactions between waves in deep stellar interiors (in particular, gravity waves) and magnetic fields of dynamically significant strengths, that it might enable a better understanding of global mode properties and the ability to reconcile with observations.

The loss of spherical symmetry associated with the inclusion of magnetic fields renders it a mathematically complex problem to tackle, to which end we have invoked various complementary techniques: analytical treatment, numerical simulations and Hamiltonian ray tracing. We find that interactions between gravity waves and a magnetic field rely on a resonance criterion, and are always possible in some part of phase space, regardless of the field strength and the plasma β. Under these circumstances, waves may either become trapped within the field region and thereafter dissipated, or reflected in a near-specular fashion, the outcome depending on the relative orientations of the magnetic field lines, the wavevector, and the direction of stratification. Estimates of the damping rates associated with the trapping process, for realistic field configurations and field strengths of megagauss order, are consistent with those inferred from red giant observations, providing a promising resolution to the dipole dichotomy problem. The results in this thesis pave the way for an extension of the theory of stellar oscillations that incorporates the effects of dynamically significant magnetic fields.

Preface

This thesis has been organised into three parts, and comprises a total of twelve chapters, with between 3–5 chapters per part. The breakdown into such a large number of chapters stems from the use of a large number of different techniques and approaches to tackling what is not a completely straightforward problem. However, it is hoped that the manner and order in which the content has been presented makes for logical reading.

Part I, 'Physics of Gaseous Spheres', deals with stellar physics in general and comprises three chapters. Chapters 1 ('Stellar Structure and Evolution') and 2 ('Magnetism in Stellar Interiors') contain solely background material on the subject and no new research. In Chapter 3 ('Magnetohydrostatic Equilibria'), the first two sections (3.1 & 3.2) cover background material, while section 3.3 represents original work.

Part II, 'Stellar Oscillations', comprises five chapters. Chapter 4 presents the theory of linear adiabatic stellar oscillations in the absence of rotation and magnetism, while Chapter 5 focuses on the specific background to the problem addressed in this thesis, namely the "dipole dichotomy" problem. Both these chapters contain purely background material. The content of Chapter 6 is original and based on the publication 'Torsional Alfvén resonances as an efficient damping mechanism for non-radial oscillations in red giant stars' by Loi & Papaloizou (2017, MNRAS, 467, 3213). Chapters 7 and 8 also present original research, but in this case the work is preliminary and unpublished, and not related to magnetic fields.

Part III, 'Wave Propagation in a Magnetic Field', presents further investigations into the problem of local wave interactions with a dynamically significant magnetic field. It comprises four chapters, the first three of which contain results published in 'Effects of a strong magnetic field on internal gravity waves: trapping, phase mixing, reflection and dynamical chaos' by Loi & Papaloizou (2018, MNRAS, 477, 5338). Some amount of background material is contained within Chapters 9 and 10, namely those found in Sections 9.1, 9.2 and 10.1. The fourth chapter, Chapter 12, contains original though preliminary work that is as yet unpublished.

Acknowledgments

A large number of things go into making a PhD happen that aren't just the research itself. In my particular case, I would like to acknowledge and thank my college, Corpus Christi, for giving me a roof over my head and being my home away from home; my scholarship benefactor, Charles Allen, for covering my maintenance and composition fees for the three years of my degree, thus making it possible for me to be here at all; and my department, DAMTP, for providing all the necessary logistical and administrative support for me as a student. Importantly, this includes the 24/7 card access required for me to sustain my slightly eyebrow-raising office hours, which have mostly fallen during the wrong 9-to-5 and where the seven days of the week only have as much practical meaning as an arbitrary permutation thereof.

Much love to my friends and colleagues for the colour and personality they have painted into my existence here in this little town, ensuring that, for better or worse, not a single week goes by without its own unique turn of events. Thanks to all of you, the limits of my own sanity continue to be chartered and pushed to new heights. Even more love goes to my family back in Sydney for their long-distance moral support and diligently weekly Skype calls which have meant that, despite their distance, we actually talk more nowadays than when I lived at home. They have promised to visit Cambridge if I graduate.

The most significant character in this story to thank must be my PhD supervisor, John Papaloizou, for his time, encouragement, guidance and positivity, for putting up with my abysmal life management skills, for his patience with me in my darker and more dysfunctional moments, and in general, for showing far greater belief in me than I probably deserve. And of course, for being the clever one on this two-person team. Mention must also be made of my PhD advisor, Henrik Latter, for the eye he has kept out for me like a watchful older brother, for being there when my sanity has required shepherding, and for his (idiosyncratically dry, but always well intended) words of wisdom.

During its incubation phases, this thesis visited some decidedly odd locations. There are possibly not many theses in existence which can lay claim to having been partially written in the backstage bowels of the famous Minack theatre, with its author huddled in pyjamas on the dim and drafty steps of a village hall, or on a laptop balanced precariously atop the ADC stage piano just minutes pre-performance. Photographic evidence exists in the lattermost case: see below. Given the whirlwind of adventures my poor thesis has been dragged through, for which I claim sole and shameful responsibility, it is a great relief for me (and it too, if it had feelings) that it is finally finished; hope is against hope that it won't have been too much worse for the wear.

Thank you in advance to the examiners for having to read through this right mess of a tome. I willingly accept any criticism for its rather diffuse and patchy structure, which is an amusingly appropriate metaphor for me in life: a jack of all trades, master of none.

Contents

Part I

PHYSICS OF GASEOUS SPHERES

Chapter 1

Stellar Structure and Evolution

1.1 Introduction

A star is a self-gravitating body of fluid that radiates energy generated by internal processes. This may be nuclear fusion occurring deep in the interior, and/or the release of gravitational potential energy upon collapse/contraction of the gas. Throughout its lifetime, as nuclear reactions convert matter of one chemical species into another, the internal composition and structure of a star evolves (Carroll & Ostlie, 2007). Density and temperature profiles will change, and regions unstable to convection may appear and disappear. The mass of a star is an important parameter determining the timescales and nature of these changes, as well as overall properties such as radius and luminosity. Stars of different masses evolve in quite different ways and undergo different internal processes at different stages of evolution.

A quantity pertinent to later discussion is the *dynamical timescale* $t_{\rm dyn}$ of a star. If the thermal pressure supporting the gas against the pull of gravity were to suddenly vanish, then this is how long it would take the star to collapse upon itself (the "free-fall" time). Characteristically, one can expect this to occur on a timescale given by $\sqrt{R_*/g}$, where R is the stellar radius and $g \sim GM_*/R_*^2$ is the surface gravitational acceleration, G being Newton's gravitational constant and M_* being the total stellar mass. Thus

$$t_{\rm dyn} \sim \sqrt{\frac{R_*^3}{GM_*}}. \tag{1.1}$$

For a dynamically stable star, this is also the timescale on which equilibrium would be restored following a small perturbation. In the case of the Sun, $t_{\rm dyn}$ is about half an hour, while for a red giant of solar mass, $t_{\rm dyn}$ could be up to several weeks. These values are much smaller than typical evolutionary timescales, and so for most of their lives, and certainly during the phases of evolution considered in this thesis, stars can be regarded as being close to dynamical equilibrium.

A number of additional timescales may be used to characterise a star. These include the thermal or *Kelvin-Helmholtz* timescale $t_{\rm KH}$, after the two physicists who estimated it to be the evolutionary timescale of a star generating its energy output solely by gravitational contraction, and the nuclear timescale $t_{\rm nuc}$, which refers to the timescale needed to radiate away the energy generated by nuclear processes (Kippenhahn & Weigert, 1990). In the case of $t_{\rm KH}$, this is given by the gravitational binding energy E_g divided by the luminosity L, where E_g may be estimated as

$$|E_g| = \int_0^{M_*} \frac{Gm_r}{r}\,{\rm d}m_r \sim \frac{GM_*^2}{R_*} \quad \Longrightarrow t_{\rm KH} \sim \frac{GM_*^2}{R_* L}, \tag{1.2}$$

m_r being the mass enclosed within radius r. For the Sun, given that its average luminosity is about $L = 3.83 \times 10^{26}$ W, $t_{\rm KH}$ evaluates to about 10^7 years, much shorter than its current age of 4.6 Gyr. Gravitational contraction alone is thus insufficient to account for the energy output of the Sun and similar stars. Rather, this is dominated by nuclear processes, in particular the fusion of hydrogen into helium which releases about 0.7% of the rest mass energy of the consumed hydrogen. If one considers the Sun to have started out as being pure hydrogen, with 10% of this converted to helium over its lifetime, the amount of energy released would be about 10^{44} J, yielding a nuclear timescale of $t_{\rm nuc} \sim 10^{10}$ yr. In general, for stars like the Sun that produce energy through nuclear fusion of hydrogen to helium, it is the case that

$$t_{\rm dyn} \ll t_{\rm KH} \ll t_{\rm nuc}\,, \tag{1.3}$$

which enables simplifying assumptions to be made regarding the energy equation (see later in §1.2.1) in that certain derivatives can be neglected depending on the time scales of phenomena under study. In particular, it justifies the use of the adiabatic approximation used in much of the theoretical treatment of stellar oscillations.

1.2 Solving for stellar structure

1.2.1 Equations

We shall assume spherical symmetry of the system, meaning that any deformation due to centrifugal effects, magnetic fields, tidal interactions, etc. will be ignored. The governing equations can then be cast in terms of just either the radial coordinate r (Eulerian description) or the mass coordinate m_r (Lagrangian description). The forces associated with rotation and magnetism will be ignored; only those of pressure and gravity will be considered in this section.

The force per unit area acting on a mass shell element $\mathrm{d}m_r$ is given by the sum of the pressure gradient and the gravitational force per unit area. That is,

$$\frac{1}{4\pi r^2}\frac{\partial^2 r}{\partial t^2}\,\mathrm{d}m_r = -\frac{\partial p}{\partial m_r}\,\mathrm{d}m_r - \frac{g}{4\pi r^2}\,\mathrm{d}m_r \tag{1.4}$$

where

$$g = \frac{Gm_r}{r^2} \tag{1.5}$$

is the gravitational acceleration at radial coordinate r, and p is the gas pressure. This leads to

$$\frac{\partial p}{\partial m_r} = -\frac{1}{4\pi r^2}\frac{\partial^2 r}{\partial t^2} - \frac{Gm_r}{4\pi r^4} \tag{1.6}$$

as the equation of motion of the mass shell.

Next, we consider energy conservation. Defining L_r as the local luminosity, i.e. the energy per unit time passing through a sphere of radius r, we have

$$\frac{\partial L_r}{\partial m_r} = \epsilon - \frac{\mathrm{d}q}{\mathrm{d}t}\,, \tag{1.7}$$

where $\mathrm{d}q$ is the heat per unit mass exchanged between the shell and its adjacent layers within the time $\mathrm{d}t$. The quantity ϵ is the sum of the energy generated by nuclear processes per unit time per unit mass, and any losses associated with neutrino emission at radius r.

The temperature distribution depends on the efficiency of radiative transport, the associated scales of which are typically much less than the stellar radius for most the interior of a star. In non-convective zones, the radiative energy flux F is given in terms of the temperature T by

$$F = -\frac{4acT^3}{3\kappa\rho}\frac{\partial T}{\partial r}, \tag{1.8}$$

where ρ is the mass density, c is the speed of light, a is the the radiation-density constant, and κ is the Rosseland mean opacity. Since the local luminosity $L_r = 4\pi r^2 F$, this leads to

$$\frac{\partial T}{\partial r} = -\frac{3\kappa\rho L_r}{16\pi acr^2 T^3}. \tag{1.9}$$

To transform this into Lagrangian form, one requires the relationship between the mass and radial coordinates, which can be derived by considering conservation of mass. The differential change in mass contained in a shell of thickness $\mathrm{d}r$ is given by

$$\mathrm{d}m_r = 4\pi r^2 \rho\,\mathrm{d}r - 4\pi r^2 \rho v\,\mathrm{d}t, \tag{1.10}$$

where v is the radial velocity of the shell. From this, we see that

$$\frac{\partial m_r}{\partial r} = 4\pi r^2 \rho, \tag{1.11}$$

$$\frac{\partial m_r}{\partial t} = -4\pi r^2 \rho v. \tag{1.12}$$

Cross-differentiating and equating the two above expressions, we obtain

$$\frac{\partial \rho}{\partial t} = -\frac{1}{r^2}\frac{\partial}{\partial r}(\rho r^2 v), \tag{1.13}$$

which can be recognised as the spherically symmetric version of the familiar continuity equation. Equation (1.9) can then be rewritten

$$\frac{\partial T}{\partial m_r} = -\frac{3\kappa L_r}{64\pi^2 acr^4 T^3}. \tag{1.14}$$

In convective regions, it is less straightforward to obtain an expression for the energy flux owing to the need to invoke an estimate of the "mixing length", which represents the mean free path of macroscopic parcels of fluid. In this case, Equation (1.14) may be written in the more general form

$$\frac{\partial T}{\partial m_r} = -\frac{Gm_r T}{4\pi r^4 p}\nabla, \tag{1.15}$$

where the gradient $\nabla \equiv \partial \ln T / \partial \ln p$ depends on the details of the particular mixing-length theory employed. For convection occurring in the deep interior, ∇ may be approximated by the adiabatic value

$$\nabla_{\mathrm{ad}} \equiv \left(\frac{\partial \ln T}{\partial \ln p}\right)_s, \tag{1.16}$$

where the subscript s indicates that this is under constant entropy.

Equations (1.6), (1.7), (1.11), (1.14) and (1.15) are known as the equations of stellar structure. These can be further simplified if the star can be assumed to always be in hydrostatic equilibrium, a good approximation if $t_{\mathrm{nuc}}, t_{\mathrm{KH}} \gg t_{\mathrm{dyn}}$. This would allow us to neglect time derivatives if only short-term effects are under

study. In any case, the four equations in Eulerian form are

$$\frac{\partial m_r}{\partial r} = 4\pi r^2 \rho \,, \tag{1.17}$$

$$\frac{\partial p}{\partial r} = -\frac{G m_r \rho}{r^2} - \rho \frac{\partial^2 r}{\partial t^2} \,, \tag{1.18}$$

$$\frac{\partial L_r}{\partial r} = 4\pi r^2 \rho \left(\epsilon - \frac{\mathrm{d}q}{\mathrm{d}t} \right) , \tag{1.19}$$

$$\frac{\partial T}{\partial r} = -\frac{G m_r T \rho}{r^2 p} \nabla \,. \tag{1.20}$$

These are known as the continuity equation, the equation of hydrostatic balance, the energy equation, and the transport equation, respectively.

1.2.2 Polytropic models

If one considers just the first two equations of stellar structure, namely continuity and hydrostatic balance, a class of simple stellar models known as *polytropes* can be constructed (Prialnik, 2000). These are useful for simple applications when one requires only an approximate model, since they are relatively simple to compute.

For the purposes of this section, we shall work in Eulerian coordinates and regard all quantities as being functions of r only. The two aforementioned equations can be combined into the single second-order ordinary differential equation (ODE)

$$\frac{1}{r^2} \frac{\mathrm{d}}{\mathrm{d}r} \left(\frac{r^2}{\rho} \frac{\mathrm{d}p}{\mathrm{d}r} \right) = -4\pi G \rho \,. \tag{1.21}$$

Next, we assume that p and ρ are related by a *polytropic equation of state*,

$$p = K \rho^{1+\frac{1}{n}} \,, \tag{1.22}$$

where K and n are constants. Then Equation (1.21) can be reduced to one with just a single dependent variable, usually referred to as the *polytropic temperature*, θ, and defined such that

$$\frac{\rho}{\rho_c} = \theta^n \,, \quad \frac{p}{p_c} = \theta^{n+1} \,, \tag{1.23}$$

where ρ_c and p_c are the central density and pressure. The constant n is known as the *polytropic index*, and controls the shape of the resulting solution. It is related to the adiabatic index γ by

$$\gamma = 1 + \frac{1}{n} \,. \tag{1.24}$$

It is convenient to rescale the radial coordinate according to

$$r = \alpha \xi \,, \tag{1.25}$$

where

$$\alpha = \left[\frac{K(n+1)\rho_c^{\frac{1}{n}-1}}{4\pi G} \right]^{1/2} \tag{1.26}$$

is a characteristic scale length and ξ is the new radial parameter. This choice of rescaling turns Equation (1.21) into

$$\frac{1}{\xi^2} \frac{\mathrm{d}}{\mathrm{d}\xi} \left(\xi^2 \frac{\mathrm{d}\theta}{\mathrm{d}\xi} \right) + \theta^n = 0 \,, \tag{1.27}$$

which is called the *Lane-Emden equation* (Lane, 1870; Emden, 1907). Analytical solutions exist only for indices $n = 0, 1$ and 5. For all other values of n, Equation (1.27) must be solved by numerical integration.

The relevant boundary conditions, up to an arbitrary normalisation factor, are

$$\theta(0) = 1\,, \quad \theta'(0) = 0\,, \tag{1.28}$$

where primes denote derivatives with respect to ξ. In practice, integration of Equation (1.27) starts at $\xi = 0$ and is terminated when θ reaches 0. We shall call the terminating value of the radial coordinate ξ_*, which represents the radius of the star. One complication is that the origin is a regular singular point of the ODE, so rather than trying to impose boundary conditions at $\xi = 0$, this needs to be done at a point arbitrary close to, but not exactly at, the origin. The corresponding form of the boundary conditions at non-zero ξ can be obtained by a power series expansion, that is assuming the form

$$\theta(\xi) = \xi^k \sum_{m=0}^{\infty} b_m \xi^m \tag{1.29}$$

and substituting this into Equation (1.27) under a chosen value of n. For example, for $n = 3$ and with the series truncated at $m = 2$, we find (again, up to an arbitrary normalisation) that as $\xi \to 0$

$$\theta(\xi) \approx 1 - \frac{1}{6}\xi^2\,, \quad \theta'(\xi) \approx -\frac{1}{3}\xi\,. \tag{1.30}$$

The five dimensionful parameters K, ρ_c, p_c, R_* and M_*, which are at this stage still undetermined, are not independent of one another. If a fully dimensional solution is desired, the values of two of these must be chosen in advance. For example, one may choose to fix the stellar mass and radius. Once the solution for $\theta(\xi)$ is obtained and the value of ξ_* known, then this determines

$$K = \frac{(4\pi)^{1/n} G}{n+1} \left[-\xi_*^2 \theta'(\xi_*)\right]^{\frac{1}{n}-1} \xi_*^{1-\frac{3}{n}} R_*^{\frac{3}{n}-1} M_*^{1-\frac{1}{n}}\,, \tag{1.31}$$

$$\rho_c = \left[\frac{4\pi G}{K(n+1)} \left(\frac{R_*}{\xi_*}\right)^2\right]^{\frac{n}{1-n}}\,, \tag{1.32}$$

$$p_c = K \rho_c^{1+\frac{1}{n}}\,. \tag{1.33}$$

Main sequence stars and stars with degenerate relativistic cores ($\gamma = 4/3$) are often modelled using a polytropic index of $n = 3$ (Shore, 1992). The value $n = 1.5$ corresponds to the case of an ideal, adiabatic, monatomic gas ($\gamma = 5/3$), and is used to model convective stellar cores. White dwarfs, which are degenerate and non-relativistic objects, can also be described by $n = 1.5$ (e.g. Suijs et al., 2008). Neutron stars, with γ between 2–3, can be modelled by polytropes of n between 0.5–1.5 (e.g. Friedman et al., 1986). The larger the polytropic index, the less centrally condensed the density distribution: for example, $n = 5$ corresponds to a sphere of infinite radius. Red giant envelopes may be modelled by polytropic indices between $n = 3$ to 5 (Eggleton & Faulkner, 1981).

1.2.3 Stellar evolution codes

It is possible to model stellar structure and its evolution by solving Equations (1.17)–(1.20). However, unless drastic simplifications are made (such as described in §1.2.2) so as to allow for analytic solutions, the problem must be solved numerically. Note that none of the results presented in this thesis involved writing or executing such a code ourselves. The relevance of the present section lies only insofar as we made some use of models which were generated by a stellar evolutionary code, this having been written by others.

In order to solve the equations of stellar structure, the physical properties of the gas forming the star must be known. More precisely, one requires constitutive relations $p(\rho, T, X_i)$, $\kappa(\rho, T, X_i)$ and $\epsilon(\rho, T, X_i)$, where i indexes a chemical species X (Choudhuri, 2010). Obtaining reasonable forms for these is a non-trivial task, since large numbers of physical processes are involved. Various evolutionary codes differ in their implementation of these relations. Broadly speaking, the equation of state for $p(\rho, T, X_i)$ to first approximation can be taken to be the ideal gas law combined with radiation pressure. However, this becomes more complex in certain regimes of high and low densities and/or temperatures, where partial ionisation, electron-positron pair production, and crystallisation may come into play. Opacities are more complicated still to compute, since there are contributions from many processes, the main four of which are bound-bound transitions, bound-free absorption, free-free absorption and electron scattering (Carroll & Ostlie, 2007). No single exact formula exists, and so stellar evolution codes often interpolate upon a pre-computed grid of $\kappa(\rho, T, X_i)$ values. The energy generation rate $\epsilon(\rho, T, X_i)$ depends on the nature of the nuclear reactions operating. These are proton-proton chain reactions for intermediate/low-mass stars, and the carbon-nitrogen-oxygen cycle for higher mass stars. In evolved stars, energy generation may also occur by way of the triple-α process and carbon-oxygen burning.

With the three constitutive relations in place, the system of equations involves four independent variables: ρ, T, m_r and L_r. This is equal to the number of independent equations, and so the system can be integrated accordingly to obtain a spatial solution at any given time. The appropriate boundary conditions are given by

$$m_r(0) = 0\,, \quad L_r(0) = 0\,, \tag{1.34}$$

$$\rho(R_*) = 0\,, \quad T(R_*) = 0\,. \tag{1.35}$$

Numerous approaches exist, both Eulerian and Lagrangian, for solving the system under these boundary conditions. A simple method one might conceive of would be to shoot two solutions from each end of the radial grid, and then match them at some intermediate point. A more efficient method developed by Henyey et al. (1964), and based on finite differencing, involves pre-specifying a grid at each time step and solving for all variables at each grid point simultaneously by inverting a large matrix. This is the method employed by the code *Modules for Experiments in Astrophysics* (MESA) written by Paxton et al. (2011). In contrast, the *Code d'Evolution Stellaire Adaptatif et Modulaire* (CESAM) code uses a B-spline collocation method (Morel, 1997). Driven by changes in chemical composition, the solution also evolves in time, which can be handled by an appropriate choice of time-stepping scheme.

1.2.4 Existence and uniqueness

The question of whether the equations of stellar structure admit a single unique equilibrium solution given M_* and X_i was addressed independently by Heinrich Vogt and Henry Norris Russell (Vogt, 1926; Russell, 1931), who proposed on the basis of simple considerations that this should be true. The conjecture, now known as the *Vogt-Russell theorem* (though not a theorem in the strict sense of the word), has since been disproven by way of counterexample, but nonetheless remains a popular assumption that holds in most astrophysically relevant conditions. That is, given a certain mass and chemical composition, nature appears to favour only one particular solution. An illustrative, non-rigorous argument for the Vogt-Russell theorem is that pre-selection of the mass and composition fixes all gradients in the stellar structure equations, and

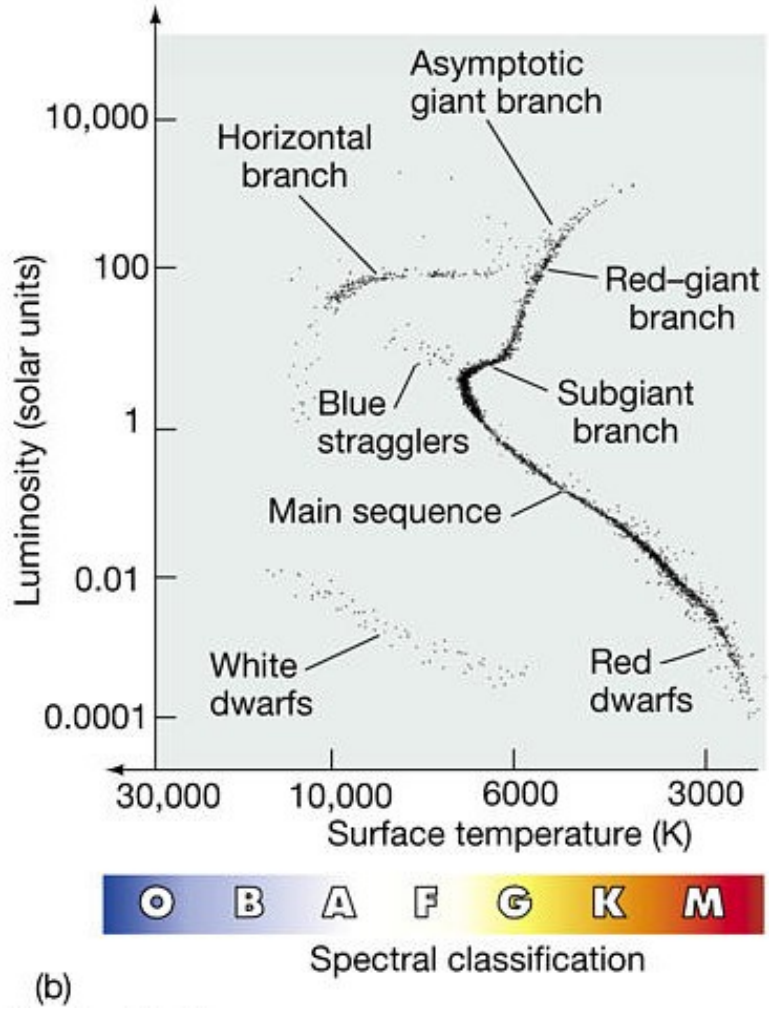

Figure 1.1: The Hertzsprung-Russell diagram labelled with various evolutionary stages (Chaisson & McMillan, 2014).

so it is not possible to independently specify the radius and luminosity. However, there may be stages in a star's evolution where the usual approximations break down and the system reaches a branching point where statistical instabilities determine its subsequent fate (Kähler & Weigert, 1974).

1.3 Evolutionary stages

Stars of different masses evolve on different timescales and go through somewhat different phases of evolution. In general, lower mass stars evolve on longer timescales. The various stages of evolution can be visualised using a Hertzsprung-Russell (H-R) diagram, which separates types of stars in luminosity-temperature space (see Figure 1.1).

1.3.1 Pre-main sequence

Star formation begins when the gravitational force in a gas cloud overcomes that associated with pressure (the Jean's instability criterion), resulting in collapse of the cloud on a timescale t_{KH} (around 10^7 yr for a solar-mass star). The release of gravitational potential energy heats the gas and surrounding dust, generating infrared emission. The collapsing object, known as a *protostar*, moves leftward on the H-R diagram

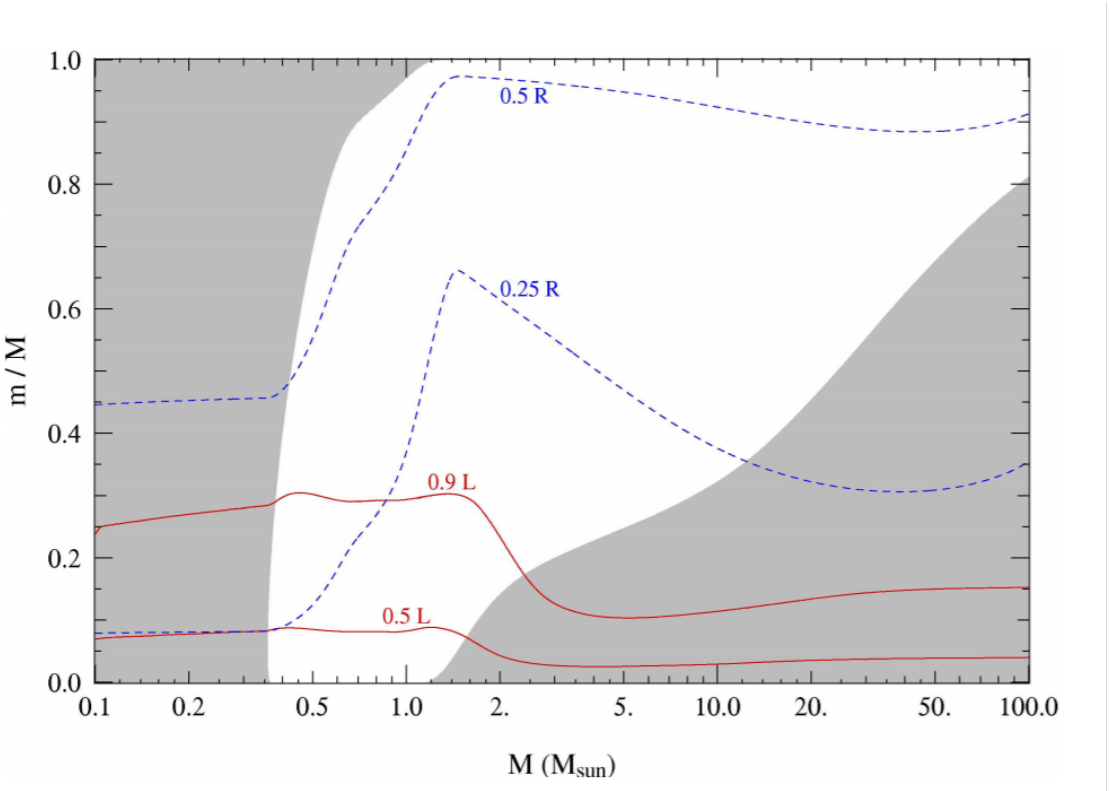

Figure 1.2: Diagram showing convective regions (greyscale) for zero-age main sequence stars in fractional mass coordinates (Kippenhahn & Weigert, 1990).

until it reaches what is known as the *Hayashi track* (Hayashi, 1961) and becomes fully convective. The efficiency with which convection allows the star to lose energy causes it to move down and slightly to the left on the H-R diagram following the Hayashi track, until the efficiency of radiative transport surpasses that of convection as a means of energy loss. At this point, stars move massive than about $0.5\,M_\odot$ move onto the *Henyey track* (Henyey et al., 1955), which is a horizontal path leading eventually to the main sequence. Those of lower masses move straight downward and end up on the main sequence without going through a Henyey track phase. When a star first reaches the main sequence, it is known as a zero-age main-sequence (ZAMS) object. The structure of convective and radiative regions on the ZAMS is mass dependent. These regions are indicated in Figure 1.2. Stars below $0.35\,M_\odot$ end up fully convective, while those between 0.35 and $1.2\,M_\odot$ possess radiative cores and convective envelopes. Stars of still higher masses have convective cores and radiative envelopes.

1.3.2 Main sequence

A main sequence star is defined to be one which is generating its energy mainly by the fusion of hydrogen into helium. Stars in this phase occupy a narrow track on the H-R diagram running diagonally from bottom-right to top-left (see Figure 1.1). What separates stars along the main sequence is predominantly stellar mass. More massive stars are hotter and more luminous, because the larger central pressures and densities enable the more rapid consumption of nuclear fuel. The length of time a star spends in this phase is of order $t_{\rm nuc}$, which is about 10^{10} yr for a solar-mass star.

As mentioned in the previous section, a star more massive than about $1.2\,M_\odot$ has a convective core,

and one smaller than 0.35 $M_\odot$ is fully convective. The presence of convection efficiently mixes the material, maintaining chemical homogeneity and allowing a greater fraction of hydrogen to be converted into helium. Note that convective turnover times are much shorter than $t_{\rm nuc}$. In the case of stars over 1.2 $M_\odot$, the convective core retreats over the course of the main sequence, leaving behind a compositional gradient. Eventually, as the convective zone vanishes, hydrogen becomes exhausted in the core and continues to burn in a shell. The helium produced by this hydrogen shell-burning rains into the layers below. Since at this stage no nuclear burning takes place in the helium core, and all energy generation occurs in a shell around it, the core becomes isothermal. A maximum mass exists for an isothermal core beyond which it is unable to support the weight of overlying material, known as the *Schönberg-Chandrasekhar limit* (Schönberg & Chandrasekhar, 1942). Once this limit is reached, the core collapses on a timescale $t_{\rm KH}$, the envelope expands and the star evolves off the main sequence to become a red giant.

Stars with masses between 0.35–1.2 $M_\odot$ have radiative cores, and so as hydrogen burning proceeds, helium is deposited in the centre of the star. After the core becomes depleted of hydrogen, hydrogen burning continues in a shell around the helium core. In a similar fashion to higher-mass stars, when the Schönberg-Chandrasekhar limit is exceeded, the helium core begins to collapse. This defines the end of the main sequence for intermediate mass stars, which thereafter go on to become red giants.

In the case of stars below 0.35 $M_\odot$, which are fully convective throughout the main sequence, the picture differs. Continued convection prevents composition gradients or a helium core surrounded by a hydrogen-burning shell from forming (Laughlin et al., 1997). Such stars can build up a large mass fraction of helium in their interiors. If less massive than about 0.25 $M_\odot$, the star will not expand to become a red giant, but instead gradually become hotter and turn into a "blue dwarf" (Adams et al., 2005). After running out of nuclear fuel, it will collapse slowly and eventually become a helium white dwarf. Stars slightly more massive may evolve into red giants, but without sufficient core temperatures to ignite helium, they may never reach the tip of the red giant branch. Rather, they will leave prematurely to become white dwarfs. White dwarfs are compact objects supported by electron degeneracy pressure, and are not significantly convecting in any part of their volume.

1.3.3 Post-main sequence

Contraction of the core on timescale $t_{\rm KH}$ due to crossing of the Schönberg-Chandrasekhar limit at the end of the main sequence is accompanied by expansion of the envelope (the "mirror principle"), resulting in a drop in surface temperature. The star moves rapidly to the right on the H-R diagram, crossing what is known as the *Hertzsprung gap*, and lands at the base of the red giant branch (RGB). During this intermediate phase, the star is referred to as a subgiant.

As the star ascends the RGB, a thick convective envelope forms, starting at the surface and subsequently deepening. This proceeds until it reaches the top of the core, where nuclear reactions had previously modified the chemical composition. Processed material becomes mixed with the overlying untouched material, producing observable changes in chemical composition at the surface. This is known as the *first dredge-up* phase.

Eventually, the core contracts and heats up to the point where helium fusion via the triple-α process can begin. This occurs at the tip of the RGB. Associated with helium ignition is an expansion of the core, pushing the overlying hydrogen-burning shell outward and causing it to cool. The diminished energy output from

the shell causes the overall luminosity to drop, and together with contraction of the envelope the surface temperature also increases. The result is a reversal of motion of the star back down the RGB. A notable difference in the nature of helium ignition arises between stars more and less massive than about $1.8\,M_\odot$. For stars less massive, the helium core acquires a significant degree of degeneracy as the star ascends the RGB. The ignition of helium initially in a shell around the core rapidly lifts the degeneracy of the core, momentarily reaching tremendous luminosities ($\sim 10^{11}\,L_\odot$) in what is known as a *helium flash*. More massive stars do not experience such a dramatic ignition, since their helium cores remain non-degenerate: in these cases, helium burning begins gently.

Accompanying the onset of helium burning is the development of a convective core due to the high temperature sensitivity of the triple-α process, while the convective envelope retreats upward. The star evolves onto the *horizontal branch* (HB), which may be regarded as the helium-burning analogue of the main sequence. It is during their time spent on the HB that stars may fall into what is known as the *instability strip*, and undergo self-excited, periodic oscillations (as in Cepheid variables). More details and the physics behind this will be discussed further in §4.4.

When the luminosity of the helium-burning core overtakes that of the hydrogen-burning shell, the star evolves onto the asymptotic giant branch (AGB), which closely parallels the RGB. During this phase, a carbon-oxygen core develops, fed by products of the triple-α process, while helium burning continues in a surrounding shell. As the core becomes increasing degenerate, it shrinks and heats up, and the helium burning rate increases. At the same time the envelope expands further still, the hydrogen-burning shell extinguishes, and the convective envelope advances further down. This causes material processed by the hydrogen-burning shell and below to be brought up to the surface in the *second dredge-up* phase. More hydrogen from the overlying layers is brought down, allowing for a re-ignition of the hydrogen-burning shell. The configuration in this state, with two burning shells (hydrogen and helium) above a degenerate core, is unstable to thermal pulses associated with the Härm-Schwarzschild instability (Schwarzschild & Härm, 1965). This causes yet more processed material to surface in a *third dredge-up* phase.

1.3.4 Degenerate stars

The endpoints of stellar evolution are compact, degenerate objects that no longer generate energy by nuclear processes, but rather are faintly luminous owing to the emission of thermal radiation. As already discussed above, low-mass stars unable to attain temperatures sufficient for igniting helium end their lives as helium white dwarfs. More massive stars, but those still less than $8\,M_\odot$, lose significant amounts of mass during the thermal pulse phase, where almost their entire envelopes are shed and expand outwards as *planetary nebulae*. This exposes the underlying core, which is a carbon-oxygen white dwarf.

If the star is more massive than $8\,M_\odot$, nuclear burning continues on to heavier and heavier elements within the core until a degenerate iron core is formed. Since fusion of iron into heavier elements is endothermic, the iron core remains inert and grows until the Chandrasekhar limit of $1.4\,M_\odot$ is reached, beyond which electron degeneracy pressure can no longer counterbalance self-gravity (Chandrasekhar, 1931). At this point the star implodes in a Type II supernova. This produces either a neutron star, if the original star was less massive than about $25\,M_\odot$, or otherwise a black hole may be formed.

Chapter 2

Magnetism in Stellar Interiors

2.1 General concepts

2.1.1 Magnetohydrodynamics

The equations of magnetohydrodynamics (MHD) are obtained by combining Maxwell's equations, given by

$$\nabla \cdot \mathbf{E} = \frac{\rho_e}{\epsilon_0}, \tag{2.1}$$

$$\nabla \cdot \mathbf{B} = 0, \tag{2.2}$$

$$\nabla \times \mathbf{E} = -\frac{\partial \mathbf{B}}{\partial t}, \tag{2.3}$$

$$\nabla \times \mathbf{B} = \mu_0 \left(\mathbf{J} + \epsilon_0 \frac{\partial \mathbf{E}}{\partial t} \right), \tag{2.4}$$

with those of fluid dynamics:

$$\frac{\partial \rho}{\partial t} = -\nabla \cdot (\rho \mathbf{u}) \tag{2.5}$$

$$\rho \left(\frac{\partial \mathbf{u}}{\partial t} + \mathbf{u} \cdot \nabla \mathbf{u} \right) = -\nabla p - \nabla \Phi + \mathbf{F}. \tag{2.6}$$

Here ϵ_0 is the vacuum permittivity, μ_0 is the vacuum permeability, ρ_e is the charge density, $\mathbf{E}$ is the electric field, $\mathbf{B}$ is the magnetic field, $\mathbf{J}$ is the electric current density, $\mathbf{u}$ is the fluid velocity, Φ is the combined gravitational and centrifugal potential, and $\mathbf{F}$ is the sum of additional body forces (e.g. arising from rotation or magnetic fields). Consider Ohm's law:

$$\mathbf{J} = \sigma \left(\mathbf{E} + \mathbf{u} \times \mathbf{B} \right), \tag{2.7}$$

where σ is the electrical conductivity. In the limit of ideal MHD, i.e. $\sigma \to \infty$ (perfectly conducting fluid), to prevent unphysically infinite current densities, it must be that

$$\mathbf{E} + \mathbf{u} \times \mathbf{B} = 0. \tag{2.8}$$

Note that the fluid equations apply in the non-relativistic limit. If we were to extend this approximation to Maxwell's equations, the displacement current in Ampère's law (Equation 2.4) can be neglected. To see this, consider motions on a characteristic length scale L, occurring with some characteristic speed $u \ll c$. Since $\mu_0 \epsilon_0 = 1/c^2$, the last term on the right-hand side of Equation (2.4) has a magnitude of roughly $uB/(c^2\tau)$, where $\tau \sim L/u$ is the characteristic time scale, and B is a characteristic field strength. Now the

left-hand side of Equation (2.4) goes as B/L, which is larger than $uB/(c^2\tau)$ by a factor $c^2/u^2 \gg 1$. This justifies neglect of the displacement current in the non-relativistic limit.

In the absence of rotation, we incorporate the Lorentz force by setting $\mathbf{F} = \mathbf{J} \times \mathbf{B}$. Using Equation (2.8) to eliminate $\mathbf{E}$ in favour of $\mathbf{B}$, we arrive at the equations of ideal MHD (e.g. Ogilvie, 2016):

$$\frac{\partial \rho}{\partial t} = -\nabla \cdot (\rho \mathbf{u}) \,, \tag{2.9}$$

$$\rho \left(\frac{\partial \mathbf{u}}{\partial t} + \mathbf{u} \cdot \nabla \mathbf{u} \right) = -\nabla p - \rho \nabla \Phi + \frac{1}{\mu_0} (\nabla \times \mathbf{B}) \times \mathbf{B} \,, \tag{2.10}$$

$$\nabla \cdot \mathbf{B} = 0 \,, \tag{2.11}$$

$$\frac{\partial \mathbf{B}}{\partial t} = \nabla \times (\mathbf{u} \times \mathbf{B}) \,. \tag{2.12}$$

These are the continuity equation, the momentum equation, the solenoidal condition, and the induction equation, respectively. In the case of finite conductivity σ (non-ideal MHD), where σ is a constant over scales of interest, the induction equation contains an extra resistive term (e.g. Shore, 1992):

$$\frac{\partial \mathbf{B}}{\partial t} = \nabla \times (\mathbf{u} \times \mathbf{B}) + \frac{\nabla^2 \mathbf{B}}{\mu_0 \sigma} \,. \tag{2.13}$$

These equations neglect the effects of non-adiabatic heating, which we will not be dealing with in this thesis. If other sources of heating are to be accounted for, then the system would involve an additional equation enforcing conservation of specific entropy. Note that an additional relation is required to close the system, which is usually provided in the form of an equation of state. For example, an adiabatic ideal gas would be governed by $p \propto \rho^\gamma$, where γ is the ratio of specific heats (the adiabatic index).

2.1.2 Magnetic pressure and tension

With aid of an appropriate vector identity, the Lorentz force can be written

$$\mathbf{J} \times \mathbf{B} = \frac{1}{\mu_0} (\nabla \times \mathbf{B}) \times \mathbf{B} \tag{2.14}$$

$$= -\nabla \left(\frac{B^2}{2\mu_0} \right) + \frac{1}{\mu_0} (\mathbf{B} \cdot \nabla) \mathbf{B} \,. \tag{2.15}$$

These two terms can be interpreted in terms of the gradient of a pressure $p_m \equiv B^2/(2\mu_0)$ associated with the magnetic field, and a magnetic tension. The former is related to the magnetic energy density, whose ratio with the thermal energy density (given by the gas pressure p) defines the plasma $\beta \equiv p/p_m$. Stellar interiors are characterised by plasma β values greatly in excess of unity, indicating that the thermal pressure always dominates over the magnetic pressure in shaping the overall stellar structure.

One physical significance of the magnetic pressure is the role it plays in the buoyant rise of magnetic flux tubes. Pressure balance dictates that $p + p_m$ is constant (at least, on some reasonably local scale), and so where fields are stronger, the gas pressure is lower. If the fluid is an ideal gas in thermal equilibrium, then the lower gas pressure must imply a lower density. Regions of strong field are thus more buoyant than the surrounding gas, and tend to rise.

The magnetic tension is so named because it is analogous to the tension in a stretched string. To see

this, define the field-aligned unit vector $\mathbf{b} \equiv \mathbf{B}/|\mathbf{B}|$, and consider

$$\begin{aligned}\frac{1}{\mu_0}(\mathbf{B}\cdot\nabla)\mathbf{B} &= \frac{1}{\mu_0}(B\mathbf{b}\cdot\nabla)(B\mathbf{b}) \\ &= \frac{B^2}{2\mu_0}(\mathbf{b}\cdot\nabla)\mathbf{b} + \mathbf{b}\mathbf{b}\cdot\nabla\left(\frac{B^2}{2\mu_0}\right).\end{aligned} \tag{2.16}$$

The second term on the right-hand side can be identified as the component of the magnetic pressure in the direction of the field lines (note that the magnetic pressure itself is independent of the field direction). The first term on the right-hand side points locally perpendicular to the magnetic field lines, and is larger when the field lines are more tightly curved, as interpreted from $(\mathbf{b}\cdot\nabla)\mathbf{b}$ which is inversely proportional to the spatial rate of change of the field line vector. This part represents the tension force, which on a string acts perpendicularly and increases with increasing curvature of the string.

2.1.3 Magnetic flux

A useful quantity which may be defined is the *magnetic flux*, which can be thought of as a measure of the number of field lines passing through a given closed loop. Suppose this loop defines a surface $\mathscr{S}$, with area element $\mathrm{d}\mathbf{S}$. Then the magnetic flux is

$$\psi = \int_{\mathscr{S}} \mathbf{B}\cdot\mathrm{d}\mathbf{S}. \tag{2.17}$$

The induction equation has a physical interpretation in terms of advection of magnetic flux. This can be demonstrated if one considers how material lines are advected through the fluid. Let us follow the motion of one such material line which happens to coincide with a certain magnetic field line at a given instant. Now a material line can be defined by the intersection of two material surfaces, described by the loci of points satisfying $\alpha(\mathbf{x}, t) = 0$ and $\beta(\mathbf{x}, t) = 0$. Suppose we write

$$\mathbf{B} = \nabla\alpha \times \nabla\beta, \tag{2.18}$$

where $\mathbf{x}$ represents the position vector. Note that α and β can be rescaled to absorb any factors associated with the magnitude or units of $\mathbf{B}$. In the ideal MHD limit (no diffusion or resistivity), the surfaces are advected perfectly and retain their identity, meaning that their material derivatives $D/Dt \equiv \partial/\partial t + \mathbf{u}\cdot\nabla$ vanish, i.e.

$$\frac{\partial\alpha}{\partial t} = -\mathbf{u}\cdot\nabla\alpha \tag{2.19}$$

$$\frac{\partial\beta}{\partial t} = -\mathbf{u}\cdot\nabla\beta. \tag{2.20}$$

Consider the time derivative of Equation (2.18):

$$\begin{aligned}\frac{\partial\mathbf{B}}{\partial t} &= \nabla\left(\frac{\partial\alpha}{\partial t}\right)\times\nabla\beta + \nabla\alpha\times\nabla\left(\frac{\partial\beta}{\partial t}\right) \\ &= -\nabla\left(\mathbf{u}\cdot\nabla\alpha\right)\times\nabla\beta - \nabla\alpha\times\nabla\left(\mathbf{u}\cdot\nabla\beta\right) \\ &= -\nabla\times\left[\left(\mathbf{u}\cdot\nabla\alpha\right)\nabla\beta - \left(\mathbf{u}\cdot\nabla\beta\right)\nabla\alpha\right] \\ &= \nabla\times\left[\mathbf{u}\times\left(\nabla\alpha\times\nabla\beta\right)\right] \\ &= \nabla\times(\mathbf{u}\times\mathbf{B})\end{aligned} \tag{2.21}$$

which is precisely the induction equation. This implies that in the ideal MHD limit, magnetic field lines are *frozen in* to the fluid and are advected along with it.

2.1.4 Magnetic helicity

A measure of the topology of a field configuration is the *magnetic helicity*, defined over a volume V by

$$\mathscr{H} = \int_V \mathbf{A}\cdot\mathbf{B}\,\mathrm{d}V\,, \tag{2.22}$$

where $\mathbf{A}$ is the magnetic vector potential satisfying $\mathbf{B} = \nabla\times\mathbf{A}$. It is a measure of both the local twisting and the global linkage of the field: configurations with no linkage have zero helicity.

One property of $\mathscr{H}$ is that is perfectly conserved in the limit of ideal MHD, meaning that field reconfiguration requires non-ideal processes (diffusion of magnetic field lines). To see this, let us consider the resistive induction equation, given by Equation (2.13), which can be expressed as

$$\frac{\partial(\nabla\times\mathbf{A})}{\partial t} = \nabla\times(\mathbf{u}\times\mathbf{B}) - \frac{1}{\mu_0\sigma}\nabla\times(\nabla\times\mathbf{B})\,. \tag{2.23}$$

The "uncurled" version of this is

$$\frac{\partial\mathbf{A}}{\partial t} = \mathbf{u}\times\mathbf{B} - \frac{1}{\mu_0\sigma}\nabla\times\mathbf{B} - \nabla\Phi_e\,, \tag{2.24}$$

where Φ_e is some scalar potential. From this we form

$$\begin{aligned}\frac{\partial}{\partial t}(\mathbf{A}\cdot\mathbf{B}) &= \mathbf{A}\cdot\frac{\partial\mathbf{B}}{\partial t} + \mathbf{B}\cdot\frac{\partial\mathbf{A}}{\partial t}\\ &= \nabla\cdot\left[(\mathbf{u}\times\mathbf{B})\times\mathbf{A} - \frac{1}{\mu_0\sigma}(\nabla\times\mathbf{B})\times\mathbf{A} - \Phi_e\mathbf{B}\right] - \frac{2}{\mu_0\sigma}(\nabla\times\mathbf{B})\cdot\mathbf{B}\,.\end{aligned} \tag{2.25}$$

Then,

$$\frac{\partial\mathscr{H}}{\partial t} = \frac{\partial}{\partial t}\int_V \mathbf{A}\cdot\mathbf{B}\,\mathrm{d}V = -\frac{2}{\sigma}\int_V \mathbf{J}\cdot\mathbf{B}\,\mathrm{d}V\,. \tag{2.26}$$

In the final step, we are considering a large enough volume that all surface terms vanish, and so the volume integral over the divergence term is zero.

This result demonstrates that in the limit of perfect conductivity, $\mathscr{H}$ is conserved. Furthermore, we can also see that the sign of change (growing or diminishing helicity) depends on whether the current has a component parallel or antiparallel to $\mathbf{B}$.

2.2 Dynamical aspects

2.2.1 Generation

The process whereby fluid motions convert kinetic energy into magnetic energy is referred to as *dynamo action*. A notable result in dynamo theory is that it is not possible to sustain steady-state magnetic field generation if the configuration is axisymmetric. This result is known as *Cowling's antidynamo theorem* (Cowling, 1934). To demonstrate this, consider the following axisymmetric decomposition of the magnetic and velocity fields in cylindrical polar coordinates (R,ϕ,z):

$$\mathbf{u} = \mathbf{u}_t + \mathbf{u}_p = R\Omega\hat{\boldsymbol{\phi}} + \left(\nabla\times\frac{\Theta}{R}\right)\hat{\boldsymbol{\phi}} \tag{2.27}$$

$$\mathbf{B} = \mathbf{B}_t + \mathbf{B}_p = B\hat{\boldsymbol{\phi}} + \nabla\times\left(A\hat{\boldsymbol{\phi}}\right), \tag{2.28}$$

where A and B represent the poloidal and toroidal components of the field, Ω is the angular rotation frequency, and Θ is the fluid stream function. Subscripts t and p denote toroidal and poloidal components.

Substituting these forms into Equation (2.13), we end up with the pair

$$\frac{\partial A}{\partial t} + \frac{1}{R}(\mathbf{u}_p \cdot \nabla)(RA) = \frac{1}{\mu_0 \sigma}\left(\nabla^2 - \frac{1}{R^2}\right) A\,, \tag{2.29}$$

$$\frac{\partial B}{\partial t} + R(\mathbf{u}_p \cdot \nabla)\left(\frac{B}{R}\right) = \frac{1}{\mu_0 \sigma}\left(\nabla^2 - \frac{1}{R^2}\right) B + R\mathbf{B}_p \cdot \nabla\Omega\,. \tag{2.30}$$

The last term on the right-hand side of Equation (2.30) can be regarded as a source term that comes from the existence of a poloidal magnetic field. The remaining terms on the right-hand sides of both equations correspond to diffusive decay, while the terms on the left-hand sides represent advection. Considering that the poloidal equation has no source terms at all, the poloidal field must steadily decay. Given that the only source term in the toroidal equation comes from the poloidal field, this must likewise decay together with the poloidal field. Sustained field generation under a strictly axisymmetric configuration is therefore impossible.

Two processes which can break axisymmetry are differential rotation and turbulent convection. It is thought that a combination of these is required to regenerate the poloidal component from the toroidal one, thus 'closing' the dynamo loop. In the Parker (1955) picture, generation of the toroidal component from a pre-existing poloidal component proceeds by way of the Ω-effect, where differential rotation distorts the poloidal field thus inducing a toroidal component. The proposed mechanism of generating poloidal field from a pre-existing toroidal field is coalescence of small-scale flux loops having a systematic handedness, owing to the symmetry-breaking effects of rotation on turbulent convection. This second process is called the α-effect, and the combination of the two referred to as an $\alpha\Omega$ dynamo. Variants such as α^2 and $\alpha^2\Omega$ dynamos have been proposed for systems in which the shear provided by differential rotation plays less of a role, such as in fully convective stars or the cores of high-mass main sequence stars (Charbonneau & MacGregor, 2001).

2.2.2 Characteristic timescales

A number of notable timescales govern the behaviour and evolution of magnetic fields. In the context of stellar dynamos which involve rotation and turbulent convection, one expects growth rates to depend on the rotation period $P_{\rm rot}$ and convective turnover timescale τ_c. For typical pre-main-sequence and main-sequence stars, these timescales range from weeks to months (Landin et al., 2010). Their ratio defines the *Rossby number*, $\mathrm{Ro} = P_{\rm rot}/\tau_c$, related to the *dynamo number*, $N_D \sim 1/\mathrm{Ro}^2$ (describing the efficiency of the dynamo), which in the case of late-type main sequence stars exhibits a correlation with magnetic activity (Noyes et al., 1984). Theoretical modelling to predict dynamo growth rates is not a trivial task, however, since the whole process is expected to involve a wide of range of spatial scales, and the nature of the local-scale process of field generation is not well constrained (Tobias & Cattaneo, 2008). No straightforward correspondence between these timescales exists; for example, in the case of the solar dynamo, despite rotation and convection occurring on roughly month-long timescales, observed magnetic activity cycles are much longer (decades). However, given that actively-generated magnetic fields are widely observed in many stars, including those on the pre-main sequence (see later discussion in §2.3), one may conclude that dynamos are able to operate on time scales far smaller than $t_{\rm KH}$, and certainly $t_{\rm nuc}$. Further discussion on the topic is beyond the scope of this thesis.

For fields that reside in radiative regions and are not being actively generated, the main timescale governing their evolution is that of Ohmic dissipation. Examining the resistive term in Equation (2.13), we

identify the decay time scale

$$t_\Omega \sim \mu_0 \sigma l_B^2 \,, \tag{2.31}$$

where l_B is a characteristic length scale associated with the magnetic field. Given parameters typical of main-sequence stellar interiors, Ohmic dissipation should occur over a time scale roughly given by $t_\Omega \sim 10^9$ yr, which greatly exceeds $t_{\rm dyn}$.

A third relevant timescale is the *Alfvén crossing time*, which is the time it takes disturbances propagating via the magnetic field to carrying information across the star. The speed of such disturbances can be derived by considering a plane-wave expansion of the MHD equations and linearising, that is, assuming that each dependent variable $\eta \in \{\rho, \mathbf{B}, \mathbf{u}\}$ can be written

$$\eta(\mathbf{x}, t) = \eta_0(\mathbf{x}) + \eta_1 \exp\left[\,\mathrm{i}(\mathbf{k}\cdot\mathbf{x} - \omega t)\right] \,, \tag{2.32}$$

where $\mathbf{k}$ and ω are the angular wavenumber and angular frequency of the wave. Subscripts 0 and 1 denote backgrounds and perturbations, and it will be assumed that $|\eta_1| \ll |\eta_0|$. We shall neglect all forces except the Lorentz force, and for simplicity assume that the fluid is incompressible, i.e. $\nabla\cdot\mathbf{u} = 0$. Defining the fluid displacement $\boldsymbol{\xi}$ by $\mathbf{u} = \partial\boldsymbol{\xi}/\partial t = -\mathrm{i}\omega\boldsymbol{\xi}$, the ideal induction equation (2.12) becomes

$$\begin{aligned} -\mathrm{i}\omega\mathbf{B}_1 &= \omega\mathbf{k}\times(\boldsymbol{\xi}\times\mathbf{B}_0) \\ \mathbf{B}_1 &= \mathrm{i}(\mathbf{k}\cdot\mathbf{B}_0)\boldsymbol{\xi} \,. \end{aligned} \tag{2.33}$$

The linearised momentum equation incorporating just the Lorentz force, and neglecting spatial derivatives of the background in favour of those of the perturbations, is

$$-\rho_0\omega^2\boldsymbol{\xi} = \frac{1}{\mu_0}(\mathrm{i}\mathbf{k}\times\mathbf{B}_1)\times\mathbf{B}_0 \,.$$

Using Equation (2.33) to eliminate $\mathbf{B}_1$ in favour of $\boldsymbol{\xi}$, we arrive at the dispersion relation for Alfvén waves,

$$\omega^2 = \frac{(\mathbf{k}\cdot\mathbf{B}_0)^2}{\mu_0\rho_0} = (\mathbf{k}\cdot\mathbf{v}_A)^2 \,, \tag{2.34}$$

where we define

$$\mathbf{v}_A \equiv \frac{\mathbf{B}_0}{\sqrt{\mu_0\rho_0}} \tag{2.35}$$

to be the *Alfvén velocity*. The associated crossing time is then given by $t_A \sim R_*/v_A$, where $v_A \equiv |\mathbf{v}_A|$ is the Alfvén speed. It is akin to $t_{\rm dyn}$ but associated with the magnetic field rather than pressure or buoyancy; that is, it is the time scale on which magnetic equilibrium would be restored following a perturbation to the field. Alfvén timescales tend to be long compared to $t_{\rm dyn}$: for densities typical of main-sequence stellar cores, a field of 10 kG would yield a t_A of several years.

As mentioned earlier, magnetic pressure causes flux tubes to be buoyant, and so an additional way in which fields might evolve is through the buoyant advection of flux tubes from the interior and out through the surface. For stars operating core dynamos, this represents one loss process for the magnetic field. Theoretical modelling of such a process (MacGregor & Cassinelli, 2003) has shown that the rise speed of magnetic flux tubes depends on the rate at which heat diffuses in from the surroundings. This timescale goes as the cross-sectional area of the tube, implying that small tubes are able to rise more quickly. For megagauss fields and flux-tube radii of 10^{-3}–10^{-4} times the pressure scale height, buoyant rise timescales were calculated to be of the order 10^6–10^8 yr. While this value appears to be small compared to the evolutionary timescales of

many stars, the sizes of flux tubes generated via core dynamos are not well constrained. Some simulations suggest that global-scale structures can dominate the quasi-steady-state configuration (Featherstone et al., 2009). These would not be subject to such rapid timescales of buoyant rise.

2.2.3 Stability

A mechanical configuration is said to be stable if all perturbations to it result in an increase in potential energy. If there exists any perturbation pattern that acts to decrease the potential energy, then the system will be unstable. Formally, this may be stated in terms of the *energy principle* (Bernstein et al., 1958), a brief sketch of which is given below.

An equation of motion can be cast in the general form

$$\frac{\partial^2 \boldsymbol{\xi}}{\partial t^2} + \mathscr{L}[\boldsymbol{\xi}] = 0\,, \tag{2.36}$$

where $\mathscr{L}$ is a linear differential operator containing the spatial derivatives of the system. In the case of ideal MHD, it can be shown that $\mathscr{L}$ is self-adjoint with respect to the inner product

$$\langle \boldsymbol{\xi}, \boldsymbol{\eta} \rangle = \int \rho \boldsymbol{\xi}^* \cdot \boldsymbol{\eta}\, \mathrm{d}V\,, \tag{2.37}$$

meaning that it satisfies $\langle \boldsymbol{\xi}, \mathscr{L}[\boldsymbol{\eta}] \rangle = \langle \mathscr{L}[\boldsymbol{\xi}], \boldsymbol{\eta} \rangle$.

Now the change in potential energy associated with a perturbation $\boldsymbol{\xi}$ is

$$W[\boldsymbol{\xi}] = -\frac{1}{2}\langle \boldsymbol{\xi}, \ddot{\boldsymbol{\xi}} \rangle \tag{2.38}$$

and the kinetic energy is

$$K[\boldsymbol{\xi}] = \frac{1}{2}\langle \dot{\boldsymbol{\xi}}, \dot{\boldsymbol{\xi}} \rangle\,, \tag{2.39}$$

where a dot indicates a time derivative. We can show with aid of the self-adjointness property that total energy is conserved:

$$\begin{aligned}
\frac{\mathrm{d}}{\mathrm{d}t}\left(K[\boldsymbol{\xi}] + W[\boldsymbol{\xi}]\right) &= \frac{\mathrm{d}}{\mathrm{d}t}\left(\frac{1}{2}\langle \dot{\boldsymbol{\xi}}, \dot{\boldsymbol{\xi}} \rangle - \frac{1}{2}\langle \boldsymbol{\xi}, \ddot{\boldsymbol{\xi}} \rangle\right) \\
&= \langle \ddot{\boldsymbol{\xi}}, \dot{\boldsymbol{\xi}} \rangle + \frac{1}{2}\left(\langle \dot{\boldsymbol{\xi}}, \mathscr{L}[\boldsymbol{\xi}] \rangle + \langle \boldsymbol{\xi}, \mathscr{L}[\dot{\boldsymbol{\xi}}] \rangle\right) \\
&= -\langle \mathscr{L}[\boldsymbol{\xi}], \dot{\boldsymbol{\xi}} \rangle + \langle \dot{\boldsymbol{\xi}}, \mathscr{L}[\boldsymbol{\xi}] \rangle \\
&= 0\,.
\end{aligned} \tag{2.40}$$

Adopting a time-harmonic expansion for $\boldsymbol{\xi} \propto \exp(-\mathrm{i}\omega t)$ gives us an expression for the eigenvalues of $\mathscr{L}$ in terms of $W[\boldsymbol{\xi}]$ as being

$$\omega^2 = \frac{2W[\boldsymbol{\xi}]}{\langle \boldsymbol{\xi}, \boldsymbol{\xi} \rangle}\,. \tag{2.41}$$

Now consider an initial perturbation $\boldsymbol{\xi}_0$ for which $W[\boldsymbol{\xi}_0] < 0$, and thereby also $\omega^2 < 0$. Suppose we apply this perturbation by setting the displacement pattern to $\boldsymbol{\xi}_0$ and the velocity pattern to $\alpha\boldsymbol{\xi}_0$, where $\alpha > 0$ and $\alpha^2 \ll -\omega^2$ (a gentle perturbation). The total energy associated with this perturbation is

$$E = K[\boldsymbol{\xi}_0] + W[\boldsymbol{\xi}_0] = \frac{1}{2}\left(\alpha^2 + \omega^2\right)\langle \boldsymbol{\xi}_0, \boldsymbol{\xi}_0 \rangle\,. \tag{2.42}$$

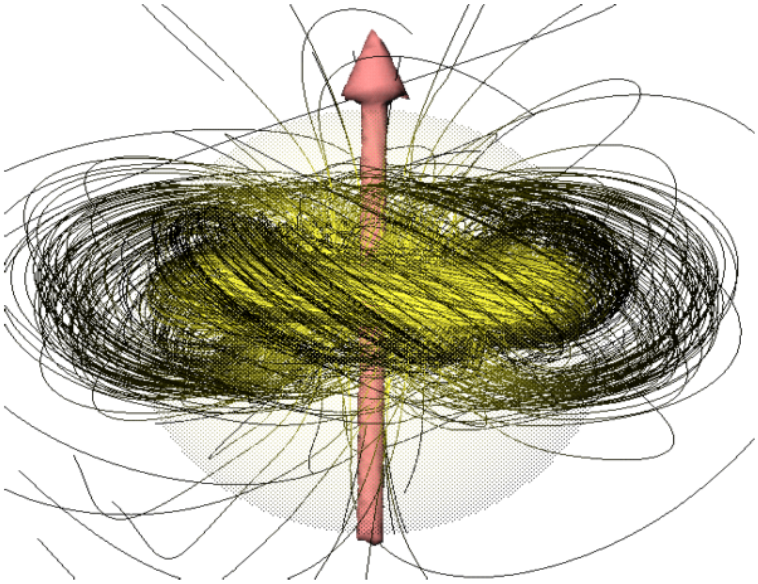

Figure 2.1: Example twisted torus magnetic field configuration obtained in simulations of Braithwaite & Nordlund (2006).

Now define

$$f(t) = \ln \frac{\langle \boldsymbol{\xi}, \boldsymbol{\xi} \rangle}{\langle \boldsymbol{\xi}_0, \boldsymbol{\xi}_0 \rangle} \,. \tag{2.43}$$

One can show that

$$\ddot{f}(t) = 4 \frac{\langle \dot{\boldsymbol{\xi}}, \dot{\boldsymbol{\xi}} \rangle \langle \boldsymbol{\xi}, \boldsymbol{\xi} \rangle - \langle \dot{\boldsymbol{\xi}}, \boldsymbol{\xi} \rangle^2}{\langle \boldsymbol{\xi}, \boldsymbol{\xi} \rangle^2} - \frac{2E}{\langle \boldsymbol{\xi}, \boldsymbol{\xi} \rangle} > 0 \,, \tag{2.44}$$

as a consequence of the Cauchy-Schwarz inequality and the fact that $E \approx \frac{1}{2}\omega^2 \langle \boldsymbol{\xi}, \boldsymbol{\xi} \rangle < 0$. This implies that the perturbation will grow with time.

Studies of the stability of various field configurations have yielded a number of noteworthy results. For instance, it has been established that *purely toroidal* fields, that is, fields with only a ϕ-component, are unstable. This was first treated through an analytic approach by Tayler (1973), and followed up numerically by Braithwaite (2006). Such configurations can be conceived as being formed of a collection of stacked field loops centred around some axis (the magnetic axis). The fastest-growing unstable modes in such configurations tend to be kink modes with $m = 1$. This involves the stack of loops "buckling" sideways at some location along the axis, and the resulting imbalance of magnetic pressure on each side thereafter acts to reinforce the perturbation.

On the opposite extreme, it is also the case that *purely poloidal* fields are unstable (Markey & Tayler, 1973, 1974; Flowers & Ruderman, 1977). These configurations are ones in which all field lines lie in meridional planes (the R, z-plane in cylindrical coordinates). In these cases, reduction in overall magnetic energy can be achieved by cutting the star in half parallel to the magnetic axis and rotating one half by 180°. One might envisage collapse of such a field involving halves of the star twisting against each other, like two bar magnets placed alongside and parallel to each other spontaneously flipping to become antiparallel.

In light of these results, one can only conclude that if stable configurations exist, they must necessarily involve a combination of both poloidal and toroidal components. One such equilibrium solution, of "twisted-torus" topology, was derived by Prendergast (1956), which resembles a dipole but is threaded by an additional toroidal component imparting a twist to the field. Its stability was later verified numerically

for $n = 3$ polytropes by Duez et al. (2010). Simulations following the evolution of initially random fields have found that these tend to settle into large-scale, dipole-like configurations with mixed poloidal-toroidal topology (Braithwaite & Nordlund, 2006), bearing strong resemblance to the solution found by Prendergast (1956). A plot of the configuration found in their simulations is shown in Figure 2.1. On the basis of these studies, it appears as though the most likely magnetic equilibrium configuration that might be found in nature is that of a twisted torus, and so this is the type of structure we adopt in later chapters of this thesis for applications where an equilibrium field is required. A more quantitative description of the configurations used will be presented in the following chapter.

2.3 Occurrence

2.3.1 Pre-main sequence

As mentioned in §1.3.1, stars of all masses will experience a fully convective stage during their formation. Many during this phase are observed to have strong surface fields of kilogauss order, taking the form of primarily large-scale, axisymmetric, dipolar configurations aligned with the rotation axis (Braithwaite & Spruit, 2017). As they approach the ZAMS, a radiative core develops and the convective envelope retreats upward. If the star is sufficiently massive ($\gtrsim 1.2\mathrm{M}_\odot$), this convective envelope eventually vanishes, and a convective core develops leading on to the main sequence stage. Pre-main sequence stars which have developed a radiative core are observed to have more complex magnetic field topologies (Hussain, 2012).

There is some debate as to the origin of magnetic fields in pre-main sequence objects. Some observations have shown that surface field strengths do not change appreciably during contraction of the protostar (Yang & Johns-Krull, 2011). Since flux conservation would lead to an increase of the field strength upon contraction, this implies that magnetic flux is being lost. This has been taken as evidence of a primordial origin of protostellar magnetic fields (accretion from the parent cloud), which would dissipate over time as a result of turbulent convection and the associated high magnetic diffusivity. However, it is believed that the fields present in later stages might be generated by dynamo processes, as suggested by measurements of decade-scale variability in surface fields (Hussain & Alecian, 2014). The increase in complexity of the field (appearance of higher multipole moments) with the appearance of a radiative core is likely to be linked to a fundamental change in the nature of the dynamo process. It is thought that the shear between radiative and convective zones of a star has an important role to play in the operation of an $\alpha\Omega$ dynamo, such as occurs in the Sun; this shearing region is known as a *tachocline* and is a site where fields may be amplified.

2.3.2 Main sequence

In low-mass stars possessing convective zones that extend to the surface, magnetic activity is widespread and detectable in the form of starspots, high-energy radiation associated with flaring and coronal mass ejections, and scattering events associated with prominences (Donati & Landstreet, 2009). Our Sun is one such example. The short timescales (weeks/months to decades) on which these phenomena are observed to occur point strongly to a dynamo origin, as does the observed anticorrelation of activity with the Rossby number, a property predicted by most dynamo theories. Surface field strengths measured for low-mass stars tend to be in equipartition with the ambient gas (magnetic and thermal pressures of the same order); this is around 400 G in the case of the Sun (Stix, 1989). However, the activity does not increase indefinitely

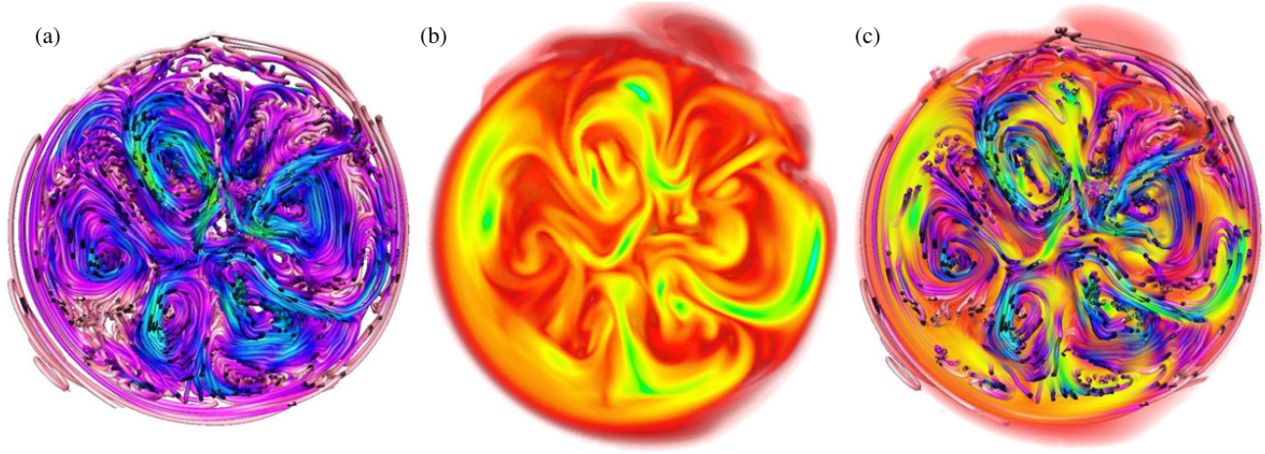

Figure 2.2: The results of MHD simulations of convective stellar cores undertaken by Featherstone et al. (2009), showing (a) flow tangent lines, (b) magnetic energy, and (c) a superposition of the two. Large rolls are seen to form. The colour scale for the magnetic field runs from 30 kG (red) to 250 kG (green).

with decreasing Ro: evidence exists for a saturation point occurring at about Ro∼0.1 (Reiners et al., 2009). For a solar-mass star, this corresponds to a rotation period of about two days. This suggests that sufficiently strong magnetic fields are capable of feeding back on and modifying the underlying convective motions that generate it. For rapidly-rotating stars in this saturated regime, an unusual feature found in their topology has been the presence of strong toroidal fields at the surface (Petit et al., 2008).

For very low-mass stars in the fully convective regime, there is a pronounced transition from the more complex field topologies of higher-mass stars to a strong, large-scale, axisymmetric, poloidal configuration. This transition coincides with a significant drop in surface shear, which may reflect the quenching of differential rotation by the strong field (Morin et al., 2008). Note that a dramatic change in internal structure occurs when decreasing from 0.5 $M_\odot$ to 0.4 $M_\odot$: over this small range in mass, the radiative core shrinks from around 0.5 R_* to almost nothing. It appears that the disappearance of the radiative zone has an impact on the fundamental nature of the dynamo, which in a fully convective regime becomes much more efficient at producing large-scale, axisymmetric poloidal fields.

In contrast to the lower-mass stars, those of higher masses with radiative envelopes show much weaker surface magnetic activity on average. In most of these stars, upper limits of several gauss have been placed on their surface fields. However, a small subset (∼10%) of spectral types A and B have been found to harbour strong magnetic fields, ranging between around 200 G up to 30 kG (Aurière et al., 2007). These are known as Ap and Bp stars, where the label 'p' indicates that these stars exhibit chemical peculiarities, thought to be a consequence of disruption to surface convection by a strong magnetic field leading to gravitational settling and radiative levitation, which separates different chemical species. Stars having intermediate field strengths between several gauss and several hundred gauss appear not to exist; separating Ap/Bp stars and the remainder of the population is a 'magnetic desert'. There is some evidence that this bimodality in field strengths extends to earlier types as well (Henrichs, 2012; Wade et al., 2015), but chemical peculiarities are not evident in hotter stars owing to the dominance of mass loss (driven by stellar winds) over microscopic diffusion.

There has been some debate as to the explanation for the magnetic bimodality and the origin of the

strong surface fields for those stars that possess them (Donati & Landstreet, 2009). Arguments against these being of dynamo origin include an absence of short-term variability, the lack of dependence of field strength on rotation rate (both predicted by theory and observed to hold for lower-mass stars), and the long timescales of buoyant rise of magnetic flux from the possibly dynamo-operating convective core. Rather, they are believed to be of *fossil* origin, meaning that they are relics from the accretion of ambient field during protostellar formation. The bimodality may possibly be explained by the fact that only the strongest of such accreted fields are capable of halting the development of differential rotation, which would act to shear the field and generate a strong toroidal component. Such a configuration would then be subject to collapse on the Alfvén timescale due to the kink instability (see §2.2.3), and so for this reason fields weaker than some threshold might not survive.

While magnetism present at the surface of a star can be directly observed through a wide variety of complementary techniques, it is much less straightforward to study magnetism generated or otherwise present deep within the interiors of stars. For stars massive enough to possess convective cores, it is not unreasonable to suppose that some sort of dynamo process might operate there. However, characterising these interior fields has relied almost exclusively on MHD simulations, for example those carried out by Brun et al. (2005) and Featherstone et al. (2009). On the basis of such studies, it has been speculated that dynamo-generated core fields might attain strengths of 10–100 kG. An example of the flow and magnetic field structures appearing in these simulations is shown in Figure 2.2, showing the formation of a highly structured configuration of large-scale rolls.

2.3.3 Post-main sequence

As previously mentioned, all stars evolving off the main sequence develop a substantial convective envelope, and the inner regions become radiative. One might therefore expect an $\alpha\Omega$-type dynamo to operate in post-main sequence objects. Indeed, red giants show evidence for surface magnetic activity that exhibits an anticorrelation with Ro, which supports a dynamo origin (Aurière et al., 2015). Their greatly expanded envelopes and lower surface pressures yield correspondingly lower equipartition field strengths: typical values measured for red giant surface fields are around 1–10 G. However, a number of red giants have been noted to possess anomalously strong fields for their Rossby numbers. It has been suggested that these might represent the descendants of magnetic Ap/Bp stars (and higher-mass equivalents), where a significant portion of the surface flux is fossil in origin (Aurière et al., 2008).

In the case of stars more massive than $1.2\,\mathrm{M}_\odot$, a question arises as to what becomes of the magnetic field that may have been generated in the core. If the dynamo undergoes periodic reversals on appreciably short timescales (much less than t_{nuc}), such as in the Sun, then as the convective boundary slowly retreats over the course of the main sequence, this would leave behind small-scale magnetic structures in the form of thin radial shells of alternating sign. Such features are likely to dissipate rapidly as a result of Ohmic diffusion. Even if cyclic flipping were not to occur, it is still possible that the field configuration left behind after cessation of the dynamo could become unstable and collapse upon itself, resulting in significant loss of flux through self-cancellation. Given that it is not possible to directly observe fields in the interiors of stars, and that a large number of reasons might prohibit such fields from existing, one might be hesitant to speculate upon the matter. However, suggestions that strong remnant fields in the cores of evolved stars have been argued on the basis of multiple pieces of indirect evidence (Fuller et al., 2015). It is the goal of

this thesis to explore the consequences of such *hidden fields*, should they indeed exist. Further details on the background behind this topic will be presented in Chapter 5.

2.3.4 Degenerate stars

Around 10% of white dwarfs have been detected to possess surface magnetic fields, these spanning a wide range of strengths between 0.001–1000 MG (Ferrario et al., 2015b), where the lower bound arises from detection limits. There is some evidence that the distribution is bimodal, with a paucity of objects between 0.1–1 MG. Topologies can be complex in some instances, exhibiting higher multipole moments and non-axisymmetric structure (Putney & Jordan, 1995). Note that no significant convective regions are present in white dwarfs; the fields they harbour must therefore represent some kind of stable equilibrium that is slowly evolving under mainly Ohmic dissipation ($t_\Omega \sim 10^{11}$ yr). The origins of fields in magnetic white dwarfs are still a matter of debate, and it may well be that multiple processes are responsible for their generation. Magnetic white dwarfs tend to be more massive on average than their non-magnetic counterparts, and so it has been suggested that some of these may be the evolutionary descendants of magnetic Ap/Bp stars, which are higher in mass than average main sequence stars (Kanaan et al., 1999). Under the frozen-in flux assumption, the observed field strengths are not inconsistent with the magnetic flux having been conserved from previous stages of evolution. Another possible origin for the strong fields is that they could have been generated during the course of a binary interaction, where the objects coalescing to form the magnetic white dwarf underwent a transient dynamo phase (Ferrario et al., 2015a).

Neutron stars are all thought to be born magnetised, with fields ranging between 10^{11}–10^{15} G (Harding, 2013). The most highly magnetised neutron stars are known as magnetars, having fields of 10^{14}–10^{15} G. As in the case of white dwarfs, the origin of neutron star magnetic fields is unclear. A fossil field hypothesis, where the flux is a relic of previous stages of evolution, simply compressed to yield very high field strengths, is incompatible with the requirement that all massive stars would have to be magnetic with a continuous distribution of field strengths. Rather, it has been established that magnetism on the main sequence tends to be bimodal. There are also too few highly magnetised non-degenerate stars to account for the relatively high occurrence rate of magnetars. The fields present in neutron stars are therefore more likely to originate in dynamo processes taking place during formation of the protoneutron star (Ruderman & Sutherland, 1973).

Chapter 3

Magnetohydrostatic Equilibria

3.1 Field configurations

It was established in the preceding chapter that a magnetic field not being actively generated can only survive in the long term if it is in a stable equilibrium configuration. Otherwise, collapse of the field occurs rapidly on the Alfvén timescale. Neglecting rotation, the condition for mechanical equilibrium is that

$$\nabla p + \rho \nabla \Phi = \frac{1}{\mu_0} (\nabla \times \mathbf{B}) \times \mathbf{B}\,, \tag{3.1}$$

i.e. for the forces of pressure and buoyancy to balance the Lorentz force.

In this section, we will explore ideas related to the stability of magnetic fields, with the aim of formulating a physically realistic configuration for modelling fields fully confined within stellar interiors.

3.1.1 Potential fields

Consider a system in hydrostatic equilibrium, and suppose that the pressure and density distributions are completely pre-specified. If one desires to then impose a magnetic field on these backgrounds in such a way as to maintain the equilibrium state, while extremising the potential energy associated with arbitrary displacements of the fluid, then it can be shown that such a field must obey $\nabla \times \mathbf{B} = 0$. A field of this sort is referred to as a *potential field*.

To see this, let us consider perturbations to such a setup occurring within some finite volume V. From the ideal induction equation, perturbations to the field are given by

$$\delta \mathbf{B} = \nabla \times (\boldsymbol{\xi} \times \mathbf{B}) \tag{3.2}$$

$$= \nabla \times \delta \mathbf{A}\,, \tag{3.3}$$

where $\delta \mathbf{A}$ is the perturbation to the magnetic vector potential, and from the above we identify $\delta \mathbf{A} = \boldsymbol{\xi} \times \mathbf{B}$. The associated perturbation to the magnetic energy is then

$$\begin{aligned} \delta E_m &= \frac{1}{\mu_0} \int_V \mathbf{B} \cdot \delta \mathbf{B}\, \mathrm{d}V \\ &= \frac{1}{\mu_0} \int_V \left[\nabla \cdot (\delta \mathbf{A} \times \mathbf{B}) + \delta \mathbf{A} \cdot (\nabla \times \mathbf{B}) \right] \mathrm{d}V \\ &= \frac{1}{\mu_0} \int_S (\delta \mathbf{A} \times \mathbf{B}) \cdot \mathrm{d}\mathbf{S} + \frac{1}{\mu_0} \int_V \delta \mathbf{A} \cdot (\nabla \times \mathbf{B})\, \mathrm{d}V\,, \end{aligned} \tag{3.4}$$

where S indicates the surface bounding volume V and we have made use of the vector identity

$$\nabla \cdot (\mathbf{A} \times \mathbf{B}) = \mathbf{B} \cdot (\nabla \times \mathbf{A}) - \mathbf{A} \cdot (\nabla \times \mathbf{B}) \,. \tag{3.5}$$

Since V is taken to enclose all perturbations, the surface term in Equation (3.4) evaluates to zero. It follows that the condition to extremise the energy ($\delta E_m = 0$), while allowing for arbitrary $\boldsymbol{\xi}$ and thereby $\delta\mathbf{A}$, requires that $\nabla \times \mathbf{B} = 0$. In this case, a scalar potential ϕ_m exists such that $\mathbf{B} = -\nabla\phi_m$, and the solution to the configuration is governed by Laplace's equation, $\nabla^2\phi_m = 0$.

3.1.2 Force-free fields

For an ideal plasma, a constraint placed on the relaxation process is that the magnetic helicity $\mathscr{H}$ (see §2.1.4) should be conserved. This process is referred to as *Taylor relaxation* and it can be shown that the end result is a force-free state, with $\mathbf{J} \times \mathbf{B} = 0$ (Taylor, 1974). To enforce conservation of helicity, we consider extremisation of the quantity $E_m - \lambda\mathscr{H}$, where λ is the Lagrange multiplier enforcing conservation of $\mathscr{H}$. Consider

$$\delta E_m - \lambda\delta\mathscr{H} = \frac{1}{\mu_0}\int_V \mathbf{B}\cdot\delta\mathbf{B}\,\mathrm{d}V - \lambda\int_V (\mathbf{A}\cdot\delta\mathbf{B} + \mathbf{B}\cdot\delta\mathbf{A})\,\mathrm{d}V \tag{3.6}$$

$$= \frac{1}{\mu_0}\int_V [\nabla\cdot(\delta\mathbf{A}\times\mathbf{B}) + \delta\mathbf{A}\cdot(\nabla\times\mathbf{B})]\,\mathrm{d}V - \lambda\int_V [2\delta\mathbf{A}\cdot\mathbf{B} + \nabla\cdot(\delta\mathbf{A}\times\mathbf{A})]\,\mathrm{d}V \,. \tag{3.7}$$

Since all perturbations are taken to vanish within the finite enclosing volume V, the surface terms (volume integrals of divergences) evaluate to zero and we are left with

$$\delta E_m - \lambda\delta\mathscr{H} = \int_V \delta\mathbf{A}\cdot\left[\frac{1}{\mu_0}(\nabla\times\mathbf{B}) - 2\lambda\mathbf{B}\right]\mathrm{d}V \,, \tag{3.8}$$

which will be zero under arbitrary perturbations if $\nabla\times\mathbf{B} \propto \mathbf{B} \implies \mathbf{J}\times\mathbf{B} = 0$. Such fields are referred to as being *force-free*.

3.1.3 Vanishing theorem

While at first glance it might appear that force-free fields (of which potential fields are more generally an example) are a convenient modelling choice, there is a difficulty in the case of fully confined fields. Notice that the above analyses have assumed that there exists an exterior region beyond which the magnetic field lines extend. If this were not to exist, then it turns out that if the field is to be force-free, it must also vanish identically.

Consider the vector identity

$$\begin{aligned}
\mathbf{x}\cdot[(\nabla\times\mathbf{B})\times\mathbf{B}] &= x_i\epsilon_{ijk}\epsilon_{jlm}\frac{\partial B_m}{\partial x_l}B_k \\
&= x_i(\delta_{im}\delta_{kl} - \delta_{il}\delta_{km})\frac{\partial B_m}{\partial x_l}B_k \\
&= x_i\left(\frac{\partial B_i}{\partial x_j}B_j - \frac{\partial B_j}{\partial x_i}B_j\right) \\
&= -\delta_{ij}B_iB_j + \delta_{ij}B_iB_j - x_iB_j\frac{\partial B_j}{\partial x_i} + x_jB_i\frac{\partial B_j}{\partial x_i} \\
&= -B_iB_i - \frac{1}{2}x_i\frac{\partial}{\partial x_i}(B_jB_j) + B_i\frac{\partial}{\partial x_i}(x_jB_j) \\
&= -B^2 - \frac{1}{2}\mathbf{x}\cdot\nabla B^2 + \mathbf{B}\cdot\nabla(\mathbf{x}\cdot\mathbf{B}) \\
&= \frac{1}{2}B^2 - \frac{1}{2}\nabla\cdot\left[B^2\mathbf{x} - 2(\mathbf{x}\cdot\mathbf{B})\mathbf{B}\right] \,.
\end{aligned} \tag{3.9}$$

Let us suppose we have a force-free field ($[\nabla\times\mathbf{B}]\times\mathbf{B}=0$) that is fully confined within volume V. Then, using the above identity, it must be that

$$\begin{aligned}0&=\int_V \mathbf{x}\cdot[(\nabla\times\mathbf{B})\times\mathbf{B}]\,\mathrm{d}V\\&=\frac{1}{2}\int_V B^2\,\mathrm{d}V-\frac{1}{2}\int_S\left[B^2\mathbf{x}-2(\mathbf{x}\cdot\mathbf{B})\mathbf{B}\right]\cdot\mathrm{d}\mathbf{S}\,.\end{aligned}\tag{3.10}$$

Since there is no field on the boundary S, the surface term vanishes. Therefore it must be that $B^2=0$ within V, i.e. the magnetic field vanishes everywhere. This means that if we wish to model a fully confined field, we cannot invoke the force-free condition as an additional constraint that might reduce the number of free parameters. Rather, a more general approach is required, which we next discuss.

3.1.4 Grad-Shafranov equation

For a system where some spatial symmetry is present, the equilibrium condition (3.1) can be reduced to a second-order elliptic partial differential equation (PDE), which one might then attempt to solve. We now set out to derive such an equation for axisymmetric systems ($\partial/\partial\phi\equiv 0$).

Let us express the magnetic field in terms of a function $\psi=\psi(R,z)$ as follows:

$$\mathbf{B}=\frac{1}{R}\nabla\psi\times\hat{\boldsymbol{\phi}}+B_\phi\hat{\boldsymbol{\phi}}=\left(-\frac{1}{R}\frac{\partial\psi}{\partial z},B_\phi,\frac{1}{R}\frac{\partial\psi}{\partial R}\right).\tag{3.11}$$

Considering that

$$\nabla\psi\cdot\mathbf{B}=\frac{1}{R}\nabla\psi\cdot\left(\nabla\psi\times\hat{\boldsymbol{\phi}}\right)+\nabla\psi\cdot B_\phi\hat{\boldsymbol{\phi}}=0\,,\tag{3.12}$$

it must be that ψ is constant on flux surfaces. Notice that $\psi=\int B_z R\,\mathrm{d}R$, which (up to a factor of 2π) corresponds to poloidal magnetic flux in an axisymmetric system, and so ψ can be interpreted as a poloidal flux function. Next, we define an auxilliary function, $F=RB_\phi$, in terms of which the Lorentz force is

$$(\nabla\times\mathbf{B})\times\mathbf{B}=-\frac{1}{R^2}\nabla\psi\left[\frac{\partial^2\psi}{\partial z^2}-\frac{1}{R}\frac{\partial\psi}{\partial R}+\frac{\partial^2\psi}{\partial R^2}\right]-\frac{F}{R^2}\nabla F\,.\tag{3.13}$$

Taking the dot product of both sides with $\mathbf{B}$, we see that $\nabla F\cdot\mathbf{B}=0$, and so $F=F(\psi)$ is invariant on flux surfaces.

Consider the curl of the force-balance condition, given by Equation (3.1):

$$\begin{aligned}\nabla\times(\mathbf{J}\times\mathbf{B})&=\nabla\times(\nabla p+\rho\nabla\Phi)\\&=\nabla\rho\times\nabla\Phi\\&=-\frac{\nabla\rho\times\nabla p}{\rho}+\frac{\nabla\rho\times(\mathbf{J}\times\mathbf{B})}{\rho}\,.\end{aligned}\tag{3.14}$$

So then

$$\begin{aligned}\nabla\times\left(\frac{\mathbf{J}\times\mathbf{B}}{\rho}\right)&=\frac{1}{\rho}\nabla\times(\mathbf{J}\times\mathbf{B})-\frac{1}{\rho^2}\nabla\rho\times(\mathbf{J}\times\mathbf{B})\\&=-\frac{\nabla\rho\times\nabla p}{\rho^2}\,.\end{aligned}\tag{3.15}$$

If, in addition, we make the barotropic assumption ($\nabla p\times\nabla\rho=0$, i.e. isobars and constant-density surfaces coincide), then invoking the result (3.13) we have that

$$0=\nabla\times\left(\frac{\mathbf{J}\times\mathbf{B}}{\rho}\right)=-\frac{1}{\mu_0}\nabla\left[\frac{1}{R^2\rho}\left(\Delta^*\psi+F\frac{\mathrm{d}F}{\mathrm{d}\psi}\right)\right]\times\nabla\psi\,,\tag{3.16}$$

where we define the elliptic operator

$$\Delta^* \equiv \frac{\partial^2}{\partial z^2} - \frac{1}{R}\frac{\partial}{\partial R} + \frac{\partial^2}{\partial R^2}\,, \tag{3.17}$$

and so we identify the quantity

$$G(\psi) = -\frac{1}{\mu_0 R^2 \rho}\left(\Delta^*\psi + F\frac{\mathrm{d}F}{\mathrm{d}\psi}\right) \tag{3.18}$$

to be another flux-surface invariant. This yields the *Grad-Shafranov equation*

$$\Delta^*\psi + F\frac{\mathrm{d}F}{\mathrm{d}\psi} = -\mu_0 R^2 \rho G\,, \tag{3.19}$$

with as-yet unspecified functions $F(\psi)$ and $G(\psi)$. The functional forms of F and G control the shape of the resulting equilibrium solution. The next section will present a solution for Equation (3.19) with chosen forms for F and G.

3.2 Prendergast solution

3.2.1 Derivation

The choice made by Prendergast (1956) for the two arbitrary functions was of the simplest kind in order to yield a non-trivial linear DE: F proportional to ψ and G being a constant. Following this approach, we let $F = \lambda\psi$ and $G = -\beta/\mu_0$, where λ and β are constants. This turns Equation (3.19) into

$$\Delta^*\psi + \lambda^2\psi = \beta\rho R^2\,. \tag{3.20}$$

For reasons which will become apparent, we shall switch from cylindrical polars (R,ϕ,z) to spherical polars (r,θ,φ). The elliptic operator becomes

$$\Delta^* = \frac{\partial^2}{\partial r^2} + \frac{\sin\theta}{r^2}\frac{\partial}{\partial\theta}\left(\frac{1}{\sin\theta}\frac{\partial}{\partial\theta}\right) \tag{3.21}$$

$$= \frac{\partial^2}{\partial r^2} + \frac{1-\mu^2}{r^2}\frac{\partial^2}{\partial\mu^2}\,, \qquad \text{where } \mu \equiv \cos\theta\,. \tag{3.22}$$

An insight made by Prendergast (1956) was to introduce the separation $\psi(r,\theta) = \Psi(r)\sin^2\theta = \Psi(r)(1-\mu^2)$, which, when substituted into Equation (3.20), yields the linear, second-order, inhomogeneous ODE

$$\Psi'' - \left(\frac{2}{r^2} - \lambda^2\right)\Psi = \beta\rho r^2\,. \tag{3.23}$$

This may be solved via a Green's function approach. However, one non-trivial aspect to the problem is the existence of three boundary conditions that must be satisfied by what is only a second-order ODE. These arise from the need to ensure that all three components of the field vanish continuously at the boundary of the field region, whose location we designate as $r = r_f$. The field outside $r > r_f$ is zero, so if the solution does not itself taper continuously to zero by that point, then this would give rise to the presence of infinite current sheets at r_f, which would be unphysical. The components of the field are given by

$$\begin{aligned}\mathbf{B} &= (B_r, B_\theta, B_\varphi)\\ &= -\frac{1}{r\sin\theta}\left(-\frac{1}{r}\frac{\partial\psi}{\partial\theta}\,,\ \frac{\partial\psi}{\partial r}\,,\ \lambda\psi\right)\\ &= \left(\frac{2}{r^2}\Psi(r)\cos\theta\,,\ -\frac{1}{r}\Psi'(r)\sin\theta\,,\ -\frac{\lambda}{r}\Psi(r)\sin\theta\right),\end{aligned} \tag{3.24}$$

meaning that we require

$$\Psi(0) = 0\,, \quad \Psi(r_f) = 0\,, \quad \Psi'(r_f) = 0\,. \tag{3.25}$$

Again following Prendergast (1956), the trick to satisfying all three boundary conditions is to apply the usual Green's function method to obtain a solution satisfying the first two, and then choosing λ in an appropriate way that the third becomes satisfied.

The two fundamental solutions satisfying the homogeneous version of Equation (3.23) are $r\,j_1(\lambda r)$ and $r\,y_1(\lambda r)$, where j_1 and y_1 are spherical Bessel functions:

$$j_1(x) = \frac{\sin x}{x^2} - \frac{\cos x}{x}\,, \quad y_1(x) = -\frac{\cos x}{x^2} - \frac{\sin x}{x}\,. \tag{3.26}$$

From these, we construct the independent solutions $\Psi_1(r)$ and $\Psi_2(r)$, which separately satisfy the first and second of (3.25), respectively. These are

$$\Psi_1(r) = r\,j_1(\lambda r)\,, \quad \Psi_2(r) = c\,r\,j_1(\lambda r) + r\,y_1(\lambda r)\,, \tag{3.27}$$

where

$$c = -\frac{y_1(\lambda r_f)}{j_1(\lambda r_f)} = \frac{\cos(\lambda r_f) + \lambda r_f \sin(\lambda r_f)}{\sin(\lambda r_f) - \lambda r_f \cos(\lambda r_f)}\,. \tag{3.28}$$

These satisfy $\Psi_1(0) = 0$ and $\Psi_2(r_f) = 0$. The associated Wronskian is

$$W[\Psi_1, \Psi_2] = \Psi_1\Psi_2' - \Psi_1'\Psi_2 = \lambda r^2\left[j_1(\lambda r)y_1'(\lambda r) - j_1'(\lambda r)y_1(\lambda r)\right]\,,$$

where it can be shown that

$$j_1(x)y_1'(x) - j_1'(x)y_1(x) = \frac{1}{x^2} \implies W = \frac{1}{\lambda}\,. \tag{3.29}$$

The general solution is then

$$\Psi(r) = \frac{\Psi_2(r)}{W}\int_0^r \beta\rho\xi^2\Psi_1(\xi)\,\mathrm{d}\xi + \frac{\Psi_1(r)}{W}\int_r^{r_f} \beta\rho\xi^2\Psi_2(\xi)\,\mathrm{d}\xi\,, \tag{3.30}$$

with Ψ_1 and Ψ_2 given in (3.27). Defining the auxilliary function

$$f_\lambda(r_1, r_2) \equiv j_1(\lambda r_2)y_1(\lambda r_1) - j_1(\lambda r_1)y_1(\lambda r_2)\,, \tag{3.31}$$

the solution can be written

$$\Psi(r) = \frac{\beta\lambda r}{j_1(\lambda r_f)}\left[f_\lambda(r, r_f)\int_0^r \rho\xi^3 j_1(\lambda\xi)\,\mathrm{d}\xi + j_1(\lambda r)\int_r^{r_f} \rho\xi^3 f_\lambda(\xi, r_f)\,\mathrm{d}\xi\right]\,. \tag{3.32}$$

The condition on λ that must be imposed to satisfy the third boundary condition can be found by setting

$$0 = \Psi'(r_f) = \frac{\beta}{r_f\,j_1(\lambda r_f)}\int_0^{r_f} \rho\xi^3 j_1(\lambda\xi)\,\mathrm{d}\xi \tag{3.33}$$

$$\implies \int_0^{r_f} \rho\xi^3 j_1(\lambda\xi)\,\mathrm{d}\xi = 0\,. \tag{3.34}$$

Equations (3.32) and (3.34) define what we shall refer to as the *Prendergast solution*. The result for an $n = 3$ polytrope, with r_f set to $0.3\,R_*$, is shown in Figure 3.1. It can be seen that this qualitatively resembles a dipole configuration, but with several notable differences: (i) it is fully confined within a sphere of finite radius r_f, unlike a dipole which extends to infinity; (ii) it is finite everywhere, whereas a dipole is singular at the origin; (iii) there is a non-zero toroidal component. These are all attributes one desires a confined equilibrium field to possess, making the Prendergast solution a convenient modelling choice, especially since it can be written down in closed form. Note, however, that in general λ needs to be obtained by numerical root-finding in the case of arbitrary density profiles.

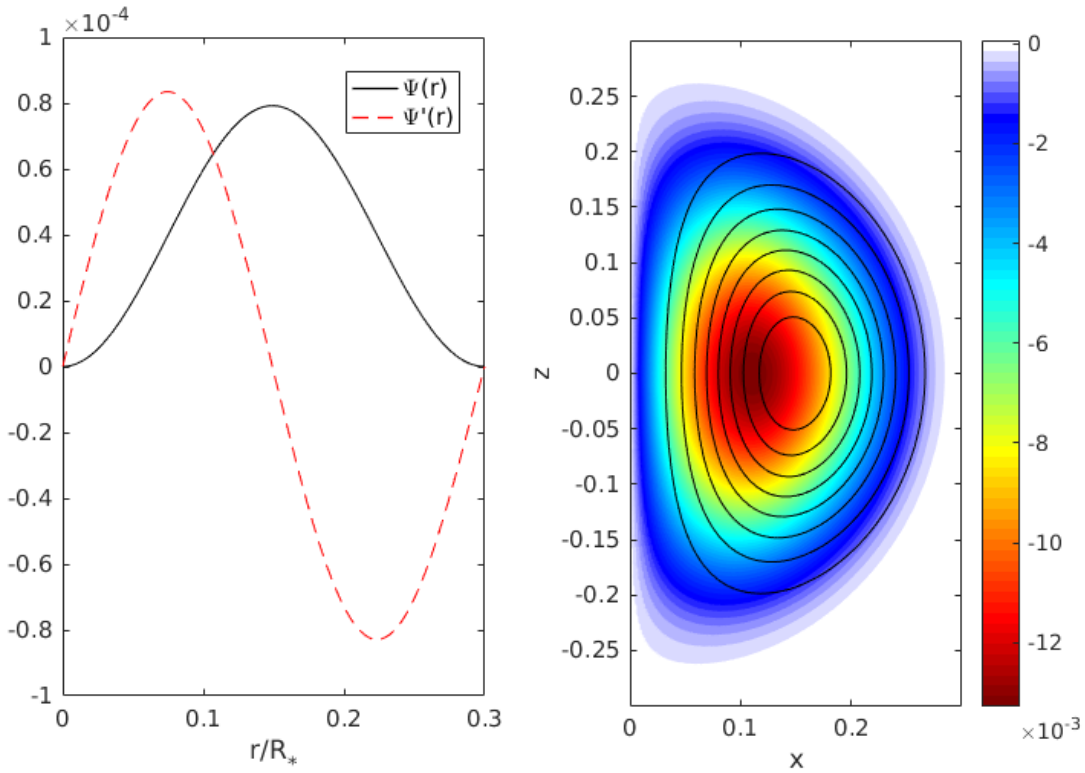

Figure 3.1: Plots of the Prendergast solution for an $n = 3$ polytrope, where the magnetic field resides within the inner 0.3 of the stellar radius. Left: the radial flux function Ψ and its derivative (amplitudes and relative scalings are arbitrary and for visual convenience). Right: The toroidal component of the field, B_φ, in colour, overlaid with a selection of poloidal field lines (level surfaces of ψ). The value of λ satisfying Equation (3.34) in this case was 21.969.

3.2.2 Variational interpretation

It is possible to derive the Grad-Shafranov equation through a different route, namely through a variational treatment, and in doing so arrive at a physical interpretation of the constants λ and β (Duez et al., 2010). Let us consider an equilibrium field configuration to be the solution minimising the magnetic energy

$$E_m = \int_V \frac{B^2}{2\mu_0}\,\mathrm{d}V \tag{3.35}$$

subject to the conservation of the following quantities:

$$M_0 = \int_V \rho\,\mathrm{d}V\,, \quad M_1 = \int_V \rho\psi\,\mathrm{d}V\,, \quad \Phi_t = \int_S \mathbf{B}\cdot\mathrm{d}\mathbf{S}\,, \quad \mathscr{H} = \int_V \mathbf{A}\cdot\mathbf{B}\,\mathrm{d}V\,, \tag{3.36}$$

which are the total mass, the mass contained within each flux surface, the toroidal flux (here S refers to a meridional plane), and the helicity. Noting that the volume element in cylindrical polar coordinates is $\mathrm{d}V = R\,\mathrm{d}R\,\mathrm{d}\phi\,\mathrm{d}z$, and that the surface element for a meridional plane is $\mathrm{d}\mathbf{S} = \mathrm{d}R\,\mathrm{d}z\hat{\boldsymbol{\phi}}$, the toroidal flux can then be written

$$\Phi_t = \frac{1}{2\pi}\int_V \frac{B_\phi}{R}\,\mathrm{d}V\,. \tag{3.37}$$

This allows us to define the functional

$$\begin{aligned}\mathscr{F} &= E_m + \lambda_0 M_0 + \lambda_1 M_1 + \lambda_2\Phi_t + \lambda_3\mathscr{H} \\ &= \int_V \left(\frac{B^2}{2\mu_0} + \lambda_0\rho + \lambda_1\rho\psi + \lambda_2\frac{B_\phi}{2\pi R} + \lambda_3\mathbf{A}\cdot\mathbf{B}\right) R\,\mathrm{d}R\,\mathrm{d}\phi\,\mathrm{d}z\,,\end{aligned} \tag{3.38}$$

from which we identify the relevant Lagrangian as

$$L = R\left(\frac{B^2}{2\mu_0} + \lambda_0\rho + \lambda_1\rho\psi + \lambda_2\frac{B_\phi}{2\pi R} + \lambda_3\mathbf{A}\cdot\mathbf{B}\right), \tag{3.39}$$

where λ_0, λ_1, λ_2 and λ_3 are the Lagrange multipliers enforcing conservation of the four quantities listed above.

It is possible to express this in terms of the magnetic vector potential $\mathbf{A}$, in terms of which

$$\mathbf{B} = \left(-\frac{\partial A_\phi}{\partial z}, \frac{\partial A_R}{\partial z} - \frac{\partial A_z}{\partial R}, \frac{A_\phi}{R} + \frac{\partial A_\phi}{\partial R}\right) \quad \text{and} \quad \psi = RA_\phi\,, \tag{3.40}$$

$$\begin{aligned}\implies L = \frac{R}{2\mu_0}&\left[(\partial_z A_\phi)^2 + (\partial_z A_R)^2 - 2(\partial_z A_R)(\partial_R A_z) + (\partial_R A_z)^2 + \left(\frac{A_\phi}{R}\right)^2 + 2\frac{A_\phi}{R}\partial_R A_\phi + (\partial_R A_\phi)^2\right] \\ &+ \lambda_0\rho R + \lambda_1\rho R^2 A_\phi + \frac{\lambda_2}{2\pi}(\partial_z A_R - \partial_R A_z) \\ &+ \lambda_3 R\left[-A_R\partial_z A_\phi + A_\phi(\partial_z A_R - \partial_R A_z) + A_z\left(\frac{A_\phi}{R} + \partial_R A_\phi\right)\right],\end{aligned} \tag{3.41}$$

where we invoke the shorthand $\partial_\alpha \equiv \partial/\partial\alpha$. The corresponding Euler-Lagrange equations are

$$\frac{\partial L}{\partial A_R} = \frac{\mathrm{d}}{\mathrm{d}z}\left(\frac{\partial L}{\partial(\partial_z A_R)}\right), \tag{3.42}$$

$$\frac{\partial L}{\partial A_z} = \frac{\mathrm{d}}{\mathrm{d}R}\left(\frac{\partial L}{\partial(\partial_R A_z)}\right), \tag{3.43}$$

$$\frac{\partial L}{\partial A_\phi} = \frac{\mathrm{d}}{\mathrm{d}R}\left(\frac{\partial L}{\partial(\partial_R A_\phi)}\right) + \frac{\mathrm{d}}{\mathrm{d}z}\left(\frac{\partial L}{\partial(\partial_z A_\phi)}\right). \tag{3.44}$$

Substituting (3.41) into these three equations yields

$$A_R: \quad -2\lambda_3 R\partial_z A_\phi = \frac{R}{\mu_0}(\partial_z^2 A_R - \partial_{Rz} A_z) \tag{3.45}$$

$$A_z: \quad 2\lambda_3 \partial_R \psi = \frac{1}{\mu_0}\left[-\partial_z A_R + \partial_R A_z - R\partial_{Rz} A_R + R\partial_R^2 A_z\right] \tag{3.46}$$

$$A_\phi: \quad \frac{A_\phi}{R\mu_0} + \lambda_1 \rho R^2 = 2\lambda_3 R(\partial_R A_z - \partial_z A_R) + \frac{1}{\mu_0}\partial_R A_\phi + \frac{R}{\mu_0}(\partial_R^2 A_\phi + \partial_z^2 A_\phi)\,. \tag{3.47}$$

Noting that $B_\phi = \partial_z A_R - \partial_R A_z$ and $\psi = RA_\phi$, the above equations can be maniputed into a single PDE involving ψ, as follows. Equation (3.45) becomes

$$0 = \frac{R}{\mu_0}\partial_z B_\phi + 2\lambda_3 \partial_z \psi\,.$$

Integrating both sides with respect to z, we get

$$B_\phi = \frac{\mu_0}{R}\left[f(R) - 2\lambda_3\psi\right], \tag{3.48}$$

$$\partial_R B_\phi = -\frac{B_\phi}{R} + \frac{\mu_0}{R}\left[f'(R) - 2\lambda_3 \partial_R \psi\right], \tag{3.49}$$

where $f(R)$ is an arbitrary function. Substituting these results into (3.46), we find that $f'(R) = 0$ and so f must be a constant. However, to maintain finite B_ϕ at the origin, we must have $f(0) = 0$, which means that f vanishes everywhere. Substituting

$$B_\phi = -\frac{2\lambda_3\mu_0\psi}{R} \tag{3.50}$$

into (3.47) and simplifying, we end up with

$$\lambda_1\mu_0\rho R^2 = 4\lambda_3^2\mu_0^2\psi + \partial_z^2\psi - \frac{1}{R}\partial_R\psi + \partial_R^2\psi\,, \tag{3.51}$$

which we recognise as the Grad-Shafranov equation of (3.20). From this we identify $\beta = \lambda_1\mu_0$ and $\lambda = 2\lambda_3\mu_0$, indicating that they are related to the Lagrange multipliers for conservation of mass and helicity, respectively.

3.3 Related solutions

Variants of the Prendergast solution may be constructed for other applications. In this section we describe some of these.

3.3.1 Cylindrical Prendergast

In a later chapter, we shall present simulations where an axisymmetric star has been modelled in a Cartesian geometry, that is, with curvature in the azimuthal direction neglected. A box is taken to represent the meridional section of the star, and translational symmetry in the z-direction ($\partial/\partial z \equiv 0$) mimicks rotational symmetry. The corresponding analogue of the Prendergast solution that would need to be imposed in this model is a helix whose axis aligns along z, i.e. what one would get by cutting open a torus and straightening it out. For simplicity of modelling, we will take the helix to be circular, and describe it in terms of cylindrical coordinates (R, ϕ, z), where R is radial distance from the centre of the helix, z is the distance along it, and ϕ is the azimuthal coordinate around the helix (note: although we reuse the symbols, these are *not* the same set of coordinates as has been used so far in this chapter). We shall refer to the result as the *cylindrical Prendergast solution*.

To obtain this, one follows a very similar procedure to that for the spherical Prendergast solution, but with a number of minor differences. To start with, the flux function ψ is now taken to obey

$$\mathbf{B} = \nabla \times \psi \hat{\mathbf{z}} + B_z \hat{\mathbf{z}}, \tag{3.52}$$

which under $\partial/\partial\phi \equiv 0$ corresponds to a field with no R-component. It is straightforward to show that

$$\begin{aligned}(\nabla \times \mathbf{B}) \times \mathbf{B} &= -\frac{\mathrm{d}B_z}{\mathrm{d}R} B_z \hat{\mathbf{R}} + \frac{B_\phi}{R} \frac{\mathrm{d}}{\mathrm{d}R}\left(R \frac{\mathrm{d}\psi}{\mathrm{d}R}\right) \hat{\mathbf{R}} \\ &= -B_z \nabla B_z - \nabla\psi \Delta^* \psi\,, \end{aligned} \tag{3.53}$$

where

$$\Delta^* = \nabla^2 = \frac{1}{R}\frac{\mathrm{d}}{\mathrm{d}R}\left(R\frac{\mathrm{d}}{\mathrm{d}R}\right). \tag{3.54}$$

Taking the dot product with $\mathbf{B}$ of both sides of Equation (3.53) yields the result $\nabla B_z \cdot \mathbf{B} = 0$, which means that $B_z = B_z(\psi)$. Following Prendergast, we choose $B_z(\psi) = \lambda\psi$, with λ a constant. As before, adopting the barotropic equation of state implies that

$$0 = \nabla \times \left[\frac{(\nabla \times \mathbf{B}) \times \mathbf{B}}{\rho}\right] = \nabla\psi \times \nabla\left(\frac{\Delta^*\psi + \lambda^2\psi}{\rho}\right), \tag{3.55}$$

which means

$$\frac{\Delta^*\psi + \lambda^2\psi}{\rho} = G(\psi)\,. \tag{3.56}$$

Again following Prendergast, we choose this to be a global constant $\kappa = G(\psi)$, in which case we end up with

$$\frac{1}{R}\frac{\mathrm{d}}{\mathrm{d}R}\left(R\frac{\mathrm{d}\psi}{\mathrm{d}R}\right) + \lambda^2\psi = \kappa\rho \tag{3.57}$$

as the cylindrical analogue of the Grad-Shafranov equation. The independent solutions to the homogeneous problem in this case are $J_0(\lambda R)$ and $Y_0(\lambda R)$. The appropriate boundary conditions, given that

$$(B_R, B_\phi, B_z) = (0, -\psi', \lambda\psi)\,, \tag{3.58}$$

are

$$\psi'(0) = 0\,, \quad \psi'(a) = 0\,, \quad \psi(a) = 0\,, \tag{3.59}$$

where a is the radius of the helix (the radius beyond which the field vanishes). The solution to (3.57) satisfying these boundary conditions is

$$\psi(R) = \frac{\kappa\rho}{\lambda^2}\left[1 - \frac{J_0(\lambda R)}{J_0(\lambda a)}\right], \tag{3.60}$$

with λ satisfying

$$J_1(\lambda a) = 0\,. \tag{3.61}$$

The overall field solution within $R < a$ is then

$$\mathbf{B} = \frac{\kappa\rho}{\lambda}\left(0, -\frac{J_1(\lambda R)}{J_0(\lambda a)}, 1 - \frac{J_0(\lambda R)}{J_0(\lambda a)}\right). \tag{3.62}$$

This is shown plotted in Figure 3.2. It can be seen that this is a helix whose pitch angle increases towards the centre, with all components vanishing on the boundary.

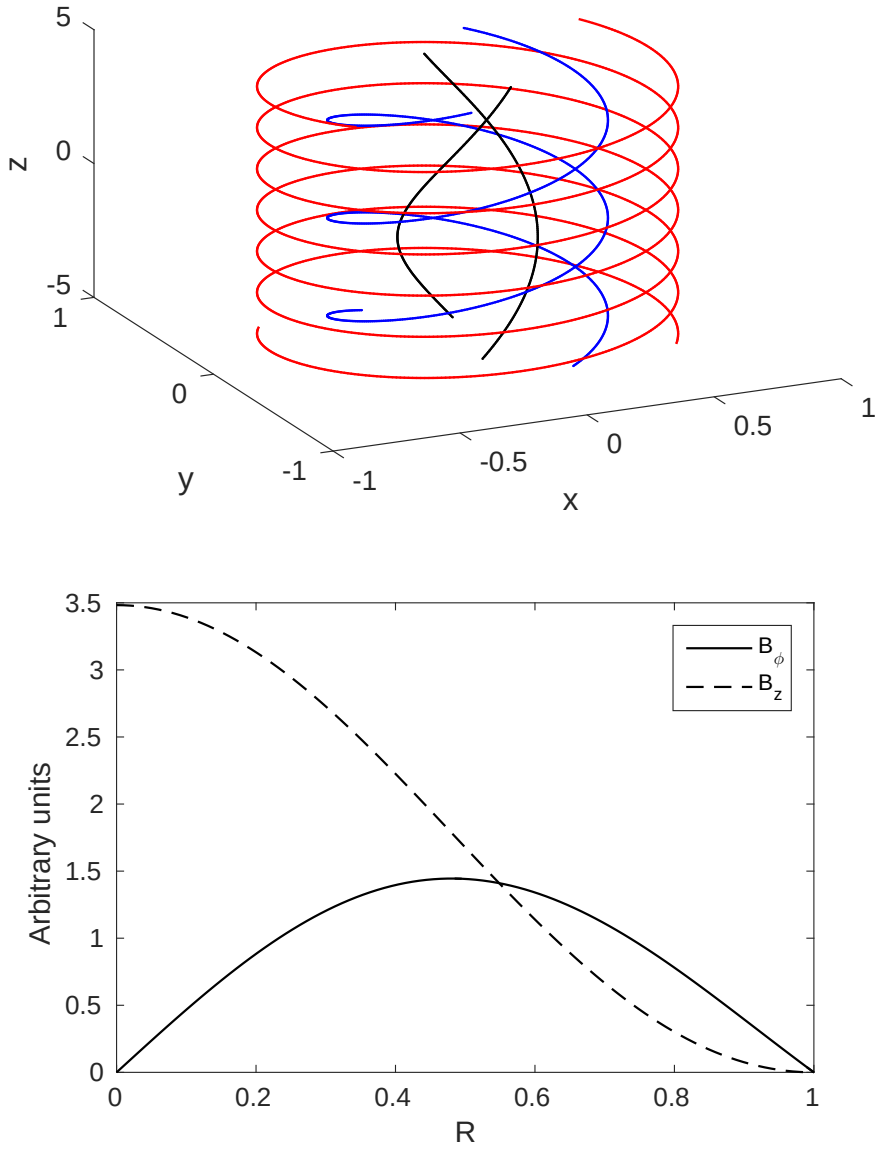

Figure 3.2: Top: A selection of field lines at radial distances of 0.25 (black), 0.5 (blue), and 0.75 (red) units from the axis of the cylinder, which has a radius of $a = 1$. Bottom: The ϕ- and z-components of the cylindrical Prendergast solution, as a function of radius.

3.3.2 Unconfined spherical Prendergast

Suppose we want to model a star that is pervaded by a magnetic field, and that this field penetrates the surface. Outside the star the field would be a potential field, since there is no force-bearing or current-carrying medium (this is taken to be a vacuum). A dipole field is an example of a plausible model for the vacuum field. Inside the star, we would expect the field to contain a mixture of poloidal and toroidal components, as in the Prendergast solution. Note that a dipole field has an unphysical singularity at the origin and so cannot be used to model the field throughout the whole interior. In this section, we will demonstrate how an exterior dipole field can be matched to a Prendergast-like solution to obtain an overall field model that is continuous and finite everywhere. Such a field may perhaps be used to model a stably-stratified, magnetised object such as a white dwarf or neutron star.

Let us define two regions within the star, which we will refer to as A and B, with region A occupying $0 \le r \le R_0$ and region B lying between $R_0 < r \le R_*$. Here R_* is the stellar radius, and R_0 is the radius at which the toroidal component of the field vanishes. The reason for introducing an intermediate region B is because it is not possible to stitch the Prendergast field directly to a dipole: to cancel the ϕ-component at the boundary we require $\Psi = 0$ there, but this also cancels the r-component which is inconsistent with a dipole field. Rather, the plan is to cancel the r- and ϕ-components at the radius R_0, and then have the solution evolve towards a dipole field by the radius R_*. Let the solutions for the two regions be denoted $\Psi_{\rm A}(r)$ and $\Psi_{\rm B}(r)$, and the exterior solution be $\Psi_{\rm ext}(r) \propto 1/r$. These are governed by the DEs

$$\Psi_{\rm A}'' - \left(\frac{2}{r^2} - \lambda^2\right)\Psi_{\rm A} = \beta\rho r^2\,, \tag{3.63}$$

$$\Psi_{\rm B}'' - \frac{2}{r^2}\Psi_{\rm B} = \beta\rho r^2\,. \tag{3.64}$$

The relevant boundary and matching conditions are

$$\begin{aligned} &\Psi_{\rm A}(0) = 0\,, \quad \Psi_{\rm A}(R_0) = 0\,, \quad \Psi_{\rm A}'(R_0) = \Psi_{\rm B}'(R_0)\,,\\ &\Psi_{\rm B}(R_0) = 0\,, \quad \Psi_{\rm B}(R_*) + R_*\Psi_{\rm B}'(R_*) = 0\,, \end{aligned} \tag{3.65}$$

which must be satisfied by two second-order ODEs. Notice there are five conditions, so we require an additional parameter besides the four constants of integration. This is conveniently provided by λ, which we shall use to satisfy the third of (3.65) after we have obtained the solution satisfying the remaining four. The solution for region A, satisfying the first two of (3.65), is given by the same expression as found previously for the usual Prendergast solution, i.e.

$$\Psi_{\rm A}(r) = \frac{\beta\lambda r}{j_1(\lambda R_0)}\left[f_\lambda(r,R_0)\int_0^r \rho\xi^3 j_1(\lambda\xi)\,{\rm d}\xi + j_1(\lambda r)\int_r^{R_0}\rho\xi^3 f_\lambda(\xi,R_0)\,{\rm d}\xi\right], \tag{3.66}$$

where f_λ is defined in (3.31).

In the case of region B, the fundamental solutions to the homogeneous version of (3.64) are r^2 and $1/r$, yielding the independent solutions

$$\Psi_{\rm 1B}(r) = r^2 - \frac{R_0^3}{r}\,, \quad \Psi_{\rm 2B}(r) = \frac{1}{r}\,, \tag{3.67}$$

satisfying the last two of (3.65). The overall Green's function solution for region B is

$$\Psi_{\rm B}(r) = -\frac{\beta}{3r}\left[\int_{R_0}^r \rho\xi(\xi^3 - R_0^3)\,{\rm d}\xi + (r^3 - R_0^3)\int_r^{R_*}\rho\xi\,{\rm d}\xi\right]. \tag{3.68}$$

From (3.66) and (3.68), it can be shown that the condition on λ to satisfy $\Psi'_{\rm A}(R_0) = \Psi'_{\rm B}(R_0)$ is

$$\frac{1}{j_1(\lambda R_0)} \int_0^{R_0} \rho \xi^3 j_1(\lambda \xi)\, \mathrm{d}\xi + R_0 \int_{R_0}^{R_*} \rho \xi \, \mathrm{d}\xi = 0\,. \tag{3.69}$$

Finally, we solve for the constant of proportionality K for the exterior solution $\Psi_{\rm ext} = K/r$ by matching this to $\Psi_{\rm B}$:

$$\begin{aligned} \Psi_{\rm B}(R_*) = \Psi_{\rm ext}(R_*) \implies K &= -\frac{\beta}{3} \int_{R_0}^{R_*} \rho \xi (\xi^3 - R_0^3)\, \mathrm{d}\xi \\ \Psi_{\rm ext}(r) &= -\frac{\beta}{3r} \int_{R_0}^{R_*} \rho \xi (\xi^3 - R_0^3)\, \mathrm{d}\xi\,. \end{aligned} \tag{3.70}$$

The overall solution, which we call the *unconfined spherical Prendergast solution*, is given by the combination of (3.66), (3.68), (3.69) and (3.70), and is illustrated in Figure 3.3 for an $n = 3$ polytrope with R_0 set to 0.7 of the stellar radius. The smallest value of λ satisfying (3.69) in this case was $\lambda = 32.3218$.

3.3.3 Unconfined shell Prendergast

Suppose we wish to model the field in a radiative envelope that connects to a potential field extending beyond the star, and let us assume that the field vanishes *below* some radius $r \le R_1$. One might use a configuration like this to model a fossil field anchored in a radiative envelope that surrounds a convective core, since it is thought that convection should expel such a field (cf. Weiss, 1966). This may be constructed as follows.

Let us define three regions A, B, and C, where A corresponds to the field-free core, B lies between $R_1 < r \le R_2$ and corresponds to the region containing mixed poloidal-toroidal field, and C lies between $R_2 < r \le R_*$ and contains only poloidal field. Beyond $r > R_*$, the solution is given by a dipole. We shall call the solutions in the three regions $\Psi_{\rm A}(r)$, $\Psi_{\rm B}(r)$ and $\Psi_{\rm C}(r)$, and the exterior dipole solution $\Psi_{\rm ext}(r)$. The DEs governing these solutions are

$$\Psi''_{\rm A} - \frac{2\Psi_{\rm A}}{r^2} = 0\,, \tag{3.71}$$

$$\Psi''_{\rm B} - \left(\frac{2}{r^2} - \lambda^2\right)\Psi_{\rm B} = \beta\rho r^2\,, \tag{3.72}$$

$$\Psi''_{\rm C} - \frac{2\Psi_{\rm C}}{r^2} = \beta\rho r^2\,, \tag{3.73}$$

subject to the boundary and matching conditions

$$\Psi_{\rm A}(R_1) = 0\,, \quad \Psi'_{\rm A}(R_1) = 0\,, \quad \Psi_{\rm B}(R_1) = 0\,, \quad \Psi'_{\rm B}(R_1) = 0\,, \quad \Psi_{\rm B}(R_2) = 0\,, \tag{3.74}$$

$$\Psi'_{\rm B}(R_2) = \Psi'_{\rm C}(R_2)\,, \quad \Psi_{\rm C}(R_2) = 0\,, \quad \Psi_{\rm C}(R_*) + R_*\Psi'_{\rm C}(R_*) = 0\,. \tag{3.75}$$

In region A, which is governed by a second-order homogeneous DE with homogeneous boundary conditions, the solution is simply the zero solution, i.e.

$$\Psi_{\rm A}(r) = 0\,. \tag{3.76}$$

In region B, the two fundamental solutions are $r\,j_1(\lambda r)$ and $r\,y_1(\lambda r)$, from which we construct the two independent solutions

$$\Psi_{\rm 1B}(r) = r\,j_1(\lambda r) - \frac{j_1(\lambda R_1)}{y_1(\lambda R_1)} r\,y_1(\lambda r) \tag{3.77}$$

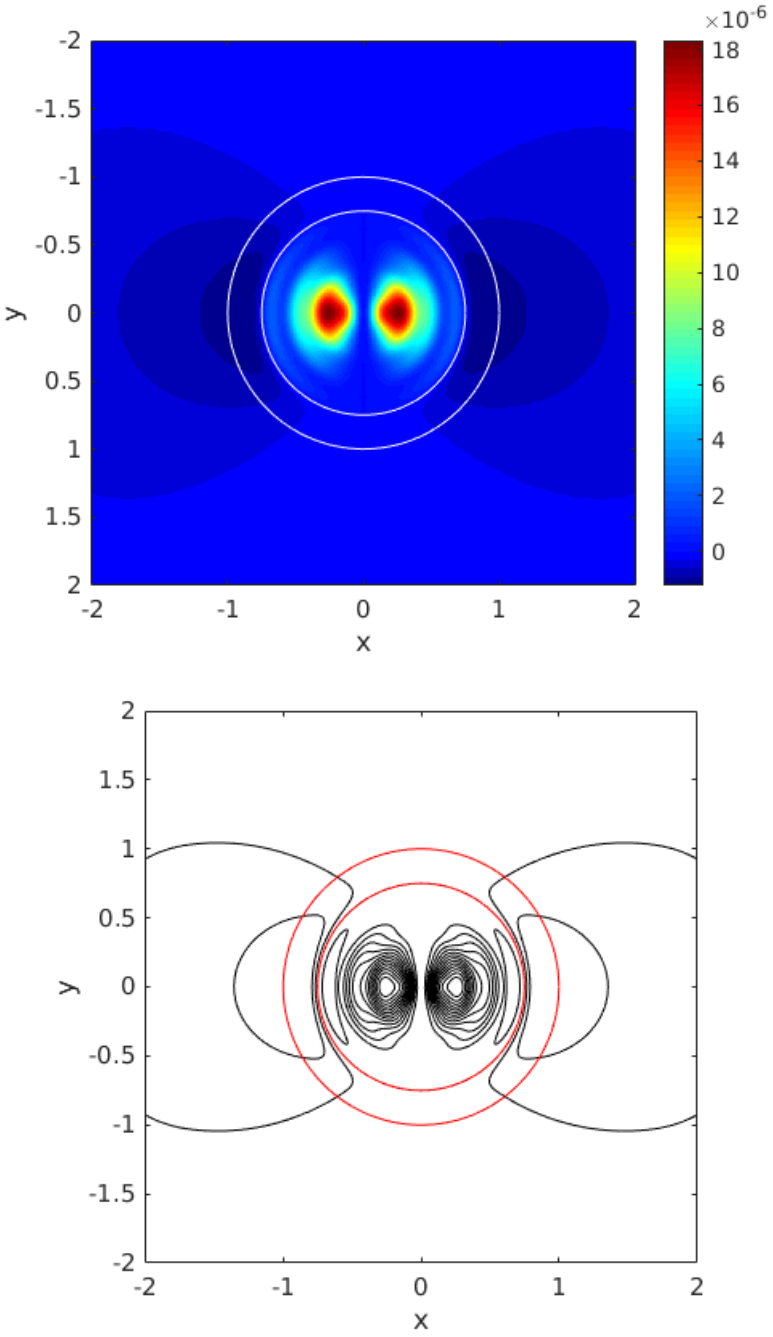

Figure 3.3: The unconfined spherical Prendergast solution, computed for an $n = 3$ polytrope. The top panel shows the value of the flux function ψ in a meridional section, while the bottom panel shows the poloidal projections of a selection of magnetic field lines (level surfaces of ψ). White and red circles mark the locations of $R_0 = 0.7$ and $R_* = 1$. The value of λ for this solution is 32.3218.

and

$$\Psi_{2\mathrm{B}}(r) = r\,y_1(\lambda r) - \frac{y_1(\lambda R_2)}{j_1(\lambda R_2)}\,r\,j_1(\lambda r) \tag{3.78}$$

satisfying $\Psi_{1\mathrm{B}}(R_1) = 0$ and $\Psi_{2\mathrm{B}}(R_2) = 0$. The Wronskian is given by

$$W[\Psi_{1\mathrm{B}}, \Psi_{2\mathrm{B}}] = \frac{1}{\lambda}\left[1 - \frac{j_1(\lambda R_1)\,y_1(\lambda R_2)}{y_1(\lambda R_1)\,j_1(\lambda R_2)}\right], \tag{3.79}$$

from which we obtain

$$\Psi_{\mathrm{B}}(r) = \frac{\beta\lambda r}{f_\lambda(R_1, R_2)}\left[f_\lambda(r, R_2)\int_{R_1}^{r}\rho\xi^3 f_\lambda(R_1,\xi)\,\mathrm{d}\xi + f_\lambda(R_1, r)\int_{r}^{R_2}\rho\xi^3 f_\lambda(\xi, R_2)\,\mathrm{d}\xi\right]. \tag{3.80}$$

For region C, the solution is the same as given by region B for the unconfined spherical solution (described in the previous section), i.e.

$$\Psi_{\mathrm{C}}(r) = -\frac{\beta}{3r}\left[\int_{R_2}^{r}\rho\xi(\xi^3 - R_2^3)\,\mathrm{d}\xi + (r^3 - R_2^3)\int_{r}^{R_*}\rho\xi\,\mathrm{d}\xi\right], \tag{3.81}$$

which satisfies the conditions $\Psi_{\mathrm{C}}(R_2) = 0$ and $\Psi_{\mathrm{C}}(R_*) + R_*\Psi'_{\mathrm{C}}(R_*) = 0$. The exterior solution is also as before:

$$\Psi_{\mathrm{ext}}(r) = -\frac{\beta}{3r}\int_{R_2}^{R_*}\rho\xi(\xi^3 - R_2^3)\,\mathrm{d}\xi\,. \tag{3.82}$$

There remain two conditions to be satisfied, namely

$$\Psi'_{\mathrm{B}}(R_1) = 0 \implies \int_{R_1}^{R_2}\rho\xi^3 f_\lambda(R_2,\xi)\,\mathrm{d}\xi = 0 \tag{3.83}$$

and

$$\Psi'_{\mathrm{B}}(R_2) = \Psi'_{\mathrm{C}}(R_2) \implies R_2^2 f_\lambda(R_1, R_2)\int_{R_2}^{R_*}\rho\xi\,\mathrm{d}\xi + \int_{R_1}^{R_2}\rho\xi^3 f_\lambda(R_1,\xi)\,\mathrm{d}\xi = 0\,. \tag{3.84}$$

However, it would appear that we only have one free parameter, λ, at our disposal, suggesting that the problem is overconstrained. The resolution to this dilemma is to let one of R_1, R_2 or R_* vary. Ideally, we would like to fix two parameters such that the remaining two can be obtained by two separate one-dimensional searches. Notice that (3.83) depends on R_1, R_2 and λ, while (3.84) depends on R_1, R_2, R_* and λ. The obvious choice is then to fix R_1 and R_2, solve for λ by numerical root-finding on (3.83), then substitute this into (3.84) and perform numerical root-finding to obtain R_*.

While it might seem strange that the radius of the star is not known until the very last step, it would be more appropriate to interpret this as the inner boundary of the dipole solution region. Inspecting the first term of Equation (3.84) shows that values of R_* extending beyond where ρ drops to zero are equivalent to setting R_* to this location, and so the calculated value of R_* would never lie in the vacuum region. We do not suppose it unreasonable that the dipole solution could encroach some way into the stellar interior, and so this construction method seems acceptable on the whole. This solution, which we call the *unconfined shell Prendergast solution*, is given by the combination of (3.76), (3.80), (3.81), (3.82), (3.83) and (3.84), and is illustrated in Figure 3.4 for an $n = 3$ polytrope with $R_1 = 0.4R_2$. For this model, the value of λ satisfying (3.83) was 9.3083 and the value of R_* satisfying (3.84) was 1.3069.

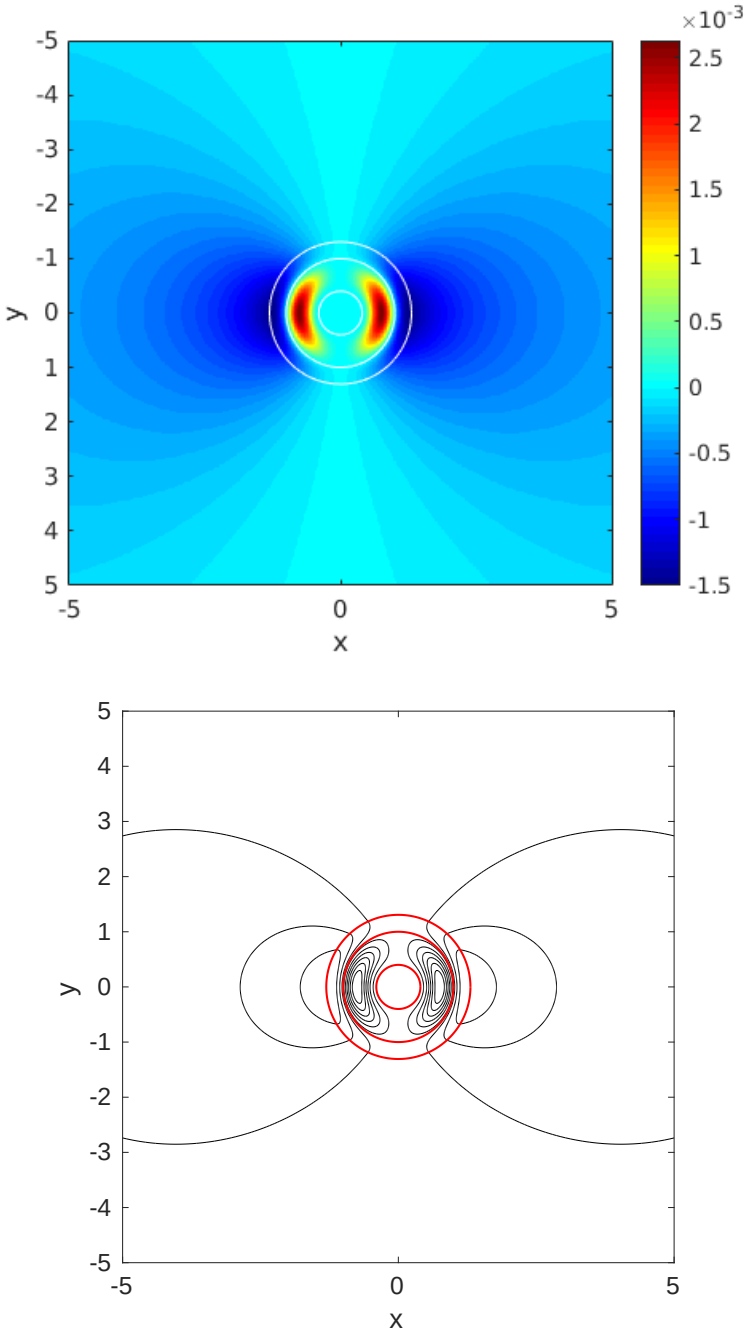

Figure 3.4: The unconfined shell Prendergast solution, displayed in the same manner as Figure 3.3. White and red circles mark the locations of $R_1 = 0.4$, $R_2 = 1$ and $R_* = 1.3069$. The value of λ for this solution is 9.3083.

Part II

STELLAR OSCILLATIONS

Chapter 4

Linear Adiabatic Theory

4.1 The oscillation equations

4.1.1 Derivation

In this section we derive the equations of stellar oscillation with rotation and magnetism neglected. We impose a time-harmonic dependence $\propto \exp(-\mathrm{i}\omega t)$, and all backgrounds are assumed to be spherically symmetric, allowing the system of DEs to be reduced to one with a single independent variable, r. The starting equations are the continuity equation, the momentum equation, Poisson's equation for the gravitational potential Φ and the adiabatic equation of state:

$$\frac{\partial \rho}{\partial t} = -\nabla \cdot (\rho \mathbf{u}) \,, \tag{4.1}$$

$$\rho \frac{\mathrm{D}\mathbf{u}}{\mathrm{D}t} = -\nabla p - \rho \nabla \Phi \,, \tag{4.2}$$

$$\nabla^2 \Phi = 4\pi G \rho \,, \tag{4.3}$$

$$\frac{\mathrm{D}}{\mathrm{D}t}\left(p\rho^{-\gamma}\right) = 0 \,. \tag{4.4}$$

We shall adopt the following expansion for all scalar quantities (p, ρ, Φ), that

$$p(\mathbf{r}, t) = p_0(r) + p'(r) Y_\ell^m(\theta, \phi) \exp(-\mathrm{i}\omega t) \,, \tag{4.5}$$

where Y_ℓ^m are spherical harmonics obeying the normalisation

$$\iint \left| Y_\ell^m \right|^2 \sin\theta \, \mathrm{d}\theta \, \mathrm{d}\phi = 1 \,, \tag{4.6}$$

subscript '0's denote background quantities, and primes denote Eulerian perturbations, which are assumed to be small ($|p'| \ll p_0$, etc.). We will consider the fluid displacement to be of the form

$$\boldsymbol{\xi}(\mathbf{r}, t) = \left[\xi_r(r) Y_\ell^m(\theta, \phi)\hat{\mathbf{r}} + \boldsymbol{\xi}_\mathrm{h}(\mathbf{r})\right] \exp(-\mathrm{i}\omega t) \,, \tag{4.7}$$

where subscript 'h' indicates the horizontal component. Background velocities are assumed to be zero. Substituting (4.5) and (4.7) into the above equations and linearising, the radial component of Equation (4.2) becomes

$$\frac{\mathrm{d}p'}{\mathrm{d}r} = \omega^2 \rho_0 \xi_r - \rho' \frac{\mathrm{d}\Phi_0}{\mathrm{d}r} - \rho_0 \frac{\mathrm{d}\Phi'}{\mathrm{d}r} \,. \tag{4.8}$$

From the adiabatic equation of state we have that $\delta p/p_0 = \gamma\delta\rho/\rho_0$, where δ denotes the Lagrangian perturbation satisfying

$$\delta p = p' + \xi_r \frac{\mathrm{d}p_0}{\mathrm{d}r}, \quad \delta\rho = \rho' + \xi_r \frac{\mathrm{d}\rho_0}{\mathrm{d}r}, \tag{4.9}$$

we get

$$\rho' = \frac{p'}{c_s^2} + \frac{\rho_0 \xi_r N^2}{g}. \tag{4.10}$$

Here

$$c_s^2 \equiv \frac{\gamma p_0}{\rho_0}, \tag{4.11}$$

$$N^2 \equiv g\left(\frac{1}{\gamma p_0}\frac{\mathrm{d}p_0}{\mathrm{d}r} - \frac{1}{\rho_0}\frac{\mathrm{d}\rho_0}{\mathrm{d}r}\right), \tag{4.12}$$

$$g = \frac{\mathrm{d}\Phi_0}{\mathrm{d}r}, \tag{4.13}$$

are the square of the adiabatic sound speed, the square of the buoyancy frequency, and the background gravitational acceleration, respectively. In addition, hydrostatic balance gives us $\mathrm{d}p_0/\mathrm{d}r = -\rho_0 g$. Substituting these results into (4.8) yields

$$\frac{\mathrm{d}p'}{\mathrm{d}r} = \rho_0(\omega^2 - N^2)\xi_r - \frac{p'}{\gamma H_p} - \rho_0\frac{\mathrm{d}\Phi'}{\mathrm{d}r}, \tag{4.14}$$

where

$$H_p \equiv \left(-\frac{1}{p_0}\frac{\mathrm{d}p_0}{\mathrm{d}r}\right)^{-1} \tag{4.15}$$

is the pressure scale height.

Next, consider the horizontal divergence of the horizontal component of Equation (4.2):

$$\rho_0\omega^2\nabla_\mathrm{h}\cdot\boldsymbol{\xi}_\mathrm{h} = \nabla_\mathrm{h}^2 p' + \rho_0\nabla_\mathrm{h}^2\Phi'. \tag{4.16}$$

The continuity equation (4.1) gives us

$$\rho' = -\frac{1}{r^2}\frac{\mathrm{d}}{\mathrm{d}r}\left(\rho_0 r^2\xi_r\right) - \rho_0\nabla_\mathrm{h}\cdot\boldsymbol{\xi}_\mathrm{h}, \tag{4.17}$$

which, combining with (4.10), can be used to eliminate $\nabla_\mathrm{h}\cdot\boldsymbol{\xi}_\mathrm{h}$ from (4.16) to yield

$$\frac{1}{r^2}\frac{\mathrm{d}}{\mathrm{d}r}\left(r^2\xi_r\right) = \frac{p'}{\rho_0 c_s^2}\left(\frac{S_\ell^2}{\omega^2} - 1\right) + \frac{\ell(\ell+1)}{r^2\omega^2}\Phi' + \frac{\xi_r}{\gamma H_p}. \tag{4.18}$$

Here

$$S_\ell^2 \equiv \frac{\ell(\ell+1)c_s^2}{r^2} \tag{4.19}$$

is the Lamb (acoustic) frequency, and we have used the property that Y_ℓ^m are eigenfunctions of ∇_h^2 with eigenvalue $-\ell(\ell+1)/r^2$.

Finally, the perturbed Poisson equation $\nabla^2\Phi' = 4\pi G\rho'$ gives us

$$\frac{1}{r^2}\frac{\mathrm{d}}{\mathrm{d}r}\left(r^2\frac{\mathrm{d}\Phi'}{\mathrm{d}r}\right) = 4\pi G\left(\frac{p'}{c_s^2} + \frac{\rho_0\xi_r N^2}{g}\right) + \frac{\ell(\ell+1)}{r^2}\Phi'. \tag{4.20}$$

The set of equations (4.14), (4.18) and (4.20) are known collectively as the equations of stellar oscillation. They form a fourth-order system that can be solved as a boundary eigenvalue problem, where ω^2 is the eigenvalue. However, in situations where the perturbation to the gravitational potential, Φ', can be neglected, this reduces to a second-order system. This is known as the *Cowling approximation* and works well

if the modes have small spatial scales. The equations of stellar oscillation in the Cowling approximation are given by

$$\frac{\mathrm{d}p'}{\mathrm{d}r} = \rho_0\left(\omega^2 - N^2\right)\xi_r - \frac{p'}{\gamma H_p} \tag{4.21}$$

$$\frac{1}{r^2}\frac{\mathrm{d}}{\mathrm{d}r}\left(r^2\xi_r\right) = \frac{p'}{\rho_0 c_s^2}\left(\frac{S_\ell^2}{\omega^2} - 1\right) + \frac{\xi_r}{\gamma H_p}\,. \tag{4.22}$$

4.1.2 Boundary conditions

The surface of the star can be regarded as a free boundary (no forces acting), so here we enforce that the Lagrangian pressure perturbation vanishes, i.e.

$$p'(R_*) = -\xi_r(R_*)\frac{\mathrm{d}p_0}{\mathrm{d}r}\Big|_{r=R_*}\,. \tag{4.23}$$

Since the equations are linear, the overall amplitude of the solution is arbitrary, and so in practice one may set $\xi_r(R_*) = 1$. As for the gravitational potential perturbation Φ', this needs to match to a vacuum solution, i.e. one satisfying $\nabla^2\Phi' = 0$. The solution by power-law expansion $\Phi \propto r^\alpha$ can be obtained by substituting this into

$$\begin{aligned}
\frac{1}{r^2}\frac{\mathrm{d}}{\mathrm{d}r}\left(r^2\frac{\mathrm{d}\Phi'}{\mathrm{d}r}\right) &= \frac{\ell(\ell+1)}{r^2}\Phi' \\
\alpha(\alpha+1)r^{\alpha-2} &= \ell(\ell+1)r^{\alpha-2} \\
\alpha^2 + \alpha - \ell(\ell+1) &= 0 \\
\implies \alpha = -(\ell+1) \quad &\text{or} \quad \ell\,.
\end{aligned} \tag{4.24}$$

The physically appropriate choice here (vanishing at infinity) is $\alpha = -(\ell+1)$, i.e.

$$\Phi'(R_*) = R_*^{-(\ell+1)}\,, \tag{4.25}$$

where we have set the arbitrary scaling factor to unity. Note that this result applies to $\ell > 0$ (non-radial oscillations). For purely radial oscillations ($\ell = 0$), the perturbation to the gravitational potential outside the star is zero, and so the appropriate boundary condition in that case would be $\Phi'(R_*) = 0$.

The inner boundary conditions are less straightforward to obtain, owing to the fact that $r = 0$ is a regular singular point of the equations. Rather, the boundary condition needs to be imposed at a small but non-zero value of r. An approximate solution near $r = 0$ can be obtained by adopting the series expansion

$$\xi_r(r) = \sum_{i=0}^{\infty} C_i r^{\alpha+i}\,. \tag{4.26}$$

Firstly, we note that ρ_0 and p_0 are nearly constant near the centre, and so

$$H_p^{-1} = -\frac{1}{p_0}\frac{\mathrm{d}p_0}{\mathrm{d}r} = \frac{1}{p_0}\frac{\rho_0 G m_r}{r^2} \approx \frac{4\pi}{3}\frac{\rho_0^2 G}{p_0}r\,. \tag{4.27}$$

Let us define the auxilliary quantity

$$K \equiv \frac{1}{\gamma}\frac{4\pi}{3}\frac{\rho_0^2 G}{p_0}\,, \tag{4.28}$$

which approaches a constant near $r = 0$. Then Equation (4.22) becomes

$$\frac{1}{r^2}\frac{\mathrm{d}}{\mathrm{d}r}\left(r^2\xi_r\right) = \frac{p'\ell(\ell+1)}{\rho_0\omega^2 r^2}\left(1 - \frac{\omega^2}{S_\ell^2}\right) + Kr\xi_r\,. \tag{4.29}$$

Given that $\omega^2 \ll S_\ell^2$ in the deep interior, this can be rearranged into

$$p' \approx \frac{\rho_0 \omega^2 r^2}{\ell(\ell+1)} \left[\frac{1}{r^2} \frac{\mathrm{d}}{\mathrm{d}r} \left(r^2 \xi_r \right) - K r \xi_r \right] . \tag{4.30}$$

If one restricts consideration to just the leading order terms in the series, then

$$\xi_r = C_0 r^\alpha , \tag{4.31}$$

$$p' = \frac{\rho_0 \omega^2}{\ell(\ell+1)} (\alpha+2) C_0 r^{\alpha+1} . \tag{4.32}$$

From (4.21), noting that $N^2 \to 0$ at the centre,

$$\frac{\mathrm{d}p'}{\mathrm{d}r} \approx \rho \omega^2 \xi_r - K r p' , \tag{4.33}$$

which upon substituting (4.32) and retaining leading order terms gives us

$$(\alpha+2)(\alpha+1) r^\alpha = \ell(\ell+1) r^\alpha \tag{4.34}$$

$$\implies \alpha = \ell - 1 \quad \text{or} - (\ell+2) . \tag{4.35}$$

Of these, the regular solution corresponds to $\alpha = \ell - 1$ whereas the other is singular, and so we have near $r = 0$ the approximate solution (taking $C_0 = 1$, since the overall scaling is arbitrary)

$$\xi_r(r) = r^{\ell-1} , \quad p'(r) = \frac{\rho \omega^2}{\ell} r^\ell . \tag{4.36}$$

The above results hold for $\ell > 0$. In the radial case, instead of (4.29) and (4.32), we have

$$\frac{1}{r^2} \frac{\mathrm{d}}{\mathrm{d}r} \left(r^2 \xi_r \right) = -\frac{p'}{\rho_0 c_s^2} + K r \xi_r \tag{4.37}$$

and

$$p' = \rho_0 c_s^2 C_0 \left[K r^{\alpha+1} - (\alpha+2) r^{\alpha-1} \right] . \tag{4.38}$$

Substituting this into (4.33) and retaining only leading order terms yields

$$(2+\alpha)(\alpha-1) C_0 = 0 \quad \implies \quad \alpha = 1 \quad \text{or} \quad -2 . \tag{4.39}$$

The regular solution corresponds to $\alpha = 1$, and so for $\ell = 0$ the appropriate boundary conditions are (again choosing $C_0 = 1$)

$$\xi_r(r) = r , \quad p'(r) = -3 \rho_0 c_s^2 . \tag{4.40}$$

The same results apply in the full fourth-order system, but in this case we also need an inner boundary condition on Φ'. A similar series expansion can be used to show that this is

$$\Phi'(r) = \begin{cases} \frac{1}{2} \left(\omega^2 + 3 K c_s^2 \right) r^2 & \text{for} \quad \ell = 0 \\ \frac{\omega^2}{\ell} r^\ell & \text{for} \quad \ell > 0 . \end{cases} \tag{4.41}$$

4.2 Classification of modes

4.2.1 Asymptotic analysis

Let us now explore the physical properties of the solutions to the oscillation equations. If we neglect curvature terms, then the change of variable

$$\zeta = \rho_0^{1/2} c_s^2 \nabla \cdot \boldsymbol{\xi} \tag{4.42}$$

reduces Equations (4.21) and (4.22) to the single second-order ODE

$$\frac{\mathrm{d}^2\zeta}{\mathrm{d}r^2} = -k_r^2\zeta\,, \tag{4.43}$$

where

$$k_r^2 = \frac{\omega^2-\omega_c^2}{c_s^2} + \frac{S_\ell^2}{c_s^2}\left(\frac{N^2}{\omega^2}-1\right) \tag{4.44}$$

$$\omega_c^2 = \frac{c_s^2}{4H_\rho^2}\left(1-2\frac{\mathrm{d}H_\rho}{\mathrm{d}r}\right) \tag{4.45}$$

$$H_\rho = \left(-\frac{1}{\rho_0}\frac{\mathrm{d}\rho_0}{\mathrm{d}r}\right)^{-1} \tag{4.46}$$

are the radial wavenumber, acoustic cutoff frequency and the density scale height. Solutions are oscillatory when $k_r^2 > 0$ and evanescent where $k_r^2 < 0$. Turning points occur where $k_r^2 = 0$, i.e. when

$$\omega^2 = \frac{1}{2}\left(S_\ell^2+\omega_c^2\right) \pm \sqrt{\frac{1}{4}\left(S_\ell^2+\omega_c^2\right)^2 - N^2S_\ell^2}\,. \tag{4.47}$$

In the limit $N^2 \ll \omega_c^2 \ll S_\ell^2$, the two roots are approximately

$$\omega_+^2 \approx S_\ell^2\,, \quad \omega_-^2 \approx N^2\,. \tag{4.48}$$

We expect oscillatory behaviour where $\omega^2 > \omega_+^2$ or $\omega^2 < \omega_-^2$, and evanescent behaviour where $\omega_-^2 < \omega^2 < \omega_+^2$.

In the high-frequency limit, where $\omega^2 \gg \omega_c^2 \gg N^2$,

$$k_r^2 \approx \frac{\omega^2-S_\ell^2}{c_s^2} = \frac{\omega^2}{c_s^2} - k_\perp^2\,. \tag{4.49}$$

with the horizontal wavenumber $k_\perp$ defined according to

$$k_\perp^2 = \frac{\ell(\ell+1)}{r^2}\,. \tag{4.50}$$

$$\implies \omega^2 \approx c_s^2k^2\,, \tag{4.51}$$

where $k^2 = k_r^2 + k_\perp^2$ is the total squared wavenumber. This is the dispersion relation for acoustic waves, implying that high-frequency modes are acoustic in nature. They are called p-modes (p for *pressure*), and are localised to the region where $\omega^2 \gtrsim S_\ell^2$, known as the p-mode cavity. The lower boundary r_p occurs where $\omega^2 = S_\ell^2$, or

$$r_p = \frac{c_s\sqrt{\ell(\ell+1)}}{\omega}\,. \tag{4.52}$$

For a fixed ω, neglecting variations in c_s, the lower boundary of the p-mode cavity lies closer to the centre for lower ℓ, meaning that lower-degree modes penetrate deeper. Near the surface, H_ρ decreases dramatically and ω_c^2 overtakes S_ℓ^2, leading to $k_r^2 \approx (\omega^2-\omega_c^2)/r^2$ and giving rise to an upper turning point where $\omega^2 = \omega_c^2$. Physically, this corresponds to where mode wavelengths become larger than the scales of background density variations.

In the low-frequency limit, where $\omega^2 \ll N^2 \ll S_\ell^2$,

$$k_r^2 \approx \frac{S_\ell^2}{c_s^2}\left(\frac{N^2}{\omega^2}-1\right) = k_\perp^2\left(\frac{N^2}{\omega^2}-1\right) \tag{4.53}$$

$$\implies \omega^2 \approx \kappa_\perp^2 N^2\,, \tag{4.54}$$

where

$$\kappa_\perp^2 \equiv \frac{k_\perp^2}{k^2}\,. \tag{4.55}$$

This is the dispersion relation for gravity waves, and so in the low-frequency limit the modes possess gravity-wave character. They are called g-modes (g for *gravity*) and are localised to the region where $\omega^2 \lesssim N^2$, known as the g-mode cavity. Turning points are located where $\omega^2 = N^2$, and in this case are independent of ℓ. The size of the g-mode cavity is thus the same for all modes of the same degree. Note that since $k_\perp^2 \propto \ell(\ell+1)$, the only $\ell = 0$ modes are trivial ($\omega^2 = 0$). Hence the lowest-degree g-modes are dipole modes.

4.2.2 Quantum numbers

For any oscillator of finite physical extent, the spectrum is quantised, i.e. only modes of certain frequencies are permitted. It is possible to derive rough expressions for the expected frequencies of p- and g-modes, by applying the Wentzel-Kramers-Brillouin (WKB) method to Equation (4.43). Let us assume the form

$$\zeta(r) = A(r)\exp[\mathrm{i}S(r)]\,, \tag{4.56}$$

where $A(r)$ is much more slowly varying than $S(r)$. Substituting this into (4.43), and neglecting the term containing the second derivative of A, we obtain

$$2\mathrm{i}\frac{\mathrm{d}A}{\mathrm{d}r}\frac{\mathrm{d}S}{\mathrm{d}r}\exp(\mathrm{i}S) + \mathrm{i}\frac{\mathrm{d}^2S}{\mathrm{d}r^2}A\exp(\mathrm{i}S) - A\left(\frac{\mathrm{d}S}{\mathrm{d}r}\right)^2\exp(\mathrm{i}S) = -k_r^2 A\exp(\mathrm{i}S)\,. \tag{4.57}$$

Considering the separation of spatial scales involved, this equation can only be balanced if the leading order and next-to-leading order terms individually cancel, i.e.

$$k_r^2 = \left(\frac{\mathrm{d}S}{\mathrm{d}r}\right)^2\,, \tag{4.58}$$

$$-2\frac{\mathrm{d}A}{\mathrm{d}r}\frac{\mathrm{d}S}{\mathrm{d}r} = A\frac{\mathrm{d}^2S}{\mathrm{d}r^2}$$

$$\implies \ln A = \ln|k_r|^{-1/2} + \text{const.} \tag{4.59}$$

giving the overall solution

$$\zeta(r) \propto |k_r(r)|^{-1/2}\exp\left[\mathrm{i}\int k_r(r')\,\mathrm{d}r'\right]\,. \tag{4.60}$$

For real ζ, this corresponds to

$$\zeta(r) = \begin{cases} C_1|k_r(r)|^{-1/2}\cos\left(\int_{r_1}^r k_r(r')\,\mathrm{d}r' + \beta\right) & \text{for } k_r^2 > 0 \\ |k_r(r)|^{-1/2}\left(C_2\exp\left[\int_{r_1}^r |k_r(r')|\,\mathrm{d}r'\right] + C_3\exp\left[-\int_{r_1}^r |k_r(r')|\,\mathrm{d}r'\right]\right) & \text{for } k_r^2 < 0\,, \end{cases} \tag{4.61}$$

where $k_r(r_1) = 0$, and C_1, C_2 and C_3 are constants which must be determined by the boundary conditions.

Neglect of the $\mathrm{d}^2A/\mathrm{d}r^2$ term in arriving at (4.57) is not justified where $k_r^2 \to 0$, since $A \to \infty$ there. Points where $k_r = 0$ must be treated separately. Consider such a point $r = r_1$, where we use the Taylor expansion

$$k_r^2(r) \approx k_r^{2\prime}(r_1)[r - r_1]\,, \tag{4.62}$$

and define

$$x \equiv [k_r^{2\prime}(r_1)]^{1/3}[r - r_1]\,. \tag{4.63}$$

Then (4.43) becomes

$$\frac{\mathrm{d}^2\zeta}{\mathrm{d}x^2} = -x\zeta\,, \tag{4.64}$$

which is Airy's equation. The general solution is

$$\zeta(x) = C_4\mathrm{Ai}(-x) + C_5\mathrm{Bi}(-x)\,, \tag{4.65}$$

where Ai and Bi are Airy functions, and C_4 and C_5 are constants. For large positive x, the asymptotic formulae for these are

$$\mathrm{Ai}(-x) \sim \frac{1}{\sqrt{\pi}x^{1/4}}\sin\left(\frac{2}{3}x^{3/2}+\frac{\pi}{4}\right), \tag{4.66}$$

$$\mathrm{Bi}(-x) \sim \frac{1}{\sqrt{\pi}x^{1/4}}\cos\left(\frac{2}{3}x^{3/2}+\frac{\pi}{4}\right). \tag{4.67}$$

To prevent the solution diverging at $x=0$, we set $C_5=0$. This then gives us the solution

$$\zeta = \frac{C_4}{\sqrt{\pi}x^{1/4}}\sin\left(\frac{2}{3}x^{3/2}+\frac{\pi}{4}\right), \tag{4.68}$$

which needs to be matched to (4.61). Near $r=r_1$, this can be written

$$\zeta \approx C_1|k_r|^{-1/2}\sin\left(\int_{r_1}^{r}\left(k_r^{2\prime}(r_1)[r-r_1]\right)^{1/2}\mathrm{d}r' + \beta + \frac{\pi}{2}\right). \tag{4.69}$$

We thus identify

$$\frac{C_4}{C_1} = \sqrt{\pi}x^{1/4}|k_r|^{-1/2}\,, \quad \beta = -\frac{\pi}{4}\,. \tag{4.70}$$

Suppose $k_r^2 > 0$ within some radial interval $r_1 < r < r_2$, where $k_r^2(r_1) = k_r^2(r_2) = 0$. Two solutions which individually satisfy the boundary conditions are

$$\zeta_1(r) = C_1|k_r|^{-1/2}\cos\left(\int_{r_1}^{r}k_r(r')\,\mathrm{d}r' - \frac{\pi}{4}\right) \tag{4.71}$$

$$\zeta_2(r) = \tilde{C}_1|k_r|^{-1/2}\cos\left(\int_{r}^{r_2}k_r(r')\,\mathrm{d}r' - \frac{\pi}{4}\right). \tag{4.72}$$

These need to match at an intermediate radius r_f, i.e.

$$\zeta_1(r_f) = \zeta_2(r_f)\,, \quad \zeta_1'(r_f) = \zeta_2'(r_f)\,. \tag{4.73}$$

For brevity, let

$$S_1 = \int_{r_1}^{r_f}k_r(r')\,\mathrm{d}r' - \frac{\pi}{4} \tag{4.74}$$

$$S_2 = \int_{r_f}^{r_2}k_r(r')\,\mathrm{d}r' - \frac{\pi}{4}\,. \tag{4.75}$$

The matching conditions imply

$$C_1\cos S_1 - \tilde{C}_1\cos S_2 = 0 \tag{4.76}$$

$$C_1\sin S_1 + \tilde{C}_1\sin S_2 = 0\,. \tag{4.77}$$

This can only be true for non-trivial C_1 and $\tilde{C}_1$ if

$$\det\begin{pmatrix}\cos S_1 & -\cos S_2\\ \sin S_1 & \sin S_2\end{pmatrix} = 0$$

$$\sin(S_1+S_2) = 0 \implies S_1+S_2 = n\pi\,, \quad n\in\mathbb{Z}\,. \tag{4.78}$$

Hence

$$\int_{r_1}^{r_2}k_r(r')\,\mathrm{d}r' = \left(n+\frac{1}{2}\right)\pi\,, \tag{4.79}$$

where n is known as the *radial order* of the mode. Roughly speaking, this measures the number of radial crossings of the spatial amplitude function ξ_r. However, uniqueness of the eigenfrequency is not guaranteed for a given number of radial crossings. This is because p- and g-modes exhibit opposite behaviour: for p-modes, the frequency increases with the number of radial crossings, but for g-modes the frequency decreases.

The conventional way of assigning radial orders to p- and g-modes is to have *negative* radial orders for g-modes, to ensure that ω increases monotonically with n. When the Cowling approximation is made, there exists a straightforward algorithm, devised by Eckart (1960); Scuflaire (1974); Osaki (1975), for determining the value of n. This involves identifying the direction (clockwise or anticlockwise) of the point traced out in (ξ_r, p') space at the location of a radial crossing. If this is anticlockwise, then the crossing is classed as p-type, otherwise if it is clockwise, then it is classed as g-type. The value of n is then the number of p-type minus the number of g-type crossings.

Equation (4.79) can be used to infer the frequency spacings of the different types of modes. In the case of p-modes, we substitute (4.49), and taking the limit of $\omega^2 \gg S_\ell^2$, we find that

$$\omega_n = \pi \left(n + \frac{1}{2}\right) \left(\int_{r_1}^{r_2} \frac{\mathrm{d}r}{c_s}\right)^{-1} \tag{4.80}$$

$$\implies \Delta\nu \equiv \frac{\omega_{n+1} - \omega_n}{2\pi} = \left(2\int_{r_1}^{r_2} \frac{\mathrm{d}r}{c_s}\right)^{-1} . \tag{4.81}$$

Hence p-modes are expected to be roughly evenly spaced in frequency.

For g-modes, substituting (4.53) into (4.79) and assuming $\omega^2 \ll N^2$, we instead get

$$\frac{\sqrt{\ell(\ell+1)}}{\omega_n} = \pi \left(n + \frac{1}{2}\right) \left(\int_{r_1}^{r_2} \frac{N}{r}\,\mathrm{d}r\right)^{-1} \tag{4.82}$$

$$\implies \Delta\Pi \equiv 2\pi \left(\frac{1}{\omega_{n+1}} - \frac{1}{\omega_n}\right) = 2\pi^2 \left(\sqrt{\ell(\ell+1)} \int_{r_1}^{r_2} \frac{N}{r}\,\mathrm{d}r\right)^{-1} . \tag{4.83}$$

This means that g-modes are roughly evenly spaced in period.

4.2.3 Torsional vs. spheroidal

Previously, we considered the decomposition of $\boldsymbol{\xi}$ (a three-component vector) into radial and horizontal components, as per Equation (4.7), where the horizontal component $\boldsymbol{\xi}_\mathrm{h}$ is a two-dimensional vector lying in the local tangent plane to the sphere. In general, a three-dimensional vector field on a sphere can be decomposed with respect to the orthonormal basis

$$\left\{\hat{\mathbf{r}},\, \nabla_{\mathbb{S}^2} Y_\ell^m,\, \hat{\mathbf{r}} \times \nabla_{\mathbb{S}^2} Y_\ell^m\right\}, \tag{4.84}$$

where $\mathbb{S}^2$ refers to the two-sphere and

$$\nabla_{\mathbb{S}^2} Y_\ell^m \equiv \frac{\partial Y_\ell^m}{\partial\theta}\hat{\boldsymbol{\theta}} + \frac{1}{\sin\theta}\frac{\partial Y_\ell^m}{\partial\phi}\hat{\boldsymbol{\phi}} . \tag{4.85}$$

This corresponds to the extension of spherical harmonic decompositions to vector fields. With this choice of basis, we now write out the fluid displacement more fully as

$$\boldsymbol{\xi}(\mathbf{r},t) = \left[\xi_r(r) Y_\ell^m(\theta,\phi)\hat{\mathbf{r}} + \xi_\mathrm{h}(r)\nabla_{\mathbb{S}^2} Y_\ell^m(\theta,\phi) + \xi_\mathrm{T}(r)\hat{\mathbf{r}} \times \nabla_{\mathbb{S}^2} Y_\ell^m(\theta,\phi)\right] \exp(-\mathrm{i}\omega t) \tag{4.86}$$

$$= \left[\boldsymbol{\xi}_\mathrm{S}(\mathbf{r}) + \boldsymbol{\xi}_\mathrm{T}(\mathbf{r})\right] \exp(-\mathrm{i}\omega t) , \tag{4.87}$$

where the *spheroidal* component $\boldsymbol{\xi}_{\rm S}$ lies in a two-dimensional vector space spanned by the first two basis vectors of (4.84) and the *torsional* component $\boldsymbol{\xi}_{\rm T}$ is spanned by the third.

This decomposition has the properties that

$$\left(\nabla\times\boldsymbol{\xi}_{\rm S}\right)_r = 0\,, \quad \nabla\cdot\boldsymbol{\xi}_{\rm T} = 0\,, \tag{4.88}$$

where the subscript r denotes the radial component. Physically, spheroidal motions involve only deformations of the fluid and no shear/twist, while the opposite is true for torsional motions. Without rotation or magnetism, the fluid cannot restore torsional (shearing) motions; one can see this by considering the r-component of the curl of Equation (4.2), which vanishes. Thus in this situation, $\xi_{\rm T} = 0$ and

$$\boldsymbol{\xi}_{\rm h}(\mathbf{r}) = \xi_{\rm h}(r)\nabla_{\mathbb{S}^2} Y_\ell^m(\theta,\phi)\,, \tag{4.89}$$

where

$$\xi_{\rm h} = \frac{1}{r\omega^2}\left(\frac{p'}{\rho_0} + \Phi'\right). \tag{4.90}$$

Torsional motions with non-trivial frequencies can only be supported in the presence of Coriolis and Lorentz forces. In the case of stars that are partially solid, such as neutron stars which are thought to possess a crust, crustal elasticity may also provide a restoring force for torsional motions (e.g. Piro, 2005; Piro & Bildsten, 2005).

4.3 Perturbative effects

In the above derivation, we considered only pressure and buoyancy, and neglected other body forces. If additional forces are present but weak, then the mode frequencies will be close to the original values, but perturbed by a small amount. The magnitude and sign of this shift, as a function of the small parameter quantifying the perturbing influence (e.g. the rotation frequency or magnetic field strength), can be obtained via perturbation theory (Unno et al., 1989). In this section we will consider separately the effects of slow rotation and weak magnetic fields.

4.3.1 Rotation

We shall neglect magnetic fields and assume slow rotation, i.e. that $\Omega \ll \omega$, where Ω is the rotation frequency and ω is the mode frequency in the inertial frame. With this in mind, we will neglect the effects of centrifugal deformation and treat the backgrounds as being spherically symmetric. We shall also make use of the Cowling approximation ($\Phi' = 0$). The linearised equation of motion under these assumptions is

$$\frac{{\rm D}^2\boldsymbol{\xi}}{{\rm D}t^2} = -\frac{\nabla p'}{\rho} + \frac{\rho'}{\rho^2}\nabla p\,, \tag{4.91}$$

where

$$\frac{\rm D}{{\rm D}t} = \frac{\partial}{\partial t} + \mathbf{u}_0\cdot\nabla\,, \tag{4.92}$$

$$\mathbf{u}_0 = \boldsymbol{\Omega}\times\mathbf{r} \tag{4.93}$$

is the velocity field describing background rotation, and we have dropped subscript '0's on remaining variables with the understanding that all unprimed quantities (with the exception of $\boldsymbol{\xi}$) are backgrounds. With

$\boldsymbol{\Omega} = \Omega\hat{\mathbf{k}} = \Omega(\cos\theta\hat{\mathbf{r}} - \sin\theta\hat{\boldsymbol{\theta}})$ and $\mathbf{u}_0 = \Omega r\sin\theta\hat{\boldsymbol{\phi}}$, it can be shown that

$$\begin{aligned}(\mathbf{u}_0\cdot\nabla)\boldsymbol{\xi} &= \Omega\left(\frac{\partial\xi_r}{\partial\phi} - \xi_\phi\sin\theta\right)\hat{\mathbf{r}} + \Omega\left(\frac{\partial\xi_\theta}{\partial\phi} - \xi_\phi\cos\theta\right)\hat{\boldsymbol{\theta}} + \Omega\left(\frac{\partial\xi_\phi}{\partial\phi} + \xi_r\sin\theta + \xi_\theta\cos\theta\right)\hat{\boldsymbol{\phi}} \\ &= \mathrm{i}\Omega m\boldsymbol{\xi} + \boldsymbol{\Omega}\times\boldsymbol{\xi}\,, \end{aligned} \tag{4.94}$$

if we assume that $\boldsymbol{\xi}\propto\exp(\mathrm{i}m\phi)$. With

$$\bar{\omega} \equiv \omega + m\Omega \tag{4.95}$$

defined to be the frequency in the rotating frame (in this convention, prograde modes have negative m), we end up with

$$\frac{\mathrm{D}^2\boldsymbol{\xi}}{\mathrm{D}t^2} = -\bar{\omega}^2\boldsymbol{\xi} + 2\,\mathrm{i}\bar{\omega}\boldsymbol{\Omega}\times\boldsymbol{\xi} + \boldsymbol{\Omega}\times(\boldsymbol{\Omega}\times\boldsymbol{\xi})\,. \tag{4.96}$$

The last term above corresponds to the centrifugal acceleration, which we shall neglect. We thus arrive at the equation of motion

$$-\bar{\omega}^2\boldsymbol{\xi} + 2\,\mathrm{i}\bar{\omega}\boldsymbol{\Omega}\times\boldsymbol{\xi} = -\frac{\nabla p'}{\rho} + \frac{\rho'}{\rho^2}\nabla p\,. \tag{4.97}$$

Let us now expand the perturbed quantities as

$$\bar{\omega} = \omega_n^{(0)} + \omega^{(1)} + \cdots\,, \tag{4.98}$$

$$X = X_n^{(0)} + X^{(1)} + \cdots\,, \quad X\in\{\rho'\,,\,p'\,,\,\boldsymbol{\xi}\}\,, \tag{4.99}$$

where the leading terms represent the unperturbed ($\Omega = 0$) mode of order n, and successively higher-order terms are proportional to successively higher powers of Ω. Substituting (4.98) and (4.99) into (4.97), and neglecting terms of order Ω^2 and higher, we get

$$-2\omega_n^{(0)}\omega^{(1)}\boldsymbol{\xi}_n^{(0)} - \omega_n^{(0)2}\boldsymbol{\xi}^{(1)} + 2\,\mathrm{i}\omega_n^{(0)}\boldsymbol{\Omega}\times\boldsymbol{\xi}_n^{(0)} = -\frac{\nabla p'^{(1)}}{\rho} + \frac{\rho'^{(1)}}{\rho^2}\nabla p\,, \tag{4.100}$$

where we have used the fact that

$$-\omega_n^{(0)2}\boldsymbol{\xi}_n^{(0)} = -\frac{\nabla p_n'^{(0)}}{\rho} + \frac{\rho_n'^{(0)}}{\rho^2}\nabla p\,. \tag{4.101}$$

Since the eigenfunctions of the unperturbed system form a complete basis, we introduce the expansion

$$X^{(1)} = \sum_i a_i X_i^{(0)}\,, \quad X\in\{\rho'\,,\,p'\,,\,\boldsymbol{\xi}\}\,. \tag{4.102}$$

Substituting this into (4.100), and invoking (4.101) again, we arrive at

$$-2\omega_n^{(0)}\omega^{(1)}\boldsymbol{\xi}_n^{(0)} + 2\,\mathrm{i}\omega_n^{(0)}\boldsymbol{\Omega}\times\boldsymbol{\xi}_n^{(0)} = \sum_i a_i\left[\omega_n^{(0)2} - \omega_i^{(0)2}\right]\boldsymbol{\xi}_i^{(0)}\,. \tag{4.103}$$

Taking the inner product of both sides with $\boldsymbol{\xi}_n^{(0)}$, which satisfies the orthogonality condition

$$\langle\boldsymbol{\xi}_i\,,\,\boldsymbol{\xi}_j\rangle = \int\rho\boldsymbol{\xi}_i\cdot\boldsymbol{\xi}_j^*\,\mathrm{d}V = 0 \quad \text{if } i\neq j\,, \tag{4.104}$$

we end up with

$$\omega^{(1)} = \frac{\mathrm{i}\langle\boldsymbol{\Omega}\times\boldsymbol{\xi}_n^{(0)}\,,\,\boldsymbol{\xi}_n^{(0)}\rangle}{\langle\boldsymbol{\xi}_n^{(0)}\,,\,\boldsymbol{\xi}_n^{(0)}\rangle} = \frac{\mathrm{i}\int\rho(\boldsymbol{\Omega}\times\boldsymbol{\xi}_n^{(0)})\cdot\boldsymbol{\xi}_n^{(0)*}\,\mathrm{d}V}{\int\rho|\boldsymbol{\xi}_n^{(0)}|^2\,\mathrm{d}V}\,. \tag{4.105}$$

This is the first-order correction to the frequency of mode n when rotation is present. If one instead takes the inner product of (4.103) with $\boldsymbol{\xi}_i^{(0)}$ for $i \neq n$, the result is

$$a_i = \frac{2\omega_n^{(0)}}{\omega_n^{(0)2} - \omega_i^{(0)2}} \frac{\mathrm{i}\langle \boldsymbol{\Omega} \times \boldsymbol{\xi}_n^{(0)}, \boldsymbol{\xi}_i^{(0)} \rangle}{\langle \boldsymbol{\xi}_i^{(0)}, \boldsymbol{\xi}_i^{(0)} \rangle} \tag{4.106}$$

for the mode n.

In the regime of slow rotation ($\Omega \ll \omega$), the effect on the seismic spectrum is to lift the m-degeneracy of the modes and produce a roughly symmetric multiplet containing $2\ell + 1$ peaks. The $m = 0$ mode is unaffected in frequency, while modes of differing sign in m are shifted in opposite directions, and the absolute shift in frequency is roughly proportional to m.

4.3.2 Magnetism

In the case of weak magnetic fields with rotation neglected, an analogous procedure may be applied. Here the linearised equation of motion reads

$$-\omega^2 \boldsymbol{\xi} = -\frac{\nabla p'}{\rho} + \frac{\rho'}{\rho^2}(\nabla p - [\nabla \times \mathbf{B}] \times \mathbf{B}) + \frac{1}{\rho}[(\nabla \times \mathbf{B}') \times \mathbf{B} + (\nabla \times \mathbf{B}) \times \mathbf{B}'], \tag{4.107}$$

where

$$\mathbf{B}' = \nabla \times (\boldsymbol{\xi} \times \mathbf{B}). \tag{4.108}$$

Adopting a similar expansion as in (4.98) and (4.99), but where this time successive terms are in increasing powers of B^2, Equation (4.107) becomes

$$-2\omega_n^{(0)}\omega^{(1)}\boldsymbol{\xi}_n^{(0)} - \omega_n^{(0)2}\boldsymbol{\xi}^{(1)} = -\frac{\nabla p'^{(1)}}{\rho} + \frac{\rho'^{(1)}}{\rho^2}(\nabla p - [\nabla \times \mathbf{B}] \times \mathbf{B}) + \frac{1}{\rho}\left[\left(\nabla \times \mathbf{B}_n'^{(0)}\right) \times \mathbf{B} + (\nabla \times \mathbf{B}) \times \mathbf{B}_n'^{(0)}\right], \tag{4.109}$$

where $\mathbf{B}_n'^{(0)} \equiv \nabla \times (\boldsymbol{\xi}_n^{(0)} \times \mathbf{B})$ and we have neglected terms of higher order than B^2. Expanding the first-order perturbed quantities in terms of the unperturbed basis and taking advantage of eigenfunction orthogonality as before, this yields

$$\omega^{(1)} = -\frac{\int \left[\left(\nabla \times \mathbf{B}_n'^{(0)}\right) \times \mathbf{B} + (\nabla \times \mathbf{B}) \times \mathbf{B}_n'^{(0)}\right] \cdot \boldsymbol{\xi}_n^{(0)*} \, \mathrm{d}V}{2\omega_n^{(0)} \int \rho |\boldsymbol{\xi}_n^{(0)}|^2 \, \mathrm{d}V} \tag{4.110}$$

as the first-order correction to the mode frequencies due to a magnetic field, and

$$a_i = \frac{1}{\omega_n^{(0)2} - \omega_i^{(0)2}} \frac{\int \left[\left(\nabla \times \mathbf{B}_n'^{(0)}\right) \times \mathbf{B} + (\nabla \times \mathbf{B}) \times \mathbf{B}_n'^{(0)}\right] \cdot \boldsymbol{\xi}_i^{(0)*} \, \mathrm{d}V}{2\omega_n^{(0)} \int \rho |\boldsymbol{\xi}_i^{(0)}|^2 \, \mathrm{d}V} \tag{4.111}$$

as the coefficients for the mode n.

Like rotation, the presence of a weak field acts to lift the m-degeneracy of the modes, but in this case modes of the same $|m|$ experience the same magnitude and direction of shift, giving rise to $\ell + 1$ peaks in the multiplet. Unlike for rotation, a magnetic field also perturbs the frequency of the $m = 0$ mode.

4.4 Mode excitation and damping

So far in this chapter we have discussed the properties of oscillations that could in principle be supported by a star. For these oscillations to actually occur, some source of energy input is required, and in physical

reality some damping process would be in operation to keep the amplitudes finite. We now outline some of these processes.

For stars in binary systems and/or with large planetary companions, global modes of oscillation can be excited through tidal forcing (e.g. Barker & Ogilvie, 2010; Xu & Lai, 2017). In strongly magnetised stars such as magnetars, it is thought that magnetic reconnection occurring in their atmospheres releases the energy that may excite global modes, which have been observed as quasi-periodic oscillations in magnetar X-ray and gamma-ray emission following flare events (Passamonti & Lander, 2014). However, in the absence of large external reservoirs of energy, global oscillations can be excited in ordinary stars through a number of more subtle internal processes. For example, it is possible for oscillations to be self-excited (have intrinsically positive growth rates) as a result of non-adiabatic processes. Such as in a car engine, if heat flows into the gas during compression and out during rarefaction, then the net work done on the surroundings is positive and the motion is self-reinforcing, resulting in growth. However, if the opposite is true (heat flows out during compression and in during rarefaction), then the work is negative and the motion is damped. For stars on the *instability strip*, which includes Cepheid variables, δ Scuti stars, rapidly oscillating Ap stars, and ZZ Ceti stars to name but a few, oscillations are of the self-excited nature. Further details of the physical processes behind these will be discussed in §4.4.1. Another internal source of energy for driving oscillations that are otherwise intrinsically stable comes from the kinetic energy of convective motions, which can potentially approach the local sound speed resulting in the efficient generation of acoustic noise. This occurs, for example, in the convective envelope of the Sun. Stars in which global modes are excited in this manner are known as *solar-like oscillators*, and will be discussed further in §4.4.2.

4.4.1 Self-excitation mechanisms

In general, expressions for the driving and damping rates of an oscillator can be obtained by considering the frequency shift associated with perturbations to the operator $\mathscr{L}$, as defined in (2.36). With the assumed time-harmonic dependence $\boldsymbol{\xi} \propto \exp(-\mathrm{i}\omega t)$, this becomes

$$\omega^2 \boldsymbol{\xi} = \mathscr{L}[\boldsymbol{\xi}] \,. \tag{4.112}$$

Let us expand this for the case of non-adiabatic perturbations:

$$\mathscr{L} = \mathscr{L}_a + \delta\mathscr{L} \,, \tag{4.113}$$

$$\boldsymbol{\xi} = \boldsymbol{\xi}_a + \boldsymbol{\delta\xi} \,, \tag{4.114}$$

$$\omega^2 = \omega_a^2 + \delta\omega^2 \,, \tag{4.115}$$

where subscript a refers to an adiabatic quantity, and δ denotes the non-adiabatic perturbation. Substituting these into (4.112) and neglecting terms of quadratic order in the perturbation, we get

$$\delta\omega^2 \boldsymbol{\xi}_a + \omega_a^2 \boldsymbol{\delta\xi} = \mathscr{L}_a[\boldsymbol{\delta\xi}] + \delta\mathscr{L}[\boldsymbol{\xi}_a] \,. \tag{4.116}$$

Taking the inner product of both sides with $\boldsymbol{\xi}_a$, we find that

$$\begin{aligned} \delta\omega^2 \langle \boldsymbol{\xi}_a, \boldsymbol{\xi}_a \rangle - \langle \delta\mathscr{L}[\boldsymbol{\xi}_a], \boldsymbol{\xi}_a \rangle = -\omega_a^2 \langle \boldsymbol{\delta\xi}, \boldsymbol{\xi}_a \rangle + \langle \boldsymbol{\delta\xi}, \mathscr{L}_a[\boldsymbol{\xi}_a] \rangle = 0 \\ \implies \delta\omega^2 = \frac{\langle \delta\mathscr{L}[\boldsymbol{\xi}_a], \boldsymbol{\xi}_a \rangle}{\langle \boldsymbol{\xi}_a, \boldsymbol{\xi}_a \rangle} \,, \end{aligned} \tag{4.117}$$

where we have made use of the self-adjointness of $\mathscr{L}_a$. Growth or decay arise if $\delta\omega^2 < 0$, in which case the sign of $\mathrm{Im}(\delta\omega)$ determines if the solution is growing or decaying. For solutions $\propto \exp(-\mathrm{i}\omega t)$, growth occurs if $\mathrm{Im}(\delta\omega) > 0$, and decay if $\mathrm{Im}(\delta\omega) < 0$.

To obtain an expression for $\delta\mathscr{L}$ for self-excited oscillations, we consider the more general version of the energy equation (1.19),

$$\nabla\cdot\mathbf{F} = \rho\left(\epsilon - \frac{\mathrm{d}q}{\mathrm{d}t}\right), \tag{4.118}$$

where $\mathbf{F}$ is the (three-dimensional) energy flux, and eliminate $\mathrm{d}q/\mathrm{d}t$ using the first law of thermodynamics, which can be cast as

$$\frac{\mathrm{d}q}{\mathrm{d}t} = \frac{1}{\rho(\gamma_3-1)}\left(\frac{\mathrm{d}p}{\mathrm{d}t} - \frac{\gamma_1 p}{\rho}\frac{\mathrm{d}\rho}{\mathrm{d}t}\right). \tag{4.119}$$

Here we define the adiabatic exponents

$$\gamma_1 = \left(\frac{\partial\ln p}{\partial\ln\rho}\right)_{\mathrm{ad}}, \quad \gamma_3 - 1 = \left(\frac{\partial\ln T}{\partial\ln\rho}\right)_{\mathrm{ad}}. \tag{4.120}$$

This gives us

$$(\gamma_3-1)(\rho\epsilon - \nabla\cdot\mathbf{F}) = \frac{\mathrm{d}p}{\mathrm{d}t} - \frac{\gamma_1 p}{\rho}\frac{\mathrm{d}\rho}{\mathrm{d}t}, \tag{4.121}$$

which, if expanded in small time-harmonic perturbations and linearised, becomes

$$\frac{\mathrm{i}(\gamma_3-1)}{\omega}(\rho\epsilon - \nabla\cdot\mathbf{F})' = p' - \frac{\gamma_1 p}{\rho}\rho' + \xi_r\left(\frac{\mathrm{d}p}{\mathrm{d}r} - \frac{\gamma_1 p}{\rho}\frac{\mathrm{d}\rho}{\mathrm{d}r}\right). \tag{4.122}$$

Now the LHS of the above vanishes under the adiabatic approximation ($\mathrm{d}q/\mathrm{d}t = 0$), so we can define the adiabatic pressure perturbation

$$p'_{\mathrm{ad}} = \frac{\gamma_1 p}{\rho}\rho' - \xi_r p\left(\frac{\mathrm{d}\ln p}{\mathrm{d}r} - \gamma_1\frac{\mathrm{d}\ln\rho}{\mathrm{d}r}\right). \tag{4.123}$$

The perturbation to $\mathscr{L}$ is thus seen to occur through the pressure gradient term, and takes the form

$$\delta\mathscr{L} = \frac{\nabla(p' - p'_{\mathrm{ad}})}{\rho} = \frac{1}{\rho}\nabla\left[\frac{\mathrm{i}(\gamma_3-1)}{\omega}(\rho\epsilon - \nabla\cdot\mathbf{F})'\right]. \tag{4.124}$$

The corresponding frequency perturbation is

$$\begin{aligned}\delta\omega^2 &= \frac{\int\nabla(p' - p'_{\mathrm{ad}})\cdot\boldsymbol{\xi}_a^*\,\mathrm{d}V}{\int\rho|\boldsymbol{\xi}_a^*|^2\,\mathrm{d}V} \\ &= \frac{\int\nabla\cdot[(p' - p'_{\mathrm{ad}})\boldsymbol{\xi}_a^*]\,\mathrm{d}V - \int(p' - p'_{\mathrm{ad}})\nabla\cdot\boldsymbol{\xi}_a^*\,\mathrm{d}V}{\int\rho|\boldsymbol{\xi}_a^*|^2\,\mathrm{d}V}.\end{aligned} \tag{4.125}$$

The first term in the numerator of (4.125) is zero for a volume integral enclosing the star. Invoking the Lagrangian perturbation of the continuity equation, $\delta\rho_a^* = -\rho\nabla\cdot\boldsymbol{\xi}_a^*$, we obtain

$$\delta\omega = \frac{\mathrm{i}}{2\omega^2\int\rho|\boldsymbol{\xi}_a^*|^2\,\mathrm{d}V}\int(\gamma_3-1)(\rho\epsilon - \nabla\cdot\mathbf{F})'\frac{\delta\rho_a^*}{\rho}\,\mathrm{d}V. \tag{4.126}$$

In the situation where energy generation is the primary source of non-adiabaticity, we can neglect the $\nabla\cdot\mathbf{F}$ term in (4.126). It can be shown that

$$(\rho\epsilon)' = \rho\epsilon\frac{\delta\rho}{\rho}\left\{\left.\frac{\partial\ln\epsilon}{\partial\ln T}\right|_\rho[\gamma_3-1] + \left.\frac{\partial\ln\epsilon}{\partial\ln\rho}\right|_T + 1\right\}. \tag{4.127}$$

If we evaluate this using the adiabatic solution ($\delta\rho \to \delta\rho_a$), i.e. we invoke the *quasi-adiabatic approximation*, we find that $\delta\omega$ is purely imaginary. The fate of the solution (growth or decay) then depends on the sign of the term in curly brackets. Since the energy generation rate ϵ increases with both temperature and

density, and $\gamma_3 \approx 5/3$, this is always positive, meaning that the perturbation grows with time. This instability is known as the ϵ-mechanism, and is thought to be important for setting an upper limit to the mass of a star, since extremely massive stars might throw off additional material as a result of pulsational instability (Schwarzschild & Härm, 1959). Physically, it arises from the enhanced heating of the gas upon compression due to increased nuclear reaction rates, and correspondingly lower rates upon rarefaction, resulting in net positive work being done on the surroundings.

If the effects of nuclear reactions can be neglected, then we need only consider the energy flux term in (4.126), with

$$\mathbf{F}' = \left[(3-\kappa_T)\frac{T'}{T} - (1+\kappa_\rho)\frac{\rho'}{\rho}\right] F_r \hat{\mathbf{r}} - \frac{4acT^3}{3\kappa\rho}\nabla T', \tag{4.128}$$

where

$$\kappa_T \equiv \left.\frac{\partial \ln \kappa}{\partial \ln T}\right|_\rho, \quad \kappa_\rho \equiv \left.\frac{\partial \ln \kappa}{\partial \ln \rho}\right|_T. \tag{4.129}$$

For low-radial order modes, the approximate expression holds for the frequency shift:

$$\delta\omega \approx -\frac{\mathrm{i}}{2\omega^2 \int \rho |\boldsymbol{\xi}_a|^2 \,\mathrm{d}V} \int (\gamma_3 - 1)\frac{\delta\rho_a^*}{\rho} L_r \frac{\mathrm{d}}{\mathrm{d}m_r}\left\{\left[(4-\kappa_T)(\gamma_3-1)-\kappa_\rho\right]\frac{\delta\rho_a}{\rho}\right\}\mathrm{d}m_r\,. \tag{4.130}$$

The factor within the curly brackets generally increases outward, leading to an overall damping. However, within partial ionisation zones the $\mathrm{d}/\mathrm{d}m_r$ term can become negative, leading to instability. This occurs due to local decreases in γ_3 and increases in κ_T, resulting in what are known as the γ- and κ-mechanisms. Physically, this is because in a partial ionisation zone, some of the work done during compression results in further ionisation, and so the temperature increases less than it otherwise would. Likewise on rarefaction, recombination between ions and electrons releases heat, causing the temperature to decrease less than usual. Since $\kappa_T < 0$ and $\kappa_\rho > 0$, the net effect is to increase the opacity on compression (resulting in greater heat absorption) and decrease it on rarefaction (resulting in greater heat loss). This drives the κ-mechanism instability. Aiding this is the inflow (outflow) of heat from (to) the layers around the partial ionisation zone, since the temperature of the zone increases (decreases) less on compression (rarefaction) than the surroundings, owing to an increase in the specific heats. This second process underlies the γ-mechanism. These processes are thought to be responsible for driving the pulsations of stars on the instability strip.

4.4.2 Stochastic excitation

The kinetic energy of convective motions is another source of energy for exciting global modes. Whether a given region of the star is convectively unstable depends on the local temperature and pressure profile. If a packet of gas is displaced upward and allowed to re-equilibrate in pressure with its surroundings, its density will change by an amount determined by its equation of state. If the final density is larger than that of its surroundings, the packet will experience a net downward buoyant restoring force and accelerate toward its original location. In this case, the system is stable to perturbations and admits the propagation of gravity waves. Otherwise, if the density ends up lower, the packet will accelerate upwards and the system will be unstable to convection. The criterion for stability, under the assumption of adiabaticity (no heat exchange with the surroundings) is therefore that

$$\left.\frac{\mathrm{d}\rho}{\mathrm{d}p}\right|_{\mathrm{ad}} < \frac{\mathrm{d}\rho}{\mathrm{d}p}, \tag{4.131}$$

which if we assume an ideal gas ($p \propto \rho T$) can be recast as

$$\left.\frac{\mathrm{d}\ln T}{\mathrm{d}\ln p}\right|_{\mathrm{ad}} > \frac{\mathrm{d}\ln T}{\mathrm{d}\ln p}\,. \tag{4.132}$$

This is known as the *Schwarzschild criterion*.

Part of the energy associated with turbulent convective motions is believed to drive oscillations that would otherwise be intrinsically damped. The evidence for this, from observations of our Sun, is the fairly even distribution of power across modes of degree $\ell < 100$, which suggests excitation in regions where the propagation of acoustic waves is almost vertical (Balmforth, 1992). This behaviour occurs in the surface layers, which in the Sun are convectively unstable. Similar oscillations, occurring over a relatively broad range of frequencies, have been observed in a large number of other stars possessing near-surface convection (Chaplin & Miglio, 2013).

The most widely-applied theory of convection incorporated in treatments of stellar structure, evolution and oscillations is the mixing-length approach (Houdek & Dupret, 2015). Stochastic turbulence can be modelled by regarding fluid variables as being the sum of a mean and a fluctuating component. Horizontal averages are taken to arrive at a set of differential equations governing the mean pressure, density, temperature, radiative flux etc., but additional relations governing the turbulent pressure and convective heat flux must be supplied through other means. Mixing length theories, introduced independently by Taylor (1915) and Prandtl (1925), are based on the picture of an overturning convective cell and provide expressions for these quantities. Multiple variants of these theories exist, but they share the simplifying approximation that only a single empirical constant is involved: the mixing length. Details of the assumptions about the dynamics of the gas in the convective cell differ from model to model: for example, the two most commonly used either (i) regard gas packets as being analogous to particles in kinetic gas theory, i.e. accelerating from rest followed by instantaneous breakup after a probabilistic lifetime that is related to the mixing length (Gough, 1977), or (ii) assume that motion occurs under a balance between buoyancy and turbulent drag, where the mixing length enters in the expression for the turbulent viscosity (Unno, 1977).

To treat the interaction between convection and stellar pulsation, oscillations are taken to induce small perturbations to the turbulent equations, in which case the contribution of convection to driving/damping can be determined from the imaginary component of the associated frequency shift (Houdek & Dupret, 2015). While turbulent pressure perturbations tend to contribute positively to the work integral over the star, turbulent dissipation and convective flux perturbations act to damp the oscillations. Observationally, the power spectrum of stochastically excited oscillations exhibits a broad bump centred around a value ν_{max} that is strongly correlated with the acoustic cutoff frequency $\nu_c = \omega_c/(2\pi)$, where ω_c is defined in Equation (4.45) (Bedding & Kjeldsen, 2003). This correlation has been explained by way of a "generalised κ-mechanism" associated with layers where the thermal relaxation time is comparable to the mode period, resulting in dynamical coupling and additional destabilisation of the mode (Balmforth, 1992; Belkacem et al., 2011). The cutoff frequency tends to scale with the surface gravity of the star, and so ν_{max} is also closely tied to this, being lower for larger stars.

4.4.3 Radiative damping

Let us again neglect the effect of nuclear reactions. For a mode whose spatial fluctuations are rapid, the perturbation to the radiative flux in (4.128) is dominated by the last term. Hence

$$\nabla \cdot \mathbf{F}' \approx \frac{4acT^3}{3\kappa\rho} k_r^2 T' \,. \tag{4.133}$$

Invoking the dispersion relation for acoustic waves, (4.126) becomes approximately

$$\delta\omega \approx -\frac{\mathrm{i}\omega^2}{2\int \rho |\boldsymbol{\xi}_a|^2 \,\mathrm{d}V} \int \nabla_{\mathrm{ad}}^2 \frac{4acT^4\rho}{3\kappa p^2} |\boldsymbol{\xi}_a|^2 \,\mathrm{d}V \,, \tag{4.134}$$

where

$$\nabla_{\mathrm{ad}} \equiv \frac{\mathrm{d}\ln T}{\mathrm{d}\ln p}\Big|_{\mathrm{ad}} = \frac{\gamma_3 - 1}{\gamma_1} \,. \tag{4.135}$$

Thus $\mathrm{Im}(\delta\omega)$ is negative, indicating that p-modes would be damped by this process. In the case of g-modes, (4.126) instead becomes

$$\delta\omega \approx -\frac{\mathrm{i}}{2\omega^2 \int \rho |\boldsymbol{\xi}_a|^2 \,\mathrm{d}V} \int \nabla_{\mathrm{ad}} (\nabla_{\mathrm{ad}} - \nabla) \frac{4acT^4\rho}{3\kappa p^2} k_r^2 (\boldsymbol{\xi}_a^* \cdot \mathbf{g})(\boldsymbol{\xi}_a \cdot \mathbf{g}) \,\mathrm{d}V \,, \tag{4.136}$$

where

$$\nabla \equiv \frac{\mathrm{d}\ln T}{\mathrm{d}\ln p} \,. \tag{4.137}$$

In stably stratified regions, where g-modes would be allowed to exist, $\nabla_{\mathrm{ad}} > \nabla$ (cf. the Schwarzschild criterion), hence g-modes are also damped by this process.

Chapter 5

The "Dipole Dichotomy" Problem

5.1 Observational background

5.1.1 Instrumentation

While the brightness variations associated with classical pulsators are often large enough to be observed by the naked eye (e.g. Cepheid variables), those of solar-like oscillators have much lower amplitudes and require sensitive photometry to detect. Even in the case of our brightest target, the Sun, oscillations were only discovered in the 1960s, and it was not until dedicated ground-based networks such as the Birmingham Solar-Oscillations Network (BiSON) and the Global Oscillations Network Group (GONG) were built that the field of helioseismology developed. For solar-like oscillators beyond the Sun, detecting their (much smaller) brightness variations proved to be nearly impossible from the ground, owing to the interfering effects of the Earth's atmosphere. This was with the exception of the brightest nearby stars, amongst which oscillations were first detected in the subgiant Procyon (α CMi), followed by β Hyi and then α Cen A (Basu & Chaplin, 2017).

It was not till the development of space-based photometry that asteroseismology of large numbers of solar-like oscillators became possible, owing to the unprecedented levels of sensitivity in measurements made from above the atmosphere. The first space mission to perform asteroseismic measurements was the Wide-Field Infrared Explorer (WIRE), which was originally meant to perform infrared surveys of extra-galactic targets. However, failure of the cryogen system shortly after launch left it unable to complete its intended mission, and so the onboard star tracker, which remained functional, was used to perform aster-

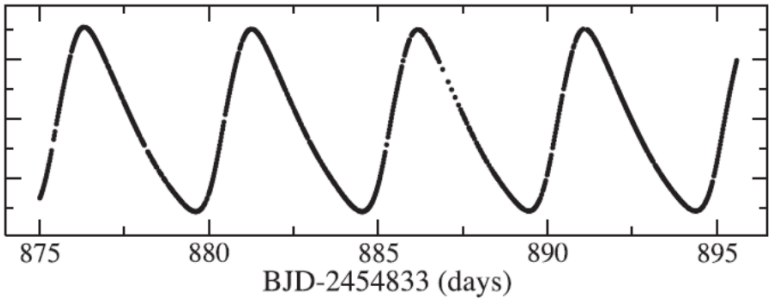

Figure 5.1: A *Kepler* light curve of the Cepheid variable V1154 Cyg, showing four cycles of modulation. Taken from Derekas et al. (2017), figure 1.

oseismic measurements instead (Schou & Buzasi, 2001). Many dedicated space-based asteroseismic missions followed, notably CNES/ESA's Convection, Rotation and Planetary Transits (CoRoT) mission (Baglin et al., 2006; Auvergne et al., 2009), launched in 2006 and decommissioned in 2014, and NASA's *Kepler* mission (Borucki et al., 2010; Koch et al., 2010), launched in 2009. After the failure of two out of its four reaction wheels, the *Kepler* mission gave way to a modified mission known as *K2* (Howell et al., 2014), which continued to carry out useful asteroseismic observations up till Oct 2018, when it was terminated following exhaustion of onboard fuel reserves. An example of a Cepheid variable light curve observed by *Kepler* is shown in Figure 5.1. New missions taking over from *Kepler*/*K2* include NASA's Transiting Exoplanet Survey Satellite (TESS) mission (Ricker, 2015), successfully launched in March 2018, and ESA's Planetary Transits and Oscillations of stars (PLATO) mission, scheduled to be launched in 2026 (Rauer et al., 2014).

Regarding technical aspects of the instrumentation, these missions are each equipped with one or more cameras operating at visible to near-infrared wavelengths (e.g. 430–890 nm for *Kepler*/*K2*, 600–1000 nm for TESS). Light is focused through the telescope onto an array of charge-coupled device (CCD) detectors at the focal plane, and the integrated signal is read out periodically. Multiple objects can be observed simultaneously, the number depending on the telescope's field of view and sensitivity. In the case of *Kepler*, the spacecraft carries a single camera with a usable field of view of ∼105 sq. deg and 94.6 megapixel resolution, while TESS carries four cameras each having a ∼576 sq. deg field of view and 16.8 megapixel resolution.

5.1.2 Data reduction & analysis

After the images have been downlinked, light curves of individual objects are extracted from the pixel data (e.g. Handberg & Lund, 2017). These are then Fourier analysed to yield the stellar seismic parameters (Campante, 2017). Given the large amounts of data returned by current and previous missions, automated software pipelines have been developed to handle the multitude of processing tasks. The whole data reduction process is considerably elaborate, and many variant approaches exist, so only a rough overview will be given here. Note that none of the work in this thesis required either developing or running any data reduction pipelines; the background in this section has been included mainly for the sake of interest.

To extract light curves, individual objects in the images must first be identified, which is done by a clustering algorithm operating on the pixels of the image according to various thresholding criteria. For each pixel cluster identified as a target object, the total flux is summed and returned, and the process is repeated for each image in the time series to obtain the light curve (flux as a function of time). Next, the light curves undergo a check for the presence of oscillations, by forming the power spectrum of the power spectrum (PS⊗PS). This step assumes that the oscillations are solar-like p-modes, meaning that they take the form of multiple peaks roughly evenly spaced in frequency (recall discussion in §4.2.2). If this is the case, then PS⊗PS will exhibit peaks at harmonics of the frequency spacing, and the value for $\Delta\nu$ can be identified. This process is carried out repeatedly for frequency windows of different widths. In this manner, the range of frequencies over which the oscillations occur, and the frequency of maximum power, $\nu_{\max}$, can be established. Excess power associated with stellar background noise is characterised by computing a fit over the power spectrum excluding the range where modes are present, by treating this contribution as the sum of two components: granulation noise (from surface convection), assumed to follow a Harvey-like profile (e.g. Kallinger et al., 2014), and photon shot noise, taken to be a constant offset. Figure 5.2 shows the light curve and power spectrum of a solar-like oscillator observed by TESS.

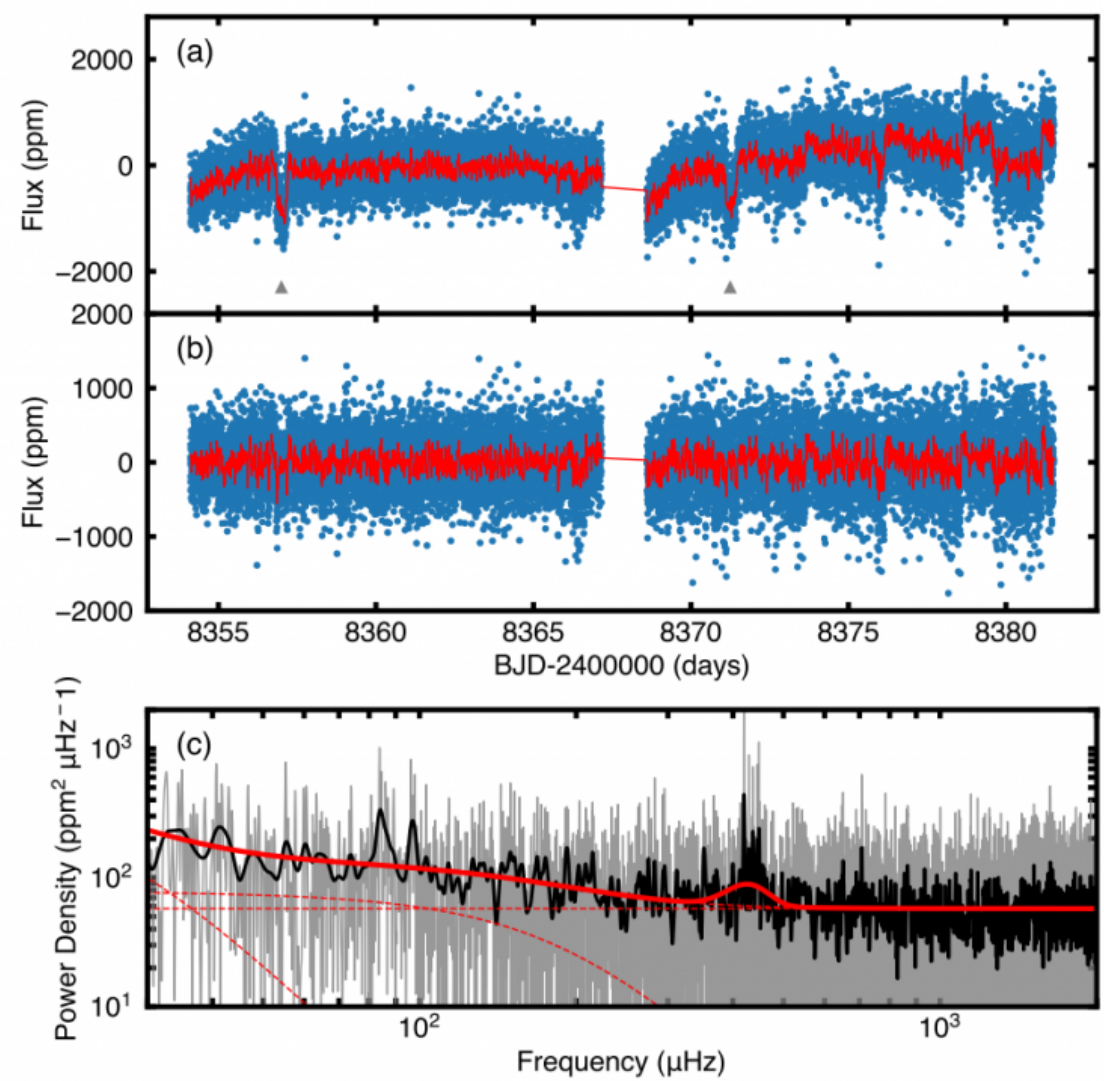

Figure 5.2: Panel (a): Raw light curve (blue points) of the subgiant star TOI-197 taken by TESS, showing dips corresponding to exoplanet transits (marked by grey triangles). The red line corresponds to a smoothed version of the blue points using a 10-min boxcar filter. Panel (b): The light curve with transits and instrumental artefacts removed. Panel (c): The power spectrum of the light curve in panel (b), where the solid red line represents a global fit to granulation noise, shot noise and the power excess associated with the oscillations (assumed to be a Gaussian bump). The dashed red lines correspond to the granulation and white noise components. Taken from Huber et al. (2019), figure 1.

If signal-to-noise levels are sufficiently high, then in addition to the global parameters described above, it will be possible to obtain fits for the individual peaks. Under the assumption that each peak is described by a Lorentzian profile, the relevant parameters for each are the height, width and central frequency. This process is called "peak-bagging" and is tackled using a Bayesian approach, which allows for a simultaneous fit of a large number of model parameters.

5.1.3 Mode heights, widths and visibilities

As mentioned above, among the quantities which can be measured from the power spectra are the heights and widths of the modes. The product of these, the area under the peak, is called the *visibility* and is physically related to the squared amplitude of the velocity variation in the surface layers, where the detected light originates (Belkacem et al., 2006). This is usually denoted by V^2 (e.g. Dupret et al., 2009). V^2 is proportional to the power P supplied to the mode through stochastic excitation, and inversely proportional to the damping rate η. For modes that are resolved, the width of the peak is given by η, and so for a given value of V^2, more heavily damped modes will have smaller peak heights H. However, if the damping time of the mode exceeds the observing duration, then the peak will be unresolved. In this scenario, the width is instead set by the instrument resolution (inverse of the observing duration), and the height of the peak will be suppressed proportionally.

Relevant quantities to introduce here are the modal mass

$$M_{\rm mode} = \frac{\int_0^{M_*} |\boldsymbol{\xi}| \, {\rm d}m_r}{|\boldsymbol{\xi}(R_*)|^2} \tag{5.1}$$

and mode inertia

$$I = \frac{M_{\rm mode}}{M_*}, \tag{5.2}$$

which are measures of the associated mass displaced by a mode. Since V^2 measures the squared velocity variation, for given P we will have $V^2 \propto I^{-1}$. Due to the increasing density towards the centre of a star, g-modes have significantly higher mode inertias than p-modes. However, driving and damping occur predominantly in the convective outer layers, resulting empirically in both P and η being inversely proportional to I. With

$$V^2 \propto \frac{P}{\eta I}, \tag{5.3}$$

we infer that the height of the peak in the power spectrum is given by

$$H = \frac{V^2}{\eta} \propto \frac{P}{\eta^2 I} \tag{5.4}$$

which is independent of I. This predicts that peak heights should be roughly the same for all modes of a given frequency, which would imply that g-modes should be just as easy to detect as p-modes, since the detection criteria are based on the height of the peak above the noise level. However, this is only true in the case of unlimited frequency resolution (infinite observing duration). In reality, g-mode lifetimes greatly exceed observing time spans and so their heights become diluted by the low resolution.

5.2 Red giant observations

Most of the asteroseismic data that have been collected have come from the *Kepler* mission, which to date has observed solar-like oscillations in several hundred main sequence stars and over ten thousand red gi-

ants (Chaplin & Miglio, 2013). Red giants are easier targets than main sequence stars for asteroseismic observation for two reasons, namely (i) that they have much higher luminosities, and (ii) that their oscillation periods are longer (owing to their lower mean densities), which means that the signals are less likely to suffer aliasing as a result of falling below instrumental cadences. This section first gives a general overview of red giant asteroseismology, and then discusses a particular aspect of the observations: the dichotomy of the population with respect to the amplitudes of their dipole modes. I have nicknamed this phenomenon the "dipole dichotomy" problem.

5.2.1 Seismic spectra

In the previous chapter, we identified the existence of two propagation cavities, one for p-modes extending to the surface with a lower turning point located at a radius given by (4.52), and the other for g-modes located where $\omega^2 \lesssim N^2$. In a main sequence star, these two cavities are well separated in radius, i.e. the lower turning point of the p-mode cavity lies well above the upper turning point of the g-mode cavity, and so oscillations occurring in each cavity interact fairly little. However, as the star evolves into a red giant, the expansion of the envelope and consequent lowering of the sound speed, together with the contraction of the core leading to a rise in the buoyancy frequency, cause the two cavities to move closer together. This increases the strength of coupling between p-mode and g-mode oscillations, giving rise to modes that have *mixed* character where there is a resonance between the two cavities (Beck et al., 2011). These modes are referred to as *mixed modes*. Such modes are characterised by having spatial amplitude functions that exhibit oscillations in both cavities, connected by an evanescent portion within the region between the two cavities (cf. quantum mechanical wave functions).

For any given star, the extent to which p and g mode mixing can occur is a strong function of spherical degree. Recall that g-modes only exist for non-radial degrees ($\ell > 0$), and that the lower turning point of the p-mode cavity lies nearer the centre for lower ℓ. Consequently radial ($\ell = 0$) modes are not mixed at all, dipole ($\ell = 1$) modes are the most heavily mixed, followed by quadrupole ($\ell = 2$), then octupole ($\ell = 3$), and so on for higher multipoles. Observationally, only the lowest degree modes can be observed, due to the geometric cancellation of bright and dark patches on the surface of the star (Bedding, 2013). It is difficult to resolve the discs of stars further away than the Sun; only the total disc-integrated flux is measured. In practice, this means that only modes with $\ell \leq 3$ can be reliably detected. Furthermore, since the brightness variations are linked to the velocity variations of the surface layers, it is the modes which possess the largest surface amplitudes that are the most easily observed (have the largest visibilities in the power spectra). Among the spectrum of mixed modes, therefore, it is those with the most p-like character that have the largest visibilities (Dupret et al., 2009). In a typical evolved star, the density of g-modes at frequencies near $\nu_{\max}$ exceeds that of p-modes by about an order of magnitude, although this varies with evolutionary stage: for example, a $1.5\,\mathrm{M}_\odot$ subgiant may have about three g-modes for each $\Delta\nu$ interval (p-mode spacing), while a $1.5\,\mathrm{M}_\odot$ red giant may have dozens of g-modes for every p-mode.

The acquisition of p-mode character by otherwise pure g-modes whose frequencies lie near each p-mode cavity resonance increases the amplitudes of their spatial amplitude functions at the surface, making them easier to observe. The result of this, which has been confirmed in observation, is the presence of clusters of peaks within each $\Delta\nu$ interval for the non-radial degrees. Dipole modes display the richest multiplicities owing to the greatest coupling between the two cavities, which raises the surface amplitudes of many

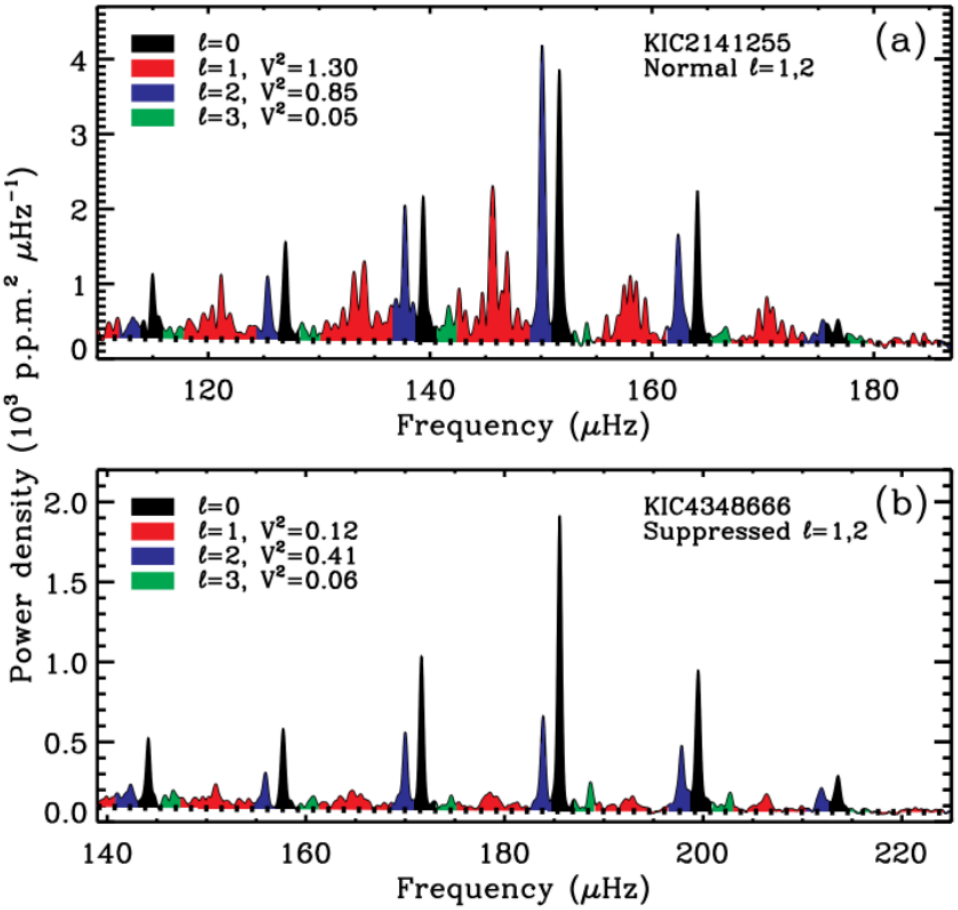

Figure 5.3: Example power spectra of two red giants, one showing normal non-radial mode visibilities (top) and the other showing depressed dipole and quadrupole modes (bottom). Modes of different degrees are shown in different colours. Taken from Stello et al. (2016b), fig. 3.

g-dominated mixed modes to observable values. For modes of successively higher degree, fewer and fewer mixed-mode peaks become observable in the vicinity of each p-mode cavity resonance, since in the limit of high ℓ the modes tend towards being either pure p-modes or pure g-modes. The ability to observe these mixed-mode clusters is highly valuable from an asteroseismic point of view, since it provides information about properties of the deep interior (recall that the g-mode spacings depend on the buoyancy frequency profile in the g-mode cavity).

5.2.2 Dipole modes with depressed amplitudes

Analysis of the red giant data from the *Kepler* mission revealed that a significant fraction (around 20%) of the stars had $\ell = 1$ visibilities that were factors of up to 2–3 lower than the remainder of the population (Mosser et al., 2012a). This was noted to be more pronounced among those with larger $\nu_{\max}$ (younger stars), but otherwise no obvious correlation was identified with other stellar properties such as bolometric luminosity or effective temperature. The authors did manage to identify that the masses of stars with depressed modes were slightly higher than average, but noted that there still existed many stars with both a high mass and normal dipole visibilities.

Attempts to uncover the origin of the dichotomy led to a follow-up case study by García et al. (2014) of

KIC 8561221, an early red giant star at the base of the RGB showing the strongest mode depression out of the known sample. It was noted to be the least-evolved star exhibiting the phenomenon, and interestingly, unlike most others, showed an abrupt transition across its frequency range occurring around $\nu_{\max}$, with dipole modes of lower frequencies being depressed and those above $\nu_{\max}$ possessing normal visibilities. In addition, the $\ell = 2$ peaks were noted to have lower than expected amplitudes, although to a lesser extent. The power spectrum of KIC 8561221 was of sufficient quality to obtain fits for the widths of the $\ell = 1$ peaks on both sides of the transition, and it was established that the widths of those below $\nu_{\max}$ were substantially larger than those of the ones above. This pointed to the reason for the low visibilities as being a larger damping rate (as opposed to, for instance, a lower excitation rate or an abnormally high mode inertia) for those modes. However, attempts to simulate the seismic spectrum using standard codes could only reproduce the frequencies of the depressed peaks, not their widths, and so it was concluded that an unknown, additional, degree-selective damping mechanism must be operating.

García et al. (2014) tentatively glossed over several possible avenues of explanation for the mode depression. They noted evidence for the existence of a surface dynamo-generated magnetic field, but that any effects would impact all low-degree modes to a similar extent, rather than being dipole-selective. Fast surface rotation, though known to potentially decrease the visibilities of dipole modes compared to other degrees (Reese et al., 2013), was discounted on the basis of the measured surface rotation rate of KIC 8561221 being far below the required value for the effect to be important. Furthermore, it would be unable to explain the strong correlation of V^2 for the dipole modes with $\nu_{\max}$, because surface rotation is not generally correlated with either $\nu_{\max}$ or age. They suggested, on the basis that non-radial modes are the only ones possessing significant amplitudes in the core, that the mode depression was due to a difference in core properties between the two groups of stars. A possibility they considered was the presence of a magnetic field buried in the stably stratified core, but they carried out no further theoretical investigation into this.

Further compelling evidence in support of the core magnetic fields idea was presented by Stello et al. (2016b,a), who analysed a large sample of over 3600 red giant stars. They established that (i) the dichotomy was only present in stars more massive than about $1.1\,M_\odot$, the mass above which a star would have possessed a convective (and possibly dynamo-hosting) core when on the main sequence, and (ii) that a dichotomy also existed for the quadrupole modes, albeit to a smaller extent. Figure 5.3 shows a pair of representative power spectra of two stars on opposing sides of the dichotomy. In the second star, peaks corresponding to $\ell = 1$ and 2 are noted to be much less pronounced relative to the radial modes. No dichotomy was detected in either the radial modes or modes of higher degree, but recall that the mixed character of these progressively weakens as ℓ increases, this being strongest for $\ell = 1$, followed by $\ell = 2$. Above this mass threshold, the fraction of stars exhibiting mode depression was observed to increase with increasing mass, this being 50–60% for stars more massive than about $1.6\,M_\odot$.

The broadest study of the red giant population with depressed dipole modes was performed by Mosser et al. (2017a), who worked from a sample of 6100 stars, 1109 of which were identified to have low $\ell = 1$ visibilities. They demonstrated that the radial mode widths, period spacings, coupling factors (related to the width of the evanescent region separating p- and g-mode cavities) and distributions of rotational splittings were indistinguishable from stars with normal $\ell = 1$ visibilities. They further established that dipole mode depression is exhibited at all evolutionary stages, not just on the RGB but also after the onset of core helium burning ("clump" and "secondary clump" stars).

5.3 Ideas and controversy

The effects of magnetic fields on stellar oscillations has been studied in most detail in the context of p-modes, in which case the magnetic field is only dynamically significant in a thin boundary layer near the surface, where the plasma β is of order unity (e.g. Roberts & Soward, 1983; Campbell & Papaloizou, 1986; Dziembowski & Goode, 1996; Cunha & Gough, 2000; Reese et al., 2004; Lee, 2007). Less work has been done to understand the effects of a dynamically significant magnetic field on g-modes, which are the relevant type of mode in the context of the dipole dichotomy problem. The most closely related work appears to be that investigating the interactions between gravity waves and magnetic fields in the vicinity of the solar tachocline (Rogers & MacGregor, 2010a,b), but with an eye out for its implications on angular momentum transport, rather than global oscillations. In this section we shall discuss ideas that have been presented by other authors as part of attempts to address the dipole dichotomy problem, and the ensuing controversy.

5.3.1 Magnetic "greenhouse effect"

A bold and novel first attempt at developing a theoretical explanation for how a magnetic field might give rise to a damping of non-radial modes was made by Fuller et al. (2015). They suggested that for field strengths above a certain threshold, gravity waves would become evanescent, destroying the g-like character of the mode. This was based on consideration of the magnetogravity dispersion relation, given by

$$\omega^2 = \omega_A^2 + \kappa_\perp^2 N^2 \tag{5.5}$$

where

$$\kappa_\perp \equiv \frac{k_\perp}{k},$$
$$\omega_A \equiv \mathbf{k}\cdot\mathbf{v}_A = k v_A \mu,$$

μ here being the cosine of the angle between the field and the wavevector. They rearranged (5.5) into

$$k^2 = \frac{\omega^2}{2v_A^2\mu^2}\left(1 \pm \sqrt{1 - \frac{4\mu^2 v_A^2 N^2 k_\perp^2}{\omega^4}}\right), \tag{5.6}$$

and then argued that when the term in the square root becomes negative, the waves would become evanescent. From this they obtained the criterion

$$2\mu v_A \geq \frac{\omega^2}{N k_\perp} \tag{5.7}$$

which translates to a critical radial field strength of

$$B_c = \sqrt{\frac{\mu_0 \rho}{8}}\frac{\omega^2 r}{N}, \tag{5.8}$$

where the expression

$$k_\perp = \frac{\sqrt{\ell(\ell+1)}}{r} \tag{5.9}$$

for $\ell = 1$ has been substituted. Assuming that $\mathbf{k}$ is dominated by the radial component, which is true for modes of low ℓ, they concluded that where $B_r > B_c$ the waves would become unable to propagate. These waves would either be converted into Alfvén waves and be trapped within the core, or they would be scattered back out into the envelope with large ℓ values and evade detection due to geometric cancellation of the patterns at the surface. The suggestion that high ℓ values might result from interaction with the magnetic

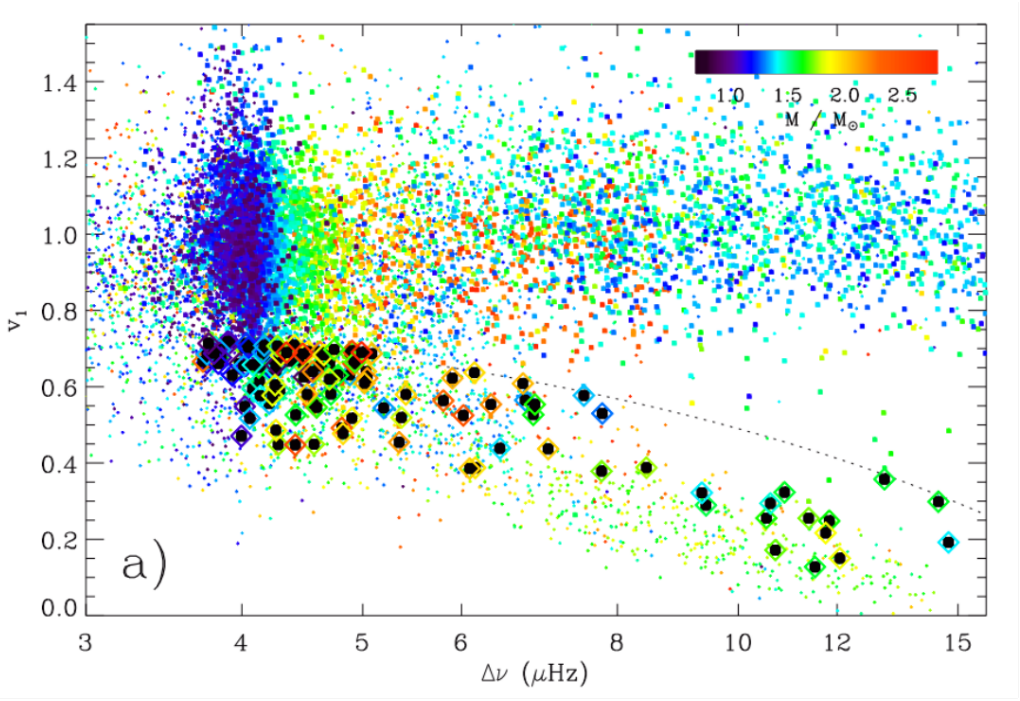

Figure 5.4: The dipole mode visibility v_1 as a function of $\Delta\nu$ for *Kepler* red giants, with points colour-coded by mass. Depressed stars are those falling on the lower branch, for which it can be seen that v_1 decreases with increasing $\Delta\nu$. The dotted line represents an empirical boundary between the two sides of the dichotomy. Points with black markers correspond to stars in which dipolar mixed modes were identified. Taken from Mosser et al. (2017a), fig. 3a.

field was based on consideration of wave packet propagation in a Hamiltonian formalism. The equations for this will be presented properly in a later chapter, but briefly, for the sake of covering their argument, the second of Hamilton's equations relating the rate of change of the wavevector to the backgrounds contains a term associated with the magnetic field, which cannot be spherically symmetric. This implies that the magnetic field should allow interchanges between the radial and horizontal components of the wavevector, allowing $k_\perp$ to attain values comparable to k_r upon interaction with the field. Either way, they argued that in the presence of a field exceeding the threshold, all of the wave energy entering the g-mode cavity would be lost, and coined the term "magnetic greenhouse effect" to describe the process. Estimates of the dipole mode visibilities resulting from a 100% loss of energy tunnelling into the g-mode cavity from the convective exterior appeared to be in quantitative agreement with the data. The authors claimed that the observations of depressed modes provided evidence for the existence of strong magnetic fields within those stars.

5.3.2 Conversion to magnetosonic waves

As a follow-up to the heuristic arguments presented by Fuller et al. (2015), a numerical study of gravity wave propagation in the presence of a field was undertaken by Lecoanet et al. (2017). In this paper, the authors presented the results of Boussinesq simulations in a local box setup, where a magnetic field was imposed over a Cartesian box and gravity waves were driven at one end. The behaviour of the waves upon propagating into a region of increasing field amplitude was studied, and it was found that 100% conversion into magnetosonic waves occurred at around the critical field strength predicted by Fuller et al. (2015).

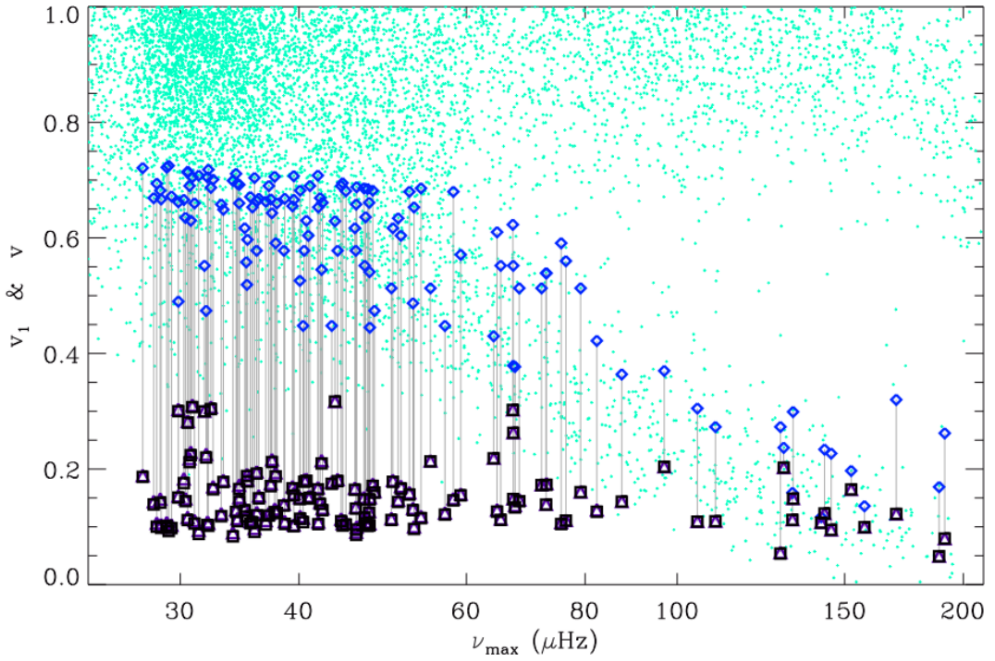

Figure 5.5: Dipole visibilities as a function of ν_{max} for *Kepler* red giants. All green points correspond to observations. Blue markers indicate stars considered to be depressed (falling below the empirical threshold indicated by the dashed line in Figure 5.4) that also exhibit mixed modes. Black markers correspond to predictions showing the predicted visibility if 100% of wave energy is lost in the g-mode cavity. Blue and black markers for each star are joined by a grey line to aid visualisation. Taken from Mosser et al. (2017a), fig. 7.

The authors concluded that strong magnetic fields caused total conversion and ultimately dissipation of gravity wave energy within the field region, supporting the claims that strong magnetic fields could result in mode depression. Between the two possible processes suggested in the earlier work, i.e. scattering into higher outgoing ℓ values, versus conversion into Alfvénic waves thereafter trapped in the core, the authors concluded that the latter process was the dominant one. In accordance with this, they noted that it should be impossible to form mixed modes in stars with a sufficiently strong core field, and therefore that the existence of mixed modes ruled out core magnetic fields above the critical value.

5.3.3 Mixed character of depressed modes

A significant blow to the ideas of Fuller et al. (2015) and Lecoanet et al. (2017) was dealt by the work of Mosser et al. (2017a). Upon more extensive analysis of the red giant data, they revealed that in a large number of cases the depressed dipole modes were in fact mixed, meaning that multiplets of partially g-like modes were present alongside the main p-dominated mixed mode, within each radial order. Figure 5.4 shows the dichotomy within the sample of red giants, with black markers indicating those in which the dipole modes were confirmed to be both mixed and depressed. The possibility of depressed yet mixed modes was already known in the case of KIC 8561221 studied by García et al. (2014), but the work of Mosser et al. (2017a) showed that it was ubiquitous among the larger population. Among the brightest stars ($m_V > 11$, having sufficient signal-to-noise for meaningful seismic analysis) exhibiting dipole mode depression, more than 90% had modes with mixed character. This indicated that the oscillatory nature of gravity waves in

the core was not being destroyed. Furthermore, upon re-computation of the predicted visibility depression based on 100% loss of energy within the g-mode cavity, Mosser et al. (2017a) found this to be inconsistent with actual measured visibilities of the depressed modes, which were higher. Figure 5.5 compares observed and predicted visibilities for red giants in the sample. This implied that the damping process, whatever its nature, was only giving rise to a partial loss of energy. It also seemed to suggest some errors or inaccuracies with the original visibility estimates of Fuller et al. (2015), which had been claimed to be consistent with the observations. A separate study of eight red giants by Arentoft et al. (2017) also measured visibilities that were consistent with partial damping.

The in-depth analysis of the observational data by Mosser et al. (2017a) placed a number of important constraints on the nature of the actual damping mechanism. By comparing the measured period spacings of mixed modes in stars on both sides of the dichotomy and finding them to be indistinguishable, it established that the damping mechanism cannot involve a significant modification to the stellar structure. In particular, it cannot affect the resonant properties of the g-mode cavity in a manner that would significantly alter the frequency spacings. It must also allow for a partial return of wave energy to the envelope, to be consistent with the measured visibilities. In later chapters we will develop and discuss mechanisms that attempt to incorporate these aspects, in the hope of providing a more convincing explanation for the dipole dichotomy problem.

Chapter 6

Modes in a Non-Rotating Star

In this chapter, we will present some preliminary ideas for how to treat the influence of a magnetic field on the modes that would ordinarily be present in an unmagnetised star. As discussed previously in §4.2.3, two orthogonal types of motion that can exist in a spherical body are spheroidal and torsional, the latter of which only has non-trivial frequencies in the presence of rotation and/or magnetism. Turbulent convection in an unmagnetised (or at most, weakly magnetised) envelope generates modes that are predominantly spheroidal in nature, but if a strong field is present deep in the core, then torsional motions corresponding to Alfvénic vibrations may be supported there. The mutual coupling between torsional Alfvén modes and spheroidal g-modes can provide a route of energy loss from the g-modes.

We will first demonstrate how the spheroidal and torsional modes are computed, and show the results for two different stellar models, one of which is a simple $n = 3$ polytrope (representing a main sequence star) and the other of which is a more realistic red giant model computed using the CESAM stellar evolutionary code (Morel, 1997). We will then proceed with the mathematical details of how the two types of modes couple and how this might give rise to a net damping. The qualitative and quantitative nature of this damping will be discussed at the end of the chapter.

6.1 Background parameters

6.1.1 Polytropic model

We solved the Lane-Emden equation (1.27) using a standard fourth-order Runge-Kutta (RK4) integration scheme under boundary conditions (1.28) to obtain a polytropic solution with index $n = 3$. The resulting pressure and density profiles provide a rough approximation to those of a main sequence star. To dimensionalise the various quantities we chose the mass and radius to be solar values, $\mathrm{M}_\odot = 1.99 \times 10^{30}$ kg and $\mathrm{R}_\odot = 6.955 \times 10^8$ m. The adiabatic index was set to $\gamma = 5/3$ throughout the star. This yielded central pressure and density values of $p_c = 1.25 \times 10^{16}$ Pa and $\rho_c = 7.64 \times 10^4$ kg/m^3. For comparison, solar values are $p_{c,\odot} = 3.4 \times 10^{16}$ Pa and $\rho_{c,\odot} = 1.6 \times 10^5$ kg/m^3 (Allen, 2000), of very similar order.

The resulting profiles for the enclosed mass, pressure, density, buoyancy frequency, sound speed and Lamb frequency as a function of radius are shown in Figure 6.1. The main qualitative difference between these and an actual solar-mass main sequence star is that in the case of the polytrope, the buoyancy frequency N is real and positive everywhere, while in a real star one expects the envelope to be convecting and thus N to be near zero in this region. Inspecting the values on the vertical axes, it can be seen that values of

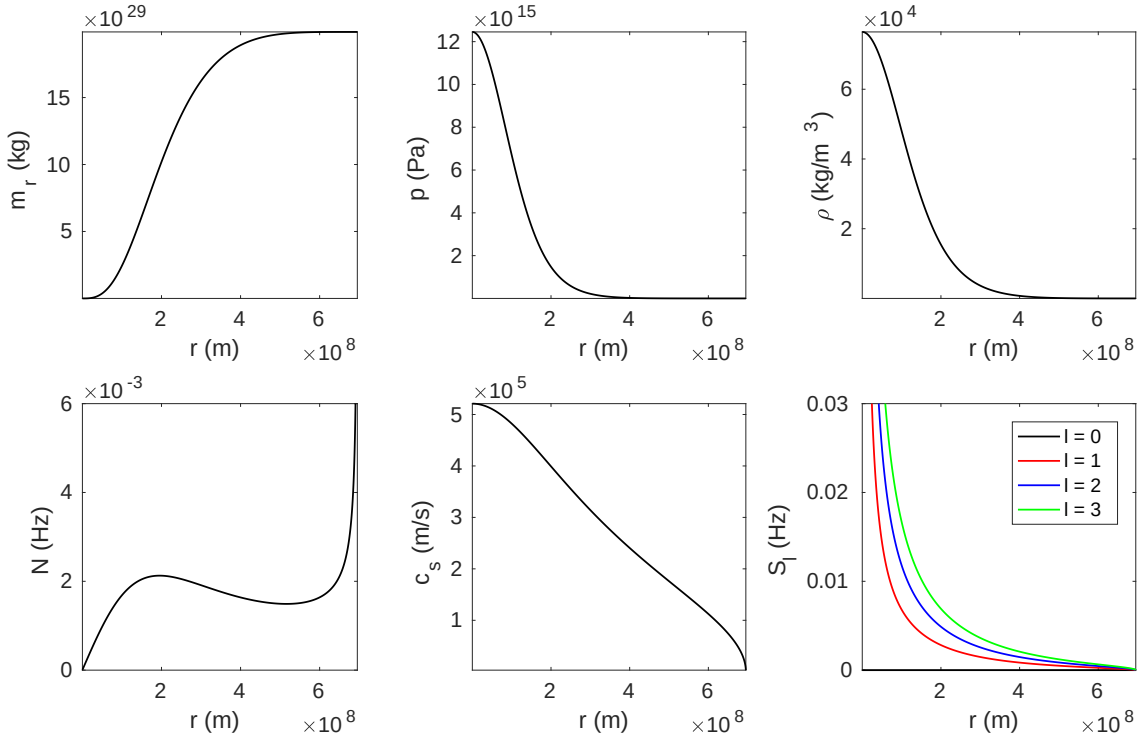

Figure 6.1: Parameters for an $n = 3$ polytrope of solar mass and radius.

N throughout most of the interior are much smaller than the local values of S_ℓ. Likewise, at any given frequency, the lower boundary of the p-mode cavity (where $\omega > S_\ell$) and upper boundary of the g-mode cavity (where $\omega < N$) are well separated radially, leading to only very weak coupling between the two cavities and implying that the modes should be relatively pure in their p-like or g-like character. We shall investigate this numerically the next section.

6.1.2 Red giant model

We obtained the parameter profiles for an evolved stellar model from an online source[1], corresponding to a $2\,M_\odot$, 962 Myr-old red giant star. Figure 6.2 shows the profiles for enclosed mass, temperature, pressure, density, adiabatic index, buoyancy frequency, sound speed and Lamb frequency, as a function of radius. Notice the extreme central condensation: around one-eighth of the mass is contained within the inner 2% of the radius, corresponding to the inert helium core. A glitch in the buoyancy frequency profile near $r = 3 \times 10^7$ m, coinciding with a local plateau in the temperature profile, is likely to be associated with the composition gradient in the H-burning shell around the helium core.

In the case of the red giant, can be seen that the N and S_ℓ values are of comparable order over much of the stellar interior, and in fact overlap for the lowest-degree modes. This suggests a very strong coupling between the p- and g-mode cavities, leading to extensive mode mixing.

[1] Downloaded from `https://www.astro.up.pt/helas/stars/cesam/A/data/`

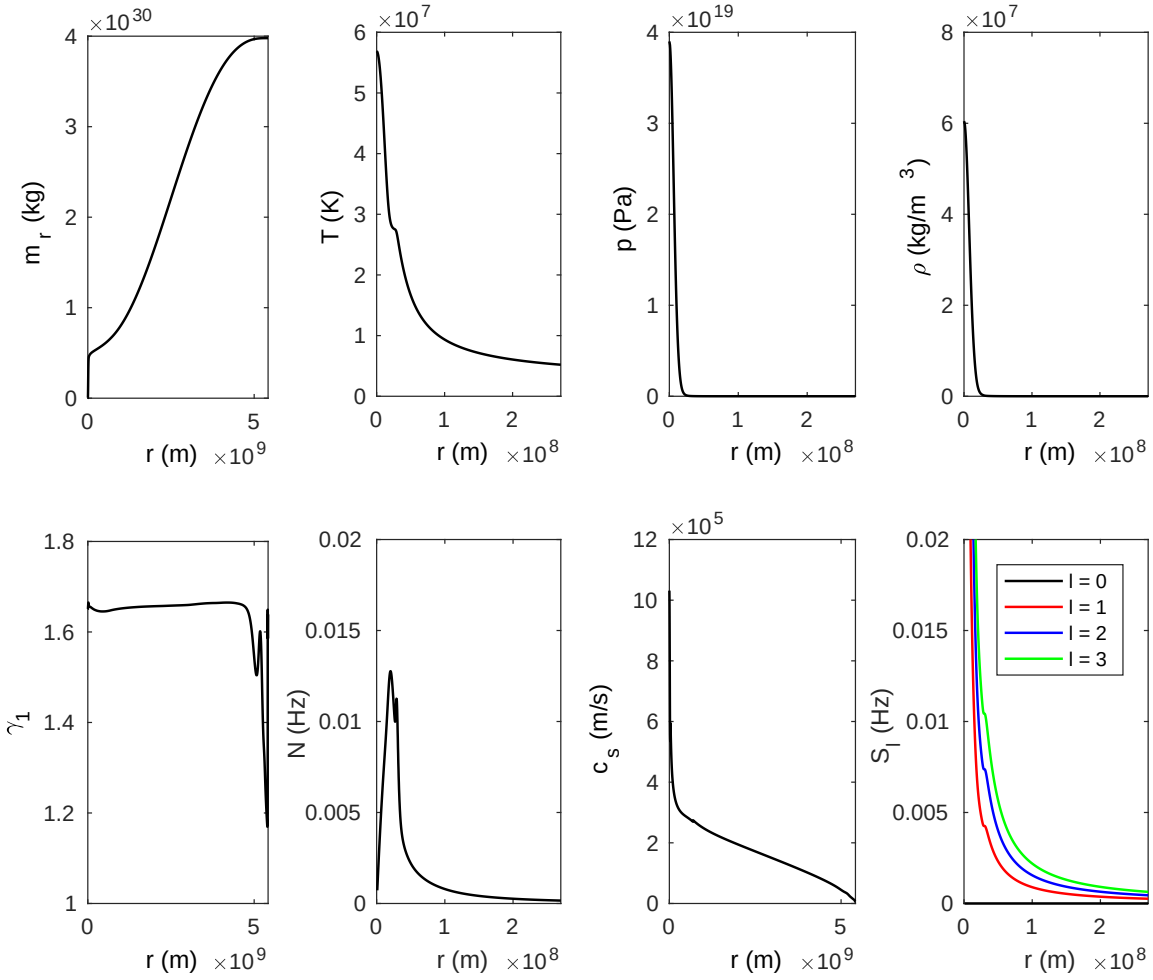

Figure 6.2: Parameters for a $2\,M_\odot$ red giant star generated by the CESAM evolutionary code. Note that the T, p, ρ, N and S_ℓ plots are only shown up to 5% of the stellar radius, which is $R_* = 5.42 \times 10^9$ m.

6.2 Hydrodynamic spheroidal modes

6.2.1 Computation

The hydrodynamic modes were obtained by solving Equations (4.21) and (4.22) as a boundary eigenvalue problem, under the boundary conditions laid out in §4.1.2. This was done using a shooting procedure where two solutions were integrated (using RK4) from the two boundaries and matched at an intermediate radius. This was chosen to be $r = r_{\rm fit} = 0.99 R_*$, favouring the search towards p-dominated modes. The requirement that the two solutions (up to an arbitrary scaling) have the same value and slope at $r_{\rm fit}$ is equivalent to demanding that the determinant of the matching matrix,

$$M = \begin{pmatrix} \xi_r(r_{\rm fit}^-) & -\xi_r(r_{\rm fit}^+) \\ p'(r_{\rm fit}^-) & -p'(r_{\rm fit}^+) \end{pmatrix}, \tag{6.1}$$

vanishes. Superscripts + and − correspond to the values at $r_{\rm fit}$ associated with the inward and outward integrations, from the outer and inner boundaries, respectively. Note that since $r = 0$ is a regular singular point of the equations, the inner boundary conditions were applied instead at $r_{\rm in} = 7.25 \times 10^{-5} R_*$ for the polytrope and $r_{\rm in} = 2 \times 10^{-10} R_*$ for the red giant.

A uniform grid spacing with 13792 radial points was used for the polytrope. For the red giant, the original model grid only had 1574 points. This was interpolated to a non-uniform grid of 10^5 points, the spacing increasing linearly from $r = 0$ to $0.5\, R_*$ and decreasing linearly from $r = 0.5$ to $1\, R_*$, so that the finest scales, occurring near the centre and surface, could be adequately resolved. The eigenvalues and a selection of eigenfunctions obtained for the two stellar models are shown in Figure 6.3 and 6.4, for the polytrope and red giant, respectively. These were obtained by performing an initial scan of 100 trial values for $1 \leq \omega \leq 20$, and then performing Newton-Raphson iteration to refine the locations of the roots of $\det M = 0$. The units of ω here are $\sqrt{GM_*/R_*^3}$. Note that due to the coarse resolution of the search, not all modes in the search range would have been found; these only represent a selection.

6.2.2 Results & discussion

For the polytrope, modes tend to fall into one of two types: either with oscillations near the surface (p-modes, occurring at higher frequencies), or oscillations near the centre (g-modes, occurring at lower frequencies). This is in contrast with the red giant model, for which almost all non-radial modes within the considered frequency range have significant oscillation amplitudes at both the centre and surface. This reflects the large extent of cavity coupling and mode mixing in the red giant, while modes in the polytrope (representative of a main sequence star) are relatively pure. The g-like character of the modes in the red giant can be inferred from the large negative values of the mode orders for the nonradial modes; recall that using the Eckart classification scheme, g-type radial crossings are counted negatively while p-type crossings are counted positively. The radial modes in both cases, on the other hand, have non-negative radial orders and are purely p-like in character, with oscillations occurring only in the envelope.

As established towards the end of §4.2.2, p-modes are expected to be evenly spaced in frequency while g-modes are expected to be evenly spaced in period. This difference in behaviour can be seen from the bottom-left plot of Figure 6.3, where at lower frequencies the modes tend to show $\nu \propto 1/|n|$ behaviour, while at higher frequencies, $\nu \propto n$. For the red giant (Figure 6.4), however, it appears that $\nu \propto 1/|n|$ for all $\ell > 0$.

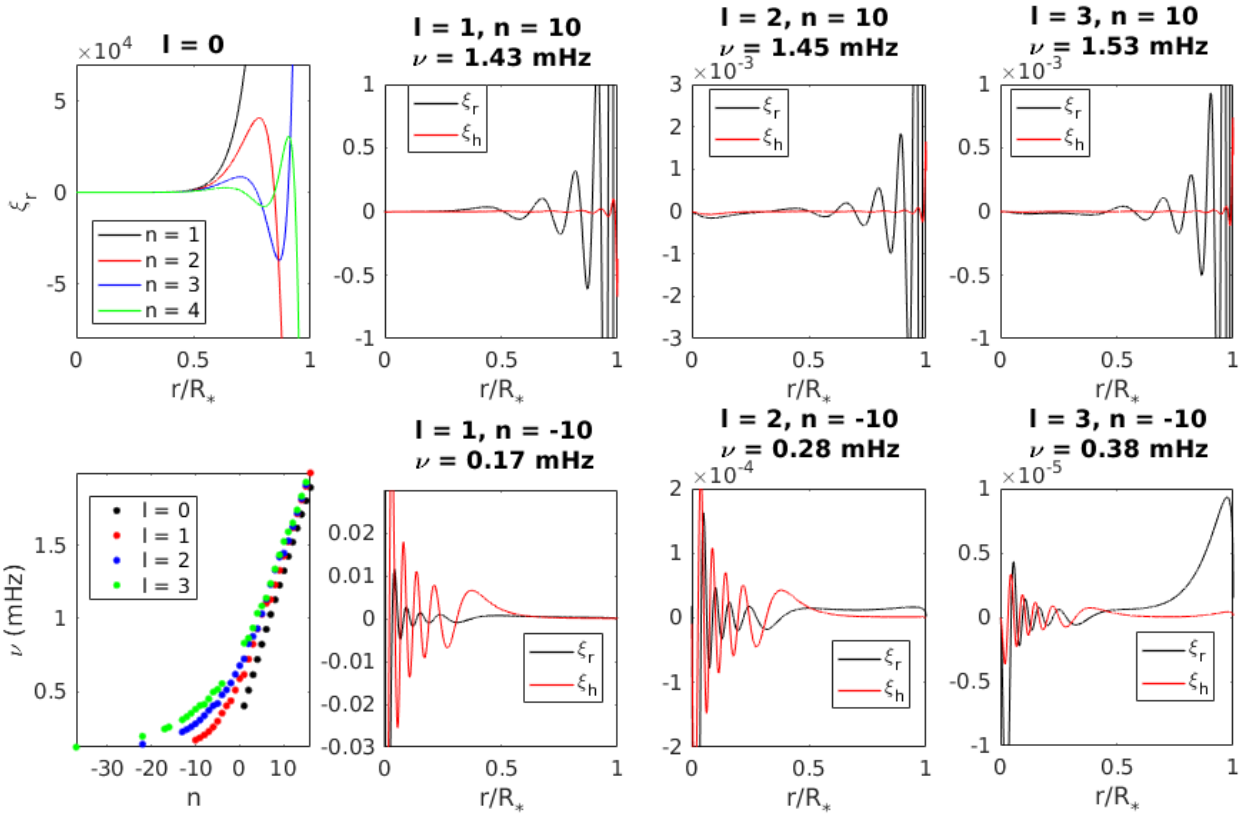

Figure 6.3: A selection of hydrodynamic modes computed for the $n = 3$ solar-mass polytropic model. Spatial amplitude functions for p-modes of different degrees are shown on the top row, while those for g-modes are shown in the rightmost three panels along the bottom row. The bottom-left panel displays a range of mode frequencies versus their radial order computed using the Eckart scheme. In the rightmost three columns the associated frequency of the mode is shown in the plot title, while for the top-left panel the frequencies of the four modes are 0.40, 0.51, 0.62 and 0.72 mHz in order of increasing n.

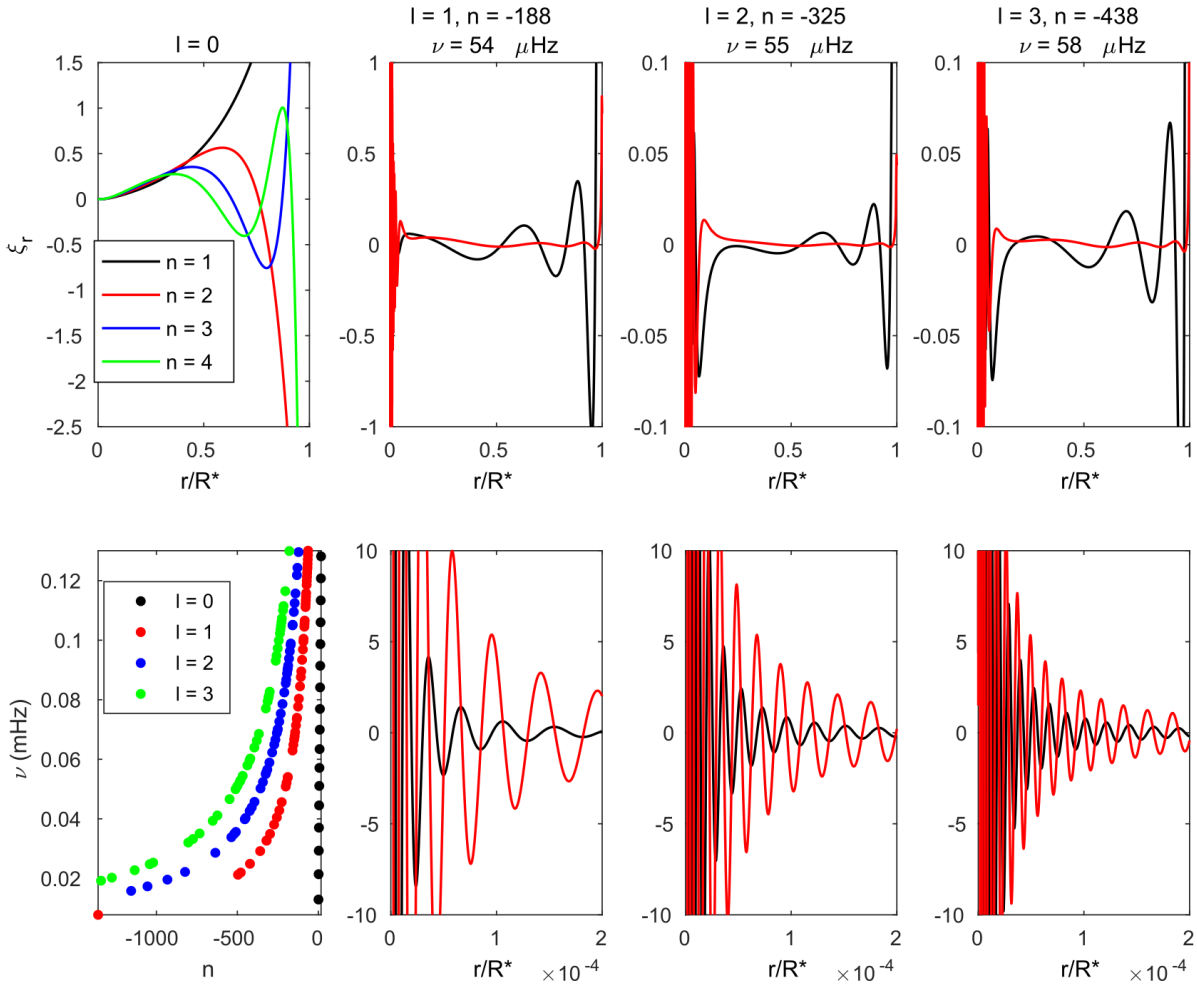

Figure 6.4: As for Figure 6.3, but this time for the CESAM red giant model, and where the bottom row instead shows a zoom-in to the core region of the mode in the panel above. In the top-left panel the modes have frequencies of 13, 21, 29 and 37 μHz in order of increasing n.

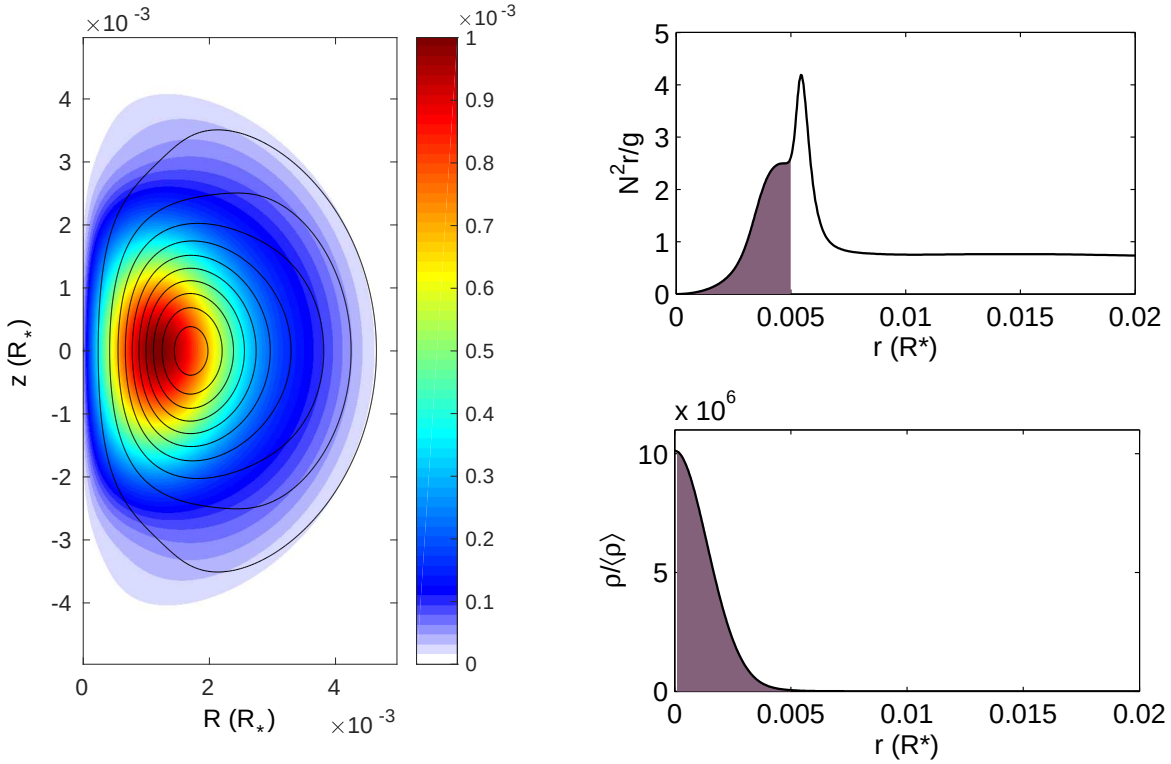

Figure 6.5: The Prendergast magnetic field solution (left) calculated for the CESAM red giant model and imposed for $r \leq 0.005\,R_*$. This region is shown shaded on the right panels, which plot the dimensionless squared buoyancy frequency and density profiles near the centre. On the left, black lines represent a selection of magnetic flux surfaces (poloidal field loops), while the underlying colour represents the strength of the toroidal component. The absolute scaling of the field is arbitrary here; illustrated is just the overall geometry. The solution is axisymmetric and so only a meridional half-plane is shown.

This indicates that over the frequency range in question, each p-mode couples to g-modes of relatively high absolute order. A further comment is that ξ_r tends to be larger than ξ_h in the envelope, while the opposite is true in the core. This reflects the fact that p-mode oscillations are associated with displacements that are larger radially than horizontally, while g-mode oscillations involve fluid displacements that are primarily horizontal.

6.3 Torsional Alfvén modes

6.3.1 Computation

The equation of motion of a driven oscillator can be written

$$\frac{\partial^2 \boldsymbol{\xi}}{\partial t^2} + \mathscr{L}[\boldsymbol{\xi}] = \mathbf{S}(\mathbf{r}, t)\,, \tag{6.2}$$

cf. (2.36) but now with a source term $\mathbf{S}$ representing the external driving/forcing. $\mathbf{S}$ is regarded as being external because it does not depend on $\boldsymbol{\xi}$, although it may be a function of position $\mathbf{r}$ and time t. The normal

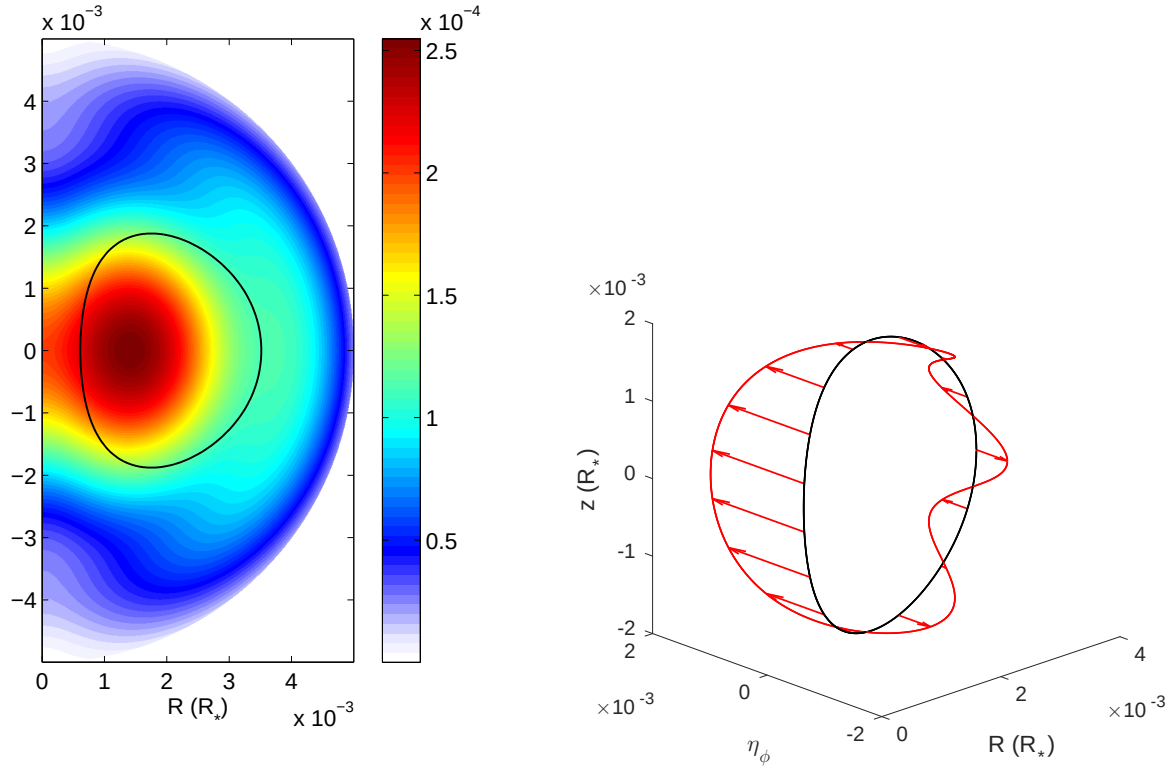

Figure 6.6: Spatial distribution of the Alfvén speed overlaid with a selected field loop (left), and the amplitude function for the $j = 7$ eigenmode on that loop (right), for the CESAM red giant model. Colour bar units are in terms of the dynamical speed $\sqrt{GM_*/R_*}$. In the right panel, the equilibrium position of the field line is shown in black and the displaced position in red. Arrows are an aid to visualising the direction of the displacement.

modes of the oscillator are the solutions of Equation (6.2) with $\mathbf{S} = \mathbf{0}$ (the homogeneous problem). Imposing a time-harmonic dependence $\boldsymbol{\xi} \propto \exp(-\mathrm{i}\omega t)$, this corresponds to the eigenproblem $\mathscr{L}[\boldsymbol{\xi}] = \omega^2\boldsymbol{\xi}$, satisfied for only special values of $\omega^2 = \omega_0^2$. These are the natural frequencies of the oscillator, and the associated forms of $\boldsymbol{\xi}$ are the eigenfunctions of the system.

For a non-rotating, magnetised fluid, the equation of motion (under the Cowling approximation) is

$$\rho\left(\frac{\partial \mathbf{u}}{\partial t} + \mathbf{u}\cdot\nabla\mathbf{u}\right) = -\nabla p - \rho\nabla\Phi - \frac{1}{2}\nabla B^2 + (\mathbf{B}\cdot\nabla)\mathbf{B}\,, \tag{6.3}$$

where we have absorbed the factors of μ_0 into the definition of $\mathbf{B}$. Upon linearising and taking the curl of Equation (6.3), one may see that the first three terms on the RHS vanish, leaving magnetic tension as the only force capable of restoring torsional motions. In the axisymmetric case, which we will focus on, torsional motions separate spatially as being those in the ϕ-direction, while spheroidal motions lie in meridional planes. Now consider the torsional component of (6.3), which linearises to give

$$\rho_0\frac{\partial^2\xi_\phi}{\partial t^2} = \frac{\mathbf{B}_0}{R}\cdot\nabla(RB'_\phi) + \frac{\mathbf{B}'}{R}\cdot\nabla(RB_{0\phi})\,. \tag{6.4}$$

From the linearised induction equation $\mathbf{B}' = \nabla\times(\boldsymbol{\xi}\times\mathbf{B}_0)$, the (R,ϕ,z) components of the perturbation to the

magnetic field can be obtained as

$$\begin{aligned} B'_R &= \frac{1}{R}\frac{\partial}{\partial z}[\boldsymbol{\xi}\cdot\nabla\psi]\,, \\ B'_\phi &= R\mathbf{B}_0\cdot\nabla\left(\frac{\xi_\phi}{R}\right) - R\boldsymbol{\xi}\cdot\nabla\left(\frac{B_{0\phi}}{R}\right) - B_{0\phi}(\nabla\cdot\boldsymbol{\xi})\,, \\ B'_z &= -\frac{1}{R}\frac{\partial}{\partial R}(\boldsymbol{\xi}\cdot\nabla\psi)\,. \end{aligned} \tag{6.5}$$

This lets us cast Equation (6.4) into the form

$$\frac{\partial^2\xi_\phi}{\partial t^2} + \mathscr{L}_\mathrm{T}[\xi_\phi] = \frac{f_\mathrm{TS}}{\rho_0}\,, \tag{6.6}$$

where

$$\mathscr{L}_\mathrm{T}[\xi_\phi] = -\frac{\mathbf{B}_0}{\rho_0 R}\cdot\nabla\left[R^2\mathbf{B}_0\cdot\nabla\left(\frac{\xi_\phi}{R}\right)\right], \tag{6.7}$$

$$f_\mathrm{TS} = -\frac{\mathbf{B}_0}{R}\cdot\left[R^2\boldsymbol{\xi}\cdot\nabla\left(\frac{B_{0\phi}}{R}\right) + RB_{0\phi}(\nabla\cdot\boldsymbol{\xi})\right] + \frac{\mathbf{B}'}{R}\cdot\nabla(RB_{0\phi})\,. \tag{6.8}$$

See that f_TS depends only on the spheroidal displacement $\boldsymbol{\xi}_\mathrm{S} \equiv (\xi_R, 0, \xi_z)$, not ξ_ϕ, and can thus be regarded as a forcing term in Equation (6.7) provided that the spheroidal displacement is assumed to be known, which will effectively be the case when the magnetic field is weak. In that case, the spheroidal modes will be relatively unperturbed.

Let us examine the operator $\mathscr{L}_\mathrm{T}$ more closely. Although, at the first glance, this appears to depend on three spatial dimensions, note that $\mathbf{B}_0\cdot\nabla = B_\mathrm{p}\partial/\partial s$, where B_p is the magnitude of the poloidal component of $\mathbf{B}$ and s is arc length (i.e. physical distance) along the poloidal projections of the field lines. Hence, the problem is intrinsically one-dimensional. Rescaling to a new distance coordinate σ obeying

$$\frac{\mathrm{d}\sigma}{\mathrm{d}s} = \frac{1}{R^2 B_\mathrm{p}}\,, \tag{6.9}$$

the eigenproblem reduces to

$$\frac{\partial^2\eta_\phi}{\partial t^2} = v_A^2\frac{\partial^2\eta_\phi}{\partial\sigma^2}\,, \tag{6.10}$$

where

$$\eta_\phi \equiv \frac{\xi_\phi}{R} \quad\text{and}\quad v_A^2 \equiv \frac{1}{\rho_0 R^4}\,. \tag{6.11}$$

Equation (6.10) is the one-dimensional wave equation with spatially varying advection speed $v_A = v_A(\sigma)$, which is the Alfvén speed with respect to this new coordinate system. From here, it becomes more convenient to work in terms of the scaled fluid displacement η_ϕ rather than ξ_ϕ. The particular form of Equation (6.10) allows the solutions to be understood intuitively as standing waves on stretched 1D loops. These are quantised vibrations whose frequencies increase as the spatial scale decreases.

We solved Equation (6.10) as a matrix eigenvalue problem on a discrete 1D grid for each flux surface, with periodic boundary conditions and spatial derivatives approximated by centred differences. The N^2 profile as a function of radius, shown in Figure 6.5, exhibits a spike at around $r = 0.0054\,R_*$. This can be interpreted as the location of the H-burning shell, below which the inert He core would be found, and where a possible magnetic field might be left from a previous core dynamo. Based on this, we chose to compute and impose the Prendergast solution over the central $0.005\,R_*$ of the red giant model. The resulting configuration is shown in Figure 6.5. We calculated the eigenmodes $X_j(\sigma,\psi)$ and eigenfrequencies $\omega^2_{0,j}(\psi)$ on 1000 evenly spaced (in ψ) flux surfaces with 5000 uniformly spaced (in σ) points on each surface. Here $j \in \mathbb{Z}^+$

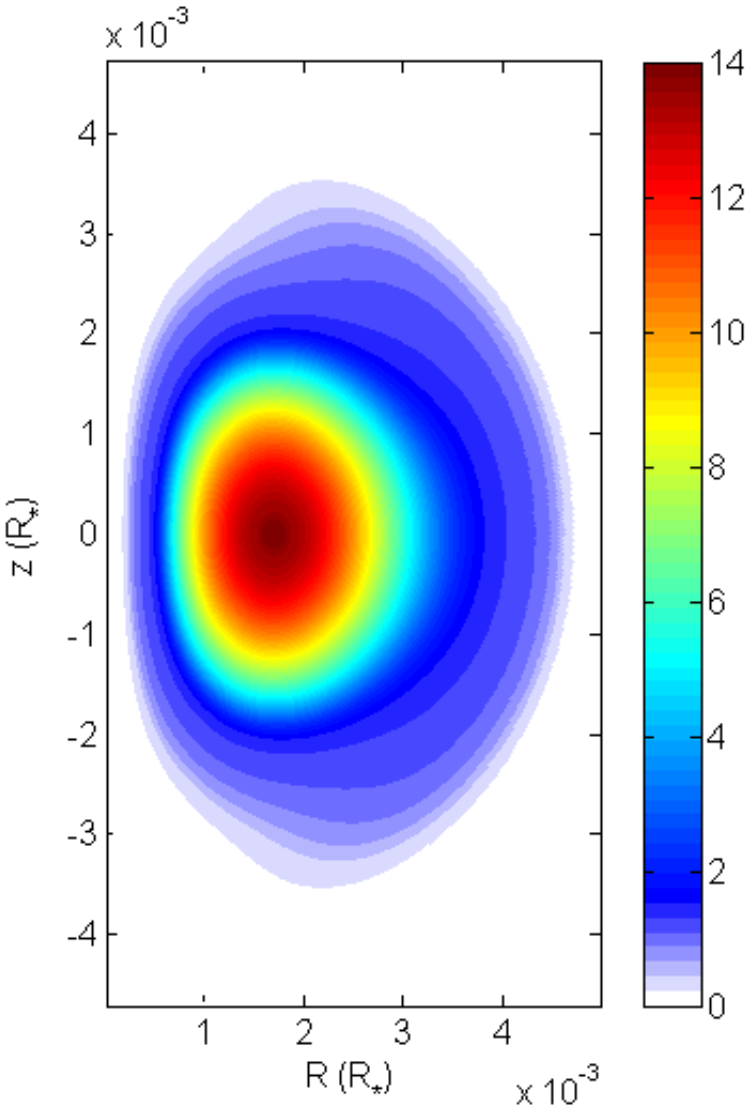

Figure 6.7: Spatial distribution of the $j = 300$ eigenfrequencies. Colour bar units are in terms of the dynamical frequency $\sqrt{GM_*/R_*^3}$. Since eigenmodes are localised to individual flux surfaces, $\omega_{0,j}$ is constant on any flux surface for a given j. Smaller flux surfaces tend to have a higher $\omega_{0,j}$ for a fixed j.

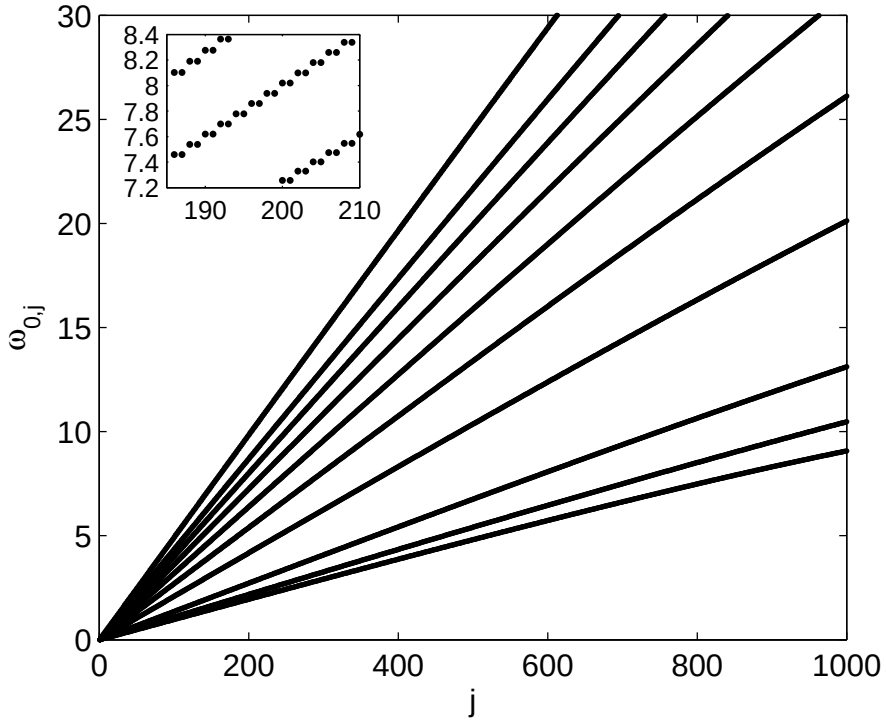

Figure 6.8: The torsional spectrum calculated for 10 evenly spaced (in ψ) flux surfaces. Each track corresponds to one flux surface, and flux surfaces of lower tracks enclose those of higher ones. Although apparently continuous, the tracks are, in fact, made up of discrete points since $j \in \mathbb{Z}^+$. The discreteness can be seen in the inset plot, which zooms in to a small portion of the overall spectrum. The paired structure reflects approximately degenerate modes, which have equal numbers of nodes but are odd and even versions of one another. Frequencies are given in units of the dynamical frequency, $\sqrt{GM_*/R_*^3}$.

is the harmonic index. Although the number of eigenfunctions obtainable by this method equals the number of grid points, the accuracy of the solutions is expected to degrade for larger $\omega_{0,j}^2$ values where spatial scales of the associated eigenfunctions become too small to be adequately resolved. On each flux surface, we restricted the eigenfunctions used in further analysis to the 1000 having the lowest eigenfrequencies.

6.3.2 Results & discussion

The spatial distribution of the Alfvén speed (whose scaling is controlled through our choice of β), and a selected torsional eigenmode, are shown in Figure 6.6 for the red giant model embedded with a Prendergast field. Since the problem is axisymmetric, the spatial amplitude function need only be displayed on a poloidal field loop, corresponding to a longitudinal slice of the flux surface. The full solution is obtained by sweeping each loop in a circle about the axis of symmetry (here the z-axis). The motion can be envisaged as segments of each flux surface (which are tori in 3D) twisting with respect to others. For a given wave speed v_A, one expects $\omega_{0,j}$ for fixed j to increase as the length of the field loop shrinks. This is indeed observed: the spatial distribution of $\omega_{0,j}$ for $j = 300$ is shown in Figure 6.7.

For a given flux surface, one also expects $\omega_{0,j}$ to increase with j. Only an even number of nodes is allowed for vibrations on a loop, so $j = 1$ has zero nodes, $j = 2,3$ have two, $j = 4,5$ have four, and so on. Hence,

j is roughly proportional to the number of wavelengths around the loop, but there is a paired structure to the spectrum. This can be seen in the inset to Figure 6.8, which plots $\omega_{0,j}$ versus j for a selection of flux surfaces. Despite having equal numbers of nodes, each pair still corresponds to distinct eigenmodes, these being odd and even versions of one another (e.g. for a constant v_A, they would be the sine and cosine solutions), with slightly different eigenfrequencies. Note that similar behaviour of the periodic solutions of the Mathieu equation occurs. The overall slope of $\omega_{0,j}$ versus j should also be proportional to the fundamental frequency (larger for smaller loops, in line with the picture of a vibrating string). As can be seen in Figure 6.8, this is indeed the case.

6.4 Resonant damping

In the presence of a magnetic field, the coupling between spheroidal and torsional motions, made possible through the Lorentz force, potentially leads to a damping process for spheroidal modes. Though fundamental frequencies of torsional modes may be small for realistic field strengths, resonances with spheroidal modes may be possible with torsional modes of high harmonic index. The strength of this interaction is determined by the quality of the match of spatial scales between the two types of modes. Under conditions of weak but non-zero dissipation, the energy lost to excitation of torsional resonances equals the work done against the Lorentz force by spheroidal motions owing to the singular nature of the interaction. In this section we outline the mathematics behind this process.

Note that although promising at first glance, this mechanism unfortunately suffers a number of shortcomings, explained at the end of this chapter.

6.4.1 Overlap integrals

The perturbation to the Lorentz force can be subdivided into terms that depend on the spheroidal displacement $\boldsymbol{\xi}_S$ but not the torsional displacement ξ_ϕ, and the terms that depend on ξ_ϕ but not $\boldsymbol{\xi}_S$ (this is possible because only terms linear in $\boldsymbol{\xi}$ are retained). Writing this out in components, we can express this separation as

$$\mathbf{f}_S(\boldsymbol{\xi}) = \mathbf{f}_{SS}(\boldsymbol{\xi}_S) + \mathbf{f}_{ST}(\xi_\phi)\,, \tag{6.12}$$

$$f_T(\boldsymbol{\xi}) = f_{TS}(\boldsymbol{\xi}_S) + f_{TT}(\xi_\phi)\,, \tag{6.13}$$

where $\mathbf{f}_S$ and f_T are the spheroidal and torsional components to the Lorentz force perturbation, $\mathbf{f}_{SS}$ are the terms in $\mathbf{f}_S$ that depend only on $\boldsymbol{\xi}_S$, $\mathbf{f}_{ST}$ are those in $\mathbf{f}_S$ that depend only on ξ_ϕ, etc. This allows us to observe the following coupled structure of the equations of motion:

$$\frac{\partial^2 \boldsymbol{\xi}_S}{\partial t^2} + \mathscr{L}_S[\boldsymbol{\xi}_S] = \frac{\mathbf{f}_{ST}(\xi_\phi)}{\rho_0}\,, \tag{6.14}$$

$$\frac{\partial^2 \xi_\phi}{\partial t^2} + \mathscr{L}_T[\xi_\phi] = \frac{f_{TS}(\boldsymbol{\xi}_S)}{\rho_0}\,, \tag{6.15}$$

where

$$\mathscr{L}_S[\boldsymbol{\xi}_S] = \frac{1}{\rho_0}\left[\nabla p' + \rho' \nabla \Phi_0 - \mathbf{f}_{SS}(\boldsymbol{\xi}_S)\right], \tag{6.16}$$

$$\mathscr{L}_T[\xi_\phi] = -\frac{f_{TT}(\xi_\phi)}{\rho_0}\,. \tag{6.17}$$

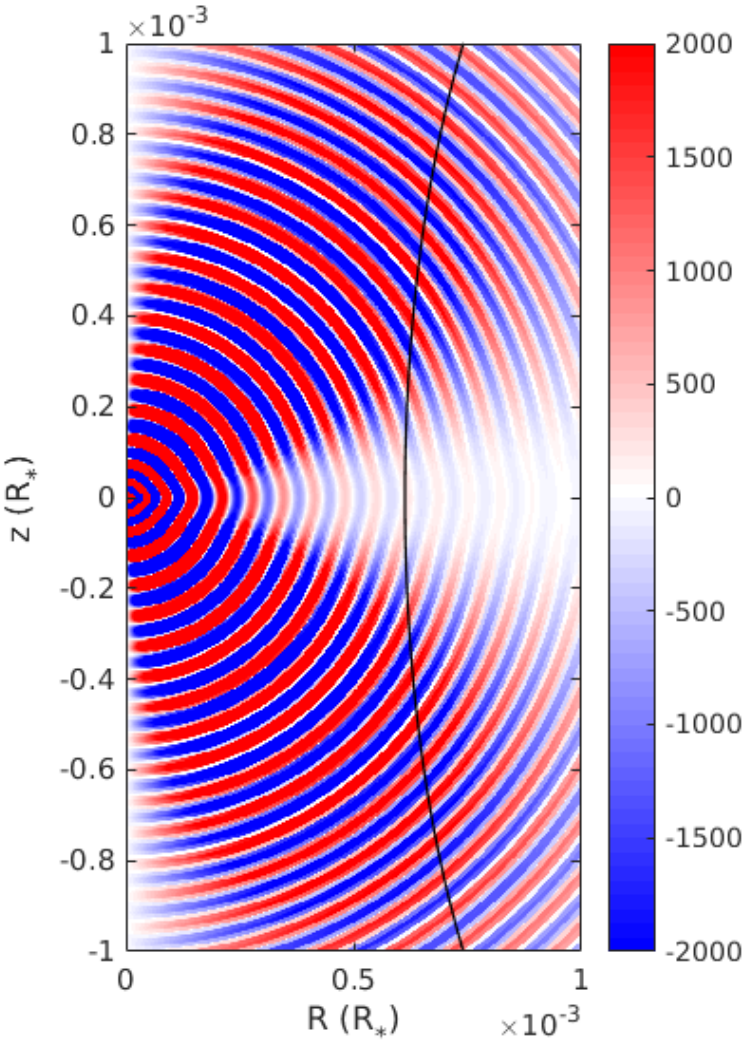

Figure 6.9: Spatial distribution of $f_{\rm TS}$ (the torsional component of the Lorentz force associated with spheroidal motions) for a selected $\ell = 1$ mode of the red giant model, overlaid with the flux surface shown in Figure 6.6. Only the region near the centre is shown. Fluid displacements have been normalised so that the total energy of the mode is unity. One sees that there is a cross-cut of the field loop across many radial nodes (sign changes) of $f_{\rm TS}$, suggesting that this should preferentially excite high-index harmonics on that loop.

We see that the coupling between spheroidal and torsional motions is provided by the Lorentz force.

To first order, given that the Lorentz force is much smaller than the forces of pressure and buoyancy, the $\mathbf{f}_{\mathrm{SS}}$ term in (6.16) can be neglected. This is akin to assuming that the magnetic field has negligible effect on the spheroidal eigensolution (i.e. we still get the usual p- and g-modes). An important term not included explicitly in Equation (6.14) is the forcing associated with (purely spheroidal) convective motions, which is the source of energy for the whole system. Given that the coupling from spheroidal motions into torsional motions and back into spheroidal motions is a second-order process, the direct contribution of convection should dominate over $\mathbf{f}_{\mathrm{ST}}$ in the spheroidal equation of motion when magnetic fields are weak (the coupling strength scales like the magnetic pressure B^2, which is far smaller than the gas pressure). We shall thus neglect all magnetic terms in (6.14). In contrast, the Lorentz force has a first-order significance in providing both the driving and the restoration of torsional motions, since there are no pressure or buoyancy forces to compete with, and cannot be neglected in Equation (6.15).

From the point of view of the torsional equation of motion, spheroidal fluid motions act as a forcing function through their associated Lorentz force. In general, if the forcing applied to a mechanical oscillator contains one or more frequencies that match its natural frequencies, then resonant excitation occurs. The strength of the excitation depends on the geometric similarity between the forcing function at the resonant frequencies and the corresponding eigenmodes, which can be quantified by way of an overlap integral (equivalently, the coefficients of the eigenfunction expansion of the forcing function). Figure 6.9 shows the spatial distribution of f_{TS} near the core for an $\ell = 1$ spheroidal mode of the red giant near $\nu \approx 70\,\mu\mathrm{Hz}$. Overlaid in black is the same field loop shown in Figure 6.6. The fine-scale oscillations of $\boldsymbol{\xi}_{\mathrm{S}}$ produce corresponding fine-scale oscillations of $f_{\mathrm{TS}}(\boldsymbol{\xi}_{\mathrm{S}})$. This illustrates how the excitation of high harmonics by low-degree modes can occur: in general, the field lines cut across many radial shells, enabling large n to map to large j.

The torsional equation of motion in terms of the scaled fluid displacement η_ϕ can be written as

$$\frac{\partial^2 \eta_\phi}{\partial t^2} - \frac{1}{\rho_0 R^4}\frac{\partial^2 \eta_\phi}{\partial \sigma^2} = F_\phi\,, \tag{6.18}$$

where $F_\phi = f_{\mathrm{TS}}/\rho_0 R$. We now wish to derive an expression for the expansion coefficients of F_ϕ (the spheroidal forcing) with respect to the torsional eigenmodes X_j identified in the previous section, i.e. the quantities a_j in

$$F_\phi(\sigma,\psi) = \sum_j a_j(\psi) X_j(\sigma,\psi)\,. \tag{6.19}$$

First, we need to establish the orthogonality relation for X_j. Substituting the eigensolution $\omega_{0,j}^2, X_j$ into the homogeneous form of Equation (6.18), we have

$$-\rho_0 R^4 \omega_{0,j}^2 X_j = \frac{\partial^2 X_j}{\partial \sigma^2}\,. \tag{6.20}$$

Integrating twice by parts and applying periodic boundary conditions, one can show that

$$\oint X_k^* \frac{\partial^2 X_j}{\partial \sigma^2}\,\mathrm{d}\sigma = \oint X_j \frac{\partial^2 X_k^*}{\partial \sigma^2}\,\mathrm{d}\sigma\,, \tag{6.21}$$

where the integral is around a closed field loop. Multiplying (6.20) by X_k^* and integrating, and using (6.21), we find that

$$\left(\omega_{0,j}^2 - \omega_{0,k}^2\right)\oint \rho_0 R^4 X_j X_k^*\,\mathrm{d}\sigma = 0\,, \tag{6.22}$$

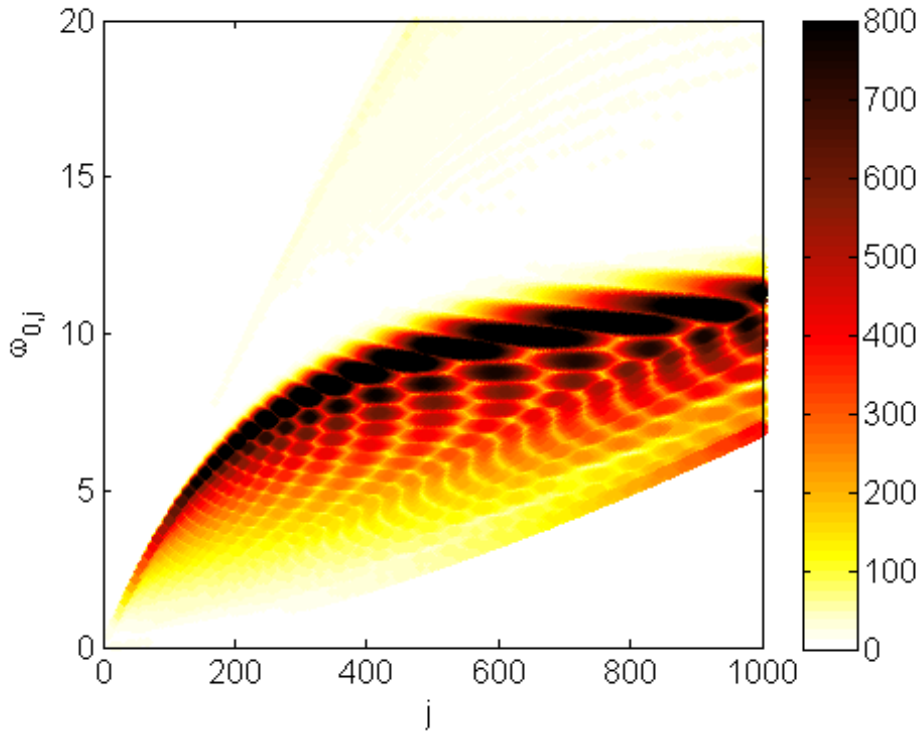

Figure 6.10: The torsional spectrum computed for 500 flux surfaces. Points are coloured according to the strength of the coupling with the mode shown in Figure 6.9. The coupling strength is quantified as $|a_j|$, the absolute value of the overlap integral defined in Equation (6.24).

which implies that unless $\omega_{0,j}^2 = \omega_{0,k}^2$, it must be that $\oint \rho_0 R^4 X_j X_k^* \, \mathrm{d}\sigma = 0$. It is possible to normalise the X_j so that

$$\oint \rho_0 R^4 X_j X_j^* \, \mathrm{d}\sigma = 1 \,. \tag{6.23}$$

Doing so, we arrive at the desired expression:

$$a_j = \oint R^3 f_{\mathrm{TS}} X_j^* \, \mathrm{d}\sigma \,. \tag{6.24}$$

The values of a_j for the mode shown in Figure 6.9 and each of the torsional modes are plotted in Figure 6.10. The spheroidal displacements have been normalised such that the total energy E (Unno et al., 1989) equals unity, i.e.

$$E = \omega^2 \int \rho_0 r^2 \left[\xi_r^2(r) + \ell(\ell+1)\xi_{\mathrm{h}}^2(r)\right] \mathrm{d}r = 1 \,. \tag{6.25}$$

As a comment, the values obtained for a_j for the red giant model are substantially lower than the maximum physically allowed values, which would occur under conditions of complete geometric overlap (perfect constructive interference). As an order-of-magnitude estimate, the upper bound on a_j is given by $R_c^{1/2} B^{3/2} \xi L^{-2}$, where R_c is the size of the core, ξ is the characteristic fluid displacement and L is the characteristic length-scale of variations in ξ. Substituting appropriate values for the red giant model yields a physical upper bound on a_j of the order of 10^4. Actual values, as seen in Figure 6.10, are more in the range of ~100.

Also apparent from Figure 6.10 is that the torsional spectrum is very dense. In fact, for every value of $j \in \mathbb{Z}^+$, there is a continuum of $\omega_{0,j}$ values, reflecting the existence of a continuum of flux surfaces. However, the

number of resonances is finite due to the discrete nature of j, and at a given ω equals the j range intersected by a horizontal line at that value of ω. For the spheroidal mode shown in Figure 6.9, which is near $\omega = 10$, we identify around 900 resonances, i.e. there exist this number of magnetic flux surfaces that have a torsional mode with this eigenfrequency.

6.4.2 Incorporating dissipation

We shall now incorporate dissipative effects, with the goal of elucidating their role in contributing to the damping of the torsional oscillations. In the following derivation, it will be assumed that the damping coefficients in units of the dynamical frequency are much less than unity (highly underdamped oscillator), so that the eigenfrequencies and eigenmodes derived above remain valid. At the end of this section, we evaluate the expression for the damping coefficient obtained and verify that it is indeed small.

With dissipative terms included, the momentum and induction equations are

$$\frac{\partial^2 \boldsymbol{\xi}}{\partial t^2} + \mathscr{L}[\boldsymbol{\xi}] - \nu \nabla^2 \frac{\partial \boldsymbol{\xi}}{\partial t} = 0\,, \tag{6.26}$$

$$\frac{\partial \mathbf{B}'}{\partial t} - \nu_m \nabla^2 \mathbf{B}' = \nabla \times \left(\frac{\partial \boldsymbol{\xi}}{\partial t} \times \mathbf{B}_0 \right), \tag{6.27}$$

where ν and ν_m are the viscous and Ohmic dissipation coefficients, and $\mathscr{L}[\boldsymbol{\xi}]$ refers to the linearised form of the right-hand side of Equation (6.3). Invoking a time-harmonic expansion $\propto \exp(-\mathrm{i}\omega t)$, Equation (6.27) becomes

$$\left(\nabla^2 - \frac{\mathrm{i}\omega}{\nu_m} \right) \mathbf{B}' = -\frac{\mathrm{i}\omega}{\nu_m} \nabla \times (\boldsymbol{\xi} \times \mathbf{B}_0)\,, \tag{6.28}$$

which we recognise as the inhomogeneous Helmholtz equation and can be solved by means of an integration kernel to yield

$$\mathbf{B}'(\mathbf{r}) = \iiint K(\mathbf{r} - \mathbf{r}') \nabla \times (\boldsymbol{\xi} \times \mathbf{B}_0)_{\mathbf{r}'} \, \mathrm{d}^3 \mathbf{r}' \approx \nabla \times (\bar{\boldsymbol{\xi}} \times \mathbf{B}_0)_{\mathbf{r}}\,, \tag{6.29}$$

where

$$\bar{\boldsymbol{\xi}}(\mathbf{r}) = \iiint K(\mathbf{r} - \mathbf{r}') \boldsymbol{\xi}(\mathbf{r}') \, \mathrm{d}^3 \mathbf{r}'\,, \tag{6.30}$$

$$K(\mathbf{r}) = \frac{\mathrm{i}\omega}{4\pi \nu_m |\mathbf{r}|} \exp\left[-(1 - \mathrm{i}) \sqrt{\frac{\omega}{2\nu_m}} |\mathbf{r}| \right]. \tag{6.31}$$

Here we have assumed that $\boldsymbol{\xi}$ varies much more rapidly over space than $\mathbf{B}_0$, which itself varies on a scale much larger than $\sqrt{\nu_m/\omega}$. As far as the Lorentz force is concerned, the effect of dissipation is thus to replace $\boldsymbol{\xi}$ by $\bar{\boldsymbol{\xi}}$, which are related through

$$\boldsymbol{\xi} = \bar{\boldsymbol{\xi}} - \frac{\nu_m}{\mathrm{i}\omega} \nabla^2 \bar{\boldsymbol{\xi}}\,. \tag{6.32}$$

Substituting this into Equation (6.26) and neglecting products of ν and ν_m under the assumption that both are very small, we end up with the torsional component

$$\frac{\partial^2 \bar{\xi}_\phi}{\partial t^2} + \mathscr{L}_\mathrm{T}[\bar{\xi}_\phi] = \nu_\mathrm{tot} \nabla^2 \frac{\partial \bar{\xi}_\phi}{\partial t}\,, \tag{6.33}$$

where $\nu_\mathrm{tot} = \nu + \nu_m$ is the combined dissipation coefficient.

Next, we shall assume that the main avenue for dissipation lies in the development of fine-scale structure perpendicular rather than parallel to the flux surfaces. The justification for this and the discussion of

the physical process underlying it will be given in §6.4.3. For now, if we were to neglect spatial derivatives of the coordinates and define $\bar{\eta}_\phi \equiv \bar{\xi}_\phi / R$, Equation (6.33) can be written

$$\frac{\partial^2 \bar{\eta}_\phi}{\partial t^2} - \frac{1}{\rho_0 R^4}\frac{\partial^2 \bar{\eta}_\phi}{\partial \sigma^2} - \nu_{\rm tot}\frac{\partial^2}{\partial n^2}\frac{\partial \bar{\eta}_\phi}{\partial t} = F_\phi \,, \tag{6.34}$$

where n is the direction normal to the flux surfaces. We seek a solution to the coefficients b_j of the eigenfunction expansion

$$\bar{\eta}_\phi(t,\sigma,\psi) = \int \sum_j b_j(\omega,\psi) X_j(\sigma,\psi)\, {\rm e}^{-{\rm i}\omega t}\, {\rm d}\omega \,, \tag{6.35}$$

where

$$F_\phi(t,\sigma,\psi) = \int \sum_j a_j(\omega,\psi) X_j(\sigma,\psi)\, {\rm e}^{-{\rm i}\omega t}\, {\rm d}\omega \,. \tag{6.36}$$

Integrals taken over ω in (6.35) and (6.36) accommodate for the general case where the input excitation may be broadband in frequency. Noting that $\partial/\partial n = RB_{\rm p}\partial/\partial\psi$, we obtain

$$\left[\omega_{0,j}^2 - \omega^2\right] b_j(\omega,\psi) + {\rm i}\nu_{\rm tot}\omega R^2 B_{\rm p}^2 \frac{\partial^2 b_j(\omega,\psi)}{\partial\psi^2} = a_j(\omega,\psi) \,. \tag{6.37}$$

Let us focus on a small region in ψ near a resonant surface ψ_0 whose j-th harmonic is of frequency $\omega_{0,j}(\psi_0) = \omega$. Locally, we have the Taylor expansion

$$\omega_{0,j}^2(\psi) \approx \omega^2 + 2\omega\omega'_{0,j}(\psi_0)[\psi - \psi_0] \,, \tag{6.38}$$

where prime denotes a derivative. Consider next the change of variable

$$x = C[\psi - \psi_0]$$

with

$$C = \left(\frac{2\omega'_{0,j}(\psi_0)}{R^2 B_{\rm p}^2}\right)^{1/3} \,,$$

which turns (6.37) into

$$b_j x + {\rm i}\nu_{\rm tot}\frac{\partial^2 b_j}{\partial x^2} = \frac{C a_j(\omega,\psi_0)}{2\omega\omega'_{0,j}(\psi_0)} \,. \tag{6.39}$$

The RHS of (6.39), which we will denote by A, can be regarded as being roughly a constant for given ω, j and ψ_0. Taking the spatial Fourier transform of each variable, so that

$$x \to k \quad \text{and} \quad b_j(\omega,x) \to \tilde{b}_j(\omega,k) \,, \tag{6.40}$$

this becomes

$$\frac{\partial \tilde{b}_j}{\partial k} + k^2\nu_{\rm tot}\tilde{b}_j = {\rm i}A\delta(k) \,. \tag{6.41}$$

With the appropriate integrating factor, we solve this to obtain

$$\tilde{b}_j(\omega,k) = \begin{cases} 0 & k > 0 \\ {\rm i}A\exp[k^3\nu_{\rm tot}/3] & k < 0 \,. \end{cases} \tag{6.42}$$

In the limit where $\nu_{\rm tot} \to 0$, $\tilde{b}_j / {\rm i}A$ tends to $1 - H(k)$, where

$$H(k) = \begin{cases} 1 & k > 0 \\ 0 & k < 0 \end{cases}$$

is the Heaviside step function. This satisfies

$$\mathrm{i}\mathscr{F}[1-H(k)] = \mathscr{P}[1/x] + \mathrm{i}\pi\delta(x) = \frac{1}{x-\mathrm{i}0}\,. \tag{6.43}$$

Here $\mathscr{F}$ denotes a Fourier transform, $\mathscr{P}$ denotes the Cauchy principle value, and i0 is an infinitesimal imaginary component that we identify with the damping contribution $\mathrm{i}\Gamma\omega$ (cf. the Landau prescription from plasma physics). Here Γ is the (small) local damping rate. The final solution for b_j is then

$$b_j(\omega,\psi) = \mathrm{i}A\mathscr{F}[1-H(k)] = \frac{a_j(\omega,\psi_0)}{\omega_{0,j}^2(\psi)-\omega^2-\mathrm{i}\Gamma\omega}\,. \tag{6.44}$$

Since the RHS of Equation (6.39) is approximately constant, we infer the characteristic scale to be $x \sim \nu_{\mathrm{tot}}^{1/3}$. The local damping rate can be estimated from the first-order term of the Taylor expansion of $\omega_{0,j}^2(\psi)$, and has the approximate expression

$$\Gamma \sim \left[2\omega_{0,j}'(\psi_0)RB_{\mathrm{p}}\right]^{2/3}\nu_{\mathrm{tot}}^{1/3}\,. \tag{6.45}$$

6.4.3 Phase mixing

We can see from Figure 6.10 that a broadband spheroidal forcing (e.g. from turbulent convection) about $\omega \approx 10$ will excite torsional modes of $j \sim 100$, for which the variation in $\omega_{0,j}$ over the core region is ~10 units. The scales of variation along flux surfaces are given roughly by the oscillatory scale of the spheroidal modes (cf. Figure 6.9). This is $\sim 10^{-5}$, which is about 1% the radius of the core. The associated $\omega_{0,j}$ variation over that length scale would then be ~0.1. We should expect those surfaces to decorrelate on a timescale corresponding to the inverse of their frequency difference, i.e. 10 dynamical times (~3 days for the red giant model), implying that structure perpendicular to the flux surfaces should develop extremely rapidly compared to the lifetime of the star. Note that the time scale of dissipation at that length scale is $\sim 10^6$ dynamical times (assuming $\nu_{\mathrm{tot}} \sim 10^{-16}$), much longer than the decorrelation time, and so this *phase mixing* process is expected to continue onto much finer scales before its development is halted by viscous/resistive effects. The shrinkage of scales due to decorrelation and eventually leading to dissipation has been previously studied in the context of Alfvén wave propagation and damping in the solar atmosphere (Heyvaerts & Priest, 1983).

Up to a factor of order unity, Γ given by the expression (6.45) turns out to be the inverse of the time scale required for decorrelation to occur over the width of the resonant layer. Further inspection reveals that this width is precisely that for which the time scales of decorrelation and dissipation are equal, providing the physical interpretation for the associated loss process as being closely linked to phase mixing. Given the small magnetic Prandtl numbers in stellar interiors, ν_{tot} is dominated by the Ohmic dissipation coefficient $\nu_m \approx 10^9 T^{-3/2}\,\mathrm{m^2\,s^{-1}}$ (Spitzer, 1962). For our model ($T \sim 10^7$ K), we find that $\Gamma \sim 10^{-3}$ inverse dynamical times, and that the widths of the resonant layers are $\sim 10^{-7} R_*$.

6.4.4 Damping rates

We now seek to estimate the overall damping rate γ of spheroidal modes due to the resonant coupling with torsional modes. The total rate of work done by the torsional component of the Lorentz force associated

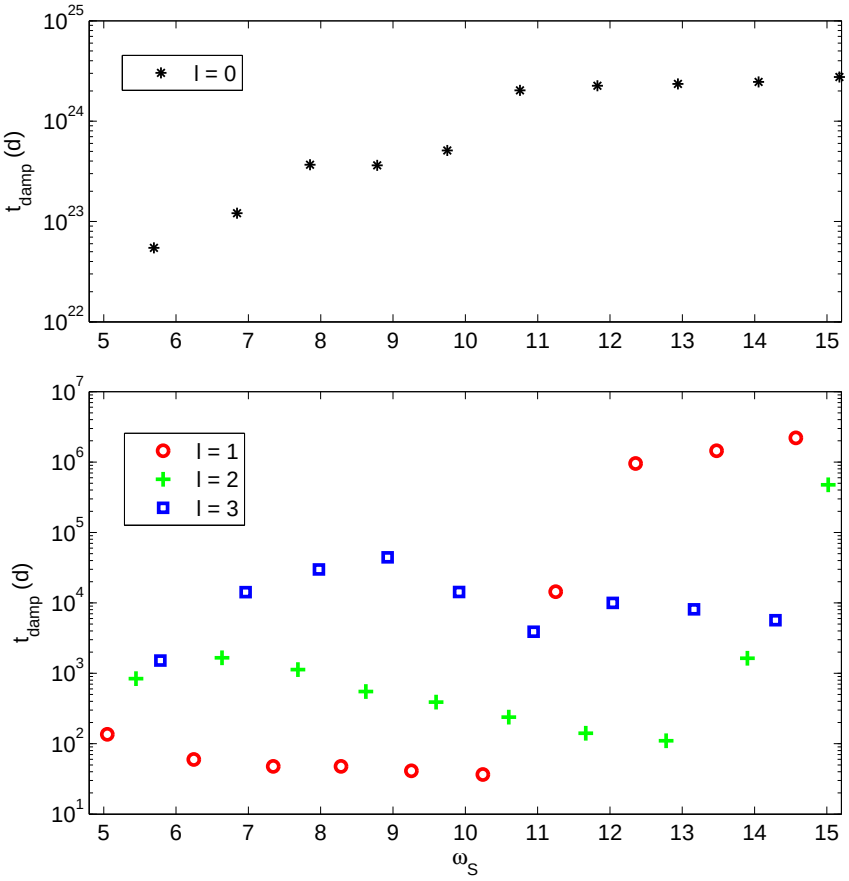

Figure 6.11: Damping times for the most p-dominated modes of the four lowest degrees. Radial modes are shown on a separate plot (top) since their damping times differ greatly from the non-radial modes (bottom). For non-radial modes, at frequencies below a certain threshold (here $\omega \approx 11$), one sees that lower degrees experience stronger damping. Note the logarithmic scale on the vertical axis. The unit of ω_S is the dynamical frequency, while t_{damp} is expressed in days.

with spheroidal motions is

$$\frac{\mathrm{d}E}{\mathrm{d}t} = \iiint \left(f_{\mathrm{TS}} \frac{\partial \xi_\phi^*}{\partial t} + f_{\mathrm{TS}}^* \frac{\partial \xi_\phi}{\partial t} \right) \mathrm{d}^3\mathbf{r}$$
$$= 4\pi \mathrm{Re} \left[\iint \rho_0 R^4 F_\phi \frac{\partial \eta_\phi^*}{\partial t} \,\mathrm{d}\sigma \,\mathrm{d}\psi \right] . \tag{6.46}$$

Adopting the eigenfunction expansions (6.35) and (6.36), invoking the orthonormality relation (6.23), substituting the result (6.44) and averaging over one oscillation period, we obtain the average rate of work

$$\left\langle \frac{\mathrm{d}E}{\mathrm{d}t} \right\rangle = 4\pi \iint \sum_j |a_j(\omega,\psi)|^2 \frac{\Gamma\omega^2}{\left[\omega_{0,j}^2(\psi) - \omega^2\right]^2 + \Gamma^2\omega^2} \,\mathrm{d}\psi \,\mathrm{d}\omega$$
$$\approx 4\pi \int \sum_j \left|a_j(\omega,\psi_0)\right|^2 \int \frac{\Gamma}{h(\psi)+\Gamma^2} \,\mathrm{d}\psi \,\mathrm{d}\omega \,, \tag{6.47}$$

assuming that a_j varies slowly over the width of the resonant region and can be evaluated at the resonant surface $\psi = \psi_0$ where $\omega_0(\psi_0) = \omega$. If the resonant region is spatially narrow, which is true in the limit of small Γ, we can approximate

$$h(\psi) \equiv \left(\frac{\omega_{0,j}^2(\psi)}{\omega} - \omega \right)^2 \tag{6.48}$$

by its Taylor expansion about ψ_0:

$$h(\psi) \approx 4 \left(\frac{\mathrm{d}\omega_{0,j}}{\mathrm{d}\psi}\bigg|_{\psi_0} \right)^2 (\psi - \psi_0)^2 . \tag{6.49}$$

In this limit, one can show that the ψ-integral in (6.47) evaluates to

$$\int \frac{\Gamma}{h(\psi)+\Gamma^2} \,\mathrm{d}\psi = \frac{\pi}{2} \left(\left| \frac{\mathrm{d}\omega_{0,j}}{\mathrm{d}\psi}\bigg|_{\psi_0} \right| \right)^{-1} , \tag{6.50}$$

which turns out to be independent of Γ. We arrive at the final expression

$$\left\langle \frac{\mathrm{d}E}{\mathrm{d}t} \right\rangle = 2\pi^2 \int \sum_j |a_j(\omega,\psi_0)|^2 \left(\left| \frac{\mathrm{d}\omega_{0,j}}{\mathrm{d}\psi}\bigg|_{\psi_0} \right| \right)^{-1} \mathrm{d}\omega \,, \tag{6.51}$$

which we see is independent of the local damping coefficient Γ. This reflects a basic property of driven-damped oscillators that near a resonance, in the limit of weak dissipation (regardless of what this may be or how it physically arises), the system always adjusts itself so that the rate of driving and dissipation are in balance. The global damping rate of a spheroidal mode is then $\gamma = \langle \mathrm{d}E/\mathrm{d}t \rangle / E$, where E is the total energy in the mode. With this normalised to $E = 1$, we have γ given directly by Equation (6.51).

The summation in (6.51) for any given spheroidal mode having frequency ω is over all torsional modes (indexed by j) whose frequencies equal this. Our approach to evaluating this was to scan over the 1000 × 1000 torsional modes computed and saved for the ones whose $\omega_{0,j}$ lay closest to the target frequency. If the difference fell below a certain threshold (taken to be 0.1 frequency units), this was classed as a resonance and the contribution of the mode was added to the sum. The typical ω spacing between the torsional modes in our set was ~0.01 frequency units, so variations about the threshold of 0.1 units affected the results very little. The purpose of the threshold was to restrict the j range of modes resonant at a given ω to be as close to the true range as possible, without losing modes comfortably within the true range. A further point to be made is that every j value was scanned independently, which restricts the resulting set of modes to one per j but not one per flux surface. At the low resolution of the grid (1000 flux surfaces) compared to the j range

of the spectrum (of the order of this value, as can be seen from Figure 6.10), there are instances where a flux surface contributes more than one mode to the sum. Though not strictly realistic, it is inevitable with this dicretised approach that the true resonant surface for given j is approximated by one close by, and this may be shared between more than one j. Given the slow variation in the structure of the torsional modes with space, however, this is unlikely to give rise to systematic errors. Our quantitative results are impacted more heavily by the fact that only a finite number of modes were generated, since this excludes some number of potentially resonant modes (implications are discussed further in the next section).

Figure 6.11 plots the damping times $t_{\rm damp} \equiv \gamma^{-1}$ calculated for the p-dominated modes of the red giant model. The field strength is scaled such that the central value is 4 MG, in line with expectations from simulations of main-sequence core dynamos (Brun et al., 2005) and magnetic flux conservation during core contraction into the red giant stage. We find that damping times for the $\ell = 0$ modes are typically in excess of 10^{23} days, many orders of magnitude longer than for the $\ell > 0$ modes, which are damped on time scales of months through this mechanism. A distinguishing feature between radial and non-radial modes, which is likely to explain this, is the structure of the spatial amplitude function within the core. For radial modes, spatial oscillations occur only near the surface; near the core, the amplitude function follows a very smooth exponential decay. This results in very tiny a_j values for the torsional modes (which are localised to the core) having frequencies near $\omega = 10$. In contrast, the spatial amplitude functions of non-radial modes near $\omega = 10$ have hundreds of finely spaced oscillations within the core, and so are able to strongly overlap with torsional modes having j values of several hundred. At the field strengths expected for red giant cores, it turns out that the eigenfrequencies associated with torsional modes having $j \sim 100$ lie in the vicinity of $\omega = 10$, making resonances between spheroidal and torsional modes possible. (For $\rho \sim 10^5\,{\rm g\,cm^{-3}}$, $B \sim 1$ MG and $R_c \sim 10$ Mm, we have $v_A \sim 10\,{\rm m\,s^{-1}}$, implying a fundamental Alfvén frequency of ~1 μHz. Spheroidal modes in red giants are excited near ~100 μHz.)

For the three non-radial degrees examined, we find systematic differences in the characteristic damping times, these differing by roughly an order of magnitude between adjacent ℓ. The physical reason for the dependence of damping rates on ℓ is likely to be the variation in the strength of coupling between the p- and g-mode cavities, which determines the extent of mode mixing. Recall that this can be quantified through the mode inertia, introduced in Equations (5.1) and (5.2). For a mode of given ℓ, and adopting a non-dimensionalisation scheme that sets $M_* = 1$, the mode inertia is given by

$$M_\ell = \frac{\int \rho_0 r^2 \left[\xi_r^2(r) + \ell(\ell+1)\xi_{\rm h}^2(r)\right] {\rm d}r}{\xi_r^2(R_*) + \ell(\ell+1)\xi_{\rm h}^2(R_*)}\,. \tag{6.52}$$

The plot of M_ℓ versus mode frequency is shown in Figure 6.12. It exhibits periodic modulations once per radial order (one unit of ω), where the modes having minimum M_ℓ are the most p-dominated ones. Observations favour the detection of p-dominated modes because these give rise to larger fluid motions at the surface, and so we selectively consider these modes here. These are marked with asterisks in Figure 6.12. One can see that the $\ell = 1$ p-dominated modes (red asterisks) have the largest inertia and thus the most g-like character compared to other ℓ. The larger core fluid displacements associated with the p-dominated $\ell = 1$ modes enhances their rate of damping due to interactions with the torsional Alfvén modes, compared with the p-dominated modes of higher ℓ (green and blue asterisks).

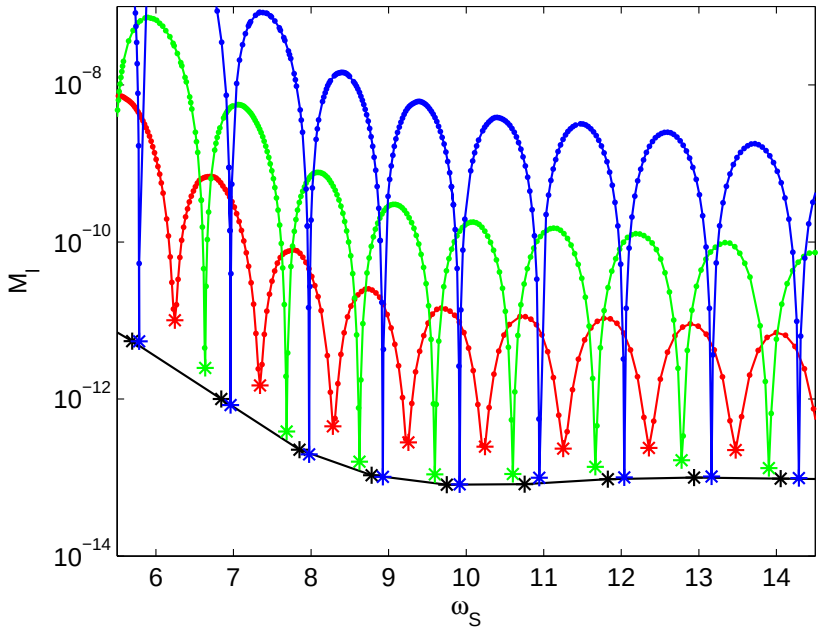

Figure 6.12: Mode inertia as a function of frequency for the spheroidal modes of the red giant model. Black, red, green and blue correspond to $\ell = 0$, 1, 2 and 3, respectively. Though the spectrum is discrete, individual points (one for each mode) have been joined by straight lines to aid visualisation of the pattern. Asterisks mark the most p-dominated modes, identified as local minima in the red, green and blue curves. These are the ones for which damping times have been computed and plotted in Figure 6.11.

6.4.5 Comparison with observations

Mode visibilities v_ℓ, which measure the area under the peaks associated with a given ℓ, are usually expressed in a form where they are normalised with respect to some other quantity. If this is with respect to the area under $\ell = 0$ peaks, then, for example, $v_1 \approx 1.54$ (Ballot et al., 2011). In the context of the dipole dichotomy problem, following Mosser et al. (2017a), it is more convenient to normalise with respect to the area under the $\ell = 1$ peaks of "normal" stars. Normal stars thus have $v_1 \approx 1$. For a fixed rate of excitation, the visibility of a mode decreases proportionally with the overall damping rate, and so the latter definition of v_1 allows it to be expressed in terms of the envelope- and core-associated damping rates γ_e and γ as

$$v_1 = \frac{\gamma_e}{\gamma_e + \gamma} = \frac{t_{\text{damp}}}{t_e + t_{\text{damp}}}, \tag{6.53}$$

where $t_e \equiv \gamma_e^{-1}$. In practice, t_e can be measured from the linewidths of the radial modes and is characteristically 15 ± 5 days Mosser et al. (see 2017a, figure 3b).

As can be seen from figure 3a of Mosser et al. (2017a), the depressed stars have v_1 values close to 0.1 for stars with $\Delta\nu$ near 12 μHz, and v_1 values around 0.7 for stars with $\Delta\nu$ near 4 μHz, with some scatter about this trend. Let us take t_e to be 15 days. From Figure 6.11, it appears that t_{damp} lies between 30 and 50 days for $\ell = 1$, producing v_1 values in the range of 0.67–0.77. Increasing the field strength increases the damping and lowers the visibilities: at triple the field strength, t_{damp} values are roughly nine-fold lower, producing v_1 in the range of 0.18–0.27. For $\ell = 2$, t_{damp} values are about an order of magnitude greater, placing v_2 at around 0.93–0.97. At triple the field strength, these decrease to 0.60–0.88. Damping times for $\ell = 3$ are an order of magnitude larger still, giving v_3 of 0.98–0.99. Hence the ℓ-dependence of the mode depression observed experimentally (Stello et al., 2016c) is reproduced by this mechanism.

6.4.6 Limitations

An important assumption underlying the results in this chapter is that the structure of the spheroidal modes is unaffected by the magnetic field. Clearly if they were to be modified significantly in the region of the core, then this would impact our quantitative results. We stress that our mechanism, as presented, is designed to operate only in the weak-field regime where this assumption holds. The works of Fuller et al. (2015) and Lecoanet et al. (2017) have suggested that drastic alteration to spheroidal mode structure is to be expected if the field exceeds a critical strength, and so we expect that if that were the case, this mechanism would break down, or require modification. Its success over previous ideas is that it does not need to disrupt the structure of the modes in any part of the star. This would allow for the existence of the depressed mixed modes reported by Mosser et al. (2017a).

However, there are two dubious aspects to this mechanism. The first is that one would expect it to produce a range of depressed v_ℓ values for any given $\Delta\nu$, since the strength of the damping depends on the magnetic field strength. However, the data show a relatively tight correlation between v_1 and $\Delta\nu$ for the depressed stars, which would seemingly require all stars of the same $\Delta\nu$ to have the same core field strength. It would be unrealistic to expect such fine tuning; the actual mechanism therefore needs to be largely independent of the field strength in the regime where it operates. The second point is that the efficiency of the coupling relies on overlap integrals being large, which is equivalent to saying that there needs to be a spatial resonance between the spheroidal and torsional modes (comparable scales of variation). This turns out to

coincide (within a factor of order unity) with the expression for the critical field strength proposed by Fuller et al. (2015). The fact that the efficiency of this damping mechanism should maximise precisely around the regime where the assumptions behind it break down suggests that this demands further investigation. This is undertaken in Part III of this thesis, which presents an improved mechanism for explaining the dipole dichotomy that is free of the above shortcomings.

Chapter 7

Non-Perturbative Treatment of Rotation

Earlier in §4.3, we described how the effects of slow rotation could be incorporated by viewing this as a perturbation to the modes that would be present without rotation. The quantities returned are the frequency shifts/distortions away from the reference mode. In this chapter, we will discuss a different approach to incorporating rotation that does not view its effect as a perturbation to some reference, but rather where the rotationally-affected modes are computed from scratch. It is known that rotation couples together modes of different ℓ, but this coupling may be neglected in the limit of slow rotation, giving rise to a set of ODEs for each ℓ and m very similar to the standard equations of stellar oscillation. Since rotation lifts the degeneracy of different m-values for each ℓ, the resulting oscillation equations (for which r is the sole independent variable) depend on both m and ℓ, rather than just ℓ. It can be shown that the predicted frequency shift matches that obtained via perturbation theory in the limit of weak rotation. However, the results from this approach extend to the regime where frequency shifts may become comparable to the separation between adjacent modes, a case where non-degenerate perturbation theory breaks down (although degenerate perturbation theory can still be applied). The material in this short chapter has been included as a prelude to its extension to the case of magnetism, which will be presented in Chapter 12.

7.1 Equations

7.1.1 Case of shellular rotation

Let us start by considering shellular rotation, i.e. a rotation frequency profile $\Omega = \Omega(r)$ that depends only on the radial coordinate, r. As before, we shall let $\bar{\omega} = \omega + m\Omega$ be the frequency in the rotating frame. The continuity equation, adiabatic equation of state and momentum equation are (in the Cowling approximation)

$$\rho' = -\boldsymbol{\xi}\cdot\nabla\rho - \rho\nabla\cdot\boldsymbol{\xi}\,, \tag{7.1}$$

$$p' + \boldsymbol{\xi}\cdot\nabla p = \frac{\gamma p}{\rho}(\rho' + \boldsymbol{\xi}\cdot\nabla\rho)\,, \tag{7.2}$$

$$-\bar{\omega}^2\boldsymbol{\xi} + 2\mathrm{i}\bar{\omega}\Omega\hat{\mathbf{k}}\times\boldsymbol{\xi} = -\frac{\nabla p'}{\rho} + \frac{\rho'}{\rho^2}\nabla p\,. \tag{7.3}$$

Next, we shall express $\boldsymbol{\xi} = (\xi_r, \xi_\theta, \xi_\phi)$ in terms of the spheroidal and torsional stream functions S and Θ, and the radial amplitude X:

$$\xi_r = X\,, \tag{7.4}$$

$$\xi_\theta = \frac{1}{r\sin\theta}\frac{\partial\Theta}{\partial\phi} + \frac{1}{r}\frac{\partial S}{\partial\theta}\,, \tag{7.5}$$

$$\xi_\phi = -\frac{1}{r}\frac{\partial\Theta}{\partial\theta} + \frac{1}{r\sin\theta}\frac{\partial S}{\partial\phi}\,. \tag{7.6}$$

Separate equations of motion for each of the three functions (S, Θ, X) can be isolated by taking linear combinations of the components of the momentum equation. Considering the r-component of the curl gives us the one for Θ:

$$\bar{\omega}^2\nabla_\perp^2\Theta = 2\,\mathrm{i}\bar{\omega}\Omega\left[\frac{\partial\Theta}{\partial\phi} + \sin\theta\frac{\partial S}{\partial\theta} - \cos\theta\nabla_\perp^2 S - \frac{r}{\sin\theta}\frac{\partial}{\partial\theta}(X\sin^2\theta)\right], \tag{7.7}$$

where

$$\nabla_\perp^2 \equiv \frac{1}{\sin\theta}\frac{\partial}{\partial\theta}\left(\sin\theta\frac{\partial}{\partial\theta}\right) + \frac{1}{\sin^2\theta}\frac{\partial^2}{\partial\phi^2}\,. \tag{7.8}$$

Taking the horizontal divergence yields that for S:

$$\bar{\omega}^2\nabla_\perp^2 S = 2\,\mathrm{i}\bar{\omega}\Omega\left[\cos\theta\nabla_\perp^2\Theta + \frac{\partial S}{\partial\phi} - \sin\theta\frac{\partial\Theta}{\partial\theta} + r\frac{\partial X}{\partial\phi}\right] + \frac{1}{\rho}\nabla_\perp^2 p'\,. \tag{7.9}$$

The r-component gives the one for X:

$$-\bar{\omega}^2 X = \frac{2\,\mathrm{i}\bar{\omega}\Omega}{r}\left(\frac{\partial S}{\partial\phi} - \sin\theta\frac{\partial\Theta}{\partial\theta}\right) - \frac{1}{\rho}\frac{\partial p'}{\partial r} + \frac{\rho'}{\rho^2}\frac{\partial p}{\partial r}\,. \tag{7.10}$$

7.1.2 General axisymmetric rotation law

In the more general case where $\Omega = \Omega(r,\theta)$, the radial component (7.10) remains the same, but the equations of motion for the remaining two components acquire the more complicated forms

$$\begin{aligned}\bar{\omega}^2\nabla_\perp^2\Theta + \frac{\partial\bar{\omega}^2}{\partial\theta}\left[\frac{\partial\Theta}{\partial\theta} - \frac{1}{\sin\theta}\frac{\partial S}{\partial\phi}\right] + 2\,\mathrm{i}\frac{\partial(\bar{\omega}\Omega)}{\partial\theta}\left[\frac{\cos\theta}{\sin\theta}\frac{\partial\Theta}{\partial\phi} + \cos\theta\frac{\partial S}{\partial\theta} + rX\sin\theta\right]\\ = 2\,\mathrm{i}\bar{\omega}\Omega\left[\frac{\partial\Theta}{\partial\phi} + \sin\theta\frac{\partial S}{\partial\theta} - \cos\theta\nabla_\perp^2 S - \frac{r}{\sin\theta}\frac{\partial}{\partial\theta}(X\sin^2\theta)\right],\end{aligned} \tag{7.11}$$

$$\begin{aligned}\bar{\omega}^2\nabla_\perp^2 S + \frac{\partial\bar{\omega}^2}{\partial\theta}\left[\frac{1}{\sin\theta}\frac{\partial\Theta}{\partial\phi} + \frac{\partial S}{\partial\theta}\right] + 2\,\mathrm{i}\frac{\partial(\bar{\omega}\Omega)}{\partial\theta}\cos\theta\left[\frac{1}{\sin\theta}\frac{\partial S}{\partial\phi} - \frac{\partial\Theta}{\partial\theta}\right]\\ = 2\,\mathrm{i}\bar{\omega}\Omega\left[\cos\theta\nabla_\perp^2\Theta + \frac{\partial S}{\partial\phi} - \sin\theta\frac{\partial\Theta}{\partial\theta} + r\frac{\partial X}{\partial\phi}\right] + \frac{1}{\rho}\nabla_\perp^2 p'\,.\end{aligned} \tag{7.12}$$

Notice that in the absence of rotation, the torsional equation of motion admits only trivial oscillation frequencies, since all terms with the exception of the first are proportional to powers of Ω. Furthermore, the only source terms involve spheroidal stream functions, implying that torsional amplitudes should be smaller by a factor of $\sim \Omega/\bar{\omega}$. The torsional terms in the spheroidal equation of motion are also proportional to powers of Ω, and so these terms would be smaller than the spheroidal terms by a factor of $\sim (\Omega/\bar{\omega})^2$. Thus in the limit of slow rotation ($\Omega \ll \bar{\omega}$), it comes justifiable to neglect the torsional terms altogether. This reduces the above to

$$\bar{\omega}^2\nabla_\perp^2 S + \frac{\partial\bar{\omega}^2}{\partial\theta}\frac{\partial S}{\partial\theta} + 2\,\mathrm{i}\frac{\partial(\bar{\omega}\Omega)}{\partial\theta}\frac{\cos\theta}{\sin\theta}\frac{\partial S}{\partial\phi} = 2\,\mathrm{i}\bar{\omega}\Omega\left[\frac{\partial S}{\partial\phi} + r\frac{\partial X}{\partial\phi}\right] + \frac{1}{\rho}\nabla_\perp^2 p' \tag{7.13}$$

$$\bar{\omega}^2 X = -\frac{2\,\mathrm{i}\bar{\omega}\Omega}{r}\frac{\partial S}{\partial\phi} + \frac{1}{\rho}\frac{\partial p'}{\partial r} - \frac{\rho'}{p^2}\frac{\partial p}{\partial r}\,. \tag{7.14}$$

7.2 Radial problem

With some further assumptions and simplifications, Equations (7.13 and (7.14) can be reduced to a system of ODEs in the radial coordinate. Adopting the spherical harmonic expansion

$$Q = \sum_{\ell=m}^{\infty} Q_\ell Y_\ell^m(\theta,\phi)\,, \quad Q \in \{S, X, p', \rho'\} \tag{7.15}$$

with the normalisation

$$\int_0^\pi Y_{\ell'}^{m*} Y_\ell^m \sin\theta \,\mathrm{d}\theta = \begin{cases} 1 & \text{if } \ell = \ell' \\ 0 & \text{if } \ell \neq \ell'\,, \end{cases} \tag{7.16}$$

Equations (7.13) and (7.14) become

$$\omega^2 S_\ell + 2m\sum_{\ell'} \frac{\ell'(\ell'+1)}{\ell(\ell+1)} D_{\ell,\ell'} S_{\ell'} + \sum_{\ell'} C_{\ell,\ell'} S_{\ell'} = \frac{2m}{\ell(\ell+1)} \sum_{\ell'} E_{\ell,\ell'}[S_{\ell'} + r X_{\ell'}] + \frac{p'_\ell}{\rho} \tag{7.17}$$

and

$$\omega^2 X_\ell + 2m\sum_{\ell'} X_{\ell'} D_{\ell,\ell'} = \frac{2m}{r}\sum_{\ell'} S_{\ell'} E_{\ell,\ell'} + \frac{1}{\rho}\frac{\partial p'_\ell}{\partial r} - \frac{\rho'_\ell}{\rho^2}\frac{\partial p}{\partial r}\,, \tag{7.18}$$

where

$$C_{\ell,\ell'} \equiv \frac{1}{\ell(\ell+1)} \int_0^\pi \left[2m \frac{\partial(\bar\omega\Omega)}{\partial\theta}\frac{\cos\theta}{\sin\theta} Y_{\ell'}^m - \frac{\partial\bar\omega^2}{\partial\theta}\frac{\partial Y_{\ell'}^m}{\partial\theta}\right] Y_\ell^{m*} \sin\theta\,\mathrm{d}\theta\,, \tag{7.19}$$

$$D_{\ell,\ell'} \equiv \frac{1}{2m}\int_0^\pi (\bar\omega^2 - \omega^2) Y_{\ell'}^m Y_\ell^{m*} \sin\theta\,\mathrm{d}\theta\,, \tag{7.20}$$

$$E_{\ell,\ell'} \equiv \int_0^\pi \bar\omega\Omega Y_{\ell'}^m Y_\ell^{m*} \sin\theta\,\mathrm{d}\theta\,. \tag{7.21}$$

Applying the same expansions to the continuity equation and adiabatic equation of state yield

$$\rho'_\ell = -\frac{\partial\rho}{\partial r} X_\ell - \frac{\rho}{r^2}\frac{\partial(r^2 X_\ell)}{\partial r} + \ell(\ell+1)\frac{\rho}{r^2} S_\ell \tag{7.22}$$

and

$$p'_\ell + X_\ell \frac{\partial p}{\partial r} = \frac{\gamma p}{\rho}\left(p'_\ell + X_\ell \frac{\partial\rho}{\partial r}\right). \tag{7.23}$$

Since

$$\rho'_\ell = p'_\ell \frac{\rho}{\gamma p} - \rho^2 \left(\frac{\partial p}{\partial r}\right)^{-1} N^2 X_\ell\,, \tag{7.24}$$

Equation (7.18) becomes

$$(\omega^2 - N^2) X_\ell + 2m\sum_{\ell'} X_{\ell'} D_{\ell,\ell'} = \frac{2m}{r}\sum_{\ell'} S_{\ell'} E_{\ell,\ell'} + \frac{p^{1/\gamma}}{\rho}\frac{\partial}{\partial r}\left(\frac{p'_\ell}{p^{1/\gamma}}\right), \tag{7.25}$$

while Equations (7.22) and (7.23) combine to give

$$p'_\ell - \ell(\ell+1)\frac{\gamma p}{r^2} S_\ell = -\frac{\gamma p^{1-1/\gamma}}{r^2}\frac{\partial(r^2 p^{1/\gamma} X_\ell)}{\partial r}\,. \tag{7.26}$$

Next, we shall eliminate S_ℓ in favour of X_ℓ by assuming that the couplings between different values of ℓ are negligible, so that the cross-terms in the summations can be neglected in favour of the diagonal terms. This is based on the argument that the coupling between different values of ℓ goes as $\Omega/\bar\omega \ll 1$, and the feedback into any given value of ℓ is second order in this. Throwing away cross-terms, Equation (7.17) can be rearranged into

$$S_\ell = \left(\frac{2mr}{\ell(\ell+1)} E_{\ell,\ell} X_\ell + \frac{p'_\ell}{\rho}\right)\left(\omega^2 + 2mD_{\ell,\ell} + C_{\ell,\ell} - \frac{2m}{\ell(\ell+1)} E_{\ell,\ell}\right)^{-1} \tag{7.27}$$

while (7.25) becomes

$$X_\ell \left[\omega^2 - N^2 + 2mD_{\ell,\ell} - \frac{4m^2 E_{\ell,\ell}^2}{\ell(\ell+1)} \left(\omega^2 + 2mD_{\ell,\ell} + C_{\ell,\ell} - \frac{2m}{\ell(\ell+1)} E_{\ell,\ell} \right)^{-1} \right]$$
$$= \frac{2mE_{\ell,\ell}}{r} \frac{p'_\ell}{\rho} \left(\omega^2 + 2mD_{\ell,\ell} + C_{\ell,\ell} - \frac{2m}{\ell(\ell+1)} E_{\ell,\ell} \right)^{-1} + \frac{p^{1/\gamma}}{\rho} \frac{\partial}{\partial r} \left(\frac{p'_\ell}{p^{1/\gamma}} \right). \tag{7.28}$$

Substituting (7.27) into (7.26), and defining

$$G_\ell(r) \equiv \left(\omega^2 + 2mD_{\ell,\ell} + C_{\ell,\ell} - \frac{2m}{\ell(\ell+1)} E_{\ell,\ell} \right)^{-1}, \tag{7.29}$$

we arrive at the pair of equations

$$X_\ell \left[\omega^2 - N^2 + 2mD_{\ell,\ell} - \frac{4m^2 E_{\ell,\ell}^2}{\ell(\ell+1)} G_\ell \right] = \frac{p^{1/\gamma}}{\rho F_\ell} \frac{\partial}{\partial r} \left(\frac{p'_\ell F_\ell}{p^{1/\gamma}} \right), \tag{7.30}$$

$$p'_\ell \left[1 - \ell(\ell+1) \frac{\gamma p}{r^2 \rho} G_\ell \right] = -\frac{\gamma p^{1-1/\gamma} F_\ell}{r^2} \frac{\partial}{\partial r} \left(\frac{r^2 p^{1/\gamma} X_\ell}{F_\ell} \right), \tag{7.31}$$

where $F_\ell(r)$ satisfies

$$\frac{1}{F_\ell} \frac{\mathrm{d}F_\ell}{\mathrm{d}r} \equiv \frac{2mE_{\ell,\ell}}{r} G_\ell. \tag{7.32}$$

7.3 Frequency shift

It is possible to obtain an approximate expression for the frequency shift associated with rotation under this formalism. Combining Equations (7.30) and (7.31), we get a second-order DE for X_ℓ:

$$X_\ell \left[\omega^2 - N^2 + 2mD_{\ell,\ell} - \frac{4m^2 E_{\ell,\ell}^2}{\ell(\ell+1)} G_\ell \right] = -\frac{p^{1/\gamma}}{\rho F_\ell} \frac{\partial}{\partial r} \left(\frac{\gamma p^{1-2/\gamma} F_\ell^2}{r^2} \left[1 - \ell(\ell+1) \frac{\gamma p}{r^2 \rho} G_\ell \right]^{-1} \frac{\partial}{\partial r} \left(\frac{r^2 p^{1/\gamma} X_\ell}{F_\ell} \right) \right). \tag{7.33}$$

For modes that are rapidly varying spatially compared to background quantities, Equation (7.33) can be cast in the form $\partial^2 X_\ell / \partial r^2 = k_r^2 X_\ell$, where

$$k_r^2 = \left[\omega^2 - N^2 + 2mD_{\ell,\ell} - \frac{4m^2 E_{\ell,\ell}^2}{\ell(\ell+1)} G_{\ell,\ell} \right] \left[1 - \ell(\ell+1) \frac{\gamma p}{r^2 \rho} G_{\ell,\ell} \right]. \tag{7.34}$$

For $\Omega \ll \omega$, we apply a binomial expansion to arrive at

$$G_{\ell,\ell} \approx \frac{1}{\omega^2} \left[1 - \frac{2mD_{\ell,\ell}}{\omega^2} - \frac{C_{\ell,\ell}}{\omega^2} + \frac{2mE_{\ell,\ell}}{\ell(\ell+1)\omega^2} \right], \tag{7.35}$$

since $C_{\ell,\ell}, D_{\ell,\ell}, E_{\ell,\ell} \sim \omega\Omega$. In addition, for the particular case of gravity modes in the deep interior, if we assume the regime where $\omega^2 \ll N^2$ and $c_s^2 = \gamma p/\rho \to \infty$, then we need only focus on the product of dominant terms in each factor, and the quantisation condition $\int k_r(r)\,\mathrm{d}r = (n+1/2)\pi$ becomes

$$\frac{\sqrt{\ell(\ell+1)}}{\omega} \int_{r_1}^{r_2} \frac{N}{r} \left(1 - \frac{1}{2\omega^2} \left[2mD_{\ell,\ell} + C_{\ell,\ell} - \frac{2mE_{\ell,\ell}}{\ell(\ell+1)} \right] \right) \mathrm{d}r = \left(n + \frac{1}{2} \right) \pi. \tag{7.36}$$

Writing $\omega = \omega_0 + \omega_1$, where $\omega_1 \ll \omega_0$ and

$$\omega_0 = \frac{\sqrt{\ell(\ell+1)}}{\left(n+\frac{1}{2}\right)\pi} \int_{r_1}^{r_2} \frac{N}{r}\,\mathrm{d}r \tag{7.37}$$

is the mode frequency in the absence of rotation, the frequency shift is then given by

$$\omega_1 \approx -\frac{\sqrt{\ell(\ell+1)}}{2\omega_0^2\left(n+\frac{1}{2}\right)\pi}\int_{r_1}^{r_2}\frac{N}{r}\left[2mD_{\ell,\ell}+C_{\ell,\ell}-\frac{2mE_{\ell,\ell}}{\ell(\ell+1)}\right]\mathrm{d}r\,. \tag{7.38}$$

See that $\omega_1 = 0$ when $m = 0$, since $C_{\ell,\ell} \propto m$. When Ω has no latitudinal dependence, we find that the expression for the frequency shift simplifies to

$$\omega_1 = -m\Omega\left(1-\frac{1}{\ell(\ell+1)}\right), \tag{7.39}$$

a result known from perturbation theory for the rotational frequency splitting of g-modes (e.g. Ballot et al., 2013).

7.4 Numerical results

Equations (7.30) and (7.31) are a pair of first-order ODEs which can be solved as a boundary eigenvalue problem in a manner identical to the usual equations of stellar oscillation. This yields a spectrum of solutions for each ℓ and m, with individual modes differing only in the radial order. Some results are shown in Figures 7.1 and 7.2, for a simple but arbitrary rotation law

$$\Omega(r,\theta) = 10^{-3}(2-r)(1-\cos\theta)\,, \tag{7.40}$$

computed for an $n = 3$ polytrope. A good agreement is seen between the computed frequencies and those predicted by the analytic expression given in Equation (7.39).

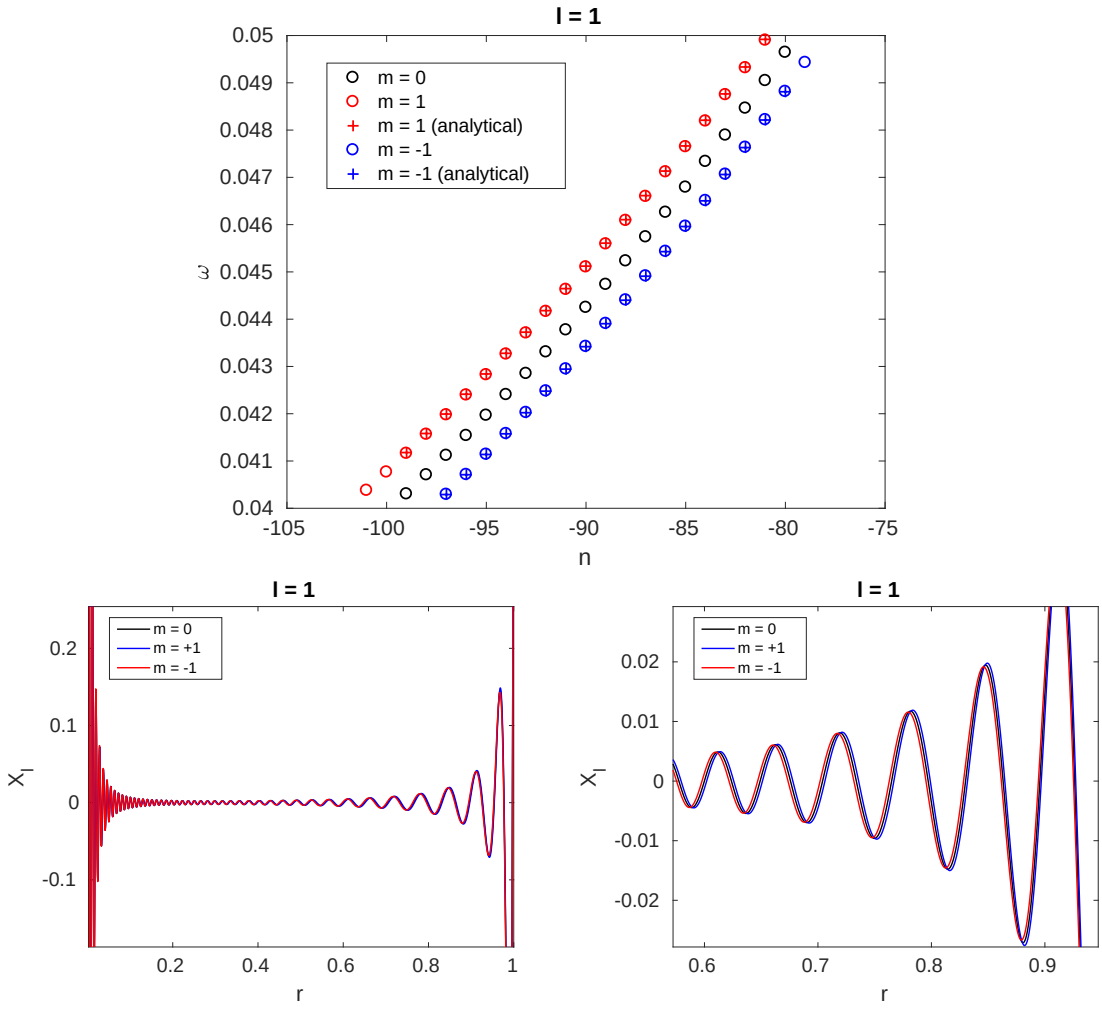

Figure 7.1: Results for a selection of modes computed by solving Equations (7.30) and (7.31), under the rotation law given in Equation (7.40), for $\ell = 1$. The underlying stellar model is an $n = 3$ polytrope. Top: mode frequencies for different azimuthal orders, overlaid with the analytical prediction given by (7.39). Bottom: eigenfunctions for the mode with $n = -90$, $\omega_0 = 0.045$ (a close-up is shown on the right), showing the slight differences between the different m. Frequencies are expressed in units of $\sqrt{GM_*/R_*^3}$.

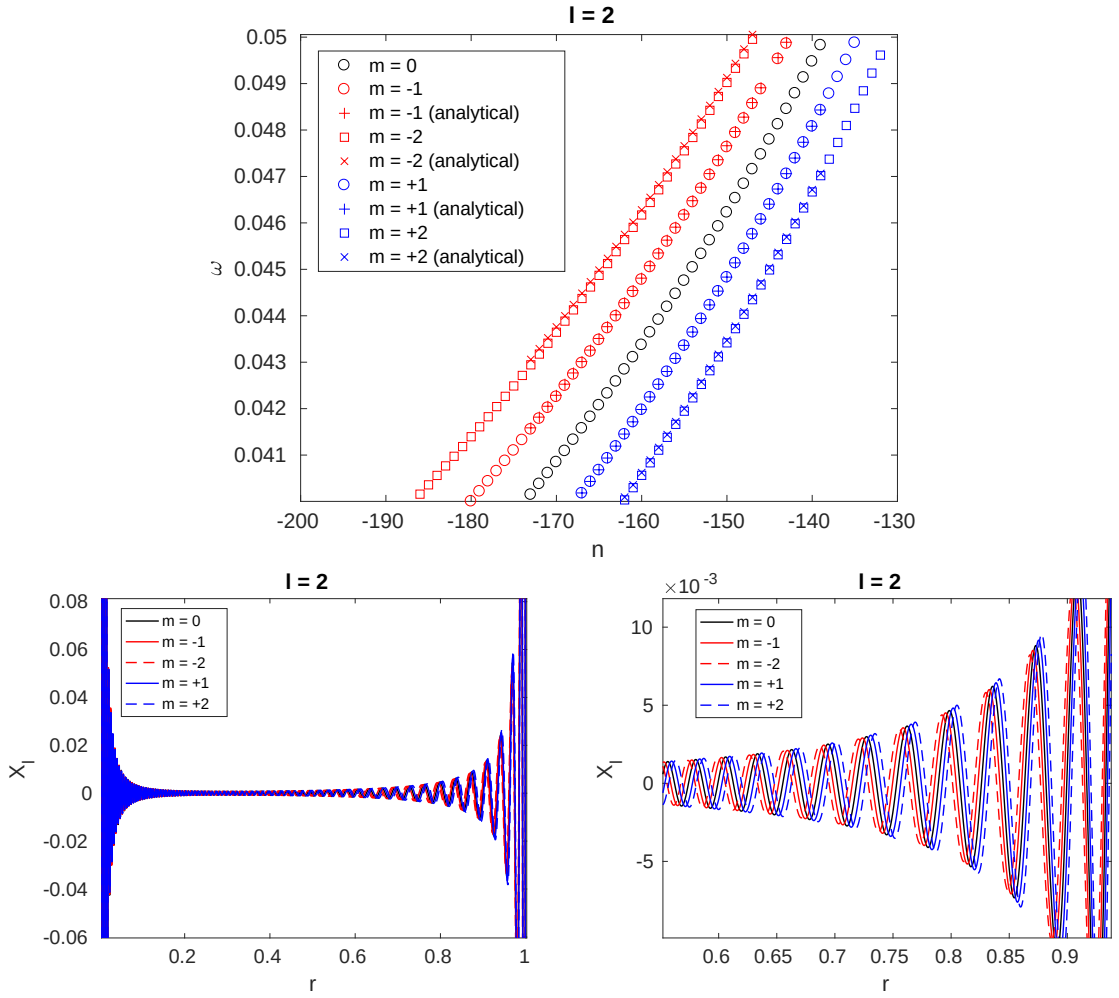

Figure 7.2: As for Figure 7.1, but with $\ell = 2$. The bottom panels are for the mode with $n = -160$, $\omega_0 = 0.0434$.

Chapter 8

Asymptotic Theory of Mixed Modes

This chapter presents preliminary work on the formulation of an analytic expression for the frequencies of p-g mixed modes in red giants. The existence of these modes was first predicted in numerical studies by Osaki (1975) and Aizenman et al. (1977), which were then followed up in analytical work by Shibahashi (1979) and Tassoul (1980). These analytical studies made use of the Cowling approximation and the assumption of a thick evanescent region separating the two cavities. The recent work of Takata (2016a,b) extended the treatment to the case of a thin evanescent zone (strong coupling) and removing the Cowling approximation, but did all this for the special case of dipole modes. Besides these papers, most other work on mixed modes has been numerical rather than analytical. However, analytical formulations of mixed mode behaviour have pertinent application to studying various aspects of red giant structure, for example, measuring the properties of the evanescent region (Mosser et al., 2012b, 2017b; Hekker et al., 2018).

We focus here on low spherical degrees (not restricted to dipole modes), and the case of strong coupling between p-mode and g-mode cavities. The derivation here neglects rotation and magnetic fields, but at the end we discuss how the results can be generalised to the inclusion of a weak magnetic field confined to the radiative region. The material in this chapter does not bear any direct relevance to the dipole dichotomy problem, but represents a side exploration of how the effects of magnetic fields on red giant oscillations may be treated.

8.1 Simplified model of a red giant

The procedure adopted here involves dividing the interior into a number of regions/layers, labelled 'C', 'G', 'E', 'L', 'U' and 'S', as shown in Figure 8.1. Regions C and G constitute the stably stratified, radiative core, while L, U and S form the convective surface layers. The core and envelope are separated by an intermediate layer, E, corresponding to the evanescent zone. In regions C and G, the sound speed c_s will be taken to be infinite. In regions L, U and S, it will be assumed that $N^2 = 0$. The g-mode cavity, labelled G, lies between $r_i < r < r_e$, which is where $\omega^2 < N^2$. The p-mode cavity is not tied to a particular label, since its radial extent varies depending on the degree ℓ. Instead, the coordinate r_0 is used to mark the base of the convective envelope, where N^2 drops to zero and one expects convection to begin. Regions L and U (the lower and upper envelopes) are distinguished by the assumed existence of a power-law dependence of p and ρ on radius in region L. S is a thin layer at the surface where the ratio p/ρ tends to zero linearly with radius. These assumptions allow for analytic solutions in each of the regions to be found (with the exception of region E,

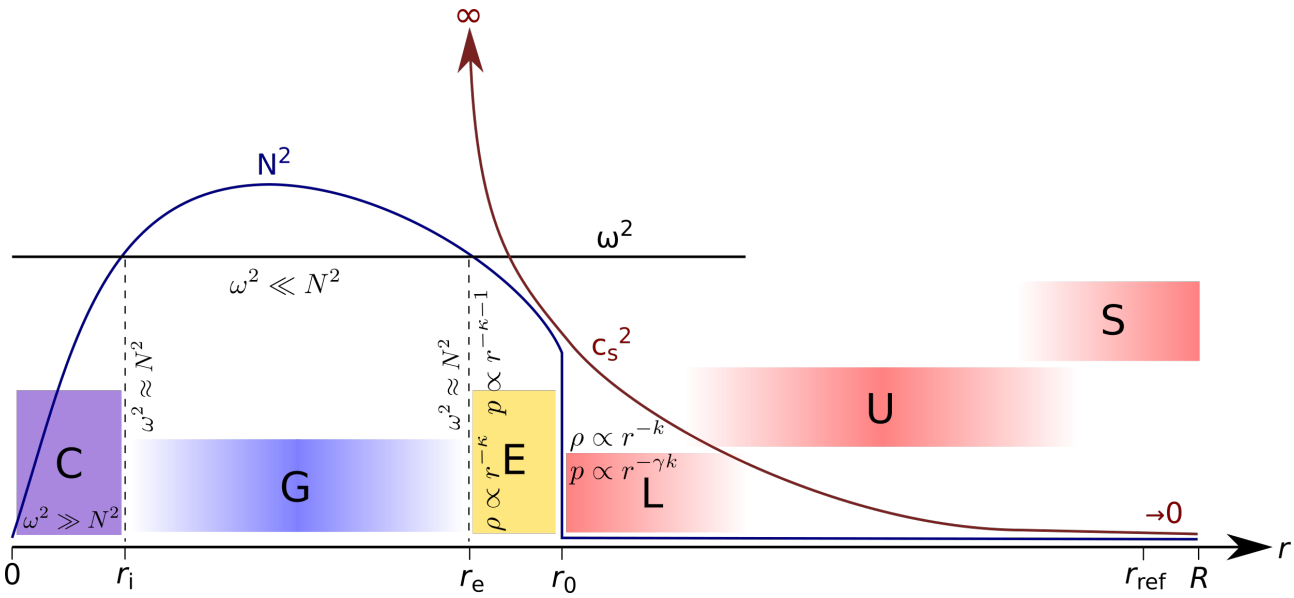

Figure 8.1: Schematic diagram (not to scale) of the regions considered: the central region "C", defined to be where $\omega > N$; the g-mode cavity "G" where $\omega < N$; the region "E" between the p-mode and g-mode cavities (roughly) where waves are evanescent; the lower and upper regions of the convective envelope "L" and "U", where L is characterised by ρ and p obeying power laws; and the surface layer "S", where p/ρ is assumed to taper linearly with r. In the convective envelope (regions L, U and S) it is assumed that $N^2 = 0$.

discussed separately in §8.4). A series of matching conditions are then derived that stitch the solution from one region to the other.

8.2 Solution in envelope

The starting equations, for purely hydrodynamic stellar oscillations, in terms of the radial fluid displacement X and pressure perturbation p' are

$$X(\omega^2 - N^2) = \frac{p^{1/\gamma}}{\rho}\frac{\partial}{\partial r}\left(\frac{p'}{p^{1/\gamma}}\right) \tag{8.1}$$

$$p'\left[1 - \frac{\gamma p}{\rho}\frac{\ell(\ell+1)}{r^2\omega^2}\right] = -\frac{\gamma p^{1-1/\gamma}}{r^2}\frac{\partial}{\partial r}\left(r^2 p^{1/\gamma} X\right). \tag{8.2}$$

Let us begin by treating the region L, in which we assume that ρ and p are given by the forms

$$\rho = \rho_0\left(\frac{r}{r_0}\right)^{-k}, \quad p = p_0\left(\frac{r}{r_0}\right)^{-\gamma k} \tag{8.3}$$

for some index k. Here r_0 is a reference radius, taken to be the lowest point of L (base of the convective envelope). Within L, $N^2 = 0$, and so Equation (8.1) becomes

$$\omega^2 X = \frac{\partial}{\partial r}\left(\frac{p'}{\rho}\right), \tag{8.4}$$

where we have invoked the adiabatic condition to take $p^{1/\gamma}/\rho = $ const. out of the derivative. Defining $\mathcal{W} \equiv p'/\rho$ and a new distance coordinate $x \equiv r/r_0$, this becomes

$$r_0\omega^2 X = \frac{\partial \mathcal{W}}{\partial x}. \tag{8.5}$$

The second of the starting pair, Equation (8.2), can be written

$$\mathscr{W}\left[\frac{\rho_0\omega^2 r_0^2}{\gamma p_0 \ell(\ell+1)}x^{2+(\gamma-1)k}-1\right]=-\frac{\omega^2 r_0}{\ell(\ell+1)}x^k\frac{\partial}{\partial x}\left(x^{2-k}X\right). \tag{8.6}$$

Eliminating X using (8.5), this can be further rearranged into

$$\mathscr{W}\frac{\rho_0\omega^2 r_0^2}{\gamma p_0}x^{(\gamma-1)k}=-\frac{\partial^2\mathscr{W}}{\partial x^2}-\frac{2-k}{x}\frac{\partial\mathscr{W}}{\partial x}+\frac{\ell(\ell+1)}{x^2}\mathscr{W}. \tag{8.7}$$

With the change of variable $z=x^{k(\gamma-1)+2}$, it can be shown that this becomes

$$\alpha^2 z\mathscr{W}=-z^2\frac{\mathrm{d}^2\mathscr{W}}{\mathrm{d}z^2}-\frac{z(\beta+1-k)}{\beta}\frac{\mathrm{d}\mathscr{W}}{\mathrm{d}z}+\frac{\ell(\ell+1)\mathscr{W}}{\beta^2}, \tag{8.8}$$

where

$$\alpha^2\equiv\frac{\omega^2\rho_0 r_0^2}{\gamma p_0[k(\gamma-1)+2]^2}, \quad \beta\equiv k(\gamma-1)+2. \tag{8.9}$$

The general solution to Equation (8.8) is

$$\mathscr{W}=z^{\frac{k-1}{2\beta}}\sqrt{\pi}\left[C_1 J_n(2\alpha z^{1/2})+C_2 J_{-n}(2\alpha z^{1/2})\right], \tag{8.10}$$

where

$$n=\frac{1}{\beta}\left[(k-1)^2+4\ell(\ell+1)\right]^{1/2}, \tag{8.11}$$

and C_1, C_2 are arbitrary coefficients. The asymptotic form of Bessel functions for large arguments is

$$J_n(x)\approx\sqrt{\frac{2}{\pi x}}\cos\left(x-\frac{n\pi}{2}-\frac{\pi}{4}\right), \tag{8.12}$$

so we end up with the asymptotic solution

$$\mathscr{W}=\alpha^{-1/2}z^{\frac{k-1}{2\beta}-\frac{1}{4}}\left[C_1\cos\left(2\alpha z^{1/2}-\frac{n\pi}{2}-\frac{\pi}{4}\right)+C_2\cos\left(2\alpha z^{1/2}+\frac{n\pi}{2}-\frac{\pi}{4}\right)\right]. \tag{8.13}$$

Recalling that $z=x^\beta$, $\rho=\rho_0 x^{-k}$ and $p=p_0 x^{-\gamma k}$, we have that

$$z^{\frac{k-1}{2\beta}-\frac{1}{4}}=\left(\frac{\rho_0}{\rho}\right)^{3/4}\left(\frac{p}{p_0}\right)^{1/4}\frac{1}{x}, \tag{8.14}$$

which gives us

$$\mathscr{W}=\alpha^{-1/2}\left(\frac{\rho_0}{\rho}\right)^{3/4}\left(\frac{p}{p_0}\right)^{1/4}\frac{r_0}{r}\left[C_1\cos\left(2\alpha z^{1/2}-\frac{n\pi}{2}-\frac{\pi}{4}\right)+C_2\cos\left(2\alpha z^{1/2}+\frac{n\pi}{2}-\frac{\pi}{4}\right)\right]. \tag{8.15}$$

Next, we consider the U region. With $N^2=0$ and $\mathscr{W}=p'/\rho$, and without assuming any particular functional form for ρ and p, Equation (8.2) becomes more generally

$$\mathscr{W}\frac{\rho\omega^2}{\gamma p}=-\frac{\partial^2\mathscr{W}}{\partial r^2}-\left(\frac{2}{r}+\frac{1}{\rho}\frac{\partial\rho}{\partial r}\right)\frac{\partial\mathscr{W}}{\partial r}+\mathscr{W}\frac{\ell(\ell+1)}{r^2}. \tag{8.16}$$

With another change of variable $V=r\rho^{1/2}\mathscr{W}$, we get the DE

$$\frac{\partial^2 V}{\partial r^2}=\left(-\frac{\rho\omega^2}{\gamma p}+\frac{\ell(\ell+1)}{r^2}+\mathscr{D}\right)V, \tag{8.17}$$

where

$$\mathscr{D}=\frac{1}{\rho r}\frac{\partial\rho}{\partial r}-\frac{1}{4\rho^2}\left(\frac{\partial\rho}{\partial r}\right)^2+\frac{1}{2\rho}\frac{\partial^2\rho}{\partial r^2}. \tag{8.18}$$

Equation (8.17) is a second-order DE of the form

$$\frac{\partial^2 V}{\partial r^2}=-\Lambda(r)V, \tag{8.19}$$

where

$$\Lambda = \frac{\rho\omega^2}{\gamma p} - \frac{\ell(\ell+1)}{r^2} - \mathscr{D}\,. \tag{8.20}$$

The first term in the expression for Λ corresponds to the square of the acoustic wavenumber ω^2/c_s^2, while the remaining terms go as the inverse squares of spatial scales of order the stellar radius. One expects the acoustic term to dominate, giving the WKB solution

$$V \approx C_3 \frac{p^{1/4}}{\rho^{1/4}} \cos\left(\int_{r_0}^{r} \Lambda^{1/2}\,\mathrm{d}r' + \eta\right), \tag{8.21}$$

or in terms of $\mathscr{W}$,

$$\mathscr{W} = C_3 \frac{p^{1/4}}{\rho^{3/4} r} \cos\left(\int_{r_0}^{r} \Lambda^{1/2}\,\mathrm{d}r' + \eta\right). \tag{8.22}$$

Here C_3 and η are arbitrary constants. Note that we have assumed the lower vanishing point of Λ lies below r_0. If this is not the case, then r_0 will need to be shifted upward to coincide with the vanishing point of Λ. Such a re-definition would affect the value of η, but otherwise has no impact on the form of the final eigenfrequency condition.

To connect the L solution, given by (8.15), to the U solution, given by (8.22), we start by applying the power-law assumption to the integrand of (8.22):

$$\Lambda(r) = \frac{\omega^2}{\gamma}\frac{\rho_0}{p_0}\left(\frac{r}{r_0}\right)^{-k+\gamma k} - \frac{\ell(\ell+1)}{r^2} - \mathscr{D}\,, \tag{8.23}$$

where $\mathscr{D}$ reduces to

$$\mathscr{D} = \frac{k(k-2)}{4r^2}\,. \tag{8.24}$$

Changing variables from r to $z = (r/r_0)^\beta$,

$$\Lambda = \alpha^2\left(1 - \frac{4\ell(\ell+1)+k(k-2)}{\alpha^2\beta^2 z}\right)\frac{\beta^2}{r_0^2} z^{-2/\beta+1}\,, \tag{8.25}$$

and in the limit of large z, specifically where

$$z \gg \frac{4\ell(\ell+1)+k(k-2)}{\alpha^2\beta^2} \sim \frac{c_s^2}{\omega^2 r^2}\,,$$

which should hold for p-modes, we invoke the binomial approximation to obtain

$$\begin{aligned}\int_{r_0}^{r} \Lambda^{1/2}\,\mathrm{d}r &\approx \int_{z_0}^{z} \alpha\left(1 - \frac{\ell(\ell+1)+k(k-4)}{2z\beta^2\alpha^2}\right)\frac{\mathrm{d}z}{z^{1/2}} \\ &\approx 2\alpha\left[z^{1/2}-1\right] - \frac{4\ell(\ell+1)+k(k-2)}{\alpha\beta^2}\left[1-z^{-1/2}\right].\end{aligned} \tag{8.26}$$

In region U, z is large, so the $z^{-1/2}$ term can be neglected. Hence going towards L, the U solution (8.22) approaches the form

$$\mathscr{W} = C_3\alpha^{-1/2}\left(\frac{\omega}{\gamma^{1/2}\beta\rho_0 r_0}\right)^{1/2} z^{\frac{k-1}{2\beta}-\frac{1}{4}} \cos\left(2\alpha\left[z^{1/2}-1\right] - \frac{4\ell(\ell+1)+k(k-2)}{\alpha\beta^2} + \eta\right). \tag{8.27}$$

Comparing this to the asymptotic form of the L solution, given by (8.15), this implies that C_1, C_2, C_3, η must satisfy

$$C_1\cos\left(2\alpha z^{1/2}+\phi_1\right) + C_2\cos\left(2\alpha z^{1/2}+\phi_2\right) = C_3\left(\frac{\omega}{\gamma^{1/2}\beta\rho_0 r_0}\right)^{1/2}\cos\left(2\alpha z^{1/2}+\phi_3+\eta\right), \tag{8.28}$$

where

$$\phi_1 \equiv -\frac{n\pi}{2} - \frac{\pi}{4}, \tag{8.29}$$

$$\phi_2 \equiv \frac{n\pi}{2} - \frac{\pi}{4}, \tag{8.30}$$

$$\phi_3 \equiv -2\alpha - \frac{4\ell(\ell+1) + k(k-2)}{\alpha\beta^2}. \tag{8.31}$$

To cast this in general terms, the relation

$$a_1\cos(x+\theta_1) + a_2\cos(x+\theta_2) = a_3\cos(x+\theta_3) \tag{8.32}$$

will be satisfied for arbitrary argument x if

$$\theta_3 = \tan^{-1}\left(\frac{a_1\sin\theta_1 + a_2\sin\theta_2}{a_1\cos\theta_1 + a_2\cos\theta_2}\right), \tag{8.33}$$

$$a_3 = \sqrt{a_1^2 + a_2^2 + 2a_1a_2\cos(\theta_2-\theta_1)}. \tag{8.34}$$

Making use of these results, we conclude that

$$\eta = \tan^{-1}\left(\frac{\sin\phi_1 + \frac{C_2}{C_1}\sin\phi_2}{\cos\phi_1 + \frac{C_2}{C_1}\cos\phi_2}\right) - \phi_3, \tag{8.35}$$

$$\frac{C_3}{C_1} = \left(\frac{\gamma^{1/2}\beta\rho_0 r_0}{\omega}\right)^{1/2}\left[1 + \left(\frac{C_2}{C_1}\right)^2 + \frac{2C_2}{C_1}\cos(\phi_2-\phi_1)\right]^{1/2}. \tag{8.36}$$

Connecting the U solution to the surface requires the solution for the layer S. Under the assumption that the sound speed near the surface becomes small, Equation (8.2) becomes approximately

$$p' \approx -\frac{\gamma p}{\rho r^2}\frac{\partial}{\partial r}\left(r^2\rho X\right), \tag{8.37}$$

where $p^{1/\gamma}/\rho$ is taken to be a constant under the adiabatic equation of state and also the assumption that the adiabatic index γ is a global constant. Eliminating p' from Equation (8.1) leaves us with

$$\omega^2 X = -\frac{\partial}{\partial r}\left[\frac{\gamma p}{\rho^2 r^2}\frac{\partial}{\partial r}\left(r^2\rho X\right)\right], \tag{8.38}$$

upon which further rearrangement gives

$$\frac{\omega^2}{\gamma}X = \frac{2pX}{\rho r^2} - \frac{2p}{\rho r}\frac{\partial X}{\partial r} + \frac{X}{\gamma}\frac{\partial g}{\partial r} + g\frac{\partial X}{\partial r} - \frac{p}{\rho}\frac{\partial^2 X}{\partial r^2} + \frac{2gX}{r}\left(1-\frac{1}{\gamma}\right). \tag{8.39}$$

Making a change of variable $\chi = X/r$, and considering the equation of hydrostatic balance $\partial p/\partial r = -\rho g$, we are left with the DE

$$\frac{\partial^2\chi}{\partial r^2} + \frac{\partial}{\partial r}\ln\left(r^4 p\right)\frac{\partial\chi}{\partial r} = -\left(\frac{\omega^2}{\gamma} - \frac{g}{r}\left[3-\frac{2}{\gamma}\right] - \frac{1}{\gamma}\frac{\partial g}{\partial r}\right)\frac{\rho}{p}\chi. \tag{8.40}$$

Not too close to the surface itself, we still expect wavelengths to be much smaller than scales of background variations, which allows us to write down the WKB solution to (8.40) as

$$\chi(r) = C_4 r^{-2} p^{-1/2}\Xi^{-1/4}\cos\left(\int_r^R \Xi^{1/2}\,\mathrm{d}r' + \mu\right), \tag{8.41}$$

where

$$\Xi(r) = \left(\frac{\omega^2}{\gamma} - \frac{g}{r}\left[3-\frac{2}{\gamma}\right] - \frac{1}{\gamma}\frac{\mathrm{d}g}{\mathrm{d}r}\right)\frac{\rho}{p}, \tag{8.42}$$

and C_4, μ are arbitrary constants.

Right at the surface $r = R$, we shall make the local approximation that

$$\frac{p}{\rho} \approx -\left(\frac{p}{\rho}\right)' (R - r) = Hs\,, \tag{8.43}$$

where

$$H \equiv -\left(\frac{p}{\rho}\right)'_{r=R} \quad \text{and} \quad s \equiv R - r\,. \tag{8.44}$$

Changing variables from r to s, Equation (8.40) becomes

$$\frac{\mathrm{d}^2\chi}{\mathrm{d}s^2} - \left(\frac{4}{r} + \frac{1}{p}\frac{\partial p}{\partial r}\right)\frac{\mathrm{d}\chi}{\mathrm{d}s} + \Xi\chi = 0\,. \tag{8.45}$$

Now the quantity $(-1/p)\partial p/\partial r$ corresponds to the inverse of the pressure scale height, which we expect to become large near the surface (i.e. the scale height becomes small), so neglecting the $4/r$ term in comparison, we get

$$s^2\frac{\mathrm{d}^2\chi}{\mathrm{d}s^2} + \delta_2 s\frac{\mathrm{d}\chi}{\mathrm{d}s} + \delta_1 s\chi = 0 \tag{8.46}$$

where

$$\delta_1 \equiv \frac{1}{H}\left(\frac{\omega^2}{\gamma} - \frac{g}{r}\left[3 - \frac{2}{\gamma}\right] - \frac{1}{\gamma}\frac{\partial g}{\partial r}\right), \tag{8.47}$$

$$\delta_2 \equiv \frac{g}{H}\,, \tag{8.48}$$

approximated by their values at $s = 0$. The general solution is

$$\chi(s) = s^{(1-\delta_2)/2}\sqrt{\pi}\left[C_5 J_{1-\delta_2}(2\delta_1^{1/2}s^{1/2}) + C_6 J_{\delta_2-1}(2\delta_1^{1/2}s^{1/2})\right], \tag{8.49}$$

where C_5, C_6 are arbitrary constants. Now Bessel functions J_n with negative non-integer n diverge as the argument approaches zero, while those with integer or positive n remain finite. Consider

$$\frac{1}{\delta_2} = 1 - \frac{p}{\rho}\frac{\mathrm{d}\rho}{\mathrm{d}p} = 1 - \frac{1}{\gamma} < 1 \tag{8.50}$$

for $\gamma \approx 5/3$, which implies that $1 - \delta_2 < 0$ and that we should set $C_5 = 0$.

As we move inward from the surface, we expect the solution in (8.49) to approach

$$\chi(s) = C_6 s^{\frac{1}{4}-\frac{1}{2}\delta_2}\delta_1^{-1/4}\cos\left(2\delta_1^{1/2}s^{1/2} + \frac{\pi}{2}(1-\delta_2) - \frac{\pi}{4}\right). \tag{8.51}$$

To match this with the solution deeper in, given by (8.41), notice that $\delta_1/s = \Xi$ and hence (8.51) can be expressed

$$\chi(s) = C_6\Xi^{-1/4}s^{-\frac{1}{2}\delta_2}\cos\left(\int_r^R \Xi^{1/2}(r')\,\mathrm{d}r' + \frac{\pi}{2}(1-\delta_2) - \frac{\pi}{4}\right). \tag{8.52}$$

With p and s related through $(1/p)\partial p/\partial r = -\delta_2/s$, which can be integrated to give $p/p_{\mathrm{ref}} = (s/s_{\mathrm{ref}})^{\delta_2}$ where $p_{\mathrm{ref}} = p(s_{\mathrm{ref}})$ is some reference pressure at coordinate $s = s_{\mathrm{ref}} = R - r_{\mathrm{ref}}$, the solution (8.41) becomes

$$\chi(s) = C_4\Xi^{-1/4}\frac{p_{\mathrm{ref}}^{-1/2}}{R^2}\left(\frac{s}{s_{\mathrm{ref}}}\right)^{-\delta_2/2}\cos\left(\int_r^R \Xi^{1/2}(r')\,\mathrm{d}r' + \mu\right). \tag{8.53}$$

From this we identify

$$\frac{C_6}{C_4} = \frac{s_{\mathrm{ref}}^{-\delta_2/2}}{R^2 p_{\mathrm{ref}}^{1/2}}\,, \quad \mu = \frac{\pi}{4}(1 - 2\delta_2)\,. \tag{8.54}$$

To connect the whole envelope (regions L, U and S) together, we need to find C_4 and C_2 in terms of C_1. Note that since the DEs are linear, the overall scaling of the solution is arbitrary and so only the relative values of the coefficients C_1, C_2 etc. can be determined. To do this, we need to relate the solutions of region L, given in asymptotic form by (8.15), and region S, given by (8.41). The solution in region L can be written

$$\mathscr{W}(r) = \left(\frac{\gamma^{1/2}\beta\rho_0 r_0}{\omega}\right)^{1/2} \frac{p^{1/4}}{r\rho^{3/4}} \left[C_1 \cos\left(\int_{r_0}^{r} \Lambda^{1/2}(r')\,\mathrm{d}r' - \phi_3 - \frac{n\pi}{2} - \frac{\pi}{4}\right) + C_2 \cos\left(\int_{r_0}^{r} \Lambda^{1/2}(r')\,\mathrm{d}r' - \phi_3 + \frac{n\pi}{2} - \frac{\pi}{4}\right)\right]. \tag{8.55}$$

Notice that χ and $\mathscr{W}$ are not related simply by a rescaling, but rather by a derivative: $r\omega^2\chi = \partial\mathscr{W}/\partial r$. Approximating

$$\Lambda \approx \Xi \approx \frac{\omega^2\rho}{\gamma p} \gg 1\,, \tag{8.56}$$

this implies the condition on C_1, C_2 and C_4:

$$\begin{aligned} C_1 \cos\left(\int_{r_0}^{r} \Lambda^{1/2}(r')\,\mathrm{d}r' - \phi_3 - \frac{n\pi}{2} + \frac{\pi}{4}\right) + C_2 \cos\left(\int_{r_0}^{r} \Lambda^{1/2}(r')\,\mathrm{d}r' - \phi_3 + \frac{n\pi}{2} + \frac{\pi}{4}\right) \\ = C_4\gamma^{1/2}\omega(\beta\rho_0 r_0)^{-1/2} \cos\left(\int_{r}^{R} \Lambda^{1/2}(r')\,\mathrm{d}r' + \mu\right). \end{aligned} \tag{8.57}$$

Consider the trigonometric identity

$$\sin(\theta_1+\theta_2+\theta_3)\cos\theta_1 - \sin(\theta_1+\theta_2)\cos(\theta_1+\theta_3) = \sin\theta_3\cos\theta_2\,. \tag{8.58}$$

This has the same structure as (8.57) with

$$\theta_1 = \int_{r_0}^{r} \Lambda^{1/2}(r')\,\mathrm{d}r' - \phi_3 - \frac{n\pi}{2} + \frac{\pi}{4}\,, \tag{8.59}$$

$$\theta_2 = \int_{r}^{R} \Lambda^{1/2}(r')\,\mathrm{d}r' + \mu\,, \tag{8.60}$$

$$\theta_3 = n\pi\,. \tag{8.61}$$

Setting $K_{+n} = \theta_1 + \theta_2$ and $K_{-n} = \theta_1 + \theta_2 + \theta_3$, this implies

$$\frac{C_2}{C_1} = -\frac{\sin K_{+n}}{\sin K_{-n}}\,, \tag{8.62}$$

$$\frac{C_4}{C_1} = \frac{(\beta\rho_0 r_0)^{1/2}}{\omega\gamma^{1/2}} \frac{\sin(n\pi)}{\sin K_{-n}}\,. \tag{8.63}$$

8.3 Solution in core

The starting equations can be recast slightly by defining $Y = r^2 p^{1/\gamma} X$ and $W \equiv p'/p^{1/\gamma}$, so that we get

$$Y(\omega^2 - N^2) = \frac{r^2 p^{2/\gamma}}{\rho}\frac{\partial W}{\partial r}\,, \tag{8.64}$$

$$W\left(1 - \frac{\gamma p}{\rho}\frac{\ell(\ell+1)}{r^2\omega^2}\right) = -\frac{\gamma p^{1-2/\gamma}}{r^2}\frac{\partial Y}{\partial r}\,. \tag{8.65}$$

In the limit of large sound speeds, the first term on the LHS of (8.65) can be neglected in favour of the second. Combining the two, we obtain a second-order ODE for Y:

$$\frac{\partial^2 Y}{\partial r^2} + \frac{\partial}{\partial r}\left(\ln\frac{\rho}{p^{2/\gamma}}\right)\frac{\partial Y}{\partial r} + \frac{\ell(\ell+1)}{r^2}\left(\frac{N^2}{\omega^2} - 1\right) Y = 0\,. \tag{8.66}$$

When $\omega^2 \ll N^2$, we employ a WKB expansion to obtain the solution

$$Y(r) = C_7 \frac{p^{1/\gamma}}{\rho^{1/2}\mathscr{S}^{1/4}} \cos\left(\int_{r_i}^{r} \mathscr{S}^{1/2}\,\mathrm{d}r' + \nu\right) \tag{8.67}$$

defined with respect to the interior turning point, or

$$Y(r) = \tilde{C}_7 \frac{p^{1/\gamma}}{\rho^{1/2}\mathscr{S}^{1/4}} \cos\left(\int_{r}^{r_e} \mathscr{S}^{1/2}\,\mathrm{d}r' + \tilde{\nu}\right) \tag{8.68}$$

defined with respect to the exterior turning point, where

$$\mathscr{S} \equiv \frac{\ell(\ell+1)}{r^2}\left(\frac{N^2}{\omega^2} - 1\right), \tag{8.69}$$

and C_7, ν, $\tilde{C}_7$, $\tilde{\nu}$ are arbitrary constants.

In the vicinity of the turning points, where $\omega^2 = N^2$, we make the local approximation

$$N^2 \approx \omega^2 + (N^2)'_{r_{i,e}}(r - r_{i,e}), \tag{8.70}$$

where $r_{i,e}$ is either r_i or r_e. Rescaling $\mathscr{Y} \equiv \rho^{1/2} p^{-1/\gamma} Y$ and defining

$$y \equiv (r - r_i)\left[\frac{\ell(\ell+1)}{\omega^2 r_i^2}(N^2)'_{r_i}\right]^{1/3}, \tag{8.71}$$

$$\tilde{y} \equiv (r - r_e)\left[\frac{\ell(\ell+1)}{\omega^2 r_e^2}(N^2)'_{r_e}\right]^{1/3}, \tag{8.72}$$

Equation (8.66) becomes

$$\frac{\partial^2 \mathscr{Y}}{\partial y^2} + y\mathscr{Y} = 0, \tag{8.73}$$

which is Airy's equation (and likewise for $\tilde{y}$). This has the solution

$$\mathscr{Y}(y) = y^{1/2}\left[C_8 J_{1/3}\left(\frac{2}{3}y^{3/2}\right) + C_9 J_{-1/3}\left(\frac{2}{3}y^{3/2}\right)\right], \tag{8.74}$$

whose asymptotic form for large y in terms of Y is given by

$$Y(y) = \sqrt{\frac{3}{\pi}}\frac{p^{1/\gamma}}{\rho^{1/2}} y^{-1/4}\left[C_8 \cos\left(\frac{2}{3}y^{3/2} - \frac{\pi}{6} - \frac{\pi}{4}\right) + C_9 \cos\left(\frac{2}{3}y^{3/2} + \frac{\pi}{6} - \frac{\pi}{4}\right)\right], \tag{8.75}$$

and likewise for $\tilde{y}$ with $\tilde{C}_8, \tilde{C}_9$. To match this with the WKB solution given by (8.67), we note that under the approximation (8.70),

$$\mathscr{S}(r) \approx \frac{\ell(\ell+1)}{\omega^2 r_{i,e}^2}(N^2)'_{r_{i,e}}(r - r_{i,e}) \tag{8.76}$$

and consequently

$$\int_{r_i}^{r} \mathscr{S}^{1/2}(r')\,\mathrm{d}r' \approx \frac{2}{3}y^{3/2}, \quad \int_{r}^{r_e} \mathscr{S}^{1/2}(r')\,\mathrm{d}r' \approx \frac{2}{3}\tilde{y}^{3/2}. \tag{8.77}$$

This leads us to

$$Y(y) = C_7 \frac{p^{1/\gamma}}{\rho^{1/2}}\left[\frac{\ell(\ell+1)}{\omega^2 r_i^2}(N^2)'_{r_i}\right]^{-1/6} y^{-1/4}\cos\left(\frac{2}{3}y^{3/2} + \nu\right) \tag{8.78}$$

and hence the condition

$$\sqrt{\frac{3}{\pi}}\left[C_8 \cos\left(\frac{2}{3}y^{3/2} - \frac{\pi}{6} - \frac{\pi}{4}\right) + C_9 \cos\left(\frac{2}{3}y^{3/2} + \frac{\pi}{6} - \frac{\pi}{4}\right)\right] = C_7\left[\frac{\ell(\ell+1)}{\omega^2 r_i^2}(N^2)'_{r_i}\right]^{-1/6}\cos\left(\frac{2}{3}y^{3/2} + \nu\right). \tag{8.79}$$

Again making use of the results (8.33)–(8.34), we find that

$$\nu = \tan^{-1}\left[\frac{\left(\frac{C_9}{C_8}-1\right)-\sqrt{3}\left(\frac{C_9}{C_8}+1\right)}{\left(\frac{C_9}{C_8}-1\right)+\sqrt{3}\left(\frac{C_9}{C_8}+1\right)}\right], \tag{8.80}$$

$$\frac{C_7}{C_8} = \sqrt{\frac{3}{\pi}}\left[\frac{\ell(\ell+1)}{\omega^2 r_i^2}(N^2)'_{r_i}\right]^{1/6}\sqrt{1+\frac{C_9}{C_8}+\left(\frac{C_9}{C_8}\right)^2}, \tag{8.81}$$

likewise for r_e with corresponding $\tilde{y}$, $\tilde{\nu}$, $\tilde{C}_7$, $\tilde{C}_8$ and $\tilde{C}_9$.

In region C, we assume that $\omega^2 \gg N^2$, allowing us to neglect the N^2/ω^2 term in (8.66), which simplifies to

$$\frac{\partial^2 \mathscr{Y}}{\partial r^2} = \frac{\ell(\ell+1)}{r^2}\mathscr{Y} \tag{8.82}$$

under the assumption that the scale heights of p and ρ are much larger than the extent of the core itself. The general solution to (8.82) is

$$\mathscr{Y}(r) = C_{10} r^{\frac{1}{2}(1+\sqrt{1+4\ell(\ell+1)})} + C_{11} r^{\frac{1}{2}(1-\sqrt{1+4\ell(\ell+1)})}. \tag{8.83}$$

Since $\ell > 0$ for g-modes, we need to set $C_{11} = 0$ to ensure the solution remains finite at $r = 0$.

To connect this to the solution in region G, which is defined only for $r \geq r_i$, we require that (up to an overall scaling) the slopes and values match at $r = r_i$. Equivalently, this requires that the slope-to-value (STV) ratio matches. In the case of region C, this is

$$\mathrm{STV}_{\mathrm{C}}(r_i) \equiv \frac{1}{\mathscr{Y}(r_i)}\frac{\partial \mathscr{Y}}{\partial r}\Big|_{r_i} = \frac{1+\sqrt{1+4\ell(\ell+1)}}{2r_i}. \tag{8.84}$$

To evaluate the corresponding quantity at the base of region G, for which the form of the solution is given by (8.74), we make use of the series expansion for Bessel functions: for small arguments, these can be approximated by

$$J_\nu(x) \approx \frac{1}{\Gamma(\nu+1)}\left(\frac{x}{2}\right)^\nu. \tag{8.85}$$

It can then be shown that

$$\mathrm{STV}_{\mathrm{G}}(r_i) = \left[\frac{\ell(\ell+1)}{\omega^2 r_i^2}(N^2)'_{r_i}\right]^{1/3}\frac{C_8}{C_9}\frac{3^{1/3}\Gamma\left(\frac{2}{3}\right)}{\Gamma\left(\frac{1}{3}\right)}, \tag{8.86}$$

which equating to (8.84) leads to the condition

$$\frac{C_9}{C_8} = \left[\frac{\ell(\ell+1)}{\omega^2 r_i^2}(N^2)'_{r_i}\right]^{1/3}\frac{3^{1/3}\Gamma\left(\frac{2}{3}\right)}{\Gamma\left(\frac{1}{3}\right)}\frac{2r_i}{1+\sqrt{1+4\ell(\ell+1)}}. \tag{8.87}$$

The scaling of the region C solution (given by C_{10}) can be determined by equating amplitudes at r_i:

$$\frac{C_{10}}{C_9} = r_i^{-\frac{1}{2}(1+\sqrt{1+4\ell(\ell+1)})}\frac{3^{1/3}}{\Gamma\left(\frac{2}{3}\right)}. \tag{8.88}$$

8.4 Evanescent zone

In this region (E) we make no assumptions about N^2 or c_s^2, hence the governing equations are the general pair

$$Y(\omega^2 - N^2) = \frac{r^2 p^{2/\gamma}}{\rho}\frac{\partial W}{\partial r} \tag{8.89}$$

$$W\left[1 - \frac{\gamma p}{\rho}\frac{\ell(\ell+1)}{r^2\omega^2}\right] = -\frac{\gamma p^{1-2/\gamma}}{r^2}\frac{\partial Y}{\partial r}\,. \tag{8.90}$$

For a thin evanescent zone, one might expect p/ρ to be well approximated by a power law whose index is constant over the zone. For the purposes of illustration we will assume that this index is roughly unity, and adopt the functional forms

$$\rho = \rho_e\left(\frac{r}{r_e}\right)^{-\kappa}, \quad p = p_e\left(\frac{r}{r_e}\right)^{-\kappa-1}, \tag{8.91}$$

where κ is a constant, and $\rho_e \equiv \rho(r_e)$, $p_e \equiv p(r_e)$. We intend this only to be representative; the purpose of this section is to point out that the governing DE is unlikely to have a simple analytic solution unless ℓ is large.

Substituting these forms into Equations (8.89)–(8.90), and making the change of variable $u \equiv r_e/r$, they become

$$Y u^{\kappa-(\kappa+1)2/\gamma}(1-u^3) = -\frac{r_e p_e^{2/\gamma}}{\omega^2\rho_e}\frac{\partial W}{\partial u} \tag{8.92}$$

$$W\frac{r_e p_e^{2/\gamma}}{\rho_e}\frac{\ell(\ell+1)}{\omega^2}\left[\frac{r_e^2\rho_e}{\gamma p_e}\frac{\omega^2}{\ell(\ell+1)} - u^3\right] = u^{4+(\kappa+1)(1-2/\gamma)}\frac{\partial Y}{\partial u}\,. \tag{8.93}$$

These can be combined into a single second-order DE

$$\frac{\partial^2 Z}{\partial u^2} + \left[\frac{(\kappa+1)\frac{2}{\gamma} - \kappa}{u} + \frac{3u^2}{1-u^3}\right]\frac{\partial Z}{\partial u} + \left[\frac{r_e^2\rho_e}{\gamma p_e}\frac{\omega^2}{\ell(\ell+1)} - u^3\right]\frac{\ell(\ell+1)}{u^5}(1-u^3)Z = 0\,, \tag{8.94}$$

where

$$Z \equiv W\frac{r_e p_e^{2/\gamma}}{\rho_e}\frac{\ell(\ell+1)}{\omega^2}\,. \tag{8.95}$$

Since κ, γ and u are all quantities of order unity, the $\partial Z/\partial u$ coefficient will be $\sim O(1)$. Inspecting the Z term coefficient, we see that the term

$$\frac{r_e^2\rho_e}{\gamma p_e}\frac{\omega^2}{\ell(\ell+1)} = \frac{\omega^2}{S_\ell^2} \sim O(1) \tag{8.96}$$

where S_ℓ is the Lamb (acoustic) frequency, since the evanescent zone is located near the turning point for acoustic waves. Thus the factor in square brackets will be of order unity. The remaining factor $\ell(\ell+1)(1-u^3)/u^5$ will be large if ℓ is large, and in this limit a WKB approach might be used to solve Equation (8.94), leading to exponential solutions. However, for low-degree modes, this term will be of order unity and WKB cannot be applied. We suggest that in this scenario, obtaining a reasonably accurate solution to region E would require a numerical integration of Equation (8.94).

8.5 Eigenfrequency condition

On the upper side of region E (i.e. in region L), we have the basis of solutions $z^{\frac{k-1}{2\beta}} J_{+n}(2\alpha z^{1/2})$ and $z^{\frac{k-1}{2\beta}} J_{-n}(2\alpha z^{1/2})$, with known relative weights C_1 and C_2. Suppose each of these independent solutions were to be integrated across region E from r_0 to r_e, and found to have STV ratios of STV_+ and STV_-, respectively, at r_e. At r_e and just below (i.e. top of region G), we found that the solution takes the form

$$Y(\tilde{y}) = \tilde{y}^{1/2} \frac{p^{1/\gamma}}{\rho^{1/2}} \left[\tilde{C}_8 J_{1/3}\left(\frac{2}{3}\tilde{y}^{3/2}\right) + \tilde{C}_9 J_{-1/3}\left(\frac{2}{3}\tilde{y}^{3/2}\right) \right], \tag{8.97}$$

which connects to the WKB solution

$$Y(r) = \tilde{C}_7 \frac{p^{1/\gamma}}{\rho^{1/2}} \mathscr{S}^{-1/4} \cos\left(\int_r^{r_e} \mathscr{S}^{1/2}(r')\,\mathrm{d}r' + \tilde{\nu} \right) \tag{8.98}$$

further below. Let us use '+' and '−' subscripts to denote the constants associated with the J_{+n} and J_{-n} integrations. Then, closely following the results derived for the turning point r_i, we have

$$\frac{\tilde{C}_{9\pm}}{\tilde{C}_{8\pm}} = \left[\frac{\ell(\ell+1)}{\omega^2 r_e^2} (N^2)'_{r_e} \right]^{1/3} \frac{3^{1/3}\Gamma\left(\frac{2}{3}\right)}{\Gamma\left(\frac{1}{3}\right)} \mathrm{STV}_\pm^{-1}, \tag{8.99}$$

$$\tilde{\nu}_\pm = \tan^{-1}\left[\frac{\left(\frac{\tilde{C}_{9\pm}}{\tilde{C}_{8\pm}} - 1\right) - \sqrt{3}\left(\frac{\tilde{C}_{9\pm}}{\tilde{C}_{8\pm}} + 1\right)}{\left(\frac{\tilde{C}_{9\pm}}{\tilde{C}_{8\pm}} - 1\right) + \sqrt{3}\left(\frac{\tilde{C}_{9\pm}}{\tilde{C}_{8\pm}} + 1\right)} \right], \tag{8.100}$$

$$\frac{\tilde{C}_{7\pm}}{\tilde{C}_{8\pm}} = \sqrt{\frac{3}{\pi}} \left[\frac{\ell(\ell+1)}{\omega^2 r_e^2} (N^2)'_{r_e} \right]^{1/6} \sqrt{1 + \frac{\tilde{C}_{9\pm}}{\tilde{C}_{8\pm}} + \left(\frac{\tilde{C}_{9\pm}}{\tilde{C}_{8\pm}}\right)^2}. \tag{8.101}$$

The solution for region G, defined with respect to the outer turning point, is therefore

$$Y(r) = \frac{p^{1/\gamma}}{\rho^{1/2}} \mathscr{S}^{-1/4} \left[C_1 \tilde{C}_{7+} \cos\left(\int_r^{r_e} \mathscr{S}^{1/2}(r')\,\mathrm{d}r' + \tilde{\nu}_+ \right) + C_2 \tilde{C}_{7-} \cos\left(\int_r^{r_e} \mathscr{S}^{1/2}(r')\,\mathrm{d}r' + \tilde{\nu}_- \right) \right], \tag{8.102}$$

which needs to be matched to Equation (8.67). Information about the properties of the evanescent region is contained implicitly in the coefficients $\tilde{C}_{7\pm}$ and $\tilde{\nu}_\pm$, through their dependence on $\tilde{C}_{8\pm}$ and $\tilde{C}_{9\pm}$ and therefore $\mathrm{STV}_\pm$.

At this point all matching conditions from the upper portion of region G to the surface and the lower portion of region G to the centre have been derived; it remains to make the connection across region G. The values of ω for which this is possible correspond to the allowed frequencies of the star. With the arbitrariness of absolute scaling of each half in mind, what we effectively require is that

$$C_1 \tilde{C}_{7+} \cos\left(\int_r^{r_e} \mathscr{S}^{1/2}(r')\,\mathrm{d}r' + \tilde{\nu}_+ \right) + C_2 \tilde{C}_{7-} \cos\left(\int_r^{r_e} \mathscr{S}^{1/2}(r')\,\mathrm{d}r' + \tilde{\nu}_- \right) \propto \cos\left(\int_{r_i}^{r} \mathscr{S}^{1/2}(r')\,\mathrm{d}r' + \nu \right), \tag{8.103}$$

which can be shown to imply that

$$C_1 \tilde{C}_{7+} \sin\left(\int_{r_i}^{r_e} \mathscr{S}^{1/2}(r)\,\mathrm{d}r + \tilde{\nu}_+ + \nu \right) + C_2 \tilde{C}_{7-} \sin\left(\int_{r_i}^{r_e} \mathscr{S}^{1/2}(r)\,\mathrm{d}r + \tilde{\nu}_- + \nu \right) = 0. \tag{8.104}$$

Invoking the result (8.62), this can be rearranged into

$$\cot\left(\int_{r_i}^{r_e} \mathscr{S}^{1/2}(r)\,\mathrm{d}r + \tilde{\nu}_+ + \nu \right) = \cot(\tilde{\nu}_+ - \tilde{\nu}_-) - \frac{\tilde{C}_{7+}}{\tilde{C}_{7-}} \frac{\sin K_{-n}}{\sin K_{+n}} \csc(\tilde{\nu}_+ - \tilde{\nu}_-). \tag{8.105}$$

The LHS depends on the properties of the g-mode cavity, while the RHS depends on the properties of the evanescent region (through $\tilde{\nu}_\pm$ and $\tilde{C}_{7\pm}$) and the p-mode cavity, through

$$K_{\pm n} = \int_{r_0}^{R} \Lambda^{1/2}(r)\,\mathrm{d}r - \phi_3 \mp \frac{n\pi}{2} + \frac{\pi}{4} + \mu. \tag{8.106}$$

Equation (8.105) describes a criterion for the frequencies of allowed modes in this star. Unlike the case of pure p- and g-modes, the RHS of this expression, and not just the phase integral itself, depends on frequency. The form of Equation (8.105) suggests two scales of behaviour for the frequency spacings of the allowed modes. The first is that associated with the phase integral on the LHS, with $\mathscr{S}$ given by (8.69), which predicts g-mode-like behaviour of even period spacings. In addition, there is a modulation by a second scale arising from the $\sin K_{\pm n}$ terms on the RHS. These are associated with the p-mode phase. This suggests that the spectrum of mixed modes comprises a collection of modes roughly evenly spaced in period, but that these would experience bunching on a scale given by the p-mode spacing, i.e. the dynamical frequency or large separation.

This formalism can be trivially extended to the case of magnetic fields confined to the core region, provided that the fields are relatively weak (so that the assumption of spherical symmetry still holds). This would contribute additional terms to the phase integral on the LHS of (8.105), with the structure of the overall condition unaffected. Analytic expressions for these additional phase contributions in the weak-field case will be derived later on in Chapter 12.

Part III

WAVE PROPAGATION IN A MAGNETIC FIELD

Chapter 9

Numerical Simulations

This chapter deals with all aspects to do with the numerical side of the work, namely fluid simulations investigating wave propagation in the presence of a magnetic field. First, I give a broad overview of techniques employed in computational fluid dynamics (§9.1). Then in §9.2 I describe in more detail the particular code used in this research. Finally, in §9.3 I present and discuss the results obtained for the problem of gravity wave interactions with a dynamically significant magnetic field.

9.1 Computational fluid dynamics

Problems in fluid dynamics tend only to be analytically tractable in the simplest of cases. For investigating moderately complex geometries, numerical simulations are often the most convenient tool. They are especially useful in the study of astrophysical systems, for which observations may be difficult to obtain (such as deep stellar interiors), or where the conditions are difficult to reproduce in experiment. While both analytical and numerical calculations are subject to their own limitations, the fact that each involves very different sets of approximations allows them to serve as a mutual cross-check when studying a given problem.

The goal of computational fluid dynamics is to evolve the system of PDEs governing mass, momentum and energy conservation (in the ideal fluids case), Maxwell's equations (in the case of MHD), and/or variants thereof, for example incorporating viscosity and resistivity (non-ideal MHD), from some initial starting configuration and under certain boundary conditions, to obtain a solution for the velocity field and/or relevant quantities. In the case of ideal MHD without rotation, these equations were given in (2.9)–(2.12). In this section we will give an overview of some common approaches.

9.1.1 Finite-difference methods

One way of treating the derivatives in the system of DEs is to approximate the solution locally by low degree piecewise polynomials, and to then differentiate these polynomials (LeVeque et al., 1998). The domain is divided into some number of grid points, with each polynomial local to the segment between individual points. This approach results in a finite set of algebraic relations between the values at the grid points, which can then be solved on a computer (e.g. by matrix inversion). There are multiple ways in which the derivatives can be discretised (one-sided or centred differences, in space and/or in time), leading to a large number of finite difference schemes.

The use of a discrete grid to represent an otherwise continuous solution leads to many complications, including artefacts and behaviour not exhibited by the real physical system. In particular, the fineness of the grid required for a certain application depends on the propagation speeds involved. If too coarse a grid or and/too large a timestep is used, resulting in an inability to resolve the dynamics, the numerical solution is rendered unconvergent and unstable. This leads to the *Courant-Friedrichs-Lewy (CFL) condition* that the Courant number $C = u\Delta t/\Delta x$ is less than a number of order unity, where u is the propagation speed of the flow, Δt is the timestep and Δx is the grid spacing. The upper bound on C depends on the particular scheme being used: for example, explicit schemes (in which the solution at a given timestep can be expressed completely in terms of the solution at the preceding timestep) require $C \leq 1$, whereas implicit schemes (which combine information from both the current and preceding timesteps) can tolerate C in excess of unity. The CFL condition is a necessary, though not sufficient, condition for stability, and so finite-difference codes require very fine grids to resolve flows having significant spatial and temporal variation.

9.1.2 Finite-volume methods

Much of the same principles for finite-difference methods apply to finite-volume methods. The main conceptual difference is that values are now interpreted as being averages over small volumes in the domain, rather than at single points on a grid. The advantage of this is that it allows physical conservation laws (of mass, momentum etc.) to be enforced. This is accomplished by discretising the equations in their integral form, where integrals are taken over each cell volume. Integrals containing divergence terms are converted to surface integrals (by Gauss' divergence theorem) and evaluated as fluxes on the surface of each cell. This ensures that whatever is lost by one cell is gained by its neighbour. Conservativeness is important when solving for flows with shocks or discontinuities in the domain; non-conservative methods tend to produce solutions that may look reasonable but have speeds of motion that are incorrect. Finite-volume methods are widely used to solve fluids problems; benefits include the flexibility for unstructured meshes and an ability to handle complex geometries.

Many implementations of finite-volume methods are based on solving the *Riemann problem* in order to obtain the flux at cell boundaries. Mathematically, a Riemann problem involves a system of conservation laws having (in one spatial dimension) the form

$$\frac{\partial q}{\partial t} + \frac{\partial}{\partial x} f(q) = 0\,, \tag{9.1}$$

where $q(x,t) \in \mathbb{R}^n$ is a vector of n state variables (density, velocity etc.) and f is a flux function, and piecewise constant initial data separated by a single discontinuity

$$q(x,0) = \begin{cases} q_L & x < 0 \\ q_R & x > 0\,. \end{cases} \tag{9.2}$$

In the case of linear advection, where $f(q) = uq$ with constant advection speed u, and initial conditions $q(x,0) = q_0(x)$, the solutions are constant along characteristics $x - ut = x_0$. These are simply given by $q(x,t) = q_0(x-ut)$, where subscript '0's denote values at $t = 0$. At a given cell boundary, the flux would be

$$f = \begin{cases} uq_L & u \leq 0 \\ uq_R & u \geq 0\,. \end{cases} \tag{9.3}$$

The global problem will involve multiple domains each with their own Riemann problems at every cell interface. Provided the timestep Δt is small enough that waves from neighbouring domains do not travel beyond the length of a single cell, the above prescription holds. This demands that $u\Delta t \leq \Delta x$, which we recognise as the CFL condition (which must be satisfied for stability in any case). The above approach, where fluxes are obtained by local solutions of the Riemann problem, is known as *Godunov's method*.

9.1.3 Spectral methods

In contrast to finite-difference and finite-volume methods, which piece together a solution from local functions, spectral methods are global in that the solution is constructed from basis functions that span the whole domain (Canuto et al., 1988). Choices for these global basis functions include trigonometric functions (Fourier series), Chebyshev polynomials and Legendre polynomials (Hussaini & Zang, 1987). The solution to the system of PDEs is represented by a truncated series expansion with respect to these basis functions, and spatial derivatives are computed by differentiating these basis functions. Because information from the entire domain (as opposed to just neighbouring points) is used to compute derivatives, spectral methods are more accurate than local methods, given the same computational resources (number of stored data values). In fact, they tend to exhibit exponential convergence, meaning that increasing the number N of basis functions decreases the error at a rate faster than any finite power of $1/N$. Spectral methods are preferable over finite-difference/finite-volume methods in situations where the solution varies rapidly in space and/or time, since similar accuracies can be achieved at less computational expense. However, they suffer a disadvantage in that their stability properties are much more sensitive to the boundary conditions than the other methods. They are most successful when turned to problems without boundaries (infinite or periodic domains). Trigonometric functions are the obvious choice for periodic boundary conditions, while Chebyshev and Legendre polynomials are preferable for non-periodic problems.

The use of a finite set of basis functions means that, as with all numerical techniques, the true solution can in general only be approximately represented. Different types of spectral method differ in the way in which they enforce that the solution satisfies the system of DEs as closely as possible. There are three common approaches, known as *Galerkin, tau* and *pseudospectral (collocation)* methods. Consider a series expansion of the solution

$$q(x,t) \approx \sum_{k=0}^{N} a_k(t)\phi_k(x)\,, \tag{9.4}$$

where ϕ_k are the basis functions and a_k are the expansion coefficients. Galerkin methods involve constructing a basis in which all functions individually satisfy the boundary conditions, and then solving for a_k such that the residual is orthogonal to as many basis functions as possible. In tau methods, individual basis functions need not satisfy the boundary conditions; rather, boundary conditions are enforced through the choice of a_k, and the residual is made to be orthogonal to as many basis functions as possible. While Galerkin and tau methods are implemented in terms of the expansion coefficients, pseudospectral methods are based on the physical values of the expansion at given points on the spatial grid. That is, the solution is required to satisfy the system of DEs exactly at a finite set of spatial points. However, the basis functions themselves are still used to evaluate spatial derivatives; e.g. in the case of Fourier series, spatial derivatives would involve multiplying by $\mathrm{i}k$ in the Fourier domain.

One disadvantage of spectral methods, besides their restrictiveness with regards to boundary conditions, is the difficulty in representing sharp gradients and discontinuous features. This stems from the "ringing" behaviour exhibited when a finite Fourier series is used to represent functions with jump discontinuities. Oscillations overshooting and undershooting the actual value of the function occur in the vicinity of the discontinuity, tending to a finite limit as the number of basis functions increases. This is known as the *Gibbs phenomenon*. Typically the effects of this can be removed through additional techniques, such as filtering (e.g. Cai et al., 1989) or reprojection onto a different basis (e.g. Gottlieb et al., 1992), allowing spectral methods to be used for modelling systems with shocks.

9.2 SNOOPY: a spectral MHD code

9.2.1 Design and features

All numerical results presented in this section were obtained using the Fourier pseudo-spectral code SNOOPY, which is a 3D incompressible MHD code written by Geoffroy Lesur. The use of a Fourier basis means that boundary conditions are periodic in each coordinate (x, y, z). Its original application was for performing shearing box simulations in the context of accretion disc modelling (Lesur & Longaretti, 2005), and so it operates in a Cartesian geometry. The full set of equations solved are thus (Lesur & Longaretti, 2009)

$$\frac{\partial \mathbf{u}}{\partial t} + \nabla \cdot (\mathbf{u} \otimes \mathbf{u}) = -\nabla \Pi + \nabla \cdot (\mathbf{B} \otimes \mathbf{B}) - 2\boldsymbol{\Omega} \times \mathbf{u} + 2\Omega S y \hat{\mathbf{y}} + \nu \nabla^2 \mathbf{u}\,, \tag{9.5}$$

$$\frac{\partial \mathbf{B}}{\partial t} = \nabla \times (\mathbf{u} \times \mathbf{B}) + \eta \nabla^2 \mathbf{B}\,, \tag{9.6}$$

$$\nabla \cdot \mathbf{u} = 0\,, \tag{9.7}$$

$$\nabla \cdot \mathbf{B} = 0\,, \tag{9.8}$$

where $\eta = 1/\sigma$ is the resistivity, ν is the kinematic viscosity, $\boldsymbol{\Omega}$ is the rotation vector, and $S = -r\partial\Omega/\partial r$ is the shear. Clearly shear is irrelevant for our purposes, as is (at this stage) rotation, and so in our simulations both these effects are turned off ($\Omega = 0, S = 0$).

The quantity Π is the generalised pressure (sum of the gas pressure p/ρ and the magnetic pressure $B^2/2\rho$), and is updated in such a way so as to preserve the incompressibility condition (9.7). This is achieved in practice through a spectral projection operation in Fourier space (Peyret, 2002), which is likewise applied to enforcing the solenoidal condition (9.8), in each case up to machine precision. Note that since SNOOPY is a pseudo-spectral code, derivatives are evaluated in Fourier space. This is with the exception of the non-linear term in (9.5), which involves products of grid quantities. Rather than implementing this as convolutions in Fourier space, which are computationally costly ($\sim O(n^2)$, n being the size of the grid), the product is taken in real space and a fast-Fourier transform (FFT) applied. The FFT operation can be done in $\sim O(n \log n)$ operations and provides a more efficient route for evaluating this term. To mitigate the appearance of aliasing artefacts that arise from the finite spatial resolution, the non-linear term is computed using a 3/2 dealiasing rule (Peyret, 2002), where a 3/2-higher grid resolution is employed. Time stepping is done via a third-order Runge-Kutta approach. The elliptic (viscous and resistive) terms are handled in an implicit fashion maintaining third-order accuracy.

We have chosen to appropriate this code for our purposes since our target system (stably stratified stellar interiors) is to a good approximation incompressible, and we are interested in studying small-scale

waves. Spectral methods afford a far greater computational efficiency in this situation compared to finite-difference/finite-volume methods. Note that spectral methods also have the property that they have intrinsically low numerical dissipation; physical dissipation must be added to prevent unstable or unconvergent behaviour. In this case, the amount of physical dissipation is controlled through the values of the Reynolds number $\mathrm{Re} = 1/\nu$ and magnetic Reynolds number $\mathrm{Rm} = 1/\eta$.

9.2.2 Boussinesq approximation

In the core of the star the density approaches a constant value, and so it is convenient to make the *Boussinesq approximation*, in which density variations are neglected except in the buoyancy term. The effect of this is to exclude the possibility of sound waves, which involve a combination of pressure and density fluctuations, while still permitting the existence of gravity waves, which are the focus of the current study. The Boussinesq option is provided as part of the SNOOPY package, which we adopt throughout our work. A brief description of the approximation and resulting set of modified equations will be given in this section.

Let the density be given by $\rho = \rho_0 + \delta\rho$, where ρ_0 is a reference density value (a spatial constant) and $\delta\rho \ll \rho_0$ the deviation from this, which may be the result of background gradients, and/or time-dependent disturbances. Without rotation, but including magnetism, the equation of motion is

$$\rho\left[\frac{\partial \mathbf{u}}{\partial t} + \mathbf{u}\cdot\nabla\mathbf{u}\right] = -\nabla p - \rho\nabla\Phi + (\nabla\times\mathbf{B})\times\mathbf{B}\,. \tag{9.9}$$

Supposing that the gravitational potential can be approximated by that which ensures magnetohydrostatic balance in the reference state (uniform density of ρ_0), we have

$$0 = -\nabla p_0 - \rho_0\nabla\Phi + (\nabla\times\mathbf{B}_0)\times\mathbf{B}_0\,, \tag{9.10}$$

$$\frac{\partial \mathbf{u}}{\partial t} + \mathbf{u}\cdot\nabla\mathbf{u} = -\frac{\nabla p'}{\rho} + \frac{\delta\rho\nabla p_0}{\rho_0^2} + \frac{(\nabla\times\mathbf{B})\times\mathbf{B}}{\rho} - \frac{(\nabla\times\mathbf{B}_0)\times\mathbf{B}_0}{\rho_0}\,, \tag{9.11}$$

where $p = p_0 + p'$ and $\mathbf{B} = \mathbf{B}_0 + \mathbf{B}'$, p_0 and $\mathbf{B}_0$ being the background pressure and magnetic field.

Recasting the density fluctuation $\delta\rho$ in terms of the entropy fluctuation δS via

$$\delta\rho = \frac{\partial\rho}{\partial S}\Big|_{S=S_0}\delta S\,, \tag{9.12}$$

and defining the potential temperature θ by

$$\delta S = \theta\frac{\mathrm{d}S_0}{\mathrm{d}x}\,, \tag{9.13}$$

where S_0 is the (time-stationary) background entropy assumed only to vary in the direction of stratification, $\hat{\mathbf{x}}$, we then define the vector field

$$\mathbf{A} = \frac{1}{\rho_0^2}\frac{\partial\rho}{\partial S}\Big|_{S=S_0}\frac{\mathrm{d}S_0}{\mathrm{d}x}\nabla p_0\,. \tag{9.14}$$

For stratification in the x-direction, $\nabla p_0 = (\mathrm{d}p_0/\mathrm{d}x)\hat{\mathbf{x}}$. Comparing with the expression (4.12) in the limit where $c_s^2 \to \infty$, we identify $\mathbf{A} = N^2\hat{\mathbf{x}}$. Neglecting $\delta\rho$ in all except the second term on the RHS of Equation (9.11) leaves

$$\frac{\partial \mathbf{u}}{\partial t} + \mathbf{u}\cdot\nabla\mathbf{u} = -\frac{\nabla p'}{\rho_0} + N^2\theta\hat{\mathbf{x}} + \frac{1}{\rho_0}\left[(\nabla\times\mathbf{B})\times\mathbf{B} - (\nabla\times\mathbf{B}_0)\times\mathbf{B}_0\right]. \tag{9.15}$$

To close the system, an equation governing the evolution of the potential temperature needs to be provided. For this, we assume adiabatic pertubations, in which case the entropy $S = S_0 + \delta S$ is conserved following the motion of a given fluid packet. This yields

$$0 = \frac{\partial(\delta S)}{\partial t} + \mathbf{u}\cdot\nabla(\delta S) + \mathbf{u}\cdot\nabla S_0\,, \tag{9.16}$$

which, upon substitution of (9.13), becomes

$$\frac{\partial\theta}{\partial t} + \mathbf{u}\cdot\nabla\theta = -u_x\,, \tag{9.17}$$

where $\mathrm{d}S_0/\,\mathrm{d}x$ is assumed to be a constant over space.

The system of equations we solve using SNOOPY are the dissipative MHD Boussinesq equations, given in non-dimensional form by

$$\frac{\partial\mathbf{u}}{\partial t} + \mathbf{u}\cdot\nabla\mathbf{u} = -\nabla\Pi + N^2\theta\,\hat{\mathbf{x}} + \mathbf{B}\cdot\nabla\mathbf{B} + \frac{\nabla^2\mathbf{u}}{\mathrm{Re}}\,, \tag{9.18}$$

$$\frac{\partial\mathbf{B}}{\partial t} = \nabla\times(\mathbf{u}\times\mathbf{B}) + \frac{\nabla^2\mathbf{B}}{\mathrm{Rm}}\,, \tag{9.19}$$

$$\frac{\partial\theta}{\partial t} + \mathbf{u}\cdot\nabla\theta = -u_x + \frac{\nabla^2\theta}{\mathrm{Rt}}\,, \tag{9.20}$$

$$\nabla\cdot\mathbf{u} = 0\,,\quad \nabla\cdot\mathbf{B} = 0\,, \tag{9.21}$$

where we have introduced another dimensionless parameter, Rt (the 'thermal Reynolds number', really the Péclet number), alongside Re and Rm for controlling the amount of physical dissipation.

9.2.3 Simulation setup

The goal of this work is to elucidate the nature of the physical processes involved in the interaction between gravity waves and a dynamically significant magnetic field. With this in mind, the geometry we adopt in the simulations is one that is uncomplicated and straightforward to implement and analyse. The setup consists of a Cartesian box stratified along a single direction (the x-direction), in which a helical magnetic field is embedded occupying a cylindrical volume whose axis is orthogonal to the stratification. We take the axis of the cylinder to be the z-direction. The field configuration is the cylindrical Prendergast model, derived in §3.3.1 and whose final form is given by Equation (3.62). Recall that this has all three field components being non-zero within the cylinder but vanishing at its boundary. We imposed this configuration as an initial condition and checked stability by observing its natural evolution over time: with the exception of a slow decay in the amplitude (by about 10% over 1000 time units), which might be attributable to the finite Ohmic resistivity, this does indeed appear to be stable. The whole setup is translationally invariant in the z-direction, which is to be associated with the azimuthal direction in a spherical star (the symmetry direction).

We have chosen to simulate a box with dimensions $[L_x, L_y, L_z] = [4, 4, 1]$ in our system of units, with a uniform grid in each dimension having a resolution of $1024\times1024\times8$. Here we aim to study motions that are independent of z, hence the small number of grid points in this dimension. The magnetic field is confined to a cylinder with radius $a = 1$ centred within the box. The width of the box effectively sets the length scale of the problem, while the buoyancy frequency, which we have chosen to be a global constant $N^2 = 1$, sets the time scale. Note that this local box model follows from the general axisymmetric case in

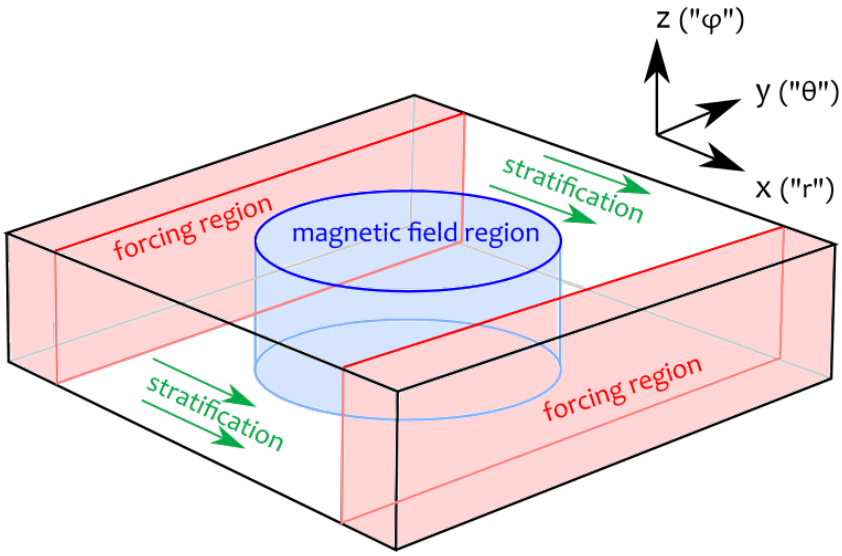

Figure 9.1: A schematic of the simulation box setup, showing the cylindrical region containing the magnetic field (blue) and forcing strip (red). The stratification is imposed along the x direction. The three Cartesian axes x, y and z are analogues of the r, θ and ϕ directions, respectively, if one considers the helix to lie on the equatorial plane of a spherical star.

the high-wavenumber limit, but applied to a special field configuration that is a slender torus encircling the equator. The simulation setup is shown in Figure 9.1.

In the absence of a magnetic field, the normal modes are plane waves having an integer number of undulations within the box in each of the x-, y- and z-directions. It is convenient to label these modes by a triplet of integers $[i, j, k]$ representing the number of wavelengths spanned in each direction: for example, $[i, j, k] = [4, 5, 2]$ denotes a plane wave with four undulations across the box in the x-direction, five in the y-direction and two in the z-direction. The associated wavevector is given by

$$\mathbf{k} = (k_x, k_y, k_z) = 2\pi \left(\frac{i}{L_x}, \frac{j}{L_y}, \frac{k}{L_z} \right) . \tag{9.22}$$

These modes are gravity modes, and so the frequency ω is given by the dispersion relation for gravity waves $\omega^2 = \kappa_\perp^2 N^2$, where

$$\kappa_\perp^2 \equiv \frac{k_y^2 + k_z^2}{k_x^2 + k_y^2 + k_z^2} . \tag{9.23}$$

Recall that in solar-like oscillators, the source of energy for gravity-wave excitation lies in the convective envelope, outside the stably stratified, possibly magnetised region. To model this, we applied a continuous forcing to the region $|x| > 1.5$, which lies exterior to the field-containing cylinder. This forcing begins at $t = 0$, and is applied to an initially stationary background. We ran two sets of simulations, with plane-wave forcing patterns having $[i, j, k] = [15, 20, 0]$ and $[25, 5, 0]$. We shall refer to these as 'steep' and 'shallow' (with respect to the stratification). These correspond to the analogues of axisymmetric modes as there is no z-(ϕ-) dependence. The fluid in the forcing regions was driven at the frequency associated with the wavevector of the mode, as given by the gravity dispersion relation. These are $\omega_f = 0.8$ and 0.196 for the steep and shallow runs, where the subscript f denotes 'forcing'. To satisfy the incompressible condition, the fluid velocity $\mathbf{u}$ at

any point $\mathbf{x}$ must obey $\mathbf{k}\cdot\mathbf{u}=0$, i.e. it must be proportional to the vector

$$\hat{\mathbf{u}} = \left(\kappa_\perp, -\frac{\kappa_x\kappa_y}{\kappa_\perp}, -\frac{\kappa_x\kappa_z}{\kappa_\perp}\right), \tag{9.24}$$

where κ_x, κ_y and κ_z are the components of $\mathbf{k}/|\mathbf{k}|$, and we additionally use the condition that the perpendicular components of $\mathbf{u}$ and $\mathbf{k}$ (with respect to the stratification) must be parallel. The functional form of the forcing function (fluid acceleration) is given by

$$\mathbf{f} \propto \begin{cases} \hat{\mathbf{u}}\cos(\mathbf{k}\cdot\mathbf{x})\cos(\omega_f t) & \text{if } |x| > 1.5 \\ 0 & \text{otherwise,} \end{cases} \tag{9.25}$$

with the overall amplitude for the moment arbitrary. In each run, internal gravity waves were generated and observed to propagate towards the centre of the box, whereupon a quasi-steady state solution was eventually reached after several information crossing times. The amplitude of the forcing was set to be the same for all runs, and was such that maximum fluid velocities did not exceed 10^{-3}. This is smaller than the group speed of gravity waves (0.015 and 0.025 for the steep and shallow runs), and translates to characteristic fluid displacements of 0.01 units, which is much smaller than the box width and extent of the field region. Note that the amplitudes of excited motions in solar-like oscillators are, likewise, much smaller than the stellar radius.

For each of the two sets of $[i, j, k]$ forcing patterns, six different field strengths, both above and below the critical value, were simulated. In the non-dimensionalisation scheme used in SNOOPY, the critical field strength is given simply by $B/\sqrt{\rho} \sim \omega_f/|\mathbf{k}|$. This evaluates to 0.02 for the steep run and 0.005 for the shallow run. To control the strength of the field, we condensed the scalar multiplying factors in (3.62) into a single parameter, $B_s \equiv \kappa\rho/\lambda$. Note that the field strength varies over space, and so B_s is only a characteristic value of the field rather than the maximum. The maximum field strength, attained at $R = 0$, is about three times this. The choice of Reynolds numbers was constrained by the need for the length scale of physical (thermal and viscous) diffusion associated with the oscillation time scale to be smaller than the wavelength of the forced mode (0.16 units) and larger than the spacing of the grid (0.004 units). This sets a usable range between $\sim 10^4$–10^6. We opted for $\mathrm{Re} = \mathrm{Rt} = 10^5$ for the steep run and $\mathrm{Re} = \mathrm{Rt} = 4\times10^5$ for the shallow run. The four-fold difference in these values owes to a desire to maintain a similar diffusion length scale, since the associated time scales (wave periods) differ by a factor of about four. See Table 9.1 for a summary of parameters used.

The characteristic box-crossing times (in the x-direction, based on the gravity wave group velocity) are 80 and 200 time units for the steep and shallow runs, respectively. Each simulation was allowed to proceed for 1200.0 time units, with the velocity fields sampled at intervals of 1.0 time units. For comparison, forcing periods were 7.85 and 32.1 units for the steep and shallow runs, consistent with the gravity dispersion relation. We chose to discard the first 200 time units of data in subsequent analysis, to remove transient signals associated with the settling-in phase. To investigate the natural response of the system, the forcing was switched off at $t = 1000.0$. Note that plots of the results in subsequent sections are restricted to either the forced interval $200 < t < 1000$ or the unforced interval $1000 < t < 1200$.

An important aspect about how the cylindrical Prendergast solution differs qualitatively from the spherical Prendergast solution must be noted here. While in the spherical version, for an incompressible fluid, there exists a coupling between axisymmetric spheroidal and torsional motions through the Lorentz force,

Table 9.1: Parameters used for the 12 SNOOPY simulation runs. The box size of $[L_x, L_y, L_z] = [4, 4, 1]$ and resolution of $1024 \times 1024 \times 8$ are common between all runs, as are the location and extent of the magnetic field and forcing regions.

$[i, j, k]$	ω_f	B_s	Re=Rt	Rm
[15, 20, 0] (steep)	0.8	0	10^5	10^6
		0.005		
		0.01		
		0.02		
		0.04		
		0.08		
[25, 5, 0] (shallow)	0.196	0	4×10^5	10^6
		1.25×10^{-3}		
		2.5×10^{-3}		
		0.005		
		0.01		
		0.02		

this coupling vanishes when the radial distance from the axis of symmetry is taken to be infinite (cylindrical limit). In our setup, the x, y-plane is analogous to the meridional plane of a sphere and the z-axis is analogous to the azimuthal direction. For the spherical Prendergast solution, the Lorentz force perturbation associated with pure spheroidal motions has, to first order, a non-zero component in the torsional direction. However, for the cylindrical Prendergast solution, the z-component of the Lorentz force perturbation associated with pure x, y motions is zero to first order.

To see this, let us begin by considering the perturbation to the Lorentz force by asixymmetric disturbances in the spherical case, denoting the azimuthal (torsional) direction by φ and distance from the axis of symmetry by r. For an axisymmetric background field, the magnetic pressure term makes no contribution to the φ-component of the Lorentz force, and so we are left to examine the magnetic tension term,

$$[(\mathbf{B}\cdot\nabla)\mathbf{B}]'_\varphi = (\mathbf{B}_0\cdot\nabla)B'_\varphi + (\mathbf{B}'\cdot\nabla)B_{0\varphi} + \frac{B'_\varphi B_{0r}}{r} + \frac{B_{0\varphi}B'_r}{r}\,. \tag{9.26}$$

Subscript '0's denote background quantities, and primes denote perturbations about the background. The cylindrical Prendergast solution corresponds to the limit where $r \to \infty$, with φ replaced by the Cartesian coordinate z. The last two terms on the right-hand side of Equation (9.26), which are associated with spatial curvature of the coordinates, thus vanish. If in addition, we impose incompressibility ($\nabla\cdot\boldsymbol{\xi} = 0$), and eliminate all other perturbed quantities in favour of $\boldsymbol{\xi}$ using the linearised induction equation $\mathbf{B}' = \nabla\times(\boldsymbol{\xi}\times\mathbf{B}_0)$, we find that in the limit of $r\to\infty$

$$[(\mathbf{B}\cdot\nabla)\mathbf{B}]'_\varphi \to [(\mathbf{B}\cdot\nabla)\mathbf{B}]'_z = -\boldsymbol{\xi}\cdot\nabla(\mathbf{B}_0\cdot\nabla B_{0z})\,. \tag{9.27}$$

This equals zero, since $\mathbf{B}_0\cdot\nabla B_{0z}$ corresponds to the z-component of the magnetic tension associated with the background (equilibrium) field. No other forces act in this direction, and so it must be zero.

It would be desirable to be able to investigate the mutual excitation of (the analogues to) spheroidal and torsional motions discussed previously in §6.3.2, using our non-linear Boussinesq simulations. Note that

this coupling in general vanishes in the limit of zero wavelengths, but is present for finite wavelengths when the appropriate curvature in the system exists. Given that the cylindrical Prendergast field configuration does not replicate this property of the spherical version owing to the lack of curvature in the symmetry direction, this coupling between x, y motions and the z-direction must be artificially induced. To achieve this, we modified the functional form of the Lorentz force within SNOOPY, namely by adding equivalents of the curvature term (proportional to $1/r$) to the z-component of the Lorentz force. More specifically, we defined a new parameter $r_{\rm fake}$ and replaced

$$\mathbf{B}\cdot\nabla B_z \rightarrow \mathbf{B}\cdot\nabla B_z + \frac{B_x B_z - B_{0x}B_{0z}}{r_{\rm fake}}, \tag{9.28}$$

where B_{0x} and B_{0z} are the x- and z-components of the initial field configuration given by (3.62), and the remaining terms correspond to values at the current time step in the simulation. The coupling parameter $r_{\rm fake}$ represents the characteristic radius of curvature in the symmetry direction. For the spherical Prendergast solution, this is of order the size of the field region itself, and so we set $r_{\rm fake} = a$.

9.3 Results & discussion

9.3.1 Hydrodynamic gravity modes

We performed a numerical test to check that the normal modes of the fluid in the box did indeed display the expected behaviour of gravity modes, meaning that their frequencies and wavenumbers matched those of the gravity dispersion relation $\omega^2 = \kappa_\perp^2 N^2$. To do this, we ran a set of 17 simulations with different values of i and j, and with k set to zero. For each, we gave the system an initial forcing for a short period of time, and then measured the resulting frequency of oscillation. For each $[i, j]$ combination, the corresponding plane-wave spatial pattern was applied under a uniform acceleration for $0 < t < 1$, then the acceleration was turned off and the system was allowed to evolve freely of its own accord. Most runs were terminated artificially at $t = 50$, but several with slower ensuing oscillations were left to run until $t = 100$. In each case, periodic oscillations were observed to develop. The frequency of oscillation was taken to be half the value of the highest peak in the power spectrum of the box-averaged kinetic energy, restricted to $t > 1$.

The resulting frequencies as a function of $\kappa_\perp$ are shown in Figure 9.2. All points appear to fall close to the expected frequency for gravity modes (red dashed line), supporting the notion that the hydrodynamic modes of the box are indeed pure gravity modes. Some small amount of scatter is present; this is likely to reflect measurement uncertainties arising from the finite frequency resolution of the Fourier transform (limited number of oscillation cycles within the duration of the simulation). Nonetheless, the results of this test reassure us that the chosen frequencies of forcing do indeed match those of the normal modes in the box. This is also important for later when we investigate the effects of the magnetic field in potentially destroying the resonant properties of the hydrodynamic modes.

9.3.2 Imposition of a magnetic field

In the remaining sections, we present the results of simulations containing a magnetic field, namely those listed in Table 9.1. Figures 9.3–9.6 show the amplitudes of the temporal Fourier transform of the x and y-components of the fluid velocity at each point on the grid, at the value of the forcing frequency (computed over the forced interval $200 < t < 1000$). Both components show very similar features, a consequence of

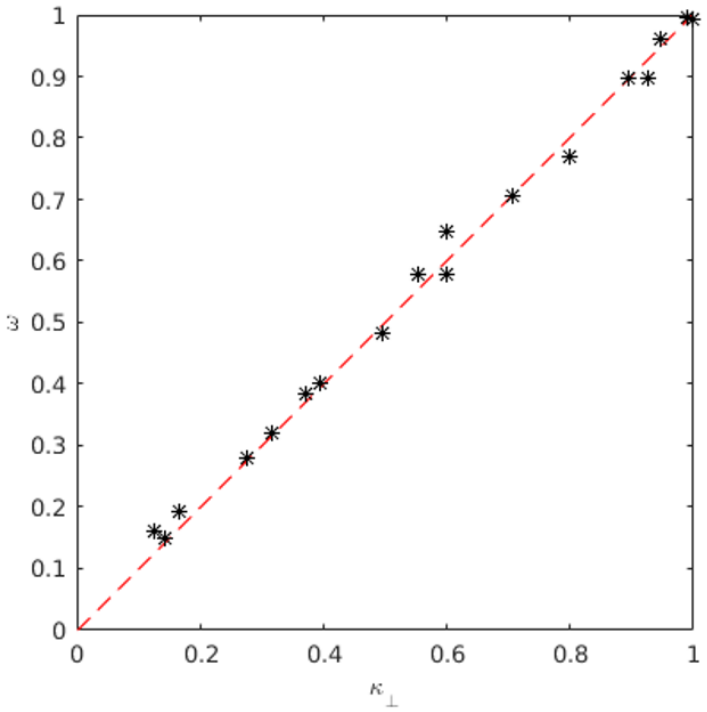

Figure 9.2: Frequency of oscillation as measured from the power spectrum of the box-averaged kinetic energy in the SNOOPY simulations, as a function of the imposed $\kappa_\perp$ (asterisks). The red dashed line has a slope of $N^2 = 1$, corresponding to the expected frequency from the gravity dispersion relation.

them being related through $\nabla \cdot \mathbf{u} = 0$. The results are displayed at the value of the forcing frequency, where the power spectrum of the fluid velocity exhibits a sharp peak as one might expect of a forced oscillator (this is shown in Figure 9.7 for one of the runs). In Figures 9.3–9.6, the six panels show different values of the field strength going from zero (purely hydrodynamic) to strongly magnetised. A convenient indication of the strength of the field is the presence or absence of what we shall refer to as *critical surfaces*, i.e. where the Alfvén frequency at the forced wavenumber equals the forcing frequency. These surfaces are plotted in blue. In the absence of modifications to the wavelength of the incoming waves, they physically represent surfaces where the resonance criterion is satisfied and the magnetic field might be expected to become important. We shall loosely refer to the simulations in which no critical surfaces exist as 'weak field' and those in which they do as 'strong field'.

In both steep and shallow sets of simulations, a qualitative transition in wave propagation coincides with the transition from weak to strong fields (appearance of critical surfaces). In the weak-field regime, small distortions to the gravity-wave phase fronts are present within the field region, but the fronts otherwise remain intact. In the strong-field regime, these become severely disrupted, but the way in which this happens depends crucially on their orientation. For the steep runs, the wave energy at the point of disruption becomes concentrated into arcs aligned along the flux surfaces roughly tangent to the critical surfaces. This can be seen most clearly in Figure 9.4, which plots the u_y field, where the arcs appear to be roughly aligned along the y-direction. There is little penetration of fluid motion past this point. The efficiency of the expulsion increases with field strength (note that the same colour scale has been used on all panels of the same figure). For shallow runs, rather than being trapped within the field region, there is instead reflection of the waves off the critical surfaces and back out of the field region. This can be seen through the organised interference patterns that form above and below the cylinder; note that the group velocity in the shallow case is directed nearly parallel to the y-axis, and so the location of the interference patterns supports the interpretation that the reflection is of a near-specular kind with respect to the stratification, where only the y-component of the group velocity flips sign.

9.3.3 What of torsional Alfvén resonances?

In §6.4, we discussed the resonant excitation of torsional modes through coupling with spheroidal modes. The analogous process here is the coupling of motion in the x, y-('meridional') plane into motions in the z-('azimuthal') direction. Axisymmetric torsional modes take the form of standing Alfvén waves on magnetic flux surfaces, which for the cylindrical Prendergast model can be shown to be simple sinusoids (since the Alfvén speed is constant on flux surfaces) with an integer number of wavelengths around the circumference. The associated fundamental vibration frequency $\omega_A(R)$ is given simply by the Alfvén speed $v_A(R)$ divided by the circumference, and multiplied by 2π. Each flux surface supports in principle an infinite number of modes corresponding to the spectrum of vibrational harmonics, with frequencies that are integer multiples of the fundamental. If the spheroidal mode can be regarded as an external driver, one expects flux surfaces on which there exist torsional modes whose frequencies match that of the spheroidal mode to resonate with that mode.

The SNOOPY simulations indeed display evidence for this resonant excitation. Fourier plots of the z-component of the fluid velocity, visualised in an identical manner to Figures 9.3–9.6, are shown in Figure 9.8 for a selection of field strengths. At low field strengths (no critical surfaces), the u_z patterns tend to be slaved

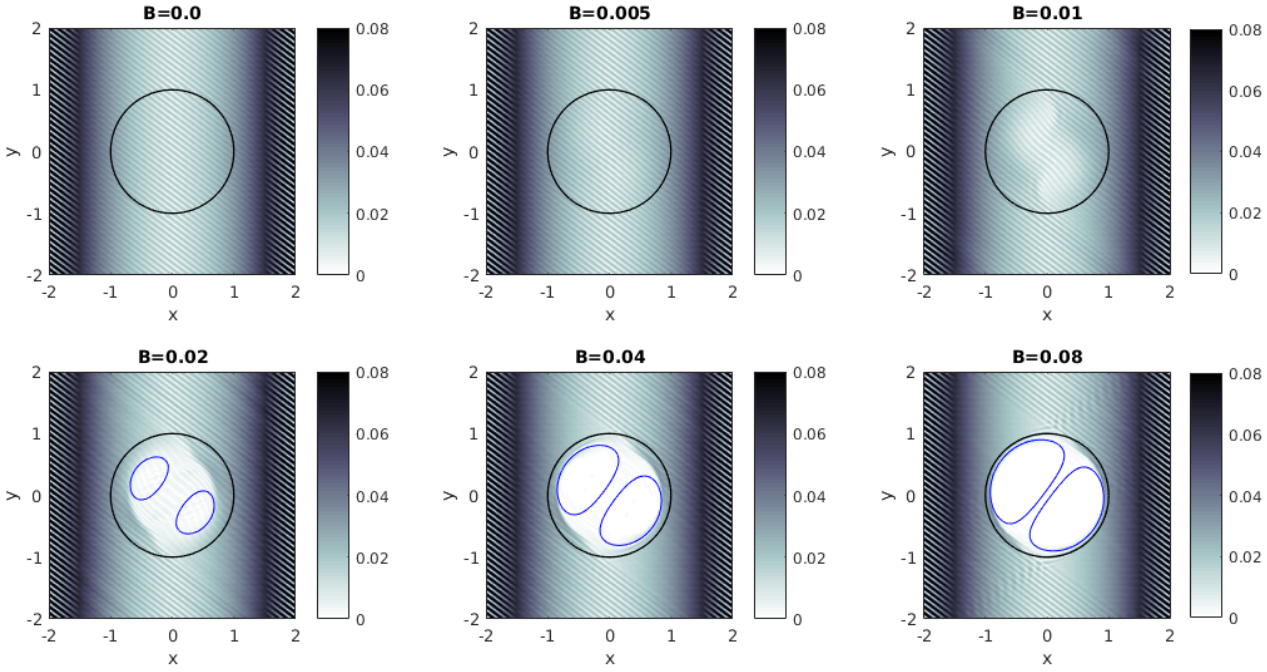

Figure 9.3: Spatial distribution of the temporal Fourier amplitude at the forcing frequency $\omega_f = 0.8$ for the u_x field, at the six values of the field strength simulated with SNOOPY. The Fourier transform is taken over the interval $200 < t < 1000$. The forced mode has $[i, j, k] = [15, 20, 0]$ (steep), and the forcing region lies in the strip outside $|x| > 1.5$. The black circle of radius 1 marks the boundary of the field region, and overlaid in blue are critical surfaces (i.e. where $\omega_f = \omega_A = \mathbf{k}\cdot\mathbf{v}_A$, $\mathbf{k}$ in this case being the forced wavenumber). The critical field strength here is $B \sim 0.02$.

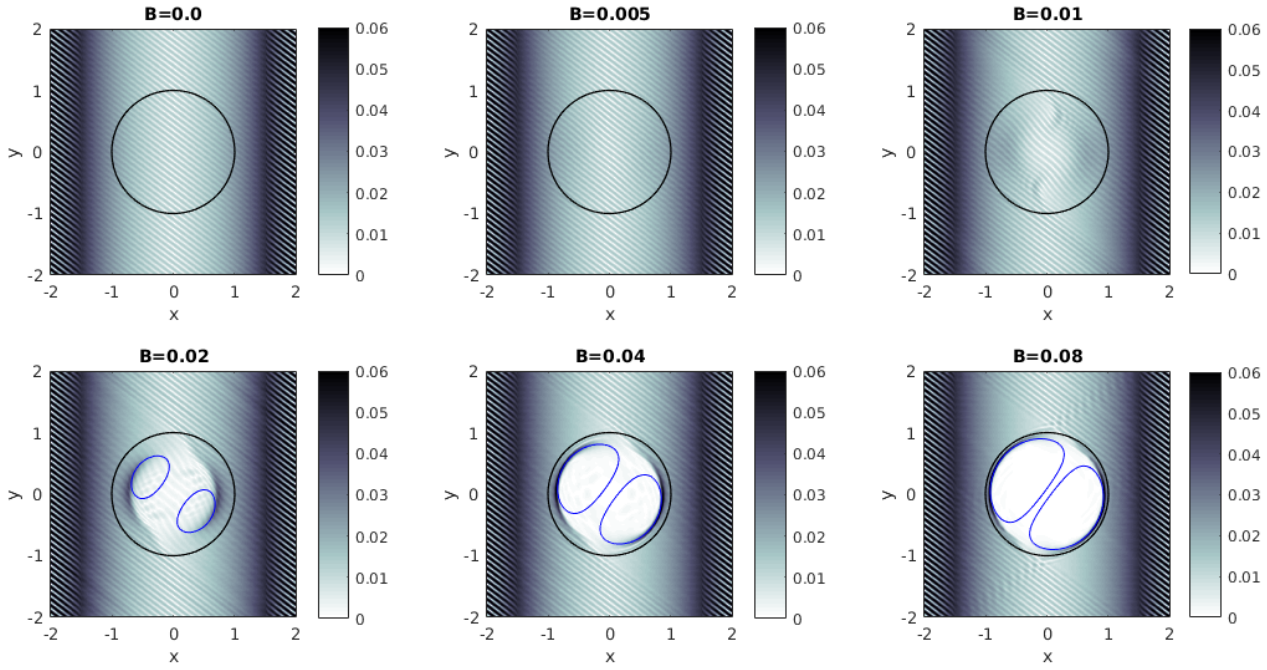

Figure 9.4: As for Figure 9.3, but showing u_y.

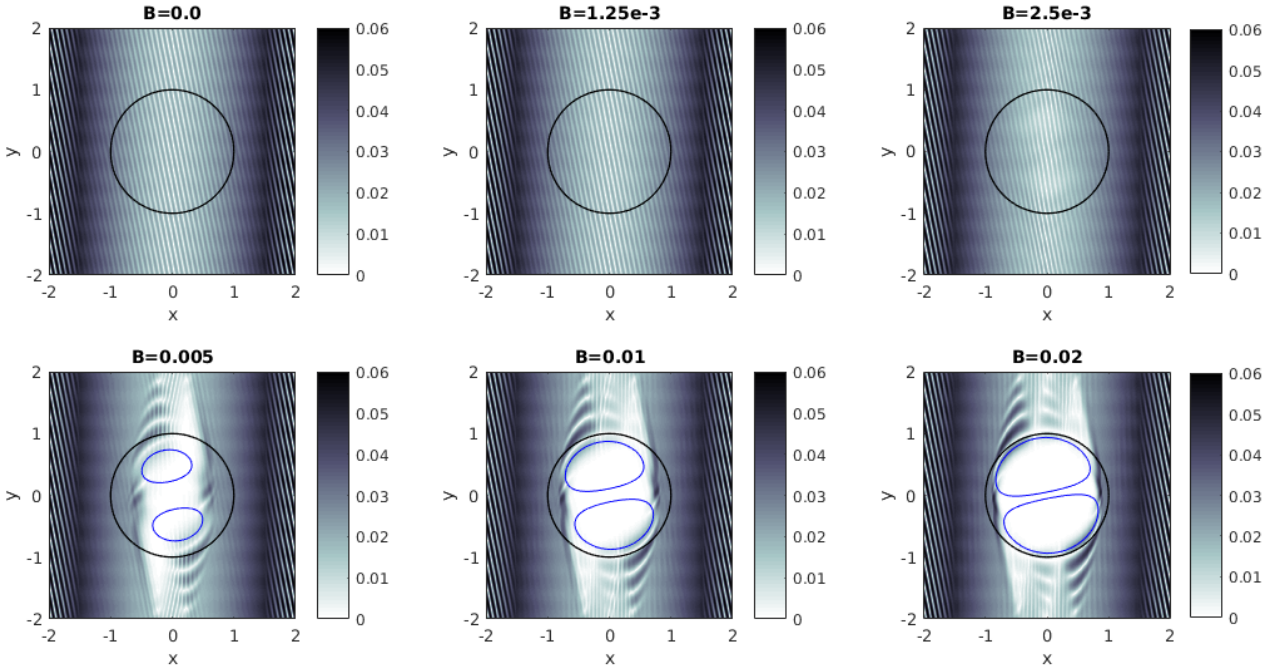

Figure 9.5: As for Figure 9.3, but for the runs with $[i, j, k] = [25, 5, 0]$ (shallow). The forcing frequency in this case is $\omega_f = 0.196$, and the critical field strength is $B \sim 0.005$.

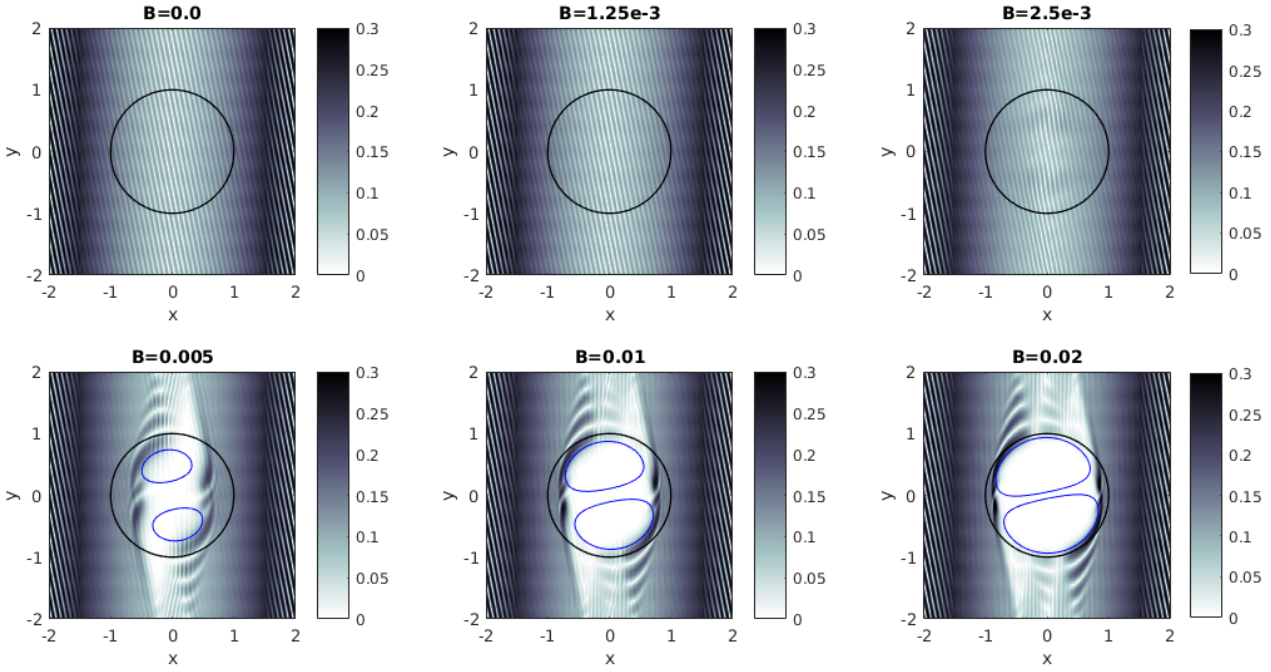

Figure 9.6: As for Figure 9.5, but showing u_y.

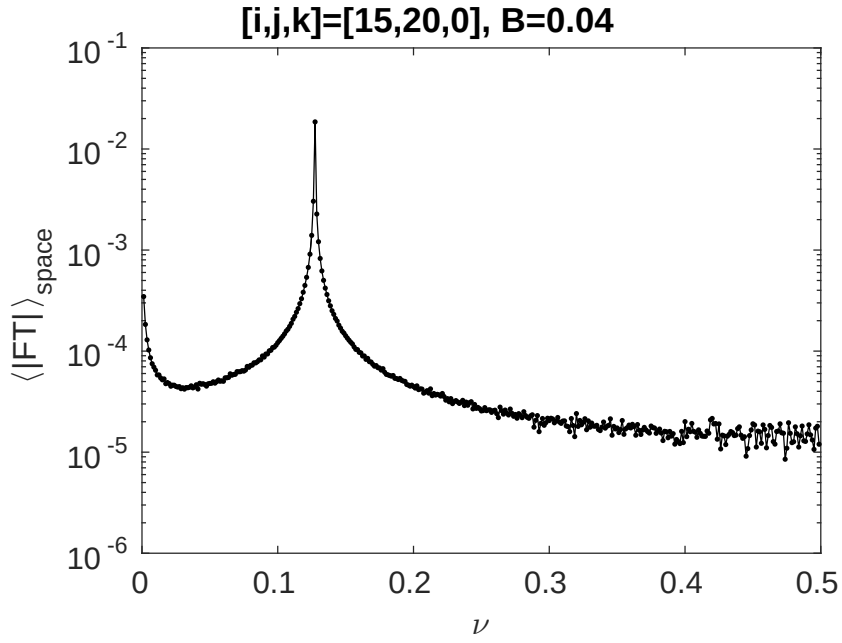

Figure 9.7: Spatially averaged u_y Fourier amplitude as a function of frequency, for the steep run, $B = 0.04$, $200 < t < 1000$. The averaging has been restricted to the region within $|x| < 1.4$ to avoid the forcing strip. Note that the vertical axis is logarithmic. A substantial peak occurs at the value of the forcing frequency, $\nu = \omega/(2\pi) = 0.127$. Very similar plots are obtained for all other field strengths and also for the shallow run.

to the underlying spheroidal velocity field. This is consistent with the magnetic field having less dynamical importance compared to buoyancy effects: the low Alfvén speed compared to the gravity-wave phase speed means the magnetic field has no time to produce its own response. However, for strong fields, the u_z patterns organise themselves along magnetic flux surfaces (concentric circles), indicating the acquisition of a substantial Alfvén character. We observe, particularly for the lower two panels, that motions tend to develop on discrete radial surfaces. We interpret these to be the resonant surfaces discussed above.

A means of quantifying the properties of the u_z patterns is through a Fourier analysis localised to magnetic flux surfaces. That is, for each value of R, we extract the u_z values from the SNOOPY simulations and then perform a Fourier transform as a function of time and distance along the circumference (azimuthal direction). The resulting Fourier amplitudes are analogous to the a_j coefficients introduced in §6.4.1, which give an indication of the coupling strengths between the driving pattern and each torsional mode. These are shown plotted in Figure 9.9 for a selection of field strengths from the steep run. What we find is that for weak fields (top row), the modes that are preferentially excited are those that have wavelengths close to that of the forcing, even if their natural frequencies are significantly discrepant with the forcing frequency. In this regime, the weakness of the magnetic field renders it dynamically unimportant, and so motions are slaved to the driving pattern (Alfvén speeds are not sufficient for the Lorentz force to back-react).

In contrast, for strong fields (two bottom rows), it is the modes whose natural frequencies match that of the forcing that are most effectively excited. We interpret this as evidence of resonant interaction with the field. There is an apparent mismatch in spatial scales, but this can be attributed to the strong modification of incoming waves by the magnetic field: on close inspection, the spatial scales of the u_x and u_y patterns found inside the critical surfaces are considerably larger than those outside, and they increase with increasing field

strength. Physically, this can be understood as the magnetic field providing an additional restoring force for the waves, boosting their phase speed at a given wavenumber. To maintain the same frequency, the wavelength must lengthen (cf. the passage of light from a medium of high to low refractive index). Thus in actuality, the wavenumbers measured for the torsional modes more closely match those of the underlying spheroidal motions than naïvely suggested by Figure 9.9.

Previously, we identified phase mixing as an important physical process for dissipating energy from torsional Alfvén waves excited resonantly by spheroidal gravity modes (see §6.4.3). The net effect is to damp the spheroidal motions at a rate that depends only on the efficiency of spheroidal-torsional mode coupling. While our results appeared to yield damping rates of a level consistent with observations, an unverified assumption was that the structure of the spheroidal modes was unaffected by the magnetic field at the strengths required for the mechanism to be efficient. The SNOOPY simulations have provided a straightforward means of checking this, a task that is analytically non-trivial to accomplish. They show that although spheroidal-torsional resonant coupling seems to be occurring, this is unlikely to be effective as a means of damping the spheroidal modes in the context of the dipole dichotomy problem. The reason for this is the expulsion of wave action from the regions within the critical surfaces, leading to very low amplitudes of the driving motions in the strong-field regions where the potentially large number of torsional resonances reside. The physical origin of this expulsion/attenuation will be discussed later in Chapter 11. Importantly, this suggests that our calculation of damping rates in Chapter 6, based on the assumption that the structure of the spheroidal modes is unaffected within the field region, is invalid in the regime of field strengths where it might otherwise be effective. The quantitative impact on the associated damping rates, if given by the square of the reduction factor in wave amplitudes inside and outside the critical region, would be to reduce these by around four orders of magnitude. This suggests that the torsional Alfvén resonance mechanism may have problems in accounting for the observations.

9.3.4 Magnetogravity modes

We now investigate the possibility of survival of modes in the presence of a field. The forcing frequencies of $\omega_f = 0.196$ and 0.8 for the shallow and steep runs were chosen to correspond to those of pure gravity modes. We saw in the previous section that during the interval where the forcing is continuously applied, the response of the system peaks at the corresponding frequency. This is an expected property of any forced oscillator, whether or not the forcing frequency matches any natural frequency of the system. One might be curious as to whether the presence of a strong magnetic field destroys the ability of the system to support normal modes, as previously suggested by other authors (Fuller et al., 2015; Lecoanet et al., 2017). In order to test this, we turned the forcing off at $t = 1000.0$ and allowed the system to evolve naturally. We considered both steep and shallow runs, at two values of the field strength: zero, and the second-largest value.

If the steady-state patterns in Figure 9.3–9.6 do not in fact correspond to normal modes, one expects their spatial and temporal coherences to break down within several oscillation periods after the forcing ceases. On the contrary, we find that the velocity field continues to undergo periodic oscillations at a frequency equal to that of the forcing (within measurement precision). Furthermore, there is no change to the spatial structure of the pattern associated with this frequency. On top of these oscillations, and independent of the field strength, there is a slower exponential decay that can be attributed to viscous dissipation. The left column of Figure 9.10 shows the spatially averaged amplitudes of the temporal Fourier transform of

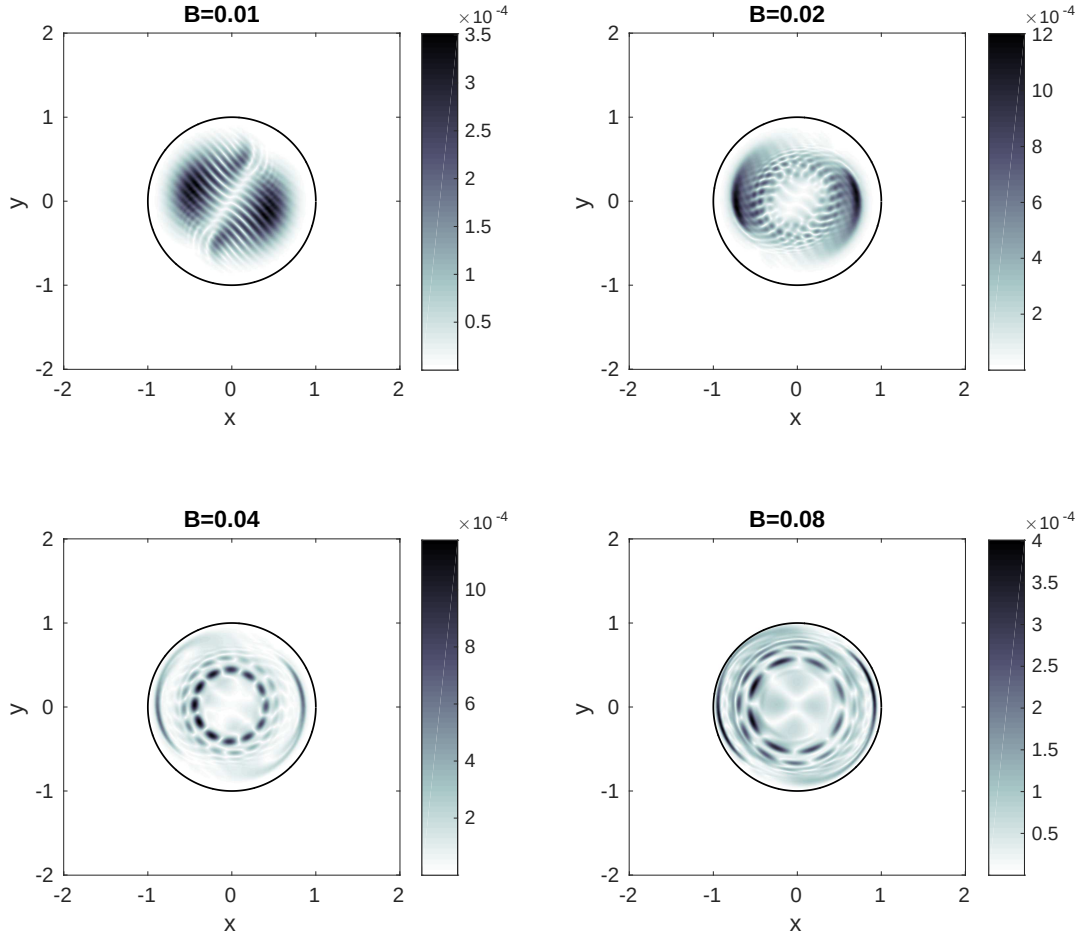

Figure 9.8: Spatial distribution of the temporal Fourier amplitudes of the u_z component, at four different values of the field strength, for the SNOOPY run with $[i, j, k] = [15, 20, 0]$ (steep) at the forcing frequency $\omega_f = 0.8$. The Fourier transform is taken over the interval $200 < t < 1000$. The field region boundary is indicated by the black circle. Critical surfaces are present for all except the top left panel ($B = 0.01$).

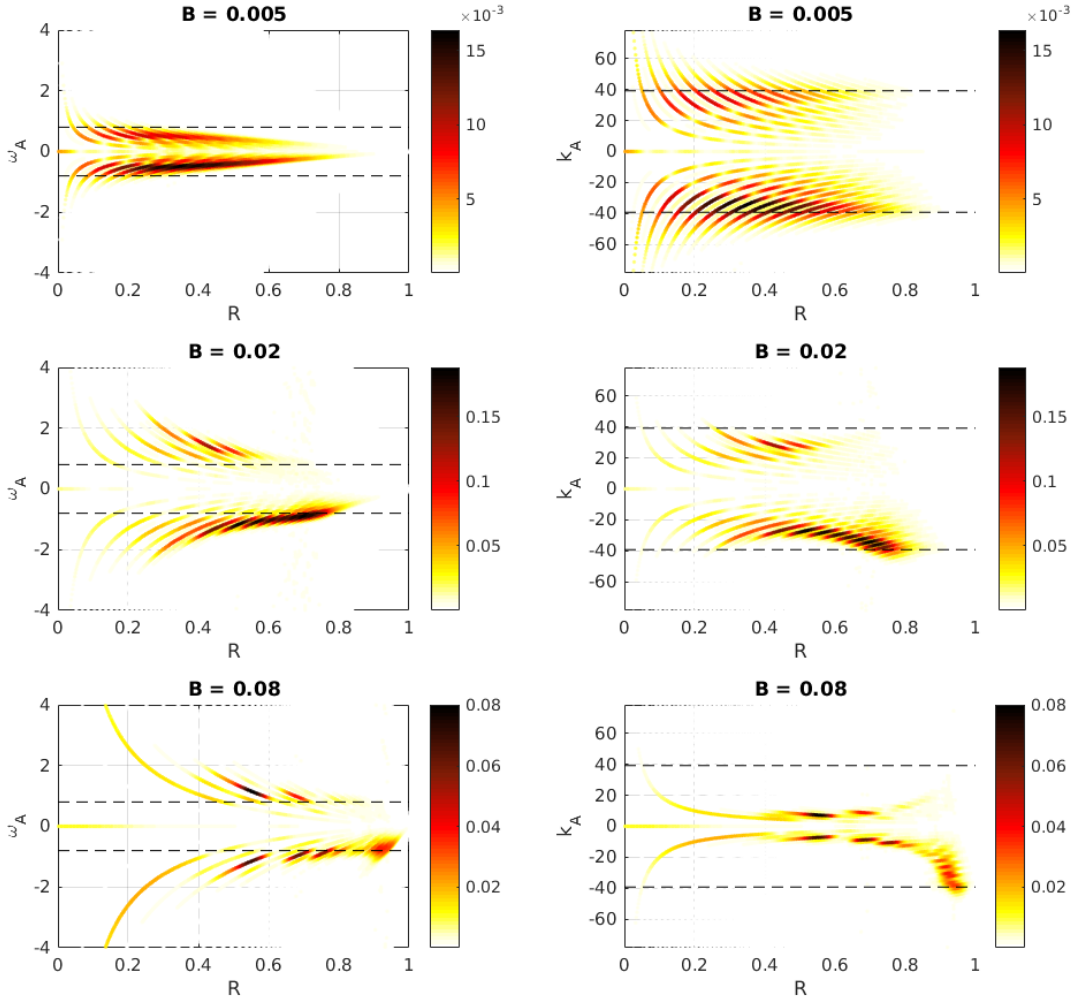

Figure 9.9: Absolute values of the coefficients of eigenfunction decomposition of the u_z response (e.g. Figure 9.8) into torsional Alfvén modes inside the region of non-zero magnetic field, as a function of radial distance. Note that $\psi = \psi(R)$, i.e. flux surfaces are concentric circles, so each value of R corresponds to a particular flux surface. These are for the SNOOPY run with $[i, j, k] = [15, 20, 0]$ (steep), at the value of the forcing frequency, over the interval $200 < t < 1000$. The three rows correspond to three different field strengths, the lower two for which critical surfaces exist. In the left-hand column, the vertical axis corresponds to the associated Alfvén freqeuncy $\omega_A = k_A v_A$, while in the right-hand column, the vertical axis corresponds to $k_A = \mathscr{J}/R$, where $\mathscr{J} \in \mathbb{Z}$ is the harmonic index. Dashed lines indicate the forcing frequency ω_f (left-hand column) and the forced wavenumber (right-hand column) for comparison.

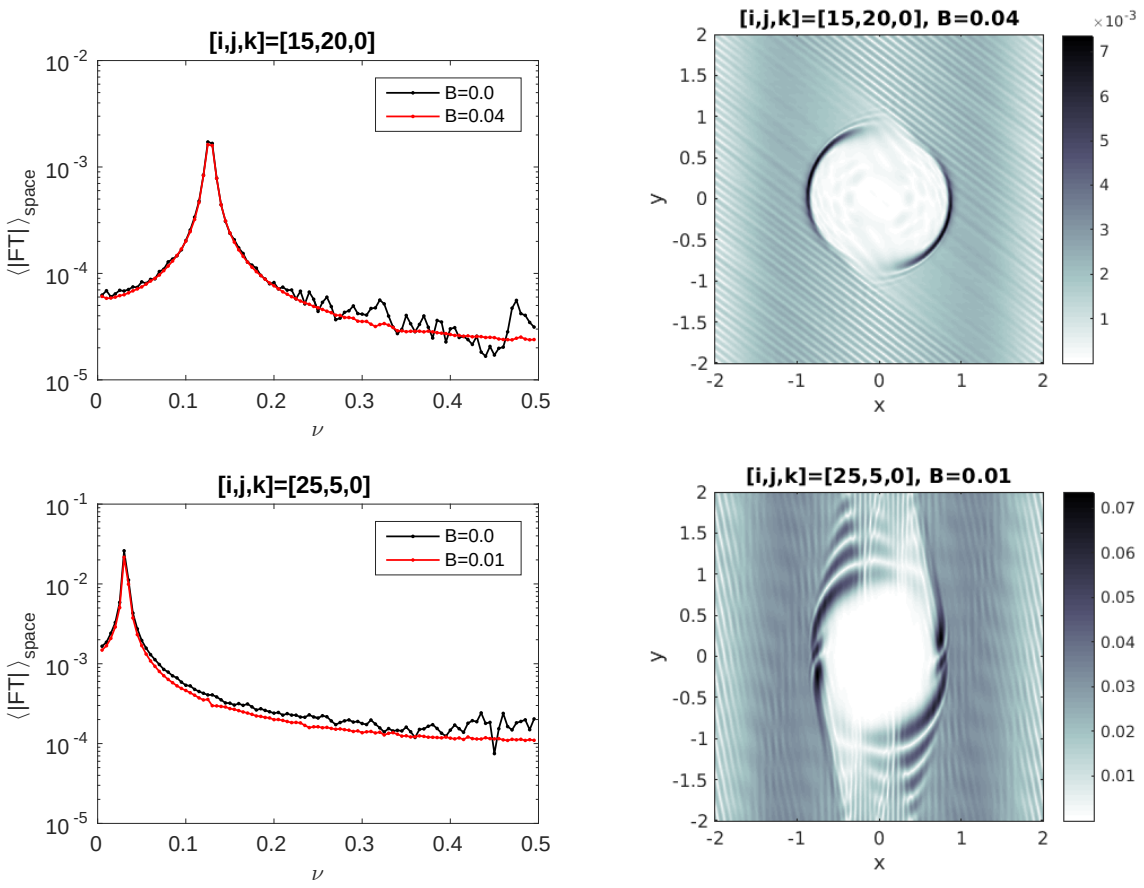

Figure 9.10: Left: Spatially averaged u_y Fourier amplitude as a function of frequency, computed over the interval $1000 < t < 1200$, i.e. after the forcing has been turned off, for the steep (top) and shallow (bottom) runs. The averaging is taken over the whole box. Black corresponds to purely hydrodynamic runs, while red corresponds to strong-field runs. Right: Corresponding spatial distribution of the u_y Fourier amplitudes, at the frequencies corresponding to the peaks on the left.

the u_y fields for each of the four cases (steep and shallow, and zero and strong fields). A clear peak appears in all cases, at the frequency matching the original forcing frequency for that run. This frequency is the same regardless of whether or not there is a field present, which suggests that a strong field does not disrupt the temporal coherence of the oscillation. The right column of Figure 9.10 shows the spatial distribution of the Fourier amplitudes associated with the frequency peaks on the left. They are remarkably similar to the patterns seen in Figures 9.3–9.6, suggesting that these do in fact correspond to normal modes of oscillation in the magnetised case. Importantly, these results demonstrate that coherent oscillations can be sustained in the presence of a strong magnetic field, even if the spatial structure is significantly modified compared to the hydrodynamic case, and the associated frequencies may not be significantly different from the pure g-modes.

Chapter 10

Hamiltonian Wave Dynamics

Previously in Chapter 9, we discussed results obtained from numerical simulations of magnetogravity waves. Useful complementary insights can be gained by applying a Hamiltonian formalism, which we will now introduce, to the same problem. While commonly encountered in the context of solving for particle trajectories in solid mechanics, Hamiltonian dynamics can also be applied to problems in continuum mechanics. Rather than providing a global description like in full wave calculations, one follows the phase-space trajectories of local wave packets (rays) to obtain information about the paths of energy flow within the system. In the present chapter, we investigate the dynamics of Hamiltonian magnetogravity rays and discuss implications for the properties of global modes. Later in Chapter 11, we shall directly compare the results of Hamiltonian ray tracing with the SNOOPY simulations.

10.1 Background

10.1.1 Formalism

Hamilton's equations can be derived from the Lagrangian formalism through a Legendre transformation with respect to the velocities. That is, for a given Lagrangian L, with coordinates q_i and conjugate momenta p_i ($i = 1, 2, \cdots, N$ where N is the dimensionality of the system), the corresponding Hamiltonian H is given by

$$H = \sum_{i=1}^{N} \left(p_i \dot{q}_i \right) - L \,. \tag{10.1}$$

Since the conjugate momenta

$$p_i = \frac{\partial L}{\partial \dot{q}_i} \tag{10.2}$$

have the property that

$$\dot{p}_i = \frac{\partial L}{\partial q_i} \,, \tag{10.3}$$

which follows from extremisation of the action integral $\int L \, \mathrm{d}t$, considering the two differentials

$$\mathrm{d}L = \frac{\partial L}{\partial t} \, \mathrm{d}t + \sum_i \dot{p}_i \, \mathrm{d}q_i + \sum_i p_i \, \mathrm{d}\dot{q}_i \tag{10.4}$$

$$\mathrm{d}H = \frac{\partial H}{\partial t} \, \mathrm{d}t + \sum_i \frac{\partial H}{\partial q_i} \, \mathrm{d}q_i + \sum_i \frac{\partial H}{\partial p_i} \, \mathrm{d}p_i \tag{10.5}$$

lets us identify

$$\dot{q}_i = \frac{\partial H}{\partial p_i}, \quad \dot{p}_i = -\frac{\partial H}{\partial q_i}. \tag{10.6}$$

These are known as *Hamilton's equations*, and their solution yields the trajectories of the system. One can immediately see that if H is independent of any coordinate q_i, then the corresponding conjugate momentum p_i will be conserved.

In solid mechanics, the Hamiltonian H has a physical interpretation as the total energy (kinetic plus potential) of the system. For example, for a one-dimensional simple harmonic oscillator of mass m attached to a spring with spring constant k, we would have

$$H = \frac{p^2}{2m} + \frac{kq^2}{2}, \tag{10.7}$$

yielding the equations of motion

$$\dot{q} = \frac{p}{m}, \quad \dot{p} = -kq \tag{10.8}$$

and solution

$$q(t) = A\cos\left(\sqrt{\frac{k}{m}}t\right) + B\sin\left(\sqrt{\frac{k}{m}}t\right), \tag{10.9}$$

where A and B are arbitrary constants to be determined by boundary conditions. While the above example is trivial, the strengths of the Hamiltonian approach can be exploited to far greater effect for complex many-body systems, such as those that occur in problems of celestial mechanics.

10.1.2 Application to continuum mechanics

Besides solid-body dynamics, Equations (10.6) can also be applied to studying wave phenomena in continuum mechanics. For example, they have been used extensively in the study of MHD wave propagation in the Earth's magnetosphere (Haselgrove, 1955; Dyson, 1967; Walker, 2004; Fung & Green, 2005). Physically, the trajectories yielded by solving Hamilton's equations correspond to those of wave packets launched in the system. This can be thought of as the classical limit of quantum mechanics, where wave packets whose wavelengths are much smaller than the length scales of variation in the background behave like particles.

To see how Hamilton's equations arise in the wave context, let us consider the Fourier-space representation $\tilde{\boldsymbol{\xi}}(\mathbf{k})$ of the fluid displacement $\boldsymbol{\xi}(\mathbf{x}, t)$, which can be written

$$\boldsymbol{\xi}(\mathbf{x}, t) = \iiint \tilde{\boldsymbol{\xi}}(\mathbf{k})\, \mathrm{e}^{\mathrm{i}\phi}\, \mathrm{d}^3\mathbf{k}, \tag{10.10}$$

where

$$\phi(\mathbf{k}, \mathbf{x}, t) = \mathbf{k}\cdot\mathbf{x} - \Omega t \tag{10.11}$$

is a phase function, and we note that in general the frequency of the wave $\omega = \Omega(\mathbf{k}, \mathbf{x}, t)$ where the position dependence enters through a dependence on background properties, which themselves may vary with space. Here Ω is a dispersion function (not to be confused with rotational frequency, which is not relevant in this chapter). The oscillatory nature of the integrand in (10.10) means that the only significant contributions come from where ϕ is extremal in $\mathbf{k}$-space (method of stationary phase), i.e. when $\nabla_{\mathbf{k}}\phi = 0$, which

leads to

$$\mathbf{x} - \frac{\partial \Omega}{\partial \mathbf{k}} t = 0 \tag{10.12}$$

$$\implies \frac{\mathrm{d}\mathbf{x}}{\mathrm{d}t} = \nabla_{\mathbf{k}} \omega \,. \tag{10.13}$$

Here we denote $\nabla_{\mathbf{k}} \equiv \partial/\partial\mathbf{k}$. This provides the definition for the group velocity $\mathbf{v}_g \equiv \nabla_{\mathbf{k}}\omega$ as the speed of propagation of the point of constructive interference of the individual components forming the wave packet.

Invoking commutativity of derivatives

$$\begin{aligned} \frac{\partial}{\partial \mathbf{x}} \frac{\partial}{\partial t} \phi &= \frac{\partial}{\partial t} \frac{\partial}{\partial \mathbf{x}} \phi \\ \implies -\frac{\partial \Omega}{\partial \mathbf{x}} &= \frac{\partial \mathbf{k}}{\partial t} \,, \end{aligned} \tag{10.14}$$

we can manipulate this in tensorial notation to get

$$\begin{aligned} 0 &= \frac{\partial k_i}{\partial t} + \frac{\partial \omega}{\partial x_i} + \frac{\partial \omega}{\partial k_j} \frac{\partial k_j}{\partial x_i} \\ &= \frac{\partial \mathbf{k}}{\partial t} + \nabla\omega + (\mathbf{v}_g \cdot \nabla)\mathbf{k} \\ &= \frac{\mathrm{d}\mathbf{k}}{\mathrm{d}t} + \nabla\omega \,, \end{aligned} \tag{10.15}$$

where we have used the fact that $\nabla \times \nabla\phi = 0 \implies \nabla \times \mathbf{k} = 0$, which in tensorial notation turns into

$$\frac{\partial k_i}{\partial x_j} - \frac{\partial k_j}{\partial x_i} = 0 \,. \tag{10.16}$$

This gives

$$\frac{\mathrm{d}\mathbf{k}}{\mathrm{d}t} = -\nabla\omega \,, \tag{10.17}$$

which together with (10.13) can be recognised as Hamilton's equations. Here the dispersion function takes the role of the Hamiltonian. The solutions obtained by integrating (10.13) and (10.17) are trajectories tracing the group-velocity paths of the associated wave packets ("rays").

The above Hamiltonian structure comes from taking the WKB limit of the usual fluid equations, and is closely analogous to the geometric optics limit of electromagnetism or the classical limit of quantum mechanics. It is formally exact in the limit of short wavelengths, a generally good approximation for solar-like oscillators in which the length scales of disturbances are much smaller than those of background variations. In practice one inserts the appropriate dispersion relation for the wave mode of interest to obtain expressions for the ODEs, then integrates these under some starting $(\mathbf{k}, \mathbf{x})$ to solve for the evolution of these parameters as a function of time along the path of the ray. There are several advantages of this approach over global wave calculations, namely the computational speed and simplicity of integrating a system of linear ODEs, and the ability to handle arbitrarily complex, fully three-dimensional background geometries at no significant computational expense.

10.1.3 Magnetogravity ray tracing

In deep stellar interiors, sound speeds greatly exceed those associated with other wave modes, and so their role in the dynamics can be neglected. A WKB treatment of the fluid equations, ignoring acoustic effects, leads to the dispersion relation for magnetogravity waves (Unno et al., 1989)

$$\omega^2 = \omega_A^2 + \kappa_\perp^2 N^2 \,, \tag{10.18}$$

where $\omega_A \equiv \mathbf{k}\cdot\mathbf{v}_A$. In Cartesian coordinates (x,y,z), and assuming stratification in the x-direction, Hamilton's equations for magnetogravity waves are

$$\frac{\mathrm{d}\mathbf{x}}{\mathrm{d}t} = \frac{\omega_A}{\omega}\mathbf{v}_A + \frac{N^2\kappa_x}{|\mathbf{k}|\omega}\left(-\kappa_\perp^2\,,\,\kappa_x\kappa_y\,,\,\kappa_x\kappa_z\right), \tag{10.19}$$

$$\frac{\mathrm{d}\mathbf{k}}{\mathrm{d}t} = -\frac{\omega_A}{\omega}\left(\mathbf{k}\cdot\frac{\partial\mathbf{v}_A}{\partial x}\,,\,\mathbf{k}\cdot\frac{\partial\mathbf{v}_A}{\partial y}\,,\,\mathbf{k}\cdot\frac{\partial\mathbf{v}_A}{\partial z}\right) + \frac{\kappa_\perp^2 N}{\omega}\frac{\partial N}{\partial x}\hat{\mathbf{x}}. \tag{10.20}$$

For simplicity, and to parallel the setup used for the SNOOPY simulations, we will assume a constant buoyancy frequency and a cylindrical Prendergast magnetic field configuration. In this situation, the last term on the RHS of (10.20) disappears, and using (3.62) we find that

$$\frac{\partial\mathbf{v}_A}{\partial x} = \frac{B_s}{J_0(\lambda a)R}\left(xyf(R)\,,\,-x^2f(R)-J_1(\lambda R)\,,\,\lambda xJ_1(\lambda R)\right), \tag{10.21}$$

$$\frac{\partial\mathbf{v}_A}{\partial y} = \frac{B_s}{J_0(\lambda a)R}\left(y^2f(R)+J_1(\lambda R)\,,\,-xyf(R)\,,\,\lambda yJ_1(\lambda R)\right), \tag{10.22}$$

$$\frac{\partial\mathbf{v}_A}{\partial z} = 0\,, \tag{10.23}$$

where

$$f(R) \equiv \frac{\lambda}{R}J_0(\lambda R) - \frac{2}{R^2}J_1(\lambda R)\,, \tag{10.24}$$

$R \equiv \sqrt{x^2+y^2}$ is the cylindrical radius, a is the radius of the magnetic cylinder, and $B_s \equiv \kappa\rho/\lambda$.

See that ω has no explicit time dependence, and so represents a conserved quantity of motion. Equations (10.13) and (10.17) were integrated using an explicit fourth-order Runge-Kutta scheme with a time step of 0.05 units up to a maximum time of 10^6. Note that the scheme does not guarantee conservation of ω; rather, we used the time variation of ω as an independent accuracy check. We verified that global fluctuations in ω were typically less than one part in 10^6.

10.1.4 Symmetries and conserved quantities

The structure of Hamilton's equations reveals that a lack of dependence on one of the coordinates q_i (known in that case as an *ignorable* coordinate) leads to conservation of the corresponding conjugate momentum p_i. In general, if it is possible to transform to a different set of coordinates $(Q_1,\cdots,Q_N)$ and momenta $(P_1,\cdots,P_N)$ where one of the new coordinates Q_j is ignorable, then the associated conjugate momentum P_j will be a conserved quantity. Without needing to try all possible transformations, it is possible to check if a certain quantity A is conserved by computing its *Poisson bracket* with H. If this vanishes, then A is conserved (in all coordinate frames). Consider the total time derivative

$$\begin{aligned}\frac{\mathrm{d}A}{\mathrm{d}t} &= \frac{\partial A}{\partial t} + \sum_{i=1}^{N}\left(\frac{\partial A}{\partial q_i}\frac{\mathrm{d}q_i}{\mathrm{d}t} + \frac{\partial A}{\partial p_i}\frac{\mathrm{d}p_i}{\mathrm{d}t}\right)\\ &= \frac{\partial A}{\partial t} + \sum_{i=1}^{N}\left(\frac{\partial A}{\partial q_i}\frac{\partial H}{\partial p_i} - \frac{\partial A}{\partial p_i}\frac{\partial H}{\partial q_i}\right)\\ &= \frac{\partial A}{\partial t} + \{A,H\}\,,\end{aligned}$$

where $\{A,H\}$ is the Poisson bracket of A and H. As a trivial example, if one of the coordinates q_i is already ignorable, then the Poisson bracket of p_i and H evaluates to

$$\{p_i,H\} = -\frac{\partial H}{\partial q_i} = 0\,, \tag{10.25}$$

since all terms like $\partial p_i/\partial p_j$, $\partial p_i/\partial q_j$ where $i \neq j$ are zero, and also $\partial p_i/\partial q_i = 0$.

The proof in the general case will not be given here. However, it leads to what is known as *Noether's theorem*, which states that symmetries are fundamentally associated with conserved quantities. A Hamiltonian system for which there exist as many conserved quantities as spatial degrees of freedom is said to be *integrable*. For example, if we were to have a spherically symmetric, non-evolving star in three-dimensional space, then this would constitute an integrable system since three symmetries exist: time, and two angular coordinates. Such systems have the property that they cannot be chaotic. The concept of *dynamical chaos* will be discussed further in §10.1.6.

10.1.5 Poincaré surfaces of section

With three spatial degrees of freedom, the phase space in the absence of any symmetries is six-dimensional: a given point is defined by three spatial coordinates (x, y, z) and three conjugate momenta (k_x, k_y, k_z). If one were to choose an initial set of (k_x, k_y, k_z, x, y, z) and integrate Equations (10.19) and (10.20), the resulting trajectory would wander around a six-dimensional volume. However, in our setup, which we shall choose to be the same as in the SNOOPY simulations, two constants of motion exist, which confine trajectories to a four-dimensional surface. These include the Hamiltonian itself, since there is no explicit time dependence, and k_z, owing to z-translational invariance.

To visualise the results it is necessary to project down to lower-dimensional space. We achieve this by artificially fixing one free parameter and plotting the remaining ones against each other. A plot generated in this manner is known as a *Poincaré surface of section* (PSS), and is commonly used to analyse the phase-space behaviour of Hamiltonian rays (Dittrich & Reuter, 2001). With four free parameters in our case, the PSS is three-dimensional. We have chosen to fix the x-coordinate and plot k_x as a function of y and z. For a given ray trajectory, the values of (y, z, k_x) are recorded each time the ray crosses the surface $x = 2$ and plotted as a point on a three-dimensional scatter plot.

10.1.6 Dynamical chaos

As mentioned earlier, systems having sufficient symmetry are integrable and will not exhibit chaotic behaviour. The conserved quantities associated with the symmetries confine the paths of the rays in phase space; such trajectories are termed *regular*. Modes which are formed from the constructive interference of such rays exhibit a spectrum that is formed of regular patterns, and these patterns can be predicted using a set of quantisation conditions (e.g. Keller & Rubinow, 1960; Gough, 1986): for example, the equal frequency spacings of p-modes and the equal period spacings of g-modes that were discussed in §4.2.2. The quantum numbers that define such a spectrum are directly related to the conserved quantities of the system. The oscillation spectrum of a star therefore contains information not just about local fluid mechanical properties, but also global symmetries.

If the symmetry is only weakly broken, the dynamical properties of the system can be regarded as small perturbations about the integrable case, and standard results/asymptotic formulae remain largely valid. However, for systems in which the symmetry is significantly broken, such as in tidally/centrifugally distorted stars and/or those with strong magnetic fields, the wave packet dynamics will undergo a transition to chaos. Such concepts, first developed and applied in the field of quantum mechanics (Gutzwiller, 1990; Hentschel & Richter, 2002; Cao & Wiersig, 2015), have in recent years been used to investigate the effects of rapid

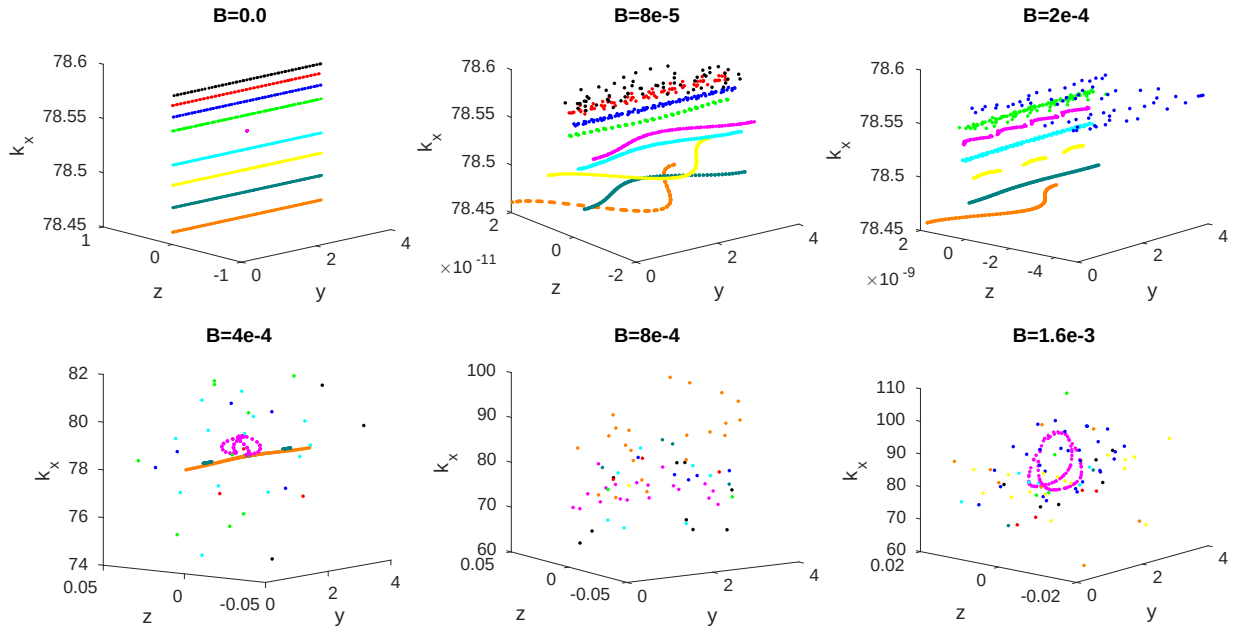

Figure 10.1: Poincaré surfaces of section for a collection of nine rays (different colours) with common $|\mathbf{k}|$, launched at slightly different angles about the ray with $[i, j, k] = [50, 20, 0]$ from $(x, y, z) = (1, -1, 0)$. This corresponds to a shallow incoming angle (N.B. shallower than for the shallow SNOOPY run). The six panels are for different field strengths. Only for the lower three panels do critical surfaces exist. Note that the plotting limits have been truncated and adjusted for clarity, meaning that some points (such as the red and black ray in the top right panel, which are sparsely scattered about a three-dimensional volume) are not shown.

stellar rotation on acoustic (Lignières & Georgeot, 2008, 2009; Lignières et al., 2010) and gravity modes (Prat et al., 2016, 2017, 2018). These studies show that associated with the breaking of spherical symmetry is the appearance of chaotic modes, which co-exist alongside regular modes and occupy a larger and larger volume of phase space as the rotation rate increases. Such modes have fundamentally different properties from regular modes in that their frequencies do not obey a predictable pattern (the conserved quantities in terms of which the spectrum might be described do not exist), and can only be characterised in a statistical sense.

In general, the normal-mode spectrum of a non-integrable system is a superposition of regular and irregular spectra (Percival, 1973; Pomphrey, 1974). The evolution of an integrable system towards chaos under a symmetry-breaking perturbation occurs in a smooth manner, as described by the Kolmogorov-Arnold-Moser theorem (Kolmogorov, 1954; Möser, 1962; Arnold, 1963). Although the existence of any such perturbation (however small) leads to chaos, the associated volume of phase space vanishes in the limit of zero perturbation, making this undetectable for near-integrable systems. The observation that many stars exhibit predominantly regular spectra implies that they are spherically symmetric to good approximation, and thus fall under this category. While the study of dynamical chaos has been undertaken in the context of wave packets propagating in rapidly rotating stars, the results in this chapter represent the first attempt at the same problem for strong magnetic fields.

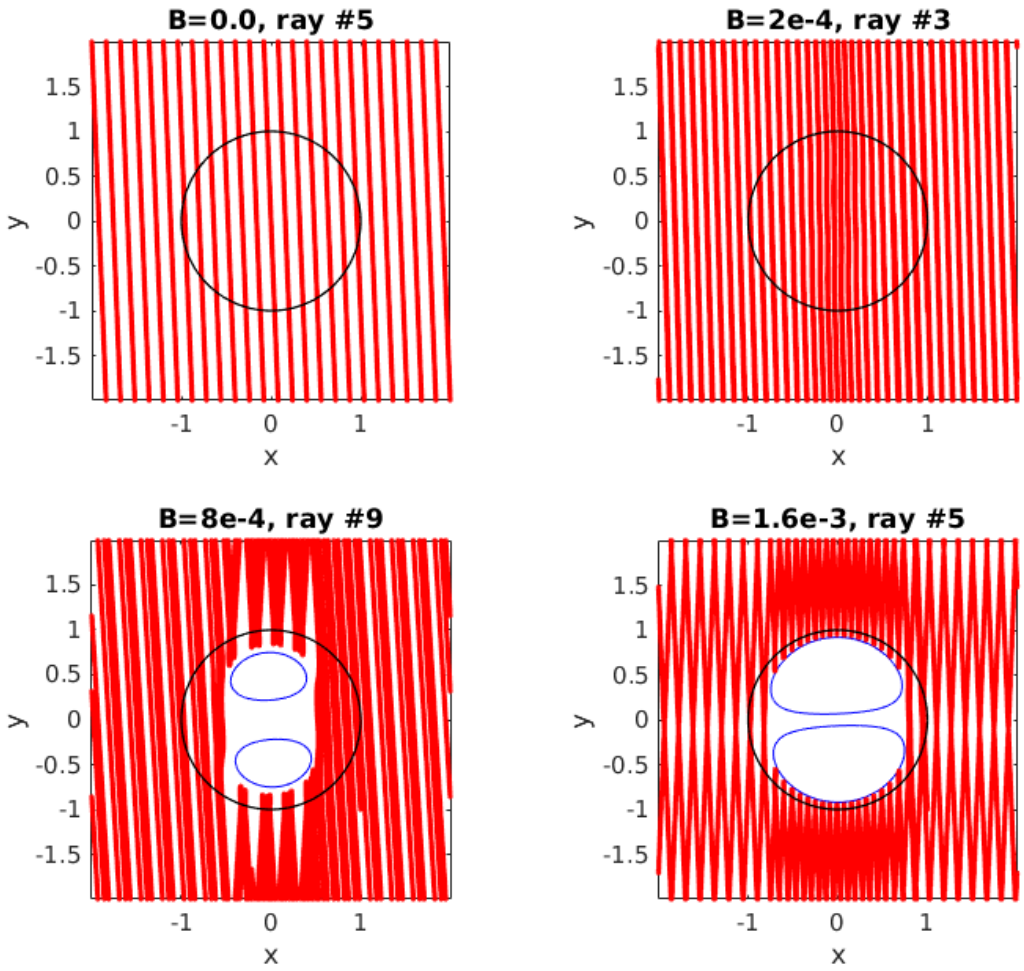

Figure 10.2: Trajectories in space for a selection of rays from Figure 10.1, overlaid with the field region boundary (black) and critical surfaces associated with the initial wavevector of the ray (blue). Rays are numbered such that #5 refers to magenta, #3 to blue, and #9 to orange in Figure 10.1. Note that ray paths in general move in three spatial dimensions, but only the x, y-projection is shown for simplicity. The trajectories shown were computed up to $t = 2.5 \times 10^5$.

10.2 Results & discussion

Compared to full non-linear wave calculations, ray tracing suffers fewer practical restrictions on the range of input parameters and is computationally inexpensive to implement. This allowed us to experiment with a wider range of input wavevectors compared to the two values used in the SNOOPY calculations, which were $[i, j, k] = [15, 20, 0]$ and $[25, 5, 0]$. Besides computing ray trajectories for those two values, which afford direct comparison, we also performed ray tracing for $[i, j, k] = [0, 10, 0]$, $[50, 5, 0]$, $[50, 2, 0]$, $[30, 40, 0]$ and $[45, 25, 0]$. For each $[i, j, k]$ combination, we tested a range of field strengths going from zero to above the critical value.

In all cases, the weak-strong magnetic field transition is associated with a transition in the ray dynamics from regular to chaotic. This can be seen in Figure 10.1, which plots the resulting PSS for $[i, j, k] = [50, 20, 0]$. The phase-space trajectories of a set of nine rays launched from the same closely spaced initial positions progressively diverge as the field strength increases. At zero field strength (top left panel), all trajectories on the PSS are one-dimensional curves, reflecting the existence of four conserved quantities (ω, k_x, k_y and k_z). These curves deform as the field increases away from zero. At low field strengths, many retain their one-dimensional (regular) nature, but this gives way to the emergence of multidimensional structures at higher field strengths. As can be seen in the middle and right-hand panels along the top row, there is a spreading of some trajectories first into two-dimensional sheet structures, and then into three-dimensional volumes (bottom row). Amidst these large, chaotic regions of phase space, there still exist a small number of regular modes (e.g. the magenta trajectory in the bottom right panel) even at high field strengths. However, these are comparatively rare; it is likely that in the strong-field regime most of the modes will be chaotic.

Figure 10.2 shows the spatial paths of a selection of regular and chaotic rays. Note that for the sake of clarity, the plotting has been restricted to the first quarter of the total integration. In the top-right and bottom-left panels, the rays, both of which are chaotic, eventually fill a large fraction of the x, y-plane (excluding critical regions, which reflect the rays). The remaining two (top-left and bottom-right panels) are regular and fill a smaller fraction of the x, y-plane (the ray paths loop back upon themselves after a finite amount of time). Ergodicity is a general property of chaotic modes, and so it would be naïvely expected that the associated regions of the PSS should eventually be completely filled with points. However, despite integrating for a large number of box-crossing times, the bottom row of Figure 10.1 remains sparsely filled. The reason for this is rather curious: it appears to be a consequence of a trapping process associated with the existence of the critical surfaces. Rays which happen to impinge upon the field region in certain locations are thereafter trapped on quasi-periodic bounce orbits, never to re-emerge. This phenomenon will be discussed further in Chapter 11.

The two lower panels of Figure 10.2 demonstrate the reflection of rays off the magnetic field region, specifically in the vicinity of the critical surfaces, which are marked in blue. See that the ingoing and outgoing angles with respect to the stratification are the same: this must be the case if we are to conserve ω. However, the dispersion relation alone sets no constraint on the magnitude of the outgoing wavevector with respect to the ingoing value. Previous work based solely on heuristic arguments (Fuller et al., 2015) suggested that upon reflection, the waves would be upscattered to systematically higher wavenumbers (the 'magnetic greenhouse effect'). Hamiltonian ray calculations can be used to check this directly, since we follow the time evolution of both the position and the wavevector of a propagating packet.

Figure 10.3 shows the time evolution of the wavevector components of two rays, one chaotic and one regular, from the $[i, j, k] = [50, 2, 0]$, $B = 1.6 \times 10^{-3}$ ray-tracing run. While there are certainly fluctuations

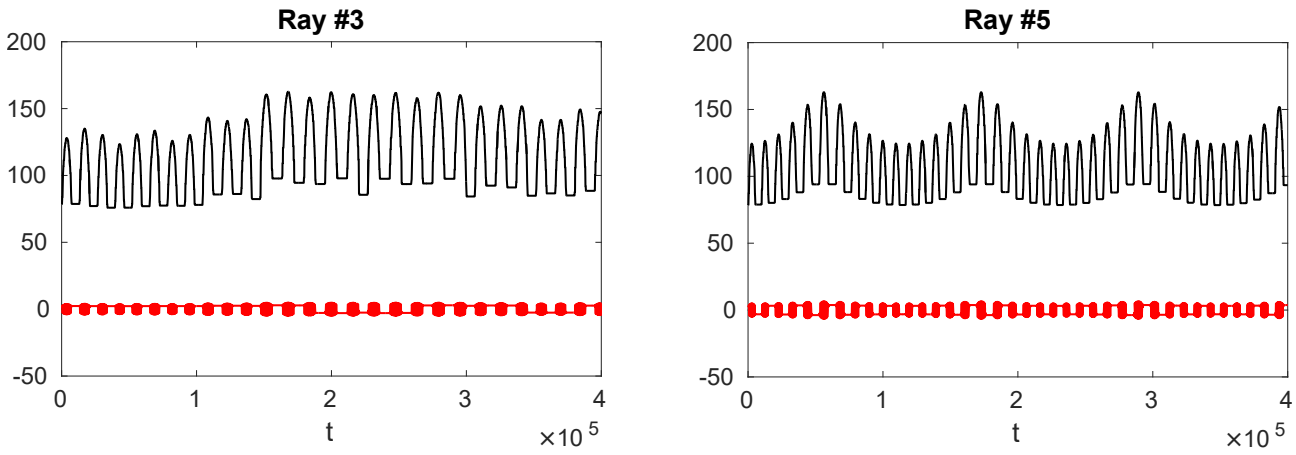

Figure 10.3: Evolution of k_x (black) and k_y (red) as a function of time, for the blue (left) and magenta (right) rays of the bottom-right panel of Figure 10.1 ($B = 1.6 \times 10^{-3}$).

in the magnitude of the wavevector, no systematic growth is seen over the course of many reflections. This explains how it might be possible to form normal modes in the strongly magnetised regime, since the organised manner of reflection (as opposed to a random scattering) might enable structured interference patterns to form and persist, such as those found in §9.3.4.

Chapter 11

Solution to the Dipole Dichotomy

In Chapter 5 we introduced the "dipole dichotomy" problem, referring to the existence of an additional but poorly-understood source of damping affecting non-radial (particularly dipole) modes in a significant fraction of evolved stars. With indirect evidence pointing towards the role of a strong core magnetic field influencing the propagation of gravity waves, much of this thesis has been concerned with studying the nature of this interaction. Some preliminary ideas for how magnetic fields might give rise to additional damping were presented in §6.4, but these proved unsatisfactory for a number of reasons.

Chapters 9 and 10 presented the results of more detailed investigations involving numerical simulations and Hamiltonian ray tracing, which individually provided useful insights. In this chapter, we will combine these two techniques to demonstrate a mechanism by which g-modes can undergo additional damping in the presence of a strong field.

11.1 Wave reflection and trapping

In the previous chapter, we used ray tracing to examine the time evolution of the wavevector for a gravity-wave packet impinging upon a region of strong field. Figure 11.1 illustrates the same quantities measured from the SNOOPY simulations for the shallow run, where the wavevector components have been obtained by taking a spatial Fourier transform of the y-component of the velocity field at the forcing frequency. The transformed region excludes the magnetic cylinder and the forcing strip. In the field-free case (left panel), peaks are only seen at the forced wavevector, as per expectation. In the presence of a strong field (right panel), we see that in addition to the peaks at the forced wavevector, there is a second pair of peaks at roughly its negation. Although a small amount of power trails off to higher wavenumbers, the response is still dominated by wavevectors with magnitudes similar to the input value. This suggests that the magnetic greenhouse effect may not be important, if it occurs at all.

Besides reflection, a second distinct phenomenon is noted to occur, and that is the trapping of rays within the field region itself. Examples of these are shown in close-up view in Figure 11.2 (left) and in projected view along the z-axis in Figure 11.3. From a ray-tracing perspective, a ray launched into the field region from outside appears to propagate inward until it reaches a flux surface roughly coincident with the critical surface, whereupon its trajectory veers to become roughly tangential to the flux surface. Physically, this can be interpreted as a conversion to some kind of modified Alfvén wave (note that the trajectories do not follow field lines exactly, and so these are not pure Alfvén waves). The right panel of Figure 11.2 plots

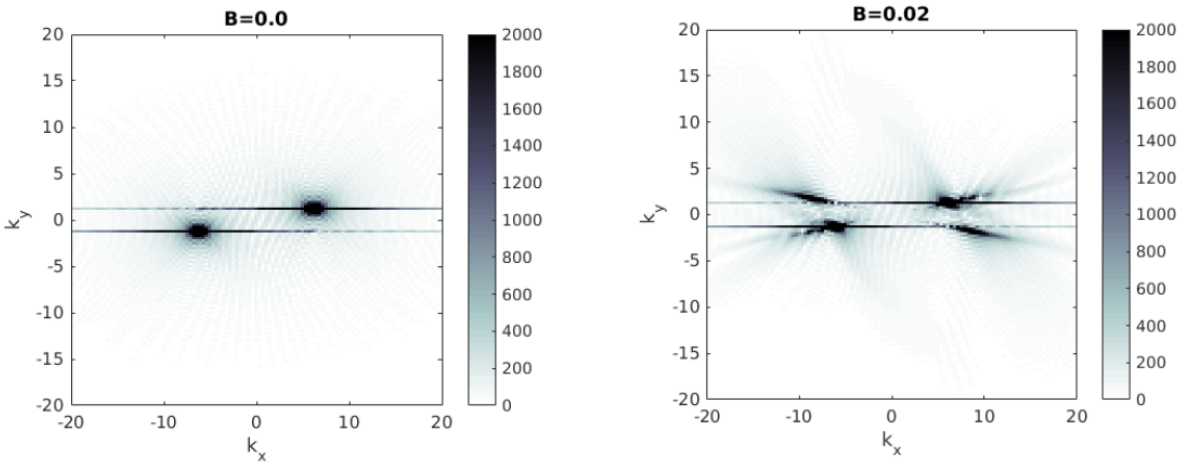

Figure 11.1: Two-dimensional spatial Fourier transform of the u_y field at the forcing frequency for $[i, j, k] = [25, 5, 0]$, taken over the region exterior to the field and interior to $|x| < 1.4$ (thus avoiding the forcing strip, which occupies $|x| > 1.5$). The temporal transform is taken over the forced interval, $200 < t < 1000$. The left panel corresponds to the zero-field case, and shows peaks at the forcing wavenumber. The right panel is for the strongest field strength simulated, and shows significant amounts of power at both the forcing wavenumber and approximately its negation, evidencing specular reflection.

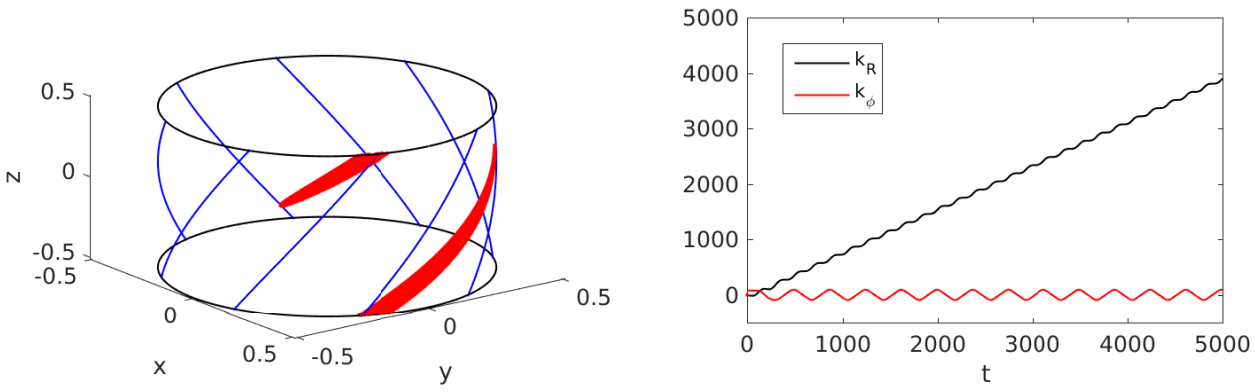

Figure 11.2: Left: trajectory of a ray with initial $[i, j, k] = [30, 40, 0]$, restricted to $1000 < t < 5000$ (red). The path appears to be confined to the flux surface at radius $R \approx 0.51$. Black circles are a visual aid marking the location of this flux surface. In blue is a selection of magnetic field lines on that surface. Note that periodic boundary conditions have been used for the ray tracing, so that the two apparently disjoint sections are in fact a continuous path. Right: the R- and ϕ-components of the wavevector as a function of time. It can be seen that on average, k_R undergoes linear growth, while k_ϕ remains constant, a property expected of Alfvén wave phase mixing.

the time evolution of the wavevector components, decomposed locally into the cylindrical polar R- and ϕ-directions. It can be seen that the radial component of the wavevector grows roughly linearly with time. Mathematically, this can be understood in the framework of Hamiltonian dynamics as being driven by the spatial gradient of the Alfvén term in the Hamiltonian being purely radial (see Equation 10.20). The fluid mechanical interpretation for this process is that it represents phase mixing, where the shrinkage of scales (growth of the wavevector) arises from decoherence in the fluctuations associated with a spatial variation in the Alfvén speed. Once a ray becomes trapped, it is never observed to re-emerge from the field region. This indicates that this process is in some sense irreversible, and in the presence of dissipation, would act as a global energy sink. Note that there is no violation of the topological phase-space segregation of bound versus unbounded Hamiltonian orbits: the 'trapping' referred to here is purely spatial, while the wavevector remains divergent.

The ray-trapping phenomenon has its correspondence in the SNOOPY simulations in the form of high-amplitude arcs tracing the flux surfaces on which ingoing rays are observed to localise. This is apparent in Figure 11.3, which shows examples of both trapped and reflected rays. The two panels correspond to the steep (left) and shallow (right) SNOOPY runs. For the sake of direct comparison, the rays are given initial wavevectors $\mathbf{k}$ equal to the forcing wavevector for the particular SNOOPY run. The two types of calculations exhibit features that can be associated with one another: where the rays are reflected, there are interference patterns in the underlying fluid velocity field, and where rays are trapped, there are high-amplitude arcs. Notably, it is clear that the ultimate fate of the ray (reflection or trapping) depends on the location where it impinges upon the field region. In the steep case, the rays impinging relatively far from the x-axis are the ones that avoid being trapped, while in the shallow case, rays are mostly reflected except for those impinging very close to the x-axis. This suggests that the mutual orientations of the incoming rays, the magnetic flux surfaces, and the stratification are important for determining the dynamics.

11.2 Wave theory explanation

We shall now attempt to explain this selective trapping/reflection phenomenon using analytic arguments. To simplify the problem, we will consider linearised Boussinesq dynamics, introduced previously in §9.2.2, in the ideal MHD (i.e. dissipation-free) regime. The linearised momentum equation is

$$\frac{\partial \mathbf{u}}{\partial t} = -\frac{\nabla p'}{\rho} + N^2 \theta' \hat{\mathbf{x}} + \frac{\mathbf{F}'_{\mathscr{L}}}{\rho}\,, \tag{11.1}$$

where $\mathbf{F}_{\mathscr{L}} = (\nabla \times \mathbf{B}) \times \mathbf{B}$ is the Lorentz force, and primes denote the Eulerian perturbation. Under a constant background entropy gradient, the potential temperature is governed by

$$\frac{\partial \theta}{\partial t} + \mathbf{u} \cdot \nabla \theta = -u_x\,. \tag{11.2}$$

Using $\mathbf{B} = \nabla \times \psi \hat{\mathbf{z}} + \lambda \psi \hat{\mathbf{z}}$, we find that

$$\mathbf{F}'_{\mathscr{L}} = -\nabla \psi' \left(\lambda^2 \psi + \nabla^2 \psi\right) - \nabla \psi \left(\lambda^2 \psi' + \nabla^2 \psi'\right). \tag{11.3}$$

In terms of the fluid displacement $\boldsymbol{\xi}$, satisfying $\mathbf{u} = \partial \boldsymbol{\xi} / \partial t$, and assuming a time-harmonic dependence $\boldsymbol{\xi} \propto \exp(-\mathrm{i}\omega t)$, Equation (11.1) becomes

$$-\omega^2 \boldsymbol{\xi} = -\frac{\nabla p'}{\rho} - N^2 \xi_x \hat{\mathbf{x}} + \frac{\mathbf{F}'_{\mathscr{L}}}{\rho}\,. \tag{11.4}$$

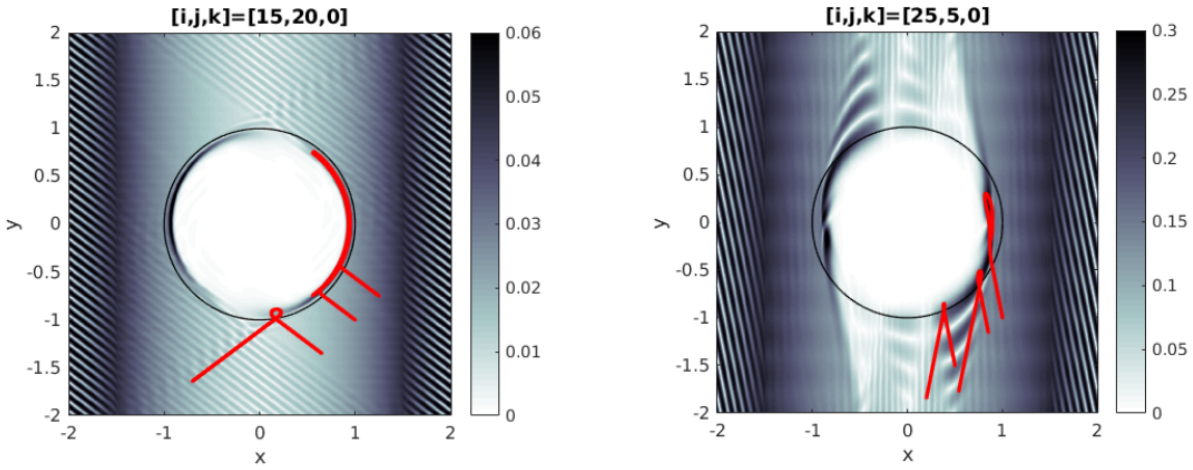

Figure 11.3: Spatial distribution of the u_y temporal Fourier amplitudes at the respective forcing frequencies for $[i, j, k] = [15, 20, 0]$ (left) and $[i, j, k] = [25, 5, 0]$ (right). The temporal transform is taken over the forced interval ($200 < t < 1000$). In both cases, the highest field strength is being shown ($B = 0.08$ and 0.02, respectively). Overlaid for comparison in red are the trajectories of three rays launched from along the line $y = x - 2$, with the same initial wavenumber as the forcing function. In the left panel, the two rays with launch points furthest on the right are trapped, while the leftmost one is reflected, and in the right panel, the two rays launched furthest on the left are reflected, while the rightmost one is trapped. This behaviour closely matches the reflection/interference patterns and high-amplitude arcs shown in grey scale.

If we invoke the fluid stream function Θ satisfying $\boldsymbol{\xi} = \hat{\mathbf{z}} \times \nabla\Theta$ and incorporate the ideal MHD condition

$$\Delta\psi = 0 \implies \psi' = -\xi_R \frac{\mathrm{d}\psi}{\mathrm{d}R}\,, \tag{11.5}$$

where Δ denotes the Lagrangian perturbation, we can eliminate $\boldsymbol{\xi}$ and $\mathbf{F}_{\mathscr{L}}$ in favour of Θ and ψ. Considering the z-component of the curl of Equation (11.4) allows us to eliminate p' and condense everything down to the single scalar equation

$$-\omega^2\nabla^2\Theta = -N^2\frac{\partial^2\Theta}{\partial y^2} + \frac{1}{\rho R}\frac{\partial}{\partial\phi}\left[\frac{\lambda^2}{R}\frac{\partial\Theta}{\partial\phi}\frac{\mathrm{d}\psi}{\mathrm{d}R} + \nabla^2\left(\frac{1}{R}\frac{\partial\Theta}{\partial\phi}\frac{\mathrm{d}\psi}{\mathrm{d}R}\right)\right]\frac{\mathrm{d}\psi}{\mathrm{d}R}\,. \tag{11.6}$$

The next step is to consider local Cartesian limits of Equation (11.6) in the vicinity of a reference point (x_0, y_0), located at some cylindrical distance R_0 from the origin, with polar coordinate ϕ_0 (angle from the x-axis, as per the usual definition). Let us define a rotated set of coordinates (l, h) aligned with the local $\hat{\mathbf{R}}$- and $\hat{\boldsymbol{\phi}}$-directions (respectively) at the reference point. We shall assume that we are far enough away from the origin that curvature of the coordinates can be neglected on the spatial scales in question (true in the short-wavelength limit), so that

$$\frac{\partial}{\partial l} \to \frac{\partial}{\partial R}\,, \quad \frac{\partial}{\partial h} \to \frac{1}{R}\frac{\partial}{\partial\phi}\,. \tag{11.7}$$

The new coordinates are related to x and y through a rotational transformation:

$$\begin{aligned} l &= (x - x_0)\cos\phi_0 + (y - y_0)\sin\phi_0 \\ h &= -(x - x_0)\sin\phi_0 + (y - y_0)\cos\phi_0\,. \end{aligned} \tag{11.8}$$

Under this change of coordinates, assuming that

$$\frac{h}{R_0}\,,\ \frac{l}{R_0} = O(\epsilon) \implies \frac{B_h^2}{\rho N^2 R_0^2} = O(\epsilon^2)\,, \tag{11.9}$$

where ϵ is small and λR_0 is of order unity, then to lowest order in ϵ, Equation (11.6) becomes

$$-\omega^2\left(\frac{\partial^2\Theta}{\partial h^2} + \frac{\partial^2\Theta}{\partial l^2}\right) = -N^2\cos^2\phi_0\frac{\partial^2\Theta}{\partial h^2} - N^2\sin(2\phi_0)\frac{\partial^2\Theta}{\partial h\partial l} - N^2\sin^2\phi_0\frac{\partial^2\Theta}{\partial l^2} + \frac{1}{\rho}\left[\frac{\partial^4\Theta}{\partial h^2\partial l^2} + \frac{\partial^4\Theta}{\partial h^4}\right]\left(\frac{\partial\psi}{\partial R}\right)^2_{R=R_0}\,. \tag{11.10}$$

Here $B_h = -\partial\psi/\partial R|_{R=R_0}$ and the ordering conditions place it in the strong-field regime. Since background variations occur only in the R-direction, in the zero-curvature limit the h-component of the wavevector would be constant over the local region considered, and separation of the equations in h is exact. Let us then expand in plane waves in the h-direction ($\partial/\partial h \to \mathrm{i}k_h$). The above simplifies to

$$\left(\omega^2 - N^2\sin^2\phi_0 - \frac{k_h^2 B_h^2}{\rho}\right)\frac{\partial^2\Theta}{\partial l^2} - \mathrm{i}N^2\sin(2\phi_0)k_h\frac{\partial\Theta}{\partial l} - k_h^2\left(\omega^2 - N^2\cos^2\phi_0 - \frac{k_h^2 B_h^2}{\rho}\right)\Theta = 0\,. \tag{11.11}$$

Defining the horizontal Alfvén speed $v_h^2 \equiv B_h^2/\rho$, Equation (11.11) then becomes

$$\left(\omega^2 - N^2\sin^2\phi_0 - k_h^2 v_h^2\right)\frac{\partial^2\Theta}{\partial l^2} - \mathrm{i}N^2\sin(2\phi_0)k_h\frac{\partial\Theta}{\partial l} - k_h^2\left(\omega^2 - N^2\cos^2\phi_0 - k_h^2 v_h^2\right)\Theta = 0\,. \tag{11.12}$$

With the h-dependence separated out through the $\propto \exp(\mathrm{i}k_h h)$ assumption, Equation (11.12) is effectively a linear, homogeneous, second-order ODE in the coordinate l. In the WKB limit, the coefficients can be regarded as approximately constant, so this can be solved by assuming a $\Theta \propto \exp(\Lambda l)$ expansion and forming

the auxilliary equation. The roots of this are given by

$$\Lambda = \frac{\mathrm{i}N^2 k_h \sin\phi_0 \cos\phi_0 \pm k_h \sqrt{(\omega^2 - k_h^2 v_h^2)(\omega^2 - N^2 - k_h^2 v_h^2)}}{\omega^2 - N^2 \sin^2\phi_0 - k_h^2 v_h^2}, \tag{11.13}$$

the inspection of which yields some useful insights, which we will now elaborate upon.

In general, if the roots of the auxilliary equation are purely imaginary, then solutions will be wave-like (propagating). If they are purely real, then the solutions will be exponentially growing/decaying (evanescent). The first term in the numerator of the expression for Λ comes from the buoyancy response and is always imaginary, indicating that the solution will always be at least partially propagating. However, the second term in the numerator, which represents the magnetic response, will be either real or imaginary depending on the strength of the field. Outside the field region $v_h^2 = 0$, and given that $\omega^2 \leq N^2$, Λ will be purely imaginary. Without a magnetic field, the solution is therefore purely propagating.

Let us consider the second term as v_h^2 is increased away from zero. The $\omega^2 - N^2 - k_h^2 v_h^2$ factor will always be negative, but the $\omega^2 - k_h^2 v_h^2$ term, which is initially positive, will eventually reach zero when the field becomes sufficiently strong. This corresponds to encountering the critical surface ($\omega^2 = k_h^2 v_h^2$). Past this point (i.e. where $k_h^2 v_h^2 > \omega^2$), the solution will acquire an evanescent component. The smaller the value of ω compared to N, the greater the magnitude of the second (evanescent) term compared to the first (propagating) term and the more strongly decaying the solution with respect to space. Physically, it predicts the expulsion of wave action from the field region when the resonance point is crossed. This explains the low velocity amplitudes within the critical surfaces seen in Figures 9.3–9.6, and also the increasing effectiveness of the observed expulsion with increasing field strength.

The answer to why two distinct types of behaviour (trapping versus reflection) occur lies in the denominator of (11.13). If $\omega^2 < N^2 \sin^2\phi_0$, then as the field strength increases away from zero, at some point, namely when

$$\omega^2 - N^2 \sin^2\phi_0 = k_h^2 v_h^2, \tag{11.14}$$

the denominator will reach zero and the wavenumber of the solution will diverge. This occurs at a lower field strength than that satisfying the resonance criterion, and so we should expect the divergent regions to be located outside the critical surfaces. Specifically, divergent (large) wavenumbers will be expected in the region where

$$\sin^2\phi_0 < \sin^2\phi_* \equiv \frac{\omega^2}{N^2}. \tag{11.15}$$

For reasons explained below, we shall refer to this region as the *trapping region*, and ϕ_* as the *trapping angle*. It can be seen in Figure 11.4, which shows the SNOOPY velocity fields overlaid with the predicted trapping regions (blue lines) that there is a close correspondence between the trapping angle and the angle subtended by the high-amplitude arcs. This is particularly clear in the top row (steep run). The trajectories of trapped rays, overlaid in red, exhibit an even closer correspondence with the predicted trapping regions, but this is somewhat less surprising given that Equation (11.15) was derived under the WKB approximation.

We conclude that the trapping phenomenon arises from a singularity in the Boussinesq equations that appears when a magnetic field is present, and applies to a frequency-dependent range of angles between the field lines and the stratification. We shall refer to Equation (11.15) as the *trapping condition*. It is a

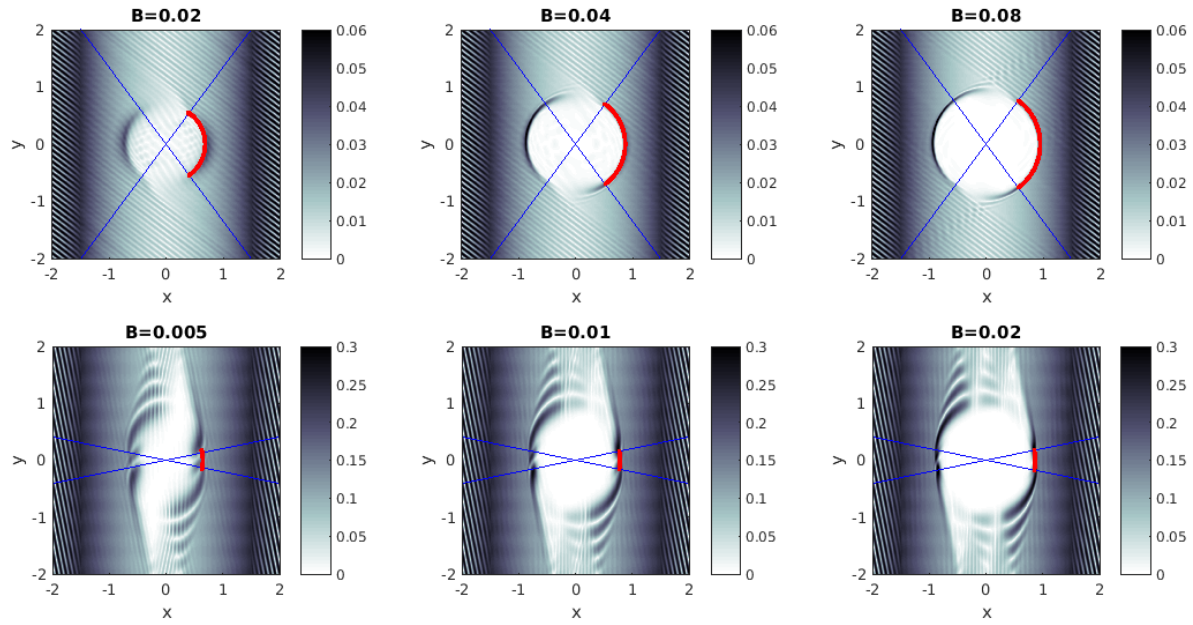

Figure 11.4: Spatial distribution of the u_y temporal Fourier amplitudes at the respective forcing frequencies for $[i,j,k] = [15,20,0]$ (top row) and $[i,j,k] = [25,5,0]$ (bottom row), for the three strongest field strengths simulated in each case. Overlaid in blue are lines subtending the trapping angle ϕ_* predicted by Equation (11.15), and in red, the path of a ray launched into the field region that subsequently becomes trapped (only the part of the trajectory after trapping occurs has been plotted). There is excellent agreement between the ray trajectories and the analytical prediction, and a fair correspondence with features in the SNOOPY simulations.

curious result that, as we shall discuss in the following section, may have important physical consequences relevant for the damping of global modes possessing gravity-mode character. Some physical insight can be gleaned by restoring derivatives with respect to h and recasting the divergence condition (11.14) in the form

$$\left(\omega^2 - N^2 \sin^2\phi_0\right)\Theta + \frac{B_h}{\rho R_0}\frac{\partial}{\partial h}\left(R_0 B_h \frac{\partial \Theta}{\partial h}\right) = 0\,, \tag{11.16}$$

which can be regarded as an equation of motion for fluid elements at the singularity. The resemblance between the last term on the LHS and the torsional operator in (6.7) is to be noted. The presence of the additional buoyancy term, compared to Equation (6.4), reflects the fact that this describes spheroidal rather than torsional motions. Nonetheless, we see that the dynamics at the singularity and those of the torsional Alfvén modes introduced in §6.3 are closely related. This, and the knowledge that a cascade to arbitrarily small scales occurs at the singularity, points to an association of the trapping regions with phase mixing, the process responsible for the damping associated with torsional Alfvén resonances previously discussed in Chapter 6.

11.3 New damping mechanism

11.3.1 Predicted damping rates

As discussed already, the torsional Alfvén resonance mechanism appears not to be efficient enough to account for the observations of dipole mode depression. However, this may be achieved through a closely

related process. Rather than a channelling of wave energy from the input motions (spheroidal in nature) into the torsional modes, followed by a loss of energy through phase mixing, our simulations indicate that a loss of energy may occur more directly through phase mixing of the Alfvén-modified spheroidal modes themselves. The occurrence of this process relies on the presence of a sufficiently strong magnetic field, but this is not the only criterion. In addition, the orientation of the magnetic field with respect to the stratification is important as it determines the fate of the incoming waves, i.e. whether they will be reflected or trapped. This property of the system has not previously been appreciated, and could explain why the data indicate only a fractional loss of energy within the g-mode cavity.

In the previous section, we derived a criterion for the trapping angle as being $\sin^{-1}(\omega/N) \approx \omega/N$ in the low-frequency limit (note that $N \gg 2\pi\nu_{\max}$ in typical red giant cores). Though at first glance, this appears specific to our cylindrical geometry, our neglect of all terms associated with geometric curvature of the coordinates implies that the result is a local one that generalises to any topologically equivalent system (including spherical stars, as long as one considers the short-wavelength limit). The trapping criterion is to be interpreted as a condition on the local angle between the flux surfaces and the stratification, and defines a set of regions upon which an impinging wave would experience complete absorption. Such regions would subtend some fraction of the surface of the magnetised core. If an oscillation mode has a spatial amplitude function that overlaps with these trapping regions, the mode would experience enhanced damping as a result of this leakage of wave energy. Note that the exact mapping between a given value of ω/N and the fraction of the core surface occupied by the trapping regions depends on the field configuration in question (we quote values for the spherical Prendergast solution below).

For example, if the trapping regions subtend 5% of the area of the core, then the associated damping time scale would be 20 times the information crossing time of the star (given roughly by the inverse of the large separation $\Delta\nu$). In general, one would also have to divide through by the square of the transmission coefficient T (which depends on the spherical harmonic degree ℓ) to account for the fact that only a fraction of wave energy is able to tunnel into the g-mode cavity from where it is input (the convection zone in the p-mode cavity). This is approximately given by the expression

$$T^2 \sim \left(\frac{r_g}{r_p}\right)^{2\sqrt{\ell(\ell+1)}}, \tag{11.17}$$

where r_g and r_p denote radial coordinates of the upper and lower boundaries of the g- and p-mode cavities, respectively (lower and upper boundaries of the evanescent region). Figure 11.5 provides a cartoon illustration of this process.

A typical red giant might have $\nu_{\max} \sim 100\,\mu$Hz and $N/(2\pi) \sim 10\,$mHz in the core, implying a trapping angle of $\phi_* \sim 0.01$. For the spherical Prendergast field solution (see §3.2), the corresponding trapping regions subtend > 13% of the area in the outer 5% of the core, which is where flux surfaces are closest to being horizontal (i.e. aligned with the stratification). As can be seen in Figures 9.3–9.6, for field strengths just a factor of several larger than the critical, trapping regions may be found in close proximity to the edge of the field region, and so it is possible that in general, the trapping might occur quite close to the surface of the core. Let us suppose a characteristic trapping area of ~10–20%. Values of T^2 estimated for the red giant model of §6.1.2 for a mode near $\nu_{\max}$ are 0.2, 8×10^{-3}, and 2×10^{-4} for $\ell = 1$, 2 and 3, respectively. Typical large separations for a red giant are $\Delta\nu \sim 10\,$Hz, implying an information crossing time of ~1 day. Damping

times then evaluate to

$$t_{\rm damp} \sim \begin{cases} 20-50\,{\rm days} & \text{for } \ell = 1 \\ 10^3\,{\rm days} & \text{for } \ell = 2 \\ 10^4\,{\rm days} & \text{for } \ell = 3\,. \end{cases} \tag{11.18}$$

In the case of the dipole modes, this process is thereby predicted to generate damping rates rivalling those associated with convection. If in operation, it could produce measurable depressions of the dipole mode visibilities: the above values yield $v_1 \sim 0.6$–0.8, with v_1 being the dipole mode visibility normalised in the manner of Mosser et al. (2017a). For quadrupole, octopule, and higher multiple modes, the damping becomes successively smaller owing to the ℓ-dependence of the transmission coefficient.

The above calculation assumes that the mode samples the entire surface of the magnetised core. It is to be noted that the spatial amplitude functions of the (well-known) regular oscillation modes are relatively localised in space. However, in contrast, chaotic modes are ergodic and thereby have spatial amplitude functions that in principle probe the entire surface of the core. This suggests that chaotic modes of a given frequency should undergo larger damping rates due to this leakage process than their regular counterparts (the restricted nature of the spatial amplitude functions of regular modes gives them a greater chance of 'avoiding' the trapping regions). As field strengths increase, one expects an increasingly large fraction of g-modes to be chaotic, and so this assumption should be justified in the strong-field limit. For the g-modes that remain regular, we predict that the non-isotropic distribution of the trapping regions (assuming that the field has a simple, large-scale geometry) would produce an orientation-dependent damping rate. That is, different m-values of a rotational multiplet might be expected to exhibit different levels of mode depression, depending on the field configuration and its orientation with respect to the rotation axis.

Equation (11.15) predicts a dependence of the leakage area on the ratio ω/N. This ratio is expected to decrease as stars evolve along the red giant branch, since continued contraction of the core leads to an increase in N and the expansion of the envelope leads to a decrease in ω. Assuming that the field configuration does not dramatically change over an evolutionary time scale, the trapping regions will shrink as the star evolves. Older red giants are therefore expected to experience smaller rates of damping due to this process, and hence exhibit larger dipole visibilities. This is qualitatively consistent with the observations (e.g. Mosser et al., 2017a, fig. 3a), which show an increase in v_1 with decreasing $\Delta\nu$ (smaller $\Delta\nu$ values indicate a larger/older star). A significant difference between this mechanism and the torsional Alfvén resonance mechanism is that in this case, the damping rate is determined by the trapping fraction, and not explicitly on the field strength itself. Recall that one difficulty with the torsional Alfvén resonance mechanism was accounting for the tightness of the v_1-$\Delta\nu$ trend, since relatively small variations in field strength would be expected to significantly alter the damping rates. In contrast, the trapping fraction is a function of both the field strength and configuration. For global-scale field configurations that vary only slowly with depth (e.g. twisted torus configurations), one expects a relatively weak dependence of the trapping fraction on field strength. It is thus much easier under the framework of this new mechanism to explain the low scatter in v_1 for given $\Delta\nu$ among the depressed group.

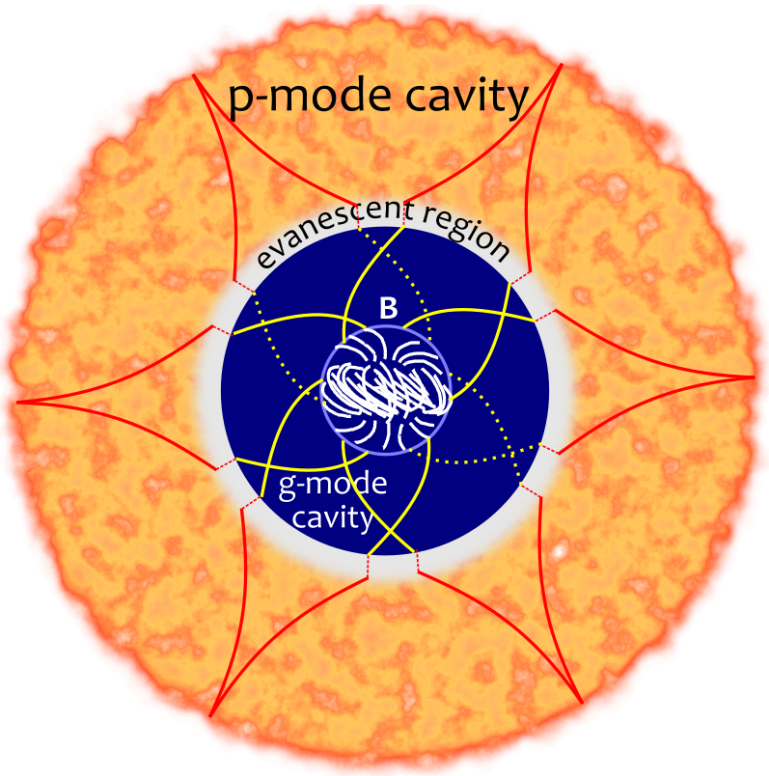

Figure 11.5: A cartoon illustration of the damping mechanism provided by the trapping phenomenon associated with a strong magnetic field. Red and yellow lines represent acoustic and gravity waves, which are constructively interfering to form global modes. Dotted yellow lines represent gravity waves that happen to hit a trapping region of the magnetised core, and are consequently dissipated. Solid yellow lines represent those that are reflected out of the core and may tunnel back into the p-mode cavity to reinforce the global mode. Overall, only a fraction of energy entering the g-mode cavity is dissipated.

11.3.2 Observational predictors

Without solving the full eigenvalue problem, it is not straightforward to predict the properties of the frequency spectrum in the strong-field regime. The most that can be said at the current stage of investigation is that the spectrum is likely to have a significant irregular component, i.e. the familiar notion of regular period spacings ceases to apply. The transition to chaotic dynamics implies that spacings between g-modes will instead follow a stochastic distribution with properties that can only be described in a statistical sense. While patterns may still exist in the subset of modes that remain regular, the fraction of such modes decreases with increasing field strength, and so in practice these would be difficult to identify. Previous work on the rapid-rotation problem has had some success with applying the Weyl formula (Weyl, 1912), which has its origins in quantum mechanics, to estimating the average density of p-modes. Below is a cursory discussion of its extension to the magnetised g-mode problem.

The density of states as a function of frequency can be regarded as the sum of two terms, one describing the average density (given by the Weyl formula) and the other describing fluctuations about it. The leading term of the Weyl formula, which dominates in the high-frequency limit, can be obtained from general principles if one assumes that each mode occupies on average a fixed volume of phase space. This is given by $(2\pi)^{\mathcal{N}}$, where $\mathcal{N}$ is the dimensionality of the system. Then, the number of modes having frequencies less than some given value ω is equal to the volume of phase space for which $H(\mathbf{x},\mathbf{k}) < \omega$, divided by $(2\pi)^{\mathcal{N}}$. This may be understood if one imagines dividing the spatial volume up into infinitesimal cubes, and assuming that in each of these modes can be taken to be a complete set of plane waves satisfying periodic boundary conditions. In the spherically symmetric g-mode case, the Hamiltonian takes the form given by (4.54). Rather than consider the region where $H(\mathbf{x},\mathbf{k}) < \omega$, as is typical in quantum mechanics, for the g-mode problem, it is more meaningful to consider instead the region where $\omega < H(\mathbf{x},\mathbf{k}) < N$ (note that an infinite volume of phase space, and so number of g-modes, exists for $H(\mathbf{x},\mathbf{k}) < \omega$).

Restricting ourselves to specified values of m and ℓ, the associated phase-space volume is given by the integral over the region where

$$|k_r| < \frac{\sqrt{\ell(\ell+1)}}{r}\left(\frac{N^2}{\omega^2}-1\right)^{1/2} \tag{11.19}$$

and $r_1 < r < r_2$, where r_1 and r_2 are the turning points of the g-mode cavity, i.e. radial coordinates where $\omega = N$. This predicts the number of g-modes with frequencies greater than ω to be

$$n_g(\omega) = \frac{1}{\pi}\int_{r_1}^{r_2} \frac{\sqrt{\ell(\ell+1)}}{r}\left(\frac{N^2}{\omega^2}-1\right)^{1/2} \mathrm{d}r\,. \tag{11.20}$$

Comparing this with Equation (4.79), one recognises the right-hand side of the above expression as being $n+1/2$, where n is the radial order. Since for fixed ℓ and m, the radial order essentially counts the number of g-modes above frequency ω, we see that the (g-mode equivalent of the) leading order term of the Weyl formula gives a result consistent with what is already known from asymptotic theory.

When a magnetic field is imposed, the effect on the Hamiltonian is to add an extra Alfvén frequency term. It is unclear as to whether the addition of this term will produce a systematic change in the volume of phase space associated with $\omega < H(\mathbf{x},\mathbf{k}) < N$, compared to the unmagnetised case. For any given frequency interval, the Alfvén term will shift some parts of phase space in and others out, with details depending on the field configuration and $N(r)$ profile. Suffice to say that the leading term of the Weyl formula alone does

not predict a systematic change in the average density of modes. Note that we have not considered higher order terms, which will become more significant at low frequencies. Further to this, sinusoidal fluctuations as a function of frequency about the average density are expected to be induced by periodic orbits of the system, as given by the Gutzwiller trace formula from periodic-orbit theory (Gutzwiller, 1990) in the quantum mechanical case. Implementation and checking the applicability of an analogue of this formula would require a knowledge of the periodic orbits of the system, in conjunction with a solution of the full eigenvalue problem.

To round off this part of the discussion, we are not aware of any straightforward method/heuristic argument for predicting the effect of a magnetic field on the density of g-modes as a function of frequency (short of solving explicitly for the full eigenspectrum). Phase-space volume considerations alone suggest that either an overall increase or decrease may be possible. Analyses of red giant data by Mosser et al. (2017a) suggest that the density of g-modes does not significantly differ between the two groups of stars. If the dichotomy is indeed a result of strong core fields, then this could be an indication that the volumes of phase space affected positively and negatively by the Alfvén term tend to cancel out, yielding approximately the same mode densities (within measurement error).

11.3.3 Summary

We have established that when fields are of sufficient strengths that the frequencies and spatial scales of Alfvén and gravity waves match (critical surfaces exist), significant alteration to gravity-wave propagation occurs. For any given field strength, this is always possible in some part of phase space, and the value of the plasma β is irrelevant. At or near critical surfaces, gravity waves may either be trapped or reflected. The fate of the waves depends on the wave frequency relative to the buoyancy frequency, and the orientation of the flux surfaces with respect to the stratification. For waves that are reflected, ingoing and outgoing wavenumbers tend to be of the same order, allowing for constructive interference of counter-propagating waves and the formation of global magnetogravity modes. These modes may be subject to additional damping if part of the wave energy enters trapping regions, whereupon acquisition of strong Alfvén character and phase mixing occurs. Since magnetic fields cannot be spherically symmetric, magnetic fields strong enough to influence the structure of a g-mode are expected to cause a transition to dynamical chaos owing to the loss of conserved quantities through symmetry breaking, implying that magnetogravity modes should form an irregular subset.

Given that an observational prediction of strong magnetic fields is mode chaos, a next step might be to implement procedures for detecting the presence of irregular components in the oscillation spectra. Borrowing ideas applied to quantum mechanical systems, one approach to this might be to use the fact that statistically, the spacing distribution of chaotic modes is expected to obey a Wigner distribution (Wigner, 1967), whereas that of regular modes obeys a Poisson distribution (Berry & Tabor, 1977). Techniques analogous to recurrence spectroscopy from experimental quantum mechanics (Main et al., 1994) might also be useful in searching for signatures of periodic orbits.

Chapter 12

Non-Perturbative Treatment of Magnetism

In this chapter we will extend the ideas introduced in Chapter 7 to the Lorentz force term. While the same overall principles apply, the magnetic problem is more complicated algebraically because the Lorentz force term involves fourth-order radial derivatives of the stream functions (these are only second-order in the Coriolis force). Nevertheless, the resulting equations can again be reduced to a pair of ODEs in the radial coordinate that can be solved by standard means, but where the effects of magnetism are incorporated in a non-perturbative manner. As for the rotation case, the results here are applicable to the regime where frequency shifts may be larger than the spacing of adjacent modes, a case not treated by non-degenerate perturbation theory.

12.1 Equations

As has been the case throughout this thesis, we will assume that the background magnetic field is axisymmetric ($\partial/\partial\phi \equiv 0$), in which case the field components can be written in terms of a scalar flux function ψ as per (3.11). Making the Cowling approximation, the equation of motion including the Lorentz force but ignoring rotation is

$$-\omega^2\boldsymbol{\xi} = -\frac{\nabla p'}{\rho} + \frac{\rho'}{\rho^2}\left[\nabla p - (\nabla\times\mathbf{B})\times\mathbf{B}\right] + \frac{1}{\rho}\left[(\nabla\times\mathbf{B}')\times\mathbf{B} + (\nabla\times\mathbf{B})\times\mathbf{B}'\right]. \tag{12.1}$$

The components of the Lorentz force in terms of ψ and B_ϕ are

$$[(\nabla\times\mathbf{B})\times\mathbf{B}]_r = -\frac{B_\phi}{r}\frac{\partial}{\partial r}[rB_\phi] - \frac{1}{r^2\sin\theta}\frac{\partial\psi}{\partial r}\left[\frac{1}{\sin\theta}\frac{\partial^2\psi}{\partial r^2} + \frac{1}{r^2}\frac{\partial}{\partial\theta}\left(\frac{1}{\sin\theta}\frac{\partial\psi}{\partial\theta}\right)\right], \tag{12.2}$$

$$[(\nabla\times\mathbf{B})\times\mathbf{B}]_\theta = -\frac{1}{r^3\sin\theta}\frac{\partial\psi}{\partial\theta}\left[\frac{1}{\sin\theta}\frac{\partial^2\psi}{\partial r^2} + \frac{1}{r^2}\frac{\partial}{\partial\theta}\left(\frac{1}{\sin\theta}\frac{\partial\psi}{\partial\theta}\right)\right] - \frac{B_\phi}{r\sin\theta}\frac{\partial}{\partial\theta}[B_\phi\sin\theta], \tag{12.3}$$

$$[(\nabla\times\mathbf{B})\times\mathbf{B}]_\phi = -\frac{1}{r^2\sin^2\theta}\frac{\partial\psi}{\partial r}\frac{\partial}{\partial\theta}[B_\phi\sin\theta] + \frac{1}{r^3\sin\theta}\frac{\partial\psi}{\partial\theta}\frac{\partial}{\partial r}[rB_\phi]. \tag{12.4}$$

With the aid of the linearised induction equation $\mathbf{B}' = \nabla\times(\boldsymbol{\xi}\times\mathbf{B})$, the components of the field perturbation can be written in terms of ψ, B_ϕ and the components of $\boldsymbol{\xi}$ as follows:

$$\begin{aligned}
B'_r &= -\frac{1}{r\sin\theta}\left[\frac{1}{r}\frac{\partial}{\partial\theta}\left(\xi_r\frac{\partial\psi}{\partial r}\right) + \frac{1}{r^2}\frac{\partial}{\partial\theta}\left(\xi_\theta\frac{\partial\psi}{\partial\theta}\right) + \frac{1}{r^2\sin\theta}\frac{\partial\psi}{\partial\theta}\frac{\partial\xi_\phi}{\partial\phi} - B_\phi\frac{\partial\xi_r}{\partial\phi}\right]\\
B'_\theta &= \frac{1}{r\sin\theta}\left[B_\phi\frac{\partial\xi_\theta}{\partial\phi} + \frac{1}{r\sin\theta}\frac{\partial\xi_\phi}{\partial\phi}\frac{\partial\psi}{\partial r} + \frac{\partial}{\partial r}\left(\xi_r\frac{\partial\psi}{\partial r} + \frac{\xi_\theta}{r}\frac{\partial\psi}{\partial\theta}\right)\right]\\
B'_\phi &= \frac{1}{r}\left[\frac{1}{\sin\theta}\frac{\partial\psi}{\partial\theta}\frac{\partial}{\partial r}\left(\frac{\xi_\phi}{r}\right) - \frac{\partial}{\partial r}(r\xi_r B_\phi) - \frac{\partial}{\partial\theta}(\xi_\theta B_\phi) - \frac{1}{r}\frac{\partial\psi}{\partial r}\frac{\partial}{\partial\theta}\left(\frac{\xi_\phi}{\sin\theta}\right)\right].
\end{aligned} \tag{12.5}$$

Let us collect the magnetic terms into

$$\mathbf{F}_L \equiv -\frac{\rho'}{\rho^2}(\nabla\times\mathbf{B})\times\mathbf{B}+\frac{1}{\rho}\left[(\nabla\times\mathbf{B})\times\mathbf{B}'+(\nabla\times\mathbf{B}')\times\mathbf{B}\right]. \tag{12.6}$$

While the full expressions for the components of $\mathbf{F}_L=(F_{Lr},F_{L\theta},F_{L\phi})$ in terms of ψ, B_ϕ and $\mathbf{B}'=(B'_r,B'_\theta,B'_\phi)$ are somewhat unwieldy, in the limit of modes with small radial scales we need only concern ourselves with those terms having the highest order derivatives of $\boldsymbol{\xi}$ with respect to radius (in this case, second), since $\partial^2/\partial r^2\sim k_r^2$. These occur only in the last term of (12.6) above, and so in this situation, we are left with

$$F_{Lr}=\frac{1}{\rho}\left[\left(B_\phi^2-\frac{B_\theta}{r\sin\theta}\frac{\partial\psi}{\partial r}\right)\frac{\partial^2\xi_r}{\partial r^2}-\frac{B_\theta}{r^2\sin\theta}\frac{\partial\psi}{\partial\theta}\frac{\partial^2\xi_\theta}{\partial r^2}-\frac{B_\phi}{r^2\sin\theta}\frac{\partial\psi}{\partial\theta}\frac{\partial^2\xi_\phi}{\partial r^2}\right], \tag{12.7}$$

$$F_{L\theta}=\frac{1}{\rho}\left[\frac{B_r}{r\sin\theta}\frac{\partial\psi}{\partial r}\frac{\partial^2\xi_r}{\partial r^2}+\frac{B_r}{r^2\sin\theta}\frac{\partial\psi}{\partial\theta}\frac{\partial^2\xi_\theta}{\partial r^2}\right], \tag{12.8}$$

$$F_{L\phi}=\frac{1}{\rho}\left[\frac{B_r}{r^2\sin\theta}\frac{\partial\psi}{\partial\theta}\frac{\partial^2\xi_\phi}{\partial r^2}-B_rB_\phi\frac{\partial^2\xi_r}{\partial r^2}\right]. \tag{12.9}$$

Taking the horizontal divergence and radial component of Equation (12.1), the spheroidal and radial equations of motion are then

$$\omega^2\nabla_\perp^2 S=\frac{1}{\rho}\nabla_\perp^2 p'-\frac{r}{\sin\theta}\left(\frac{\partial}{\partial\theta}\left[\sin\theta F_{L\theta}\right]+\frac{\partial F_{L\phi}}{\partial\phi}\right) \tag{12.10}$$

$$\omega^2 X=\frac{1}{\rho}\frac{\partial p'}{\partial r}-\frac{\rho'}{\rho^2}\frac{\partial p}{\partial r}-F_{Lr}, \tag{12.11}$$

which upon substitution of the above expressions become

$$\begin{aligned}\omega^2\nabla_\perp^2 S=\frac{1}{\rho}\nabla_\perp^2 p'&-\frac{1}{\rho r^2\sin^2\theta}\left(\sin\theta\frac{\partial}{\partial\theta}\left[\frac{1}{\sin\theta}\frac{\partial\psi}{\partial\theta}\frac{\partial\psi}{\partial r}\right]+\frac{\partial\psi}{\partial\theta}\frac{\partial\psi}{\partial r}\frac{\partial}{\partial\theta}-rB_\phi\frac{\partial\psi}{\partial\theta}\frac{\partial}{\partial\phi}\right)\frac{\partial^2 X}{\partial r^2}\\&-\frac{1}{\rho r^4\sin^2\theta}\left(\sin\theta\frac{\partial}{\partial\theta}\left[\frac{1}{\sin\theta}\left(\frac{\partial\psi}{\partial\theta}\right)^2\right]\frac{\partial}{\partial\theta}+\left(\frac{\partial\psi}{\partial\theta}\right)^2\frac{\partial^2}{\partial\theta^2}+\frac{1}{\sin^2\theta}\left(\frac{\partial\psi}{\partial\theta}\right)^2\frac{\partial^2}{\partial\phi^2}\right)\frac{\partial^2 S}{\partial r^2}\end{aligned} \tag{12.12}$$

and

$$-(\omega^2-N^2)X+\frac{p^{1/\gamma}}{\rho}\frac{\partial}{\partial r}\left(\frac{p'}{p^{1/\gamma}}\right)=\frac{1}{\rho}\left[B_\phi^2+\frac{1}{r^2\sin^2\theta}\left(\frac{\partial\psi}{\partial r}\right)^2\right]\frac{\partial^2 X}{\partial r^2}+\frac{1}{\rho r^3\sin^2\theta}\frac{\partial\psi}{\partial\theta}\left[\frac{1}{r}\frac{\partial\psi}{\partial r}\frac{\partial}{\partial\theta}-B_\phi\frac{\partial}{\partial\phi}\right]\frac{\partial^2 S}{\partial r^2}. \tag{12.13}$$

We will disregard the torsional equation of motion, which will be unimportant in the weak-field limit.

Inserting the spherical harmonic expansion given by Equation (7.15), we obtain the pair

$$\omega^2 S_\ell=\frac{p'_\ell}{\rho}+\frac{1}{\rho r^2\ell(\ell+1)}\left[\sum_{\ell'}\frac{\partial^2 X_{\ell'}}{\partial r^2}\bar{C}_{\ell,\ell'}\right]+\frac{1}{\rho r^4\ell(\ell+1)}\left[\sum_{\ell'}\frac{\partial^2 S_{\ell'}}{\partial r^2}\bar{D}_{\ell,\ell'}\right], \tag{12.14}$$

$$-(\omega^2-N^2)X_\ell+\frac{p^{1/\gamma}}{\rho}\frac{\partial}{\partial r}\left[\frac{p'_\ell}{p^{1/\gamma}}\right]=\frac{1}{\rho r^2}\left[\sum_{\ell'}\frac{\partial^2 X_{\ell'}}{\partial r^2}\bar{E}_{\ell,\ell'}\right]+\frac{1}{\rho r^4}\left[\sum_{\ell'}\frac{\partial^2 S_{\ell'}}{\partial r^2}\bar{F}_{\ell,\ell'}\right], \tag{12.15}$$

where

$$\bar{C}_{\ell,\ell'}\equiv\int_0^\pi\left(\sin\theta\frac{\partial}{\partial\theta}\left[\frac{1}{\sin\theta}\frac{\partial\psi}{\partial\theta}\frac{\partial\psi}{\partial r}\right]Y_{\ell'}^m+\frac{\partial\psi}{\partial\theta}\frac{\partial\psi}{\partial r}\frac{\partial Y_{\ell'}^m}{\partial\theta}-\mathrm{i}mrB_\phi\frac{\partial\psi}{\partial\theta}Y_{\ell'}^m\right)\frac{Y_\ell^{m*}}{\sin\theta}\,\mathrm{d}\theta, \tag{12.16}$$

$$\bar{D}_{\ell,\ell'}\equiv\int_0^\pi\left\{\frac{\partial}{\partial\theta}\left[\frac{1}{\sin\theta}\left(\frac{\partial\psi}{\partial\theta}\right)^2\right]\frac{\partial Y_{\ell'}^m}{\partial\theta}+\left(\frac{\partial\psi}{\partial\theta}\right)^2\frac{\partial^2 Y_{\ell'}^m}{\partial\theta^2}\frac{1}{\sin\theta}-m^2\left(\frac{\partial\psi}{\partial\theta}\right)^2\frac{Y_{\ell'}^m}{\sin^3\theta}\right\}Y_\ell^{m*}\,\mathrm{d}\theta, \tag{12.17}$$

$$\bar{E}_{\ell,\ell'}\equiv\int_0^\pi\left[r^2B_\phi^2+\frac{1}{\sin^2\theta}\left(\frac{\partial\psi}{\partial r}\right)^2\right]Y_{\ell'}^mY_\ell^{m*}\sin\theta\,\mathrm{d}\theta, \tag{12.18}$$

$$\bar{F}_{\ell,\ell'}\equiv\int_0^\pi\frac{\partial\psi}{\partial\theta}\left(\frac{\partial\psi}{\partial r}\frac{\partial Y_{\ell'}^m}{\partial\theta}-\mathrm{i}mrB_\phi Y_{\ell'}^m\right)\frac{Y_\ell^{m*}}{\sin\theta}\,\mathrm{d}\theta. \tag{12.19}$$

Unlike for the case of rotation, radial derivatives of S_ℓ are present and so it is more convenient to eliminate p'_ℓ in favour of S_ℓ, rather than vice versa. To do this we make use of (7.26), which gives us

$$\left(\omega^2 - \frac{\ell(\ell+1)}{r^2}\frac{\gamma p}{\rho}\right) S_\ell + \frac{\gamma p^{1-1/\gamma}}{\rho r^2}\frac{\partial}{\partial r}(r^2 p^{1/\gamma} X_\ell) = \frac{1}{\rho r^2 \ell(\ell+1)}\left(\frac{\partial^2 X_\ell}{\partial r^2}\bar{C}_{\ell,\ell} + \frac{1}{r^2}\frac{\partial^2 S_\ell}{\partial r^2}\bar{D}_{\ell,\ell}\right), \tag{12.20}$$

$$(\omega^2 - N^2)X_\ell + \frac{1}{\rho r^2}\left(\frac{\partial^2 X_\ell}{\partial r^2}\bar{E}_{\ell,\ell} + \frac{1}{r^2}\frac{\partial^2 S_\ell}{\partial r^2}\bar{F}_{\ell,\ell}\right) = \frac{\gamma p^{1/\gamma}}{\rho}\frac{\partial}{\partial r}\left[\ell(\ell+1)\frac{p^{1-1/\gamma}}{r^2}S_\ell - \frac{p^{1-2/\gamma}}{r^2}\frac{\partial}{\partial r}\left(r^2 p^{1/\gamma} X_\ell\right)\right], \tag{12.21}$$

where we have neglected cross-coupling terms between different ℓ under the assumption of weak fields. See that this is a fourth-order system, unlike the case for rotation which was second-order, with the additional derivatives arising from the Lorentz force term.

It is useful to note that in the case of the Prendergast solution, which has the separable form $\psi(r,\theta) = \Psi(r)\sin^2\theta$ and equatorial reflection symmetry, the coefficients in (12.16)–(12.19) simplify to

$$\bar{C}_{\ell,\ell} = 2\Psi\Psi'\int_0^\pi \left(\left[2\cos^2\theta - \sin^2\theta\right] Y_\ell^m + \sin\theta\cos\theta\frac{\partial Y_\ell^m}{\partial\theta}\right) Y_\ell^{m*}\sin\theta\,\mathrm{d}\theta \tag{12.22}$$

$$\bar{D}_{\ell,\ell} = 4\Psi^2\int_0^\pi \left(\left[\cos^2\theta - 2\sin^2\theta\right]\frac{\partial Y_\ell^m}{\partial\theta} + \sin\theta\cos\theta\frac{\partial^2 Y_\ell^m}{\partial\theta^2} - m^2\cot\theta Y_\ell^m\right) Y_\ell^{m*}\cos\theta\,\mathrm{d}\theta \tag{12.23}$$

$$\bar{E}_{\ell,\ell} = \Psi'^2 + \lambda^2\Psi^2\int_0^\pi Y_\ell^m Y_\ell^{m*}\sin^3\theta\,\mathrm{d}\theta \tag{12.24}$$

$$\bar{F}_{\ell,\ell} = \Psi\Psi'\int_0^\pi \sin 2\theta\frac{\partial Y_\ell^m}{\partial\theta}Y_\ell^{m*}\,\mathrm{d}\theta\,. \tag{12.25}$$

12.2 Frequency shift

An analytical expression for the frequency shift associated with the magnetic field can be obtained from Equations (12.20) and (12.21). By substituting each into the other, we can eliminate S_ℓ in favour of X_ℓ to arrive at a single fourth-order ODE in X_ℓ. We shall assume that the magnetic field is weak, thus allowing us to neglect terms quadratic or higher in powers of the coefficients (12.16)–(12.19). Using primes to denote derivatives with respect to r, we have

$$\alpha_1 X_\ell'''' + \alpha_2 X_\ell''' + \alpha_3 X_\ell'' + \alpha_4 X_\ell' + \alpha_5 X_\ell = 0\,, \tag{12.26}$$

with

$$\begin{aligned}
\alpha_1 &\equiv \frac{\mu_1\mu_4\nu_2}{\mu_2^2}\\
\alpha_2 &\equiv 2\frac{\mu_1\mu_4}{\mu_2}\left(\frac{\nu_2}{\mu_2}\right)' + \frac{\mu_1\mu_4\nu_3}{\mu_2^2} + \mu_4\left(\frac{\mu_1\nu_2}{\mu_2^2}\right)' - \frac{\mu_4\nu_1}{\mu_2} - \frac{\mu_3\nu_2}{\mu_2} + \frac{\mu_1\mu_5\nu_2}{\mu_2^2}\\
\alpha_3 &\equiv 2\mu_4\left(\frac{\mu_1}{\mu_2}\right)'\left(\frac{\nu_2}{\mu_2}\right)' + 3\frac{\mu_1\mu_4}{\mu_2}\left(\frac{\nu_2}{\mu_2}\right)'' + \mu_4\left(\frac{\mu_1\nu_3}{\mu_2^2}\right)' - \frac{\mu_4\nu_2}{\mu_2} + 2\frac{\mu_1\mu_4}{\mu_2}\left(\frac{\nu_3}{\mu_2}\right)' - \mu_4\left(\frac{\nu_1}{\mu_2}\right)'\\
&\quad - 2\mu_3\left(\frac{\nu_2}{\mu_2}\right)' - \frac{\mu_3\nu_3}{\mu_2} - \frac{\mu_5\nu_1}{\mu_2} + 2\frac{\mu_1\mu_5}{\mu_2}\left(\frac{\nu_2}{\mu_2}\right)' + \frac{\mu_1\mu_5\nu_3}{\mu_2^2} + \nu_4
\end{aligned}$$

$$\alpha_4 \equiv \nu_5 - \mu_3\left(\frac{\nu_2}{\mu_2}\right)'' - 2\mu_3\left(\frac{\nu_3}{\mu_2}\right)' - \mu_4\left(\frac{\nu_2}{\mu_2}\right)' + \mu_4\left(\frac{\mu_1}{\mu_2}\right)'\left(\frac{\nu_2}{\mu_2}\right)'' + \frac{\mu_1\mu_4}{\mu_2}\left(\frac{\nu_2}{\mu_2}\right)''' + 2\mu_4\left(\frac{\mu_1}{\mu_2}\right)'\left(\frac{\nu_3}{\mu_2}\right)'$$
$$+ 3\frac{\mu_1\mu_4}{\mu_2}\left(\frac{\nu_3}{\mu_2}\right)'' - \frac{\mu_4\nu_3}{\mu_2} - \frac{\mu_5\nu_2}{\mu_2} + \frac{\mu_1\mu_5}{\mu_2}\left(\frac{\nu_2}{\mu_2}\right)'' + 2\frac{\mu_1\mu_5}{\mu_2}\left(\frac{\nu_3}{\mu_2}\right)'$$
$$\alpha_5 \equiv \nu_6 - \mu_3\left(\frac{\nu_3}{\mu_2}\right)'' - \mu_4\left(\frac{\nu_3}{\mu_2}\right)' + \mu_4\left(\frac{\mu_1}{\mu_2}\right)'\left(\frac{\nu_3}{\mu_2}\right)'' + \frac{\mu_1\mu_4}{\mu_2}\left(\frac{\nu_3}{\mu_2}\right)''' - \frac{\mu_5\nu_3}{\mu_2} + \frac{\mu_1\mu_5}{\mu_2}\left(\frac{\nu_3}{\mu_2}\right)'' \tag{12.27}$$

$$\mu_1 \equiv -\frac{\bar{D}_{\ell,\ell}}{\rho r^4 \ell(\ell+1)} \tag{12.28}$$
$$\mu_2 \equiv \omega^2 - \frac{\ell(\ell+1)}{r^2}\frac{\gamma p}{\rho} \tag{12.29}$$
$$\mu_3 \equiv -\frac{\bar{F}_{\ell,\ell}}{\rho r^4} \tag{12.30}$$
$$\mu_4 \equiv \frac{\ell(\ell+1)}{r^2}\frac{\gamma p}{\rho} \tag{12.31}$$
$$\mu_5 \equiv \frac{\ell(\ell+1)}{\rho r^2}\left[(\gamma-1)\frac{\partial p}{\partial r} - \frac{2\gamma p}{r}\right] \tag{12.32}$$
$$\nu_1 \equiv \frac{\bar{C}_{\ell,\ell}}{\rho r^2 \ell(\ell+1)} \tag{12.33}$$
$$\nu_2 \equiv -\frac{\gamma p}{\rho} \tag{12.34}$$
$$\nu_3 \equiv -\frac{1}{\rho}\left[\frac{\partial p}{\partial r} + \frac{2\gamma p}{r}\right] \tag{12.35}$$
$$\nu_4 \equiv \frac{1}{\rho}\left(\frac{\bar{E}_{\ell,\ell}}{r^2} + \gamma p\right) \tag{12.36}$$
$$\nu_5 \equiv \frac{\gamma}{\rho}\left(\frac{\partial p}{\partial r} + \frac{2p}{r}\right) \tag{12.37}$$
$$\nu_6 \equiv \frac{1}{\rho}\left[\frac{2(\gamma-1)}{r}\frac{\partial p}{\partial r} - \frac{2\gamma p}{r^2} - \frac{1}{\gamma p}\left(\frac{\partial p}{\partial r}\right)^2 + \frac{\partial^2 p}{\partial r^2}\right] + \omega^2 - N^2\,. \tag{12.38}$$

Of the above μ and ν coefficients, the magnetic terms are contained in μ_1, μ_3, ν_1 and ν_4, so that α_1 and α_2 are both zero when the field is zero. The remaining α coefficients contain both magnetic and non-magnetic parts. Let us write them in the form

$$\alpha_i = \alpha_{i0} + \alpha_{i1}\,, \quad i = 1, \cdots, 5 \tag{12.39}$$

where the term with subscript 0 contains only non-magnetic terms, and all magnetic terms are gathered in the other. In this case, $\alpha_{10} = \alpha_{20} = 0$.

To solve for the frequency shift we will apply the WKB method to Equation (12.26). Inserting the ansatz $X_\ell = a(r)\exp[\mathrm{i}\Phi(r)]$ with $\Phi(r)$ varying much more rapidly than $a(r)$, we get an algebraic quartic equation for $k_r = \Phi'(r)$:

$$\alpha_1(r)k_r(r)^4 - \mathrm{i}\alpha_2(r)k_r(r)^3 - \alpha_3(r)k_r(r)^2 + \mathrm{i}\alpha_4(r)k_r(r) + \alpha_5(r) = 0\,. \tag{12.40}$$

Let us write $k_r(r) = k_{r0}(r) + k_{r1}(r)$, where k_{r0} is the solution in the absence of a field and k_{r1} represents the correction associated with the field. Substituting this into (12.40) and performing a binomial expansion under the assumption that $k_{r1} \ll k_{r0}$ (weak fields), we end up with

$$k_{r1} \approx -\frac{\alpha_1 k_{r0}^4 - \mathrm{i}\alpha_2 k_{r0}^3 - \alpha_3 k_{r0}^2 + \mathrm{i}\alpha_4 k_{r0} + \alpha_5}{4\alpha_1 k_{r0}^3 - 3\mathrm{i}\alpha_2 k_{r0}^2 - 2\alpha_3 k_{r0} + \mathrm{i}\alpha_4}\,. \tag{12.41}$$

Since $-\alpha_{30}k_{r0}^2 + \mathrm{i}\alpha_{40}k_{r0} + \alpha_{50} = 0$ by definition, this is equal to

$$k_{r1} \approx -\frac{\alpha_1 k_{r0}^4 - \mathrm{i}\alpha_2 k_{r0}^3 - \alpha_{31}k_{r0}^2 + \mathrm{i}\alpha_{41}k_{r0} + \alpha_{51}}{4\alpha_1 k_{r0}^3 - 3\mathrm{i}\alpha_2 k_{r0}^2 - 2\alpha_3 k_{r0} + \mathrm{i}\alpha_4} \tag{12.42}$$

For large k_{r0}, the dominant term in the numerator of (12.42) is the quartic term. Since $\omega_A \ll \omega$ where $\omega_A \sim k_{r0}v_A$,

$$\frac{\alpha_1}{\alpha_3}, \frac{\alpha_2}{\alpha_4} \sim \frac{v_A^2}{\omega^2} \ll k_{r0}^{-2} \tag{12.43}$$

and hence the dominant terms in the denominator of (12.42) are the last two. When k_{r0} is large, we may neglect the last term in favour of $2\alpha_3 k_{r0}$. Approximating this by its non-magnetic version, we then seek an expression for

$$k_{r1} \approx \frac{\alpha_1}{2\alpha_{30}} k_{r0}^3 . \tag{12.44}$$

Substituting (12.28)–(12.38) into the desired α coefficients, we find that

$$\alpha_1 = \frac{\bar{D}_{\ell,\ell}}{\rho r^6}\left(\frac{\gamma p}{\rho}\right)^2 \left[\omega^2 - \frac{\ell(\ell+1)}{r^2}\frac{\gamma p}{\rho}\right]^{-2} \tag{12.45}$$

and

$$\alpha_{30} = \left[\frac{\rho}{\gamma p} - \frac{\ell(\ell+1)}{r^2\omega^2}\right]^{-1}, \tag{12.46}$$

hence

$$k_{r1} \approx \frac{1}{2\omega^2}\frac{\bar{D}_{\ell,\ell}}{\rho r^6}\frac{\gamma p}{\rho}\left[\omega^2 - \frac{\ell(\ell+1)}{r^2}\frac{\gamma p}{\rho}\right]^{-1} k_{r0}^3 . \tag{12.47}$$

If we can assume large sound speeds, then neglecting ω^2 in favour of the other term in the brackets leaves us with

$$k_{r1} \approx -\frac{1}{2\omega^2}\frac{\bar{D}_{\ell,\ell}}{\rho r^4}\frac{1}{\ell(\ell+1)} k_{r0}^3 . \tag{12.48}$$

An approximate expression for k_{r0} can be obtained from the gravity wave dispersion relation,

$$\begin{aligned} \omega^2 &= \frac{k_\perp^2}{k_\perp^2 + k_{r0}^2} N^2 \approx \frac{k_\perp^2}{k_{r0}^2} N^2 = \frac{\ell(\ell+1)N^2}{k_{r0}^2 r^2} \\ \implies k_{r0} &= \frac{\sqrt{\ell(\ell+1)}}{r}\frac{N}{\omega} . \end{aligned} \tag{12.49}$$

Substituting this into the expression for k_{r1} given by (12.48), we obtain for the case of the Prendergast field that

$$k_{r1} = -\frac{\Psi^2 \eta [\ell(\ell+1)]^{1/2} N^3}{\omega^5 \rho r^7}, \tag{12.50}$$

where

$$\eta \equiv 2\int_0^\pi \left[(\cos^2\theta - 2\sin^2\theta)\frac{\partial Y_\ell^m}{\partial\theta} + \sin\theta\cos\theta\frac{\partial^2 Y_\ell^m}{\partial\theta^2} - m^2\cot\theta Y_\ell^m\right] Y_\ell^{m*}\cos\theta\,\mathrm{d}\theta . \tag{12.51}$$

Next, we apply the usual quantisation condition

$$\int_{r_1}^{r_2} k_{r0} + k_{r1}\,\mathrm{d}r = \left(n + \frac{1}{2}\right)\pi \tag{12.52}$$

and expand $\omega = \omega_0 + \omega_1$, with ω_0 given in (7.37). Making use of the binomial approximation under the assumption that $|\omega_1| \ll \omega_0$, we obtain

$$\omega_1 \approx \frac{\omega_0 \zeta}{4\zeta - \omega_0^5} \tag{12.53}$$

where

$$\zeta \equiv \frac{\eta[\ell(\ell+1)]^{1/2}}{\left(n+\frac{1}{2}\right)\pi} \int_{r_1}^{r_2} \frac{\Psi^2 N^3}{\rho r^7}\,\mathrm{d}r\,. \tag{12.54}$$

Consider next the relative sizes of the terms in the denominator of (12.53). For low-degree modes, the factor $\eta[\ell(\ell+1)]^{1/2}/\pi$ in the ζ term is of order unity, while the rest of it is

$$\frac{1}{n+\frac{1}{2}} \int \frac{\Psi^2 N^3}{\rho r^7}\,\mathrm{d}r \sim \frac{B^2 N^3}{\rho k_{0r} r_c^3} \sim \frac{\omega_A^2 N^3}{k_{0r}^3 r_c^3} \sim \frac{\omega_A^2 N^3}{n^3} \sim \omega_A^2 \omega_0^3 \ll \omega_0^5\,. \tag{12.55}$$

Here $n \sim k_{0r} r_c$ where r_c is the extent of the magnetised region, and we are in the non-dynamically significant regime where $\omega_A \ll \omega_0$. Hence $\zeta \ll \omega_0^5$ and $\omega_1 \approx -\zeta\omega_0^{-4}$, i.e.

$$\omega_1 \approx -\frac{1}{\omega_0^4} \frac{\eta[\ell(\ell+1)]^{1/2}}{\left(n+\frac{1}{2}\right)\pi} \int_{r_1}^{r_2} \frac{\Psi^2 N^3}{\rho r^7}\,\mathrm{d}r\,. \tag{12.56}$$

12.3 Combined with rotation

If both the Coriolis and Lorentz terms are included in the momentum equation, then the resulting set of equations would be

$$-\omega^2 S_\ell + \frac{p_\ell'}{\rho} = 2mD_{\ell,\ell} S_\ell + C_{\ell,\ell} S_\ell - \frac{2m}{\ell(\ell+1)} E_{\ell,\ell}(S_\ell + rX_\ell) - \frac{1}{\rho r^2 \ell(\ell+1)} \left(\frac{\partial^2 X_\ell}{\partial r^2} \bar{C}_{\ell,\ell} + \frac{1}{r^2} \frac{\partial^2 S_\ell}{\partial r^2} \bar{D}_{\ell,\ell} \right) \tag{12.57}$$

$$-\left(\omega^2 - N^2\right) X_\ell + \frac{p^{1/\gamma}}{\rho} \frac{\partial}{\partial r} \left(\frac{p_\ell'}{p^{1/\gamma}} \right) = 2mD_{\ell,\ell} X_\ell - \frac{2m}{r} S_\ell E_{\ell,\ell} + \frac{1}{\rho r^2} \left(\frac{\partial^2 X_\ell}{\partial r^2} \bar{E}_{\ell,\ell} + \frac{1}{r^2} \frac{\partial^2 S_\ell}{\partial r^2} \bar{F}_{\ell,\ell} \right). \tag{12.58}$$

We now set out to reduce this to a second-order system. This is possible in the limit of weak fields and slow rotation, where we may neglect terms of quadratic or higher order in the coefficients $C_{\ell,\ell}$, $D_{\ell,\ell}$, $E_{\ell,\ell}$, $\bar{C}_{\ell,\ell}$, $\bar{D}_{\ell,\ell}$, $\bar{E}_{\ell,\ell}$ and $\bar{F}_{\ell,\ell}$, which are small parameters. The process is algebraically lengthy and will not be expounded in full detail here. To summarise, it involves eliminating higher derivatives of X_ℓ and S_ℓ by repeatedly differentiating and substituting (12.57) and (12.58). During each substitution step, only the non-magnetic terms need to re-enter, since higher derivatives only appear in the magnetic terms and we are neglecting all terms of quadratic or higher order in the small parameters. As before, p_ℓ' is eliminated using

Equation (7.26). The final result is the pair of equations

$$
\begin{aligned}
X_\ell' = &\left[\frac{\ell(\ell+1)}{r^2} - \frac{\rho\omega^2}{\gamma p} - \frac{\rho}{\gamma p}\left(2mD_{\ell,\ell} + C_{\ell,\ell} - \frac{2mE_{\ell,\ell}}{\ell(\ell+1)}\right) + w_7\frac{\bar{C}_{\ell,\ell}}{\gamma p r^2\ell(\ell+1)} + w_5\frac{\bar{D}_{\ell,\ell}}{\gamma p r^4\ell(\ell+1)}\right] S_\ell \\
&+ \left[-\frac{1}{\gamma p}\frac{\partial p}{\partial r} - \frac{2}{r} + \frac{2mrE_{\ell,\ell}}{\ell(\ell+1)}\frac{\rho}{\gamma p} + w_8\frac{\bar{C}_{\ell,\ell}}{\gamma p r^2\ell(\ell+1)} + w_6\frac{\bar{D}_{\ell,\ell}}{\gamma p r^4\ell(\ell+1)}\right] X_\ell \qquad (12.59)\\
S_\ell' = &\left[-\rho N^2\left(\frac{\partial p}{\partial r}\right)^{-1} - \frac{1}{\Gamma}\left(2m\frac{\partial D_{\ell,\ell}}{\partial r} + \frac{\partial C_{\ell,\ell}}{\partial r} - \frac{2m}{\ell(\ell+1)}\frac{\partial E_{\ell,\ell}}{\partial r} + \frac{2mrE_{\ell,\ell}}{\ell(\ell+1)}\frac{\rho\omega^2}{\gamma p}\right) + \frac{1}{\Gamma\rho r^2}\left(w_7\bar{E}_{\ell,\ell} + \frac{w_5\bar{F}_{\ell,\ell}}{r^2}\right)\right. \\
&+ \frac{w_7}{\Gamma\ell(\ell+1)}\frac{1}{\rho r^2}\left(\frac{\partial\bar{C}_{\ell,\ell}}{\partial r} - \frac{2\bar{C}_{\ell,\ell}}{r} - \frac{\bar{C}_{\ell,\ell}}{\gamma p}\frac{\partial p}{\partial r}\right) + \frac{w_5}{\Gamma\ell(\ell+1)}\frac{1}{\rho r^4}\left(\frac{\partial\bar{D}_{\ell,\ell}}{\partial r} - \frac{4\bar{D}_{\ell,\ell}}{r} - \frac{\bar{D}_{\ell,\ell}}{\gamma p}\frac{\partial p}{\partial r}\right) \\
&\left.+ \frac{1}{\Gamma\gamma p r^2\ell(\ell+1)}\left(w_3\bar{C}_{\ell,\ell} + \frac{w_1\bar{D}_{\ell,\ell}}{r^2}\right)\right] S_\ell \\
&+ \left[\frac{\omega^2 - N^2}{\Gamma} + \frac{2mD_{\ell,\ell}}{\Gamma} + \frac{2m}{\Gamma\ell(\ell+1)}\left(r\frac{\partial E_{\ell,\ell}}{\partial r} - E_{\ell,\ell} + rE_{\ell,\ell}\frac{1}{\rho}\frac{\partial\rho}{\partial r}\right) + \frac{1}{\Gamma\rho r^2}\left(w_8\bar{E}_{\ell,\ell} + \frac{w_6\bar{F}_{\ell,\ell}}{r^2}\right)\right. \\
&+ \frac{w_8}{\Gamma\ell(\ell+1)}\frac{1}{\rho r^2}\left(\frac{\partial\bar{C}_{\ell,\ell}}{\partial r} - \frac{2\bar{C}_{\ell,\ell}}{r} - \frac{\bar{C}_{\ell,\ell}}{\gamma p}\frac{\partial p}{\partial r}\right) + \frac{w_6}{\Gamma\ell(\ell+1)}\frac{1}{\rho r^4}\left(\frac{\partial\bar{D}_{\ell,\ell}}{\partial r} - \frac{4\bar{D}_{\ell,\ell}}{r} - \frac{\bar{D}_{\ell,\ell}}{\gamma p}\frac{\partial p}{\partial r}\right) \\
&\left.+ \frac{1}{\Gamma\gamma p r^2\ell(\ell+1)}\left(w_4\bar{C}_{\ell,\ell} + \frac{w_2\bar{D}_{\ell,\ell}}{r^2}\right)\right] X_\ell\,, \qquad (12.60)
\end{aligned}
$$

where

$$
\begin{aligned}
\Gamma \equiv{}& \omega^2 + 2mD_{\ell,\ell} + C_{\ell,\ell} - \frac{2mE_{\ell,\ell}}{\ell(\ell+1)}\,, \qquad (12.61)\\
w_1 \equiv{}& -\left(1-\frac{N^2}{\omega^2}\right)\left(\frac{2\ell(\ell+1)}{r^2} - \frac{\rho\omega^2}{\gamma p}\right)\frac{2}{r} - \frac{2}{\omega^2}\frac{\partial N^2}{\partial r}\frac{\ell(\ell+1)}{r^2} - \left(1-\frac{N^2}{\omega^2}\right)\frac{1}{\gamma p}\frac{\partial p}{\partial r}\left(\frac{\ell(\ell+1)}{r^2} - \frac{\rho\omega^2}{p}\right) \\
&- \left(\frac{\partial p}{\partial r}\right)^{-1}\left[\rho N^2\left(1-\frac{N^2}{\omega^2}\right)\frac{2\ell(\ell+1)}{r^2} - \rho^2N^2\frac{\omega^2}{\gamma p} + \frac{\partial^2\rho}{\partial r^2}N^2 + \rho\frac{\partial^2N^2}{\partial r^2}\right] \\
&+ \left(\frac{\partial p}{\partial r}\right)^{-2}\left(2\rho N^4\frac{\partial\rho}{\partial r} + \rho^2N^2\frac{\partial N^2}{\partial r} + 2\frac{\partial\rho}{\partial r}\frac{\partial^2p}{\partial r^2}N^2 + \rho\frac{\partial^3p}{\partial r^3}N^2 + 2\rho\frac{\partial^2p}{\partial r^2}\frac{\partial N^2}{\partial r}\right) \\
&- \rho N^2\left(\frac{\partial p}{\partial r}\right)^{-3}\left[3\rho N^2\frac{\partial^2p}{\partial r^2} + 2\left(\frac{\partial^2p}{\partial r^2}\right)^2\right] \qquad (12.62)\\
w_2 \equiv{}& \left(1-\frac{N^2}{\omega^2}\right)\left(\frac{\partial p}{\partial r}\right)^2\frac{1}{\gamma p^2}\left(1+\frac{1}{\gamma}\right) + \frac{2}{\gamma p}\frac{\partial p}{\partial r}\left[\left(1-\frac{N^2}{\omega^2}\right)\frac{2}{r} + \frac{1}{\omega^2}\frac{\partial N^2}{\partial r}\right] + \left(1-\frac{N^2}{\omega^2}\right)\left(\frac{6}{r^2} - \frac{1}{\gamma p}\frac{\partial^2p}{\partial r^2}\right) \\
&+ \left(1-\frac{N^2}{\omega^2}\right)^2\left(\frac{\ell(\ell+1)}{r^2} - \frac{\rho\omega^2}{\gamma p}\right) + \frac{1}{\omega^2}\left(\frac{4}{r}\frac{\partial N^2}{\partial r} - \frac{\partial^2N^2}{\partial r^2}\right) \\
&+ \left(\frac{\partial p}{\partial r}\right)^{-1}\left[\left(1-\frac{N^2}{\omega^2}\right)\left(\frac{2}{r}\rho N^2 - \frac{\partial\rho}{\partial r}N^2 - 2\rho\frac{\partial N^2}{\partial r}\right) + \frac{\rho N^2}{\omega^2}\frac{\partial N^2}{\partial r}\right] + \left(\frac{\partial p}{\partial r}\right)^{-2}\left(1-\frac{N^2}{\omega^2}\right)2\rho N^2\frac{\partial^2p}{\partial r^2} \qquad (12.63)\\
w_3 \equiv{}& \left(\frac{\partial p}{\partial r}\right)^2\left(2+\frac{1}{\gamma}\right)\frac{1}{\gamma p^2}\left(\frac{\ell(\ell+1)}{r^2} - \frac{\rho\omega^2}{p}\right) + \frac{2}{r}\frac{1}{\gamma p}\frac{\partial p}{\partial r}\left[\frac{4\ell(\ell+1)}{r^2} - \frac{\rho\omega^2}{p}\left(2+\frac{1}{\gamma}\right)\right] \\
&+ \left(1-\frac{N^2}{\omega^2}\right)\left(\frac{\ell(\ell+1)}{r^2} - \frac{\rho\omega^2}{\gamma p}\right)^2 + 2\left(\frac{\ell(\ell+1)}{r^2} - \frac{\rho\omega^2}{\gamma p}\right)\left(\frac{4}{r^2} - \frac{1}{\gamma p}\frac{\partial^2p}{\partial r^2}\right) + \frac{10\ell(\ell+1)}{r^4} \\
&+ \frac{\rho\omega^2}{\gamma p}\left(\frac{\rho N^2}{\gamma p} + \frac{1}{p}\frac{\partial^2p}{\partial r^2} - \frac{1}{\rho}\frac{\partial^2\rho}{\partial r^2}\right) + \rho\left(\frac{\partial p}{\partial r}\right)^{-1}\left[2N^2\left(\frac{3\ell(\ell+1)}{r^3} + \frac{\omega^2}{\gamma p}\frac{\partial\rho}{\partial r}\right) - \left(\frac{\ell(\ell+1)}{r^2} - \frac{\rho\omega^2}{\gamma p}\right)\frac{\partial N^2}{\partial r}\right] \\
&+ \left(\frac{\partial p}{\partial r}\right)^{-2}\left(\frac{\ell(\ell+1)}{r^2} - \frac{\rho\omega^2}{\gamma p}\right)\rho N^2\frac{\partial^2p}{\partial r^2} \qquad (12.64)
\end{aligned}
$$

$$w_4 \equiv -\left(\frac{\partial p}{\partial r}\right)^3 \frac{1}{\gamma p^3}\left(2+\frac{1}{\gamma}\right)\left(1+\frac{1}{\gamma}\right) - \frac{6}{r}\frac{1}{\gamma p^2}\left(\frac{\partial p}{\partial r}\right)^2\left(1+\frac{1}{\gamma}\right) - \frac{1}{\gamma p}\frac{\partial p}{\partial r}\left[\left(1-\frac{N^2}{\omega^2}\right)\left(\frac{2\ell(\ell+1)}{r^2} - \frac{\rho\omega^2}{p}\left(2+\frac{1}{\gamma}\right)\right)\right.$$
$$\left. + \frac{18}{r^2} - \frac{3}{p}\frac{\partial^2 p}{\partial r^2}\left(1+\frac{1}{\gamma}\right)\right] - \left(1-\frac{N^2}{\omega^2}\right)\left(\frac{8\ell(\ell+1)}{r^3} + \frac{\omega^2}{\gamma p}\left(\frac{\partial \rho}{\partial r} - \frac{4\rho}{r}\right)\right) + \frac{6}{r}\left(\frac{1}{\gamma p}\frac{\partial^2 p}{\partial r^2} - \frac{4}{r^2}\right)$$
$$- \left(\frac{\ell(\ell+1)}{r^2} - \frac{\rho\omega^2}{\gamma p}\right)\frac{1}{\omega^2}\frac{\partial N^2}{\partial r} - \frac{1}{\gamma p}\frac{\partial^3 p}{\partial r^3} - \rho N^2\left(1-\frac{N^2}{\omega^2}\right)\frac{\ell(\ell+1)}{r^2}\left(\frac{\partial p}{\partial r}\right)^{-1} \tag{12.65}$$

$$w_5 \equiv \left(1-\frac{N^2}{\omega^2}\right)\frac{\ell(\ell+1)}{r^2} - \frac{\rho\omega^2}{\gamma p} - \left(\frac{\partial p}{\partial r}\right)^{-1}\rho\frac{\partial N^2}{\partial r} + \left(\frac{\partial p}{\partial r}\right)^{-2}\rho N^2\frac{\partial^2 p}{\partial r^2} \tag{12.66}$$

$$w_6 \equiv -\left(1-\frac{N^2}{\omega^2}\right)\left[\frac{2}{r} + \frac{1}{\gamma p}\frac{\partial p}{\partial r} + \rho N^2\left(\frac{\partial p}{\partial r}\right)^{-1}\right] - \frac{1}{\omega^2}\frac{\partial N^2}{\partial r} \tag{12.67}$$

$$w_7 \equiv -\frac{1}{\gamma p}\frac{\partial p}{\partial r}\left(\frac{\ell(\ell+1)}{r^2} - \frac{\rho\omega^2}{p}\right) - \frac{2}{r}\left(\frac{\ell(\ell+1)}{r^2} - \frac{\rho\omega^2}{\gamma p}\right) - \frac{\ell(\ell+1)}{r^2}\rho N^2\left(\frac{\partial p}{\partial r}\right)^{-1} \tag{12.68}$$

$$w_8 \equiv \left(\frac{\ell(\ell+1)}{r^2} - \frac{\rho\omega^2}{\gamma p}\right)\left(1-\frac{N^2}{\omega^2}\right) + \frac{6}{r^2} - \frac{1}{\gamma p}\frac{\partial^2 p}{\partial r^2} + \frac{4}{r}\frac{1}{\gamma p}\frac{\partial p}{\partial r} + \frac{1}{\gamma p^2}\left(\frac{\partial p}{\partial r}\right)^2\left(1+\frac{1}{\gamma}\right). \tag{12.69}$$

12.4 Numerical results

Although the algebraic form of the equations is considerably more complicated than in the non-rotating, unmagnetised case, their structure is identical and can be solved via the same shooting and matching procedure to obtain the eigenfrequencies and eigenfunctions. Figures 12.1 and 12.2 show the results for the case where magnetism is present but not rotation, for $\ell = 1$ and $\ell = 2$, respectively. These have been computed for an $n = 3$ polytrope. Besides the numerical results, also shown for comparison are the frequencies in the absence of a field, and the expected frequencies if one applies the analytic formula in (12.56). There appears to be good agreement between the analytic and numerical frequencies, suggesting the approximations to be adequate in the chosen parameter regime. Note that, as can be deduced from (12.51), for magnetic perturbations the sign of m is irrelevant: modes with the same $|m|$ experience the same frequency shift.

In the case where both rotation and magnetism are present, one expects the overall frequency shift to be given (to first order) simply by the sum of the shifts expected from each individually. Figure 12.3 shows the results for a spectrum of modes computed under influence of both rotation and magnetism, with the predicted frequencies (taken to be the sum of the rotational and magnetic frequency shifts) overlaid. It can be seen that these are also in good agreement.

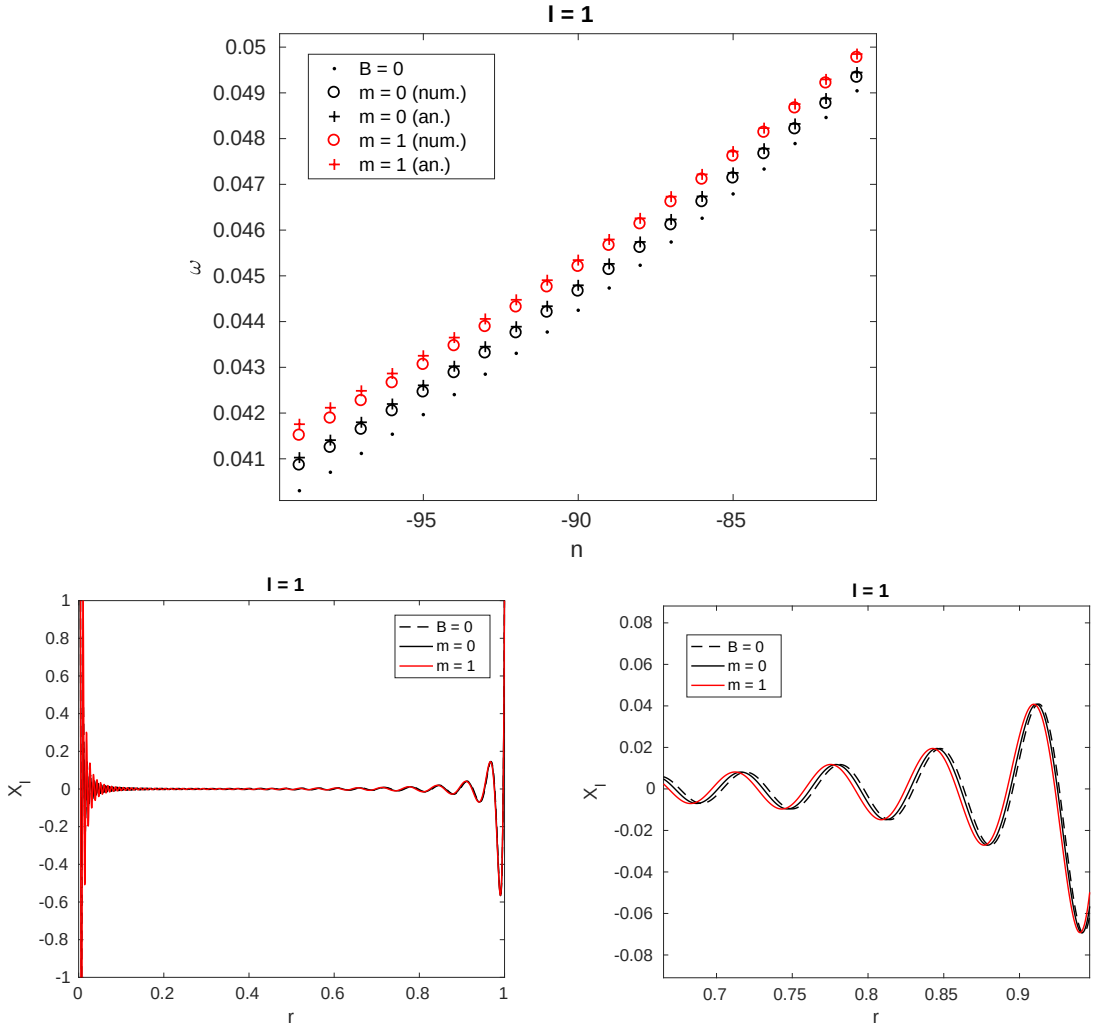

Figure 12.1: Results for a selection of modes computed by solving Equations (12.59) and (12.60), for $\ell = 1$. The underlying stellar model is an $n = 3$ polytrope with a magnetic field imposed in the central 0.3 of the stellar radius. The chosen field configuration is the Prendergast model scaled such that the central Alfvén speed is $3 \times 10^{-5}\sqrt{GM_*/R_*}$. Top: comparison of mode frequencies at zero field, and for $m = 0$ and $m = 1$ with the field switched on, overlaid with the analytical prediction given by (12.56). Bottom: eigenfunctions for the mode with $n = -90$, $\omega_0 = 0.0443$, with a close-up on the right showing the slight differences between the eigenfunctions. Frequencies are in units of $\sqrt{GM_*/R_*^3}$.

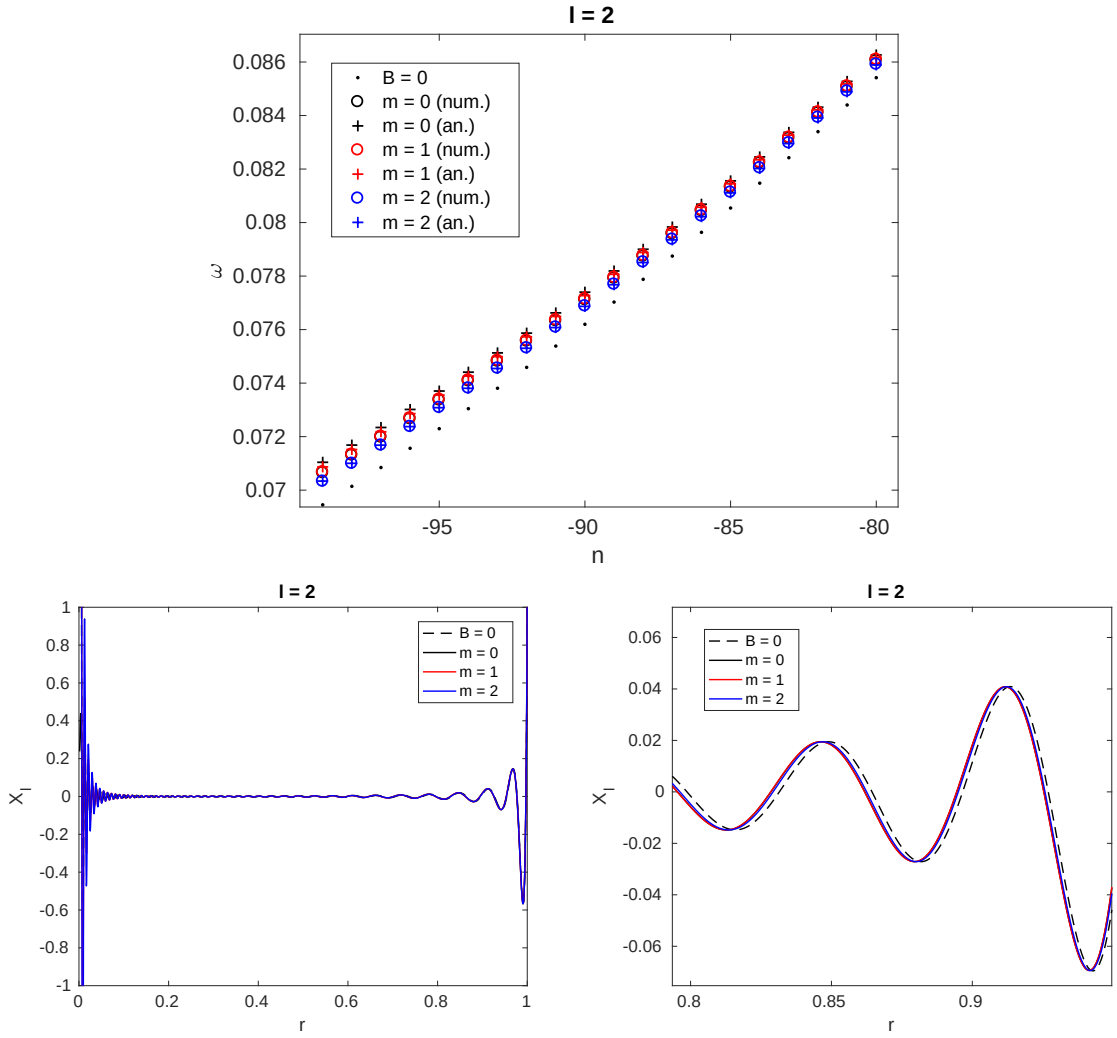

Figure 12.2: As for Figure 12.2, but for $\ell = 2$, a central Alfvén speed of $4 \times 10^{-5}\sqrt{GM_*/R_*}$, and showing in addition results for $m = 2$. The bottom panels are for a mode with $n = -90$, $\omega_0 = 0.0762\sqrt{GM_*/R_*^3}$.

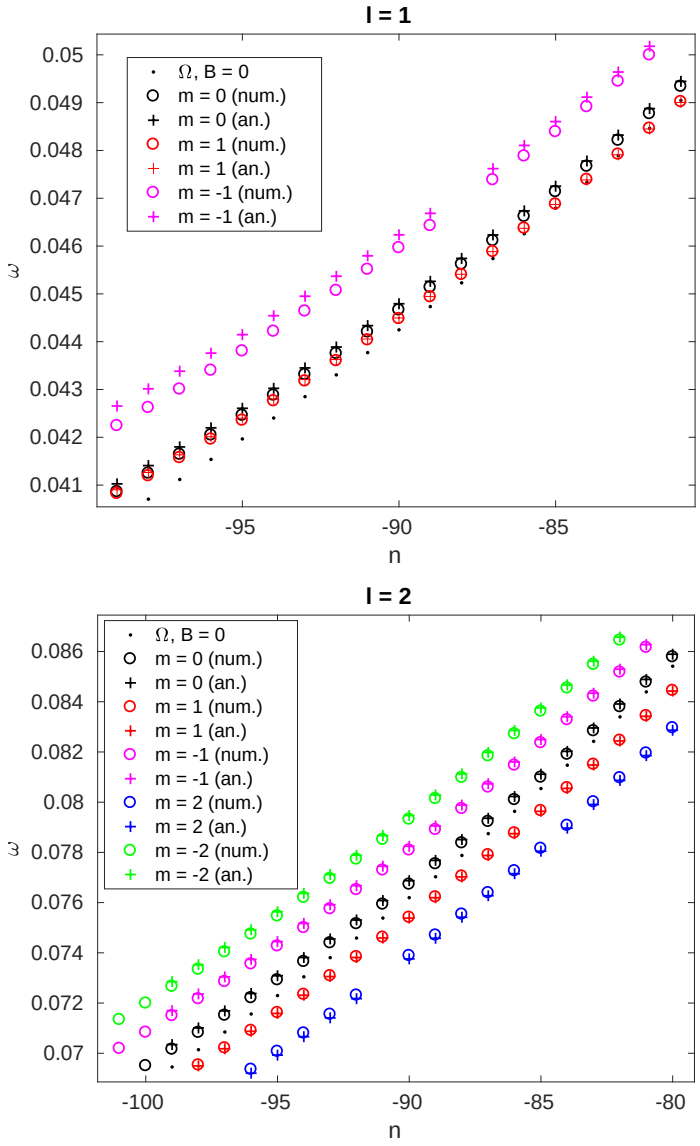

Figure 12.3: Comparison between actual and predicted frequencies of a selection of modes under influence of both rotation and magnetism, for $\ell = 1$ and 2. The functional form of the rotation profile is that given in Equation (7.40), and the central Alfvén speed is scaled to $3\times10^{-5}\sqrt{GM_*/R_*}$.

Conclusions

This thesis has explored the consequences of dynamically significant magnetic fields on the propagation of gravity waves, and attempted to connect this to the problem of global oscillation modes in stars. Most of the investigation has been focused towards the dipole dichotomy problem in red giant stars, where we have endeavoured to construct a plausible mechanism by which strong magnetic fields can damp g-mode oscillations. An initial investigation attempted to achieve this through a resonant damping process, where the energy of the observed modes coupled into torsional Alfvén modes and was lost to dissipation by phase mixing, which involves a turbulent-like cascade to small scales where there are spatial gradients in the Alfvén speed. Further work indicated that this mechanism suffered inconsistencies, and that a more likely scenario involved the disruption of gravity waves upon propagating into a region of dynamically significant field. The damping process is ultimately still phase mixing, but with this affecting the spheroidal modes directly, rather than the secondarily-excited torsional modes. This picture was drawn through a combination of Hamiltonian ray tracing, numerical simulations and analytical arguments, which suggested two possible outcomes for ingoing waves: either trapping or reflection, depending on the relative orientations of the wavevector, direction of stratification and magnetic field lines. Trapped waves would irreversibly acquire significant Alfvén character, phase-mix and thereafter dissipate, while reflected waves would return to the envelope with largely the same outgoing as ingoing wavenumber, reinforcing the global mode. We suggest that this combination of processes can provide a plausible resolution to the dipole dichotomy problem by explaining the stars with depressed mixed modes as being those in which a sufficiently strong magnetic field resides, specifically one for which critical surfaces exist satisfying the gravity-Alfvén wave resonance criterion, where trapping and dissipation by phase mixing can occur.

Besides the red giant dipole dichotomy problem, our results also have application to other astrophysical systems. One example is angular momentum transport in the Sun, which is thought to be aided in part by gravity waves propagating between the envelope (where they are excited by convective motions) and the core. At the interface between the envelope and core lies the tachocline, believed to be a region of strong and actively amplified magnetic fields, which may disrupt gravity wave propagation through the trapping/reflection phenomenon, thus impacting the viability of wave-induced angular momentum transport. The influence of the tachocline field on gravity waves has been studied by a number of authors (Schatzman, 1993; Burgess et al., 2004; Rogers & MacGregor, 2010a,b; MacGregor & Rogers, 2011; Mathis & de Brye, 2011, 2012). While these works treat the case of a purely horizontal magnetic field, our results generalise to other orientations. We draw similar conclusions in that for fields of dynamically significant strengths, significant hindrance to gravity wave propagation occurs. However, for a field of any strength, our results indicate that there will be some part of phase space where propagation will not be adversely affected. The overall consequence for the solar core rotation problem will therefore depend on the spectrum

of gravity waves excited at the base of the convective envelope, as well as the magnitude/distribution of tachocline fields, which is not well known (Barnabé et al., 2017).

Another class of astrophysical systems where our results might be relevant are compact stars (white dwarfs and neutron stars), which are stably stratified through most of their volume and would thus support g-mode oscillations. Such non-radial spheroidal oscillations can generate gravitational radiation, offering a means of probing the interiors of these objects (Papaloizou & Pringle, 1978; Andersson et al., 2011; Glampedakis & Gualtieri, 2017). A significant fraction of compact stars are known to be magnetised at some level. Our results show that strong interactions with gravity waves can occur regardless of the relative values of gas and magnetic pressures, and so it is likely that at least some of the g-mode oscillations in compact objects will be modified in spatial structure by a magnetic field. This may have implications for the efficiency with which g-modes are excited, for example through nonlinear coupling to r- and f-modes which can in turn grow through the Chandrasekhar-Friedman-Schutz instability (Friedman & Schutz, 1975). Furthermore, the enhanced damping provided by the trapping phenomenon for modes in affected regions of phase space is likely to shorten the decay times of these modes. The phenomenon of mode chaos is also expected to apply in this regime, implying the existence of an irregular component to the spectrum. Investigation into the effects of magnetic fields on various oscillation modes of compact stars has been undertaken through normal mode analyses invoking finite-series spherical harmonic expansions (Morsink & Rezania, 2002; Lee, 2010; Asai et al., 2015; Lee, 2018a,b). Such approaches could be complemented by ray calculations of the type described here, offering insight into the local-scale physics of associated wave interactions, and may be a possible course of future work.

References

Adams F. C., Bodenheimer P., Laughlin G., 2005, Astron. Nachr., 326, 913

Aizenman M., Smeyers P., Weigert A., 1977, A&A, 58, 41

Allen C. W., 2000, Allen's Astrophysical Quantities, 3rd edn. The Althone Press, University of London

Andersson N., Ferrari V., Jones D. I., Kokkotas K. D., Krishnan B., Read J. S., Rezzolla L., Zink B., 2011, General Relativity and Gravitation, 43, 409

Arentoft T., Brogaard K., Aguirre V., Kjeldsen H., Mosumgaard J. R., Sandquist E. L., 2017, ApJ, 838, 1

Arnold V. I., 1963, Russian Math. Surv., 18

Asai H., Lee U., Yoshida S., 2015, MNRAS, 3634, 3620

Aurière M., et al., 2007, A&A, 475, 1053

Aurière M., et al., 2008, A&A, 491, 499

Aurière M., et al., 2015, A&A, 574, A90

Auvergne M., Bodin P., Boisnard L., et al., 2009, A&A, 506, 411

Baglin A., et al., 2006, in 36th COSPAR Scientific Assembly.

Ballot J., Barban C., Van't Veer-Menneret C., 2011, A&A, 531, 124

Ballot J., Lignieres F., Reese D. R., 2013, in Goupil M., Belkacem K., Neiner C., Lignières F., Green J. J., eds, , Vol. 865, Studying Stellar Rotation and Convection. Springer Berlin Heidelberg, pp 91–114

Balmforth N. J., 1992, MNRAS, 255, 603

Barker A. J., Ogilvie G. I., 2010, MNRAS, 404, 1849

Barnabé R., Strugarek A., Charbonneau P., Brun A. S., Zahn J. P., 2017, A&A, 601, 1

Basu S., Chaplin W. J., 2017, Asteroseismic data analysis: foundations and techniques. Princeton University Press

Beck P. G., et al., 2011, Science, 332, 205

Bedding T. R., 2013, Solar-Like Oscillations: An Observational Perspective. Cambridge University Press, pp 60–86

Bedding T., Kjeldsen H., 2003, PASA, 20, 203

Belkacem K., Samadi R., Goupil M. J., Kupka F., Baudin F., 2006, A&A, 190, 183

Belkacem K., Goupil M. J., Dupret M. A., Samadi R., Baudin F., Noels A., Mosser B., 2011, A&A, 530, A142

Bernstein I. B., Frieman E. A., Kruskal M. D., Kulsrud R. M., 1958, Proc. Roy. Soc. A, 244, 17

Berry M. V., Tabor M., 1977, Proc. Roy. Soc. Lond. A, 356, 375

Borucki W. J., Koch D., Basri G., Batalha N., Brown T., Caldwell D., Caldwell J., et al., 2010, Science, p. 1185402

Braithwaite J., 2006, A&A, 453, 687

Braithwaite J., Nordlund A., 2006, A&A, 450, 1077

Braithwaite J., Spruit H. C., 2017, R. Soc. Open Sci., 4

Brun A. S., Browning M. K., Toomre J., 2005, ApJ, 629, 461

Burgess C. P., Dzhalilov N. S., Rashba T. I., Semikoz V. B., Valle J. W. F., 2004, MNRAS, 348, 609

Cai W., Gottlieb D., Shu C.-W., 1989, Math. Comp., 62, 389

Campante T. L., 2017, in Campante T. L., Santos N. C., Monteiro M. J. P. F. G., eds, Proceedings of the IVth Azores International Advanced School in Spaec Sciences on Asteroseismology and Exoplanets: Listening to the Stars and Searching for New Worlds. Springer International Publishing

Campbell C. G., Papaloizou J. C. B., 1986, MNRAS, 220, 577

Canuto C., Hussaini M. Y., Quarteroni A., Zang T. A., 1988, Spectral methods in fluid dynamics. Springer-Verlag

Cao H., Wiersig J., 2015, Rev. Mod. Phys., 87, 61

Carroll B. W., Ostlie D. A., 2007, An Introduction to Modern Astrophysics. Pearson Education Limited

Chaisson E., McMillan S., 2014, Astronomy Today, 7th edn. Pearson

Chandrasekhar S., 1931, ApJ, 74, 81

Chaplin W. J., Miglio A., 2013, ARA&A, 51, 353

Charbonneau P., MacGregor K. B., 2001, ApJ, 559, 1094

Choudhuri A. R., 2010, Astrophysics for physicists. Cambridge University Press

Cowling T. G., 1934, MNRAS, 94, 39

Cunha M. S., Gough D., 2000, MNRAS, 319, 1020

Derekas A., et al., 2017, MNRAS, 464, 1553

Dittrich W., Reuter M., 2001, Classical and quantum dynamics: from classical paths to path integrals. Springer-Verlag-Berlin-Heidelberg

Donati J.-F., Landstreet J., 2009, ARA&A, 47, 333

Duez V., Braithwaite J., Mathis S., 2010, ApJ, 724, L34

Dupret M. A., et al., 2009, A&A, 506, 57

Dyson P. L., 1967, JATP, 29, 857

Dziembowski W. A., Goode P. R., 1996, ApJ, 458, 338

Eckart C., 1960, Hydrodynamics of oceans and atmospheres. Pergamon Press

Eggleton P. P., Faulkner J., 1981, in Iben I., Renzini A., eds, Proceedings of the Second Workshop. pp 3–13

Emden R., 1907, Gaskugeln: Anwendungen der mechanischen Wärmetheorie auf kosmologische und meteorologische Probleme. Teubner, B. G.

Featherstone N. A., Browning M. K., Brun A. S., Toomre J., 2009, ApJ, 705, 1000

Ferrario L., de Martino D., Gänsicke B. T., 2015a, Space Sci. Rev., 191, 111

Ferrario L., Melatos A., Zrake J., 2015b, Space Sci. Rev., 191, 77

Flowers E., Ruderman M., 1977, ApJ, 215, 302

Friedman J. L., Schutz B. F., 1975, ApJ, 199, L157

Friedman J. L., Ipser J. R., Parker L., 1986, ApJ, 304, 115

Fuller J., Cantiello M., Stello D., García R. A., Bildsten L., 2015, Science, 350, 423

Fung S. F., Green J. L., 2005, JGRA, 110, 1

García R. A., et al., 2014, A&A, 563, A84

Glampedakis K., Gualtieri L., 2017, arXiv preprint arXiv:1709.07049, pp 1–39

Gottlieb D., Shu C. W., Solomonoff A., Vandeven H., 1992, J. Comput. Appl. Math., 43, 81

Gough D. O., 1977, ApJ, 214, 196

Gough D. O., 1986, in Osaki Y., ed., Hydrodynamic and Magnetohydrodynamic Problems in the Sun and Stars. University of Tokyo, Tokyo, pp 117–143

Gutzwiller M. C., 1990, Chaos in classical and quantum mechanics (Vol. 1). Springer-Verlag New York Inc.

Handberg R., Lund M. N., 2017, A&A, 597, A36

Harding A. K., 2013, Front. Phys., 8, 679

Haselgrove J., 1955, in London Physical Society Report of Conference on the Physics of the Ionosphere. pp 355–364

Hayashi C., 1961, PASJ, 13, 450

Hekker S., Elsworth Y., Angelou G. C., 2018, A&A, 610, A80

Henrichs H. F., 2012, Publications of the Astronomical Observatory of Belgrade, 91, 13

Hentschel M., Richter K., 2002, Phys. Rev. E, 66, 1

Henyey L. G., Lelevier R., Levée R. D., 1955, PASP, 67, 154

Henyey L. G., Forbes J. E., Gould N. L., 1964, ApJ, 139, 306

Heyvaerts J., Priest E. R., 1983, A&A, 117, 220

Houdek G., Dupret M.-A., 2015, Living Reviews in Solar Physics, 12, 1

Howell S. B., Sobeck C., Michael H., et al., 2014, PASP, 126, 398

Huber D., et al., 2019, submitted

Hussain G. A. J., 2012, Astron. Nachr., 333, 4

Hussain G. A. J., Alecian E., 2014, in Petit P., Jardine M., Spruit H., eds, Magnetic fields throughout stellar evolution. International Astronomical Union, pp 1–13

Hussaini M. Y., Zang T. A., 1987, Ann. Rev. Fluid Mech., 19, 339

Kähler H., Weigert A., 1974, A&A, 30, 431

Kallinger T., De Ridder J., Hekker S., et al., 2014, A&A, 570, A41

Kanaan A., Claver C. F., Liebert J., 1999, 11th European Workshop on White Dwarfs, ASP Conference Series, 169, 221

Keller J. B., Rubinow S. I., 1960, Ann. Phys., 9, 24

Kippenhahn R., Weigert A., 1990, Stellar structure and evolution. Springer

Koch D. G., Borucki W. J., Basri G., et al., 2010, ApJL, 713, L79

Kolmogorov A. N., 1954, Dokl. Akad. Nauk SSSR., 98

Landin N. R., Mendes L. T. S., Vaz L. P. R., 2010, A&A, 46, 1

Lane J. H., 1870, Am. J. Sci. Arts, 50, 57

Laughlin G., Bodenheimer P., Adams F. C., 1997, ApJ, 482, 420

LeVeque R. J., Mihalas D., Dorfi E. A., Müller E., 1998, Computational methods for astrophysical fluid flow. Springer

Lecoanet D., Vasil G. M., Fuller J., Cantiello M., Burns K. J., 2017, MNRAS, 466, 2181

Lee U., 2007, MNRAS, 374, 1015

Lee U., 2010, MNRAS, 1457, 1444

Lee U., 2018a, MNRAS, 473, 3661

Lee U., 2018b, MNRAS, 476, 3399

Lesur G., Longaretti P.-Y., 2005, A&A, 444, 25

Lesur G., Longaretti P., 2009, A&A, 320, 309

Lignières F., Georgeot B., 2008, Phys. Rev. E, 78, 1

Lignières F., Georgeot B., 2009, A&A, 500, 1173

Lignières F., Georgeot B., Ballot J., 2010, Astron. Nachr., 331, 1053

MacGregor K. B., Cassinelli J. P., 2003, ApJ, 586, 480

MacGregor K. B., Rogers T. M., 2011, Solar Physics, 270, 417

Main J., Wiebusch G., Welge K., Shaw J., Delos J. B., 1994, Phys. Rev. A, 49, 847

Markey P., Tayler R. J., 1973, MNRAS, 163, 77

Markey P., Tayler R. J., 1974, MNRAS, 168, 505

Mathis S., de Brye N., 2011, A&A, 526, A65

Mathis S., de Brye N., 2012, A&A, 540, A37

Morel P., 1997, A&ASS, 124, 597

Morin J., et al., 2008, MNRAS, 390, 567

Morsink S. M., Rezania V., 2002, ApJ, 574, 908

Möser J., 1962, Nachr. Akad. Wiss. Göttingen, II, 1

Mosser B., et al., 2012a, A&A, 537, A30

Mosser B., et al., 2012b, A&A, 540, A143

Mosser B., et al., 2017a, A&A, 598, A62

Mosser B., Pinçon C., Belkacem K., Takata M., Vrard M., 2017b, A&A, 600, A1

Noyes R. W., Hartmann L. W., Baliunas S. L., Duncan D. K., Vaughan A. H., 1984, ApJ, 279, 763

Ogilvie G. I., 2016, J. Plasma Phys., 82, 100

Osaki Y., 1975, PASJ, 27, 237

Papaloizou J., Pringle J. E., 1978, MNRAS, 184, 501

Parker E. N., 1955, ApJ, 122, 293

Passamonti A., Lander S. K., 2014, MNRAS, 438, 156

Paxton B., Bildsten L., Dotter A., Herwig F., Lesaffre P., Timmes F., 2011, ApJ, 192, 35

Percival I. C., 1973, J. Phys. B: At. Mol. Phys., 6, L229

Petit P., et al., 2008, MNRAS, 388, 80

Peyret R., 2002, Spectral methods for incompressible viscous flow. Springer

Piro A. L., 2005, ApJ, 634, L153

Piro A. L., Bildsten L., 2005, ApJ, 619, 1054

Pomphrey N., 1974, J. Phys. B: At. Mol. Phys., 7, 1909

Prandtl L., 1925, Zeitschrift für Angew. Math. Mech., 5, 136

Prat V., Lignières F., Ballot J., 2016, A&A, 587, A110

Prat V., Mathis S., Lignières F., Ballot J., Culpin P.-M., 2017, A&A, 598, A105

Prat V., Mathis S., Augustson K., Lignières F., Ballot J., Alvan L., Sacha Brun A., 2018, A&A, 615, A106

Prendergast K. H., 1956, ApJ, 123, 498

Prialnik D., 2000, An introduction to the theory of stellar structure and evolution. Cambridge University Press

Putney A., Jordan S., 1995, ApJ, 449, 863

Rauer H., Catala C., Aerts C., Appourchaux T., Benz W., et al., 2014, Experimental Astronomy, 38, 249

Reese D., Rincon F., Rieutord M., 2004, A&A, 427, 279

Reese D. R., Prat V., Barban C., van 't Veer-Menneret C., MacGregor K. B., 2013, A&A, 550, 77

Reiners A., Basri G., Browning M., 2009, ApJ, 692, 538

Ricker G. R., 2015, in American Astronomical Society, ESS meeting #3.

Roberts P. H., Soward A. M., 1983, MNRAS, 205, 1171

Rogers T. M., MacGregor K. B., 2010a, MNRAS, 401, 191

Rogers T. M., MacGregor K. B., 2010b, MNRAS, 410, 946

Ruderman M. A., Sutherland P. G., 1973, Nature Physical Science, 246, 93

Russell H. N., 1931, MNRAS, 91, 951

Schatzman E., 1993, A&A, 271, L29

Schönberg M., Chandrasekhar S., 1942, ApJ, 96, 161

Schou J., Buzasi D. L., 2001, in Proceedings of the SOHO 10/GONG 2000 workshop: Helio- and asteroseismology at the dawn of the millenium. pp 391–394

Schwarzschild M., Härm R., 1959, ApJ, 129

Schwarzschild M., Härm R., 1965, ApJ, 142, 855

Scuflaire R., 1974, A&A, 36, 107

Shibahashi H., 1979, PASJ, 31, 87

Shore S. N., 1992, An introduction to astrophysical hydrodynamics. Academic Press, Inc.

Spitzer L., 1962, Physics of fully ionized gases. John Wiley & Sons, New York

Stello D., Cantiello M., García R. A., Huber D., 2016a, PASA, 33, e011

Stello D., et al., 2016b, Nature, 529, 364

Stello D., Cantiello M., Fuller J., Huber D., García R. A., Bedding T. R., Bildsten L., Aguirre V. S., 2016c, Nature, 529, 364

Stix M., 1989, The Sun. Springer-Verlag

Suijs M. P. L., Langer N., Poelarents A. J., Yoon S. C., Heger A., Herwig F., 2008, A&A, 481, L87

Takata M., 2016a, PASJ, 68, 91

Takata M., 2016b, PASJ, 68, 109

Tassoul M., 1980, ApJSS, 43, 469

Tayler R. J., 1973, MNRAS, 161, 365

Taylor G. I., 1915, Phil. Trans. Roy. Soc. A, 215, 1

Taylor J. B., 1974, Phys. Rev. Lett., 33, 1139

Tobias S. M., Cattaneo F., 2008, JFM, 601, 101

Unno W., 1977, in Spiegel E. A., Zahn J.-P., eds, Problems of Stellar Convection. Springer Verlag, Berlin, pp 315–324

Unno W., Osaki Y., Ando H., Saio H., Shibahashi H., 1989, Nonradial oscillations of stars, 2nd edn. University of Tokyo Press

Vogt H., 1926, Astron. Nachr., 226, 301

Wade G. A., et al., 2015, MNRAS, 456, 2

Walker A. D. M., 2004, Magnetohydrodynamic waves in geospace: The theory of ULF waves and their interaction with energetic particles in the solar-terrestrial environment. IoP Publishing

Weiss N. O., 1966, Proc. R. Soc. Lond. A, 293, 310

Weyl H., 1912, Math. Ann., 71, 441

Wigner E. P., 1967, SIAM Rev., 9, 1

Xu W., Lai D., 2017, Phys. Rev. D, 96, 083005

Yang H., Johns-Krull C. M., 2011, ApJ, 729, 83